Mathematical Modeling, Motion Planning and Control of Elastic Structures with Piezoelectric Elements

Dissertation

zur Erlangung des akademischen Grades
Doktor der Ingenieurwissenschaften
(Dr.-Ing.)
der Technischen Fakultät
der Christian-Albrechts-Universität zu Kiel

vorgelegt von

Andreas Kater

Kiel 2019

Betreuer:	Prof. Dr.-Ing. habil. Thomas Meurer
Zweitgutachter:	Prof. Dr. techn. habil. Andreas Kugi
Drittgutachter:	Prof. Dr.-Ing. Dr.hc. habil. Oliver Sawodny
Datum der Disputation:	18.09.2019

Acknowledgment

Firstly, I want to thank my advisor Prof. Dr.-Ing. Thomas Meurer for his continuous support, trust and guidance. Our discussions were always helpful as well as motivating to me and I could always benefit from his knowledge.

Furthermore, my gratitude goes to all of my colleagues from the Chair of Automatic Control. In particular, I thank Julian Andrej, Philipp Rosenzweig and Dirk Siebelts for all the discussions, ideas and the great working atmosphere. Also my thanks go to Dr.-Ing. Alexander Schaum for all the technical and philosophical conversations as well as for his remarkable and motivating positive attitude.

I would also like to thank all the students I worked with. Teaching was always a pleasure and an opportunity to get an insight in different research areas apart from the smart structures. Representative for the 40 engineers which I advised during their Bachelor and Master thesis I would like to thank Dirk Siebelts, Jan Reinhold, Jan-Philipp Wriedt, Philipp Rosenzweig and Peter Lund.

Also thanks to the team of DB Regio for every extra minute writing time they provided to me.

In addition, I'd like to thank all my friends for their support and understanding. Special thanks goes to Anna-Lena Lange for hunting down typos and germanisms.

Last but certainly not least my earnest gratitude goes to my parents who always supported me during all my life. The most special thanks goes to my wife Signe for all her support, honest feedback and patience. She always offers me hammer and helmet whenever I want to go straight through all barriers. Also thanks to my daughter Ronja for her patience and the joy she brings me.

Abstract

The objective of this work is the development of a motion planning and tracking control approach for elastic structures. Motivated by the morphing wing concept of the field of aerospace engineering a so-called "smart wingsail" defines the center of the presented research.

The motion planning and tracking control approach has to achieve different rest-to-rest motions of the wingsail's transversal displacement. In contrast to existing wingsail designs, e.g., used in high class sailing events like the Americas Cup, the presented "smart wingsail" provides an elastic deformation. The capability to achieve such an elastic deformation leads to a smooth displacement profile which is beneficial considering the interaction with the acting forces of the fluid. The smooth displacement profile decreases the amount of turbulent flows compared to the currently used trimming designs by flaps which denotes a rigid body motion. In addition, the complete profile of the structure can be adjusted, i.e., it offers the possibility to relive pressure of specific parts of the sail to prevent structural damage. The resulting combination of wingsail and control concept can be used in further works as a propulsion system which adjusts the sail to the current sailing and wind condition.

The design of the mechanical structure as well as the control concept of the wingsail relies on the results of proof of concept studies. For this purpose, different systems of interconnected bending beams are considered which emulates parts of the wingsail. In addition these bending beam systems are used for benchmark tests of different control approaches.

The development of the model based control approaches requires an accurate system description. Therefore, the modeling of the distributed parameter system with embedded piezoelectric actuators and partly embedded sensors denotes a crucial part of this work. The modeling itself is done by an analytic energy based approach for the beams' systems, where for the wingsail the finite elements method is used due to the risen complexity of the curved structure. The modeling process takes different damping effects into account and analyzes their impact on the eigenvalue distribution of the system.

To achieve a precise description of the governing dynamics different parameter identification concepts are discussed and applied. This leads to a precise but rather complex system description which covers the measured behavior of the experimental setups. Considering the objective of a real time capable control approach the complexity has to be reduced without a significant loss of accuracy.

For this purpose different model order reduction techniques are discussed and applied. The characteristics of some of these techniques are used during the control design as design parameters. The resulting systems models are the bases of the control designs.

Two different control concepts are presented and evaluated. At first the two-degrees-of-freedom control approach is introduced which combines a flatness-based feedforward control approach with a feedback controller. The main part of the work is done by the feedforward controller which commands about 80 % of the control input. In fact, the flatness-based feedforward control solves the motion planning problem and provides the reference as well as the input trajectories. The algorithm provides real time capability due to its low computational effort which means that the trajectories can be calculated online without the need of offline pre-calculations. In addition, the feedback control approach ensures that the desired reference trajectories of the motion planning approach are reached.

On the other hand, the so-called model predictive control (MPC) approach is presented which is based on the solution of an optimization problem. This optimization problem has to be solved in each time step considering a finite prediction horizon. To achieve an implementation w.r.t. a real time control unit Hildreth's quadratic programming procedure as well as an downsampling by move blocking are considered.

Both concepts are evaluated by numeric analyses and by experiments considering the coupled beam structures as well as the wingsail itself. These analyses display the open loop system behavior as a baseline at first. Hereinafter, different control scenarios are considered. This includes transitions between different steady state displacement profiles as well as the reaction of the open and closed loop system to external disturbances.

Kurzfassung

Ziel dieser Arbeit ist die Entwicklung eines Regelungskonzeptes, welches die gezielte Verformung von elastischen Strukturen mit eingebetteten Aktoren ermöglicht. Als Vorbild dient das Konzept der adaptiven Tragfläche, das im Bereich der Luftfahrt seit Jahrzehnten diskutiert und in Spezialfällen auch verwendet wird.

Das betrachtete Regelungskonzept soll die transversale Auslenkung eines sogenannten elastischen Wingsails regeln. Wingsails finden immer häufiger Anwendung im Bereich von Hochleistungs-Segelveranstaltungen. Hierbei nutzen die gegenwärtigen Konzepte verbaute Klappen um die übertragenden Kräfte im Segel zu regulieren ähnlich wie bei Flugzeugtragflächen. Die verwendete Starrkörperdynamik führt allerdings zu lokalen turbulenten Strömungen oder partiellen Strömungsabrissen und damit zu Leistungseinbußen. Das vorgestellte Konzept basiert auf elastischen Verformungen der gesamten Segelfläche um diese turbulenten Strömungen zu reduzieren oder gänzlich zu vermeiden.

Ziel der Regelung ist es, verschiedene Auslenkungsprofile mittels der eingebetteten Aktorik anzufahren um das Segel an die vorherrschenden Windverhältnisse und Segelbedingungen anpassen zu können. Somit stellt das entworfene Wingsail in Kombination mit der Regelung ein Antriebssystem für weitere Arbeiten im Bereich des Segelsports oder des autonomen Segelns zur Verfügung.

Die Entwicklung der mechanischen Struktur und des Regelkonzeptes des Wingsails wird durch Vorstudien in Form von verkoppelten Balkenstrukturen erst ermöglicht. Diese Balkenstrukturen bilden Teile des Wingsails ab und dienen darüber hinaus als Benchmark Tests für verschiedenen Reglerentwürfe.

Die Verwendung der modellbasierten Reglerentwürfe setzt die mathematische Modellbeschreibung der verschiedenen experimentellen Aufbauten voraus. Aus diesem Grund ist die mathematische Modellierung wichtiger Bestandteil dieser Arbeit. Die Modellierung umfasst sowohl die mechanischen Strukturen mit ihren eingebetteten piezoelektrischen Aktoren als auch die Sensorik, die zum Teil ebenfalls in der Struktur eingebettet ist. Hierbei werden zwei verschiedene Verfahren betrachtet.

Für die Balkensysteme wird ein analytischer energiebasierter Ansatz auf Grundlage des erweiterten Hamiltonischen Prinzips verwendet. Dabei werden verschiedene Dämpfungseffekte betrachtet und ihr Einfluss auf die Eigenwertverteilung des verteilt-parametrischen Systems untersucht. Hingegen wird das Wingsail auf Grund seiner deutlich komplexeren Struktur mit Hilfe der finiten Element Methode (FEM) modelliert.

Die resultierenden Modellbeschreibungen beruhen auf Materialparametern, die zum Großteil unbekannt sind. Diese Parameter müssen in einem zweiten Schritt anhand vom statischen und dynamischen Verhalten der experimentellen Aufbauten identifiziert werden, um eine exakte Beschreibung dieser Vorgänge zu erhalten. Hierzu werden zwei verschiedene Verfahren vorgestellt.

Die resultierenden Beschreibungen spiegeln die Messergebnisse mit einer sehr hohen Genauigkeit wider, allerdings geht diese Genauigkeit mit einer erheblichen Komplexität der Modelle einher. Um die späteren modellbasierten Regler auf Echtzeit-Steuergeräten implementieren zu können, muss die Komplexität durch sogenannte Modell-Ordnungs-Reduktions-Techniken reduziert werden. Hierzu werden verschiedene Verfahren vorgestellt. Dabei weisen einige dieser Verfahren Eigenschaften auf, die im späteren Reglerentwurf berücksichtigt werden können, um so das Reglerergebnis weiter zu verbessern.

Für die Regelung der formveränderlichen Strukturen werden zwei grundlegende Konzepte vorgestellt. Zunächst wird eine Zwei-Freihheits-Grade-Regelung bestehend aus einer flachheitsbasierten Vorsteuerung und verschiedenen Trajektorien-Folgeregelungen entwickelt. Hierbei stellt die Vorsteuerung den größten Teil der Stellgröße zur Verfügung und bestimmt die notwendigen Trajektorien der Sollauslenkungen sowie der notwendigen Stellgrößen. Die Trajektorienfolgeregelung stellt ergänzend sicher, dass die gewünschten Trajektorien auch im Falle von Parameterungenauigkeiten oder externen Störungen erreicht wird.

Das zweite Konzept ist durch das Konzept des modellprädiktiven Reglers beschrieben. Hierbei wird in jedem Zeitschritt ein Optimierungsproblem gelöst, welches einen Prädiktionshorizont an zukünftigen Zeitschritten berücksichtigt. Da dieses Verfahren rechenintensiv ist, wird für die Lösung des Optimierungsproblems die sogenannte *Hildreth's quadratic programming procedure* sowie ein Downsampling für die Berechnung verwendet.

Die Regler werden sowohl anhand von Simulationen als auch mit Hilfe von experimentellen Auswertungen analysiert. Hierbei wird zunächst das jeweilige Verhalten des offenen Regelkreise in Form von Sprungantworten untersucht, um im Anschluss das Verhalten des geschlossenen Regelkreises für verschiedenen Szenarien auszuwerten.

Contents

1. Introduction

Structures equipped with embedded actuators and sensors (so-called smart structures) provide the feature of a controlled transient displacement. Such an adapting structure offers various opportunities for a large field of applications, especially if combined with a feedforward and feedback control strategy allowing to achieve resonant behavior or to reduce oscillation of a system [10, 78].

One example of use is given by the field of adaptive optics in which large telescopes uses deformable mirrors. The objective of such a system is to adjust the shape of the mirror to adapt the optical characteristics. Such an adaption can be used to cope with external atmospheric disturbances, see, e.g. [87]. In addition, the deformable shape can be used to counterbalance vibrations induced by the movements of the telescope itself or by external excitation like vibrations of the building induced by wind, see [15, 16]. The suppression or damping of such vibrations requires a fast actuator concept which is the reason why piezoelectric actuators are commonly used in this domain.

Another example is given by the interaction of a surface with an ambient fluid. An adjustment of the surface may affects the acting forces. Due to this, such an adjustment comes into the focus of the field of locomotion. Here, the main objective is defined as adapting a vehicle's surface or structure to its current situation.

For automotive applications an adaptive spoiler offers the opportunity to adjust the traction of the vehicle. Also other parts of a car can be used to adjust the traction or the drag of a vehicle. An overview of present work in academia and industry focusing on the application of smart memory alloy actuation is provided by [54].

In addition, adapting structures are also discussed in the field of marine engineering. The Maritime Research Institute Netherlands (MARIN) investigates the possibility of adapting bulbs for large vessels using numerical analysis, see [110]. Furthermore, the concept of morphing hulls analyzed by [81] considers the objective to extend the range and reduce the fuel consumption of an unmanned underwater vehicle. As stated by [81] the main idea is motivated by the research in the field of the morphing aircraft.

The idea of a morphing aircraft focuses the adaption of structural aircraft elements to the current flight situation. For this purpose, the design of the wings remains in the center of research because the wings directly affect the maneuverability and fuel consumption of the aircraft. Even small design changes may have a significant impact, e.g., the introduction of Boeing's blended winglets instead of the classic wingtip reduces the fuel consumption and CO_2 emission about 4 %, see [36].

A static wing design is always a sub-optimal design, because each flight phase has its own requirements and the static design represents only a compromise. E.g., during the start the generated lift should be maximized while the drag should be minimized. Within the landing phase the generated drag of the wings is used to decelerate the aircraft and after the touchdown the generated lift should be minimized to prevent the aircraft from bouncing. Furthermore, during the coasting or cruising phase the fuel consumption and emissions denote the center of attention of an airline, leading again to different requirements. This is why in the field of aerospace engineering the morphing wing concept has been discussed, analyzed, tested and manufactured for a long time. An overview of different concepts is provided by [11, 106] considering early designs like the aircraft of the Wright brothers as well as modern unmanned aerial vehicle (UAV) concepts.

The classic fixed-wing concept of modern civil aircrafts also considers some kind of morphing structure elements to control the acting forces via slats, flaps, ailerons, and multi-function spoiler. However, this kind of adaption is performed by rigid body motions which leads to turbulent flows reducing the efficiency and maneuverability of an aircraft.

The elastic morphing wing concept is an attempt to overcome this drawback by admitting elastic deformation of the complete wing geometry or specific parts of the wing during the flight. Due to this, the smooth shape of the wing is conserved which narrows the risk of turbulent flows. An overview of different elastic morphing wing concepts for UAV's is presented by [21], while [38] provides a detailed analysis considering the used concept of the Hydra Technologies S4 UAV.

The elastic wing concept is not only limited to UAVs. The first elastic wing concept was developed in the year 1903 by the Wright brothers considering a wing warping method which changes the twist of the flexible wing, see [11]. Due to the increased air speed and payload of modern aircraft, this lightweight and flexible wing design is not feasible any more. Nevertheless, driven by the potential of an elastic deformation of the wing's shape the recent research is not limited to UAVs or ultralight aircrafts. Currently the U.S. Airforce and the NASA are working on elastic deformable wing elements in term of the so-called "adaptive compliant trailing edge", see [47].

This project has passed flight tests using the so-called "White Knight Aircraft" as well as a modified Gulfstream II, see [55]. In addition, other companies are working on different concepts of morphing aircrafts, e.g., Lockhead Martin Corporation [51], Airbus SE [1] and Tamarack Aerospace Group Inc [108].

Considering civil aerospace engineering the elastic wing concept's market launch will presumably take some time, because these concepts affect safety critical systems. In particular, this means fundamental changes of the primary (ailerons) or secondary (slats, flaps, and multifunction spoiler) flight controls. Development and implementation of such safety critical components leads to special regulatory effects in terms of admission processes for each national or international flight agencies (EASA, FAA, and others) which massively increase the projects' development phase.

However, inspired by the results of the elastic wing concept this work considers different control concepts w.r.t. different elastic structures. The main objective is to develop and compare different control approaches for a piezoelectric actuated wingsail, where the final evaluation considers experimental tests.

The wingsail displays one of many cross links between marine and aerospace engineering. In recent years it has revolutionized high performance sailing. The sail itself defines a structure comparable to an aircraft airfoil which replaces the classic cloth made sails. Such wingsail structures produce strong lifts leading to high velocities of equipped yachts, e.g., Vestas Sailrocket 2 or competition boats like the AC72 and AC50 boat classes of the Americas Cup 2013 and 2017, respectively. In these cases the lift generated by the wingsail is currently controlled by flaps, which means a discrete rigid body motion leading to stall of the fluid and therefore to idle energy of the wind.

Motivated by the idea of the adaptive wing this contribution focuses on an actively controlled adaptive and elastic wingsail concept leading to an adjustment of the shape's profile. The results can be used by further works to actively interact with the attacking airflow depending on the sailing conditions. Besides a further increase of lift, a complete elastic and controllable structure offers the opportunity to reduce stress in specific regions during maneuvers to avoid structural damage of components like the sail itself or the mast.

Besides the wingsail structure itself this work considers two different setups of lightweight, elastic, and interconnected beam structures. These structures are used as pre-studies taking embedded actuators and sensors into account and leading to the final wingsail design.

The origin of the presented systematic and model based motion planning as well as tracking control approach is represented by the mathematical description of the governing dynamic and static effects in terms of the equations of motion, which are introduced in Chapter 2. In fact, this section is split into two parts. The first one addresses the interconnected beam structures which are used as pre-studies for the wingsail setup. Two different coupled beam structures composed by carbon made beams equipped with embedded piezoelectric actuators. Therefore, at first the analytical energy based modeling of the single beam's transversal deflection is discussed considering the extended Hamilton's principle. The deduction of the stored energy is based on the Euler-Bernoulli beam theory denoting a special case of the linear elasticity which belongs to the subject of continuum mechanics, see [76, 23, 109]. In contrast to previous publications, e.g., [98, 9], this work considers different damping models. The analysis is taking combinations of external damping [77] with Kelvin-Voigt, see [77, 78], and structural damping [96, 24, 13] into account and comparing their effects to the eigenvalue distribution of the spatial varying and the finite dimensional system. Due to this and for the sake of self-containedness and completeness the modeling of the single beam is presented in Section 2.1.1.

Hereinafter the respective mechanical setups of the interconnected beam structures are introduced and their spatial and time dependent equations of motion derived using the extended Hamilton's principle. In addition the different sensor concepts are introduced which are used to detect the displacement or the strain of the affected beams. These measurements are later on used as input signal of a state space observer to determine the displacement of the structure at arbitrary positions independent of the position at which the measurement was taken. Furthermore, a finite dimensional approximation is determined considering Galerkin's method. These finite dimensional system descriptions state the origin of the motion planning and tracking control approach used for the real time implementation.

Section 2.2 introduces the mechanical setup of the considered wingsail structure. This structure is characterized by its curved geometry considering a thin but large sailing area which increases the complexity of the modeling process. The modeling itself relies on the linear elasticity and the method of finite elements which leads directly to a finite dimensional description of the equations of motion, see [120, 17]. Here, the acting damping effects are modeled by the so-called Rayleigh damping, see [77, chap. 7] and [120, chap. 16]. Analog to the interconnected beam structures the measurement concept is addressed as well.

These mathematical descriptions rely on the proper determination of the material parameters. Some of these parameters can be measured or are provided by datasheets of the manufacturer. Taking the prototype characteristic of the considered structures into account many parameters have to be determined by an identification process. Chapter 3 presents the two used concepts. The first one relies on the physical understanding of the

considered setup and can only be used efficiently for small systems. Therefore, this applies for the interconnected beam structures which offer the possibility to detach elements and separately identify the associated parameters. The second concept deals with the identification process of the elastic wingsail. For this purpose, an adjoint based optimization process is introduced to increase the numerical efficiency which is necessary due to the fact that the full order system description is used in the identification process. This method relies on the sensitivity analysis [93], in which sensitivity functions (also called gradients of the objective function) are derived by using the equations of motion and the variational calculus. This represents a common practice in the field of aerospace engineering to optimize the airfoils' profile, see [86, 107, 39]. In addition it is quite popular in the field of seismology [111, 32, 72], medical engineering [30, 66] and flow control [43].

The resulting mathematical descriptions are capable of covering the measured behavior of the flexible structures. However, the finite dimensional systems are characterized by huge systems of ordinary differential equations (ODEs) leading to immense computational effort which is not feasible for real time applications. Therefore, Chapter 4 introduces three different model order reduction (MOR) methods with the objective to reduce the computational effort without a significant loss of accuracy w.r.t. the original system description. An overview as well as detailed information about the main MOR methods are provided by [5]. The considered methods belong to the group of singular value decomposition (SVD) based techniques. In particular, the model truncation [5], the second order balanced truncation [22, 92], and the proper orthogonal decomposition (POD) [112, 113] are introduced and applied.

Subsequently Chapter 5 introduces the considered motion planning and tracking control approaches to accomplish a desired rest-to-rest motion of the elastic structures' displacement. For this purpose, two different model based concepts are discussed and later on evaluated by simulation and tests on the experimental setups.

The first strategy is based on a systematic design of a two-degrees-of-freedom control approach composed of a feedforward control, to solve the motion planning problem, and a feedback control to acquire robustness against model uncertainties and external disturbances. The solution of the motion planning problem relies on the concept of differential flatness, which is based on a parametrization of the system states and inputs by a flat output and its derivatives' is utilized. In recent years the original concept [34] was extended to linear and nonlinear distributed parameter systems [61, 78, 97]. A flatness-based design systematic of the motion planning problem yields by taking the properties of a Riesz spectral systems [79, 78] into account considering the spatially distributed inputs. This systematic addresses late as well as early lumping approaches. It has been successfully applied in recent works considering simple structures like single bending beams [99, 101] and plates [98]. In this work the approach is extended and applied to complex structures in terms of the interconnected beams and the wingsail structure. In general, this work is focused on the early lumping approach, see Section 5.1. However, for the sake of completeness Appendix B takes the late lumping approach into account for the example of a system of interconnected Euler-Bernoulli beams. The resulting feedforward control, see Section 5.1, is amended by a feedback controller which ensures that the reference trajectory is reached. For this purpose, different controllers are introduced and evaluated. The list of considered feedback controllers reads a simple output feedback approach in terms of ID-T_1 control, different state feedback controllers based on the Ackermann and the linear quadratic regulator as well as extensions to ensure steady state accuracy, and a Lyapunov-based control approach, see Section 5.3.

The second control strategy considers a model predictive control (MPC) approach, see Section 5.4. MPC explicitly uses the mathematical model to predict the future dynamics of a system. In each sampling step the optimal control input is determined by solving an optimization problem. The associated cost or objective function consists of the predicted control error and the control input within the prediction horizon, see [20, 90]. Furthermore, the optimization process allows to consider further constraints [75, 114], e.g., limited actuator behavior. Due to this, the motion planning process as well as the design of a feedforward control is included by design. MPC is well studied for linear systems as well as for nonlinear systems [3, 42, 33, 2] and can be found in a large field of applications, e.g., process and chemical industries. In general, MPC is applied to systems characterized by slow dynamics. Due to this, the optimization problem can be solved within each sampling step in real time. On the contrary the considered smart structures are characterized by fast oscillatory dynamics which reduces the sample time of the real time process. To reduce the computational effort the optimization problem is solved by using Hildreth's quadratic programming procedure [114]. Furthermore, the degrees of freedom of the optimization problem can be reduced by fixing the input variables over several time-steps [19, 68]. Such a move blocking method by downsampling is introduced so the MPC approach can be executed in real-time with a sufficiently high sampling frequency to cover the dynamic of the system.

Both control strategies rely on the state information of a state observer. To improve the signal to noise ratio a Kalman filter is used, see Section 5.2.

In addition to the presented control strategies there exist other control concepts which can be used to adjust a desired shape, e.g., passivity based methods [64], H_2 and H_∞ control approaches [63]. In addition, for the

attenuation of vibrations also fuzzy [71, 28] and back propagation neural network control approaches [88] have been applied.

Chapter 6 evaluates the different control strategies considering transient simulations and full functionality tests on the experimental setup. The experimental evaluation is taking a real time implementation of the control approaches into account driven by a rapid prototyping system. At the beginning of this chapter, the results of the interconnected beam structures are analyzed. As mentioned before these structures are proof of concept studies as well as benchmark tests of the wingsail's mechanical as well as control design. The results of the wingsail structure are subsequently discussed in detail.

Finally, Chapter 7 concludes the result of this work and provides an outlook of further actions within the smart wingsail project.

2. Mathematical Modeling

The mathematical description of the governing dynamic and static effects of a considered process enables the efficient development of control and observer concepts. In addition, such a description speeds up the complete development process and reduces costs by the use of numeric simulations. Simulations can be used during the complete development cycle, e.g., for proof of concept studies, the selection of actuators and sensors, software in the loop tests, control design, and complete system tests.

Below, the mathematical modeling of the considered flexible structures is introduced. The objective of such a model is to achieve a high fidelity system description enabling the design of model based control concepts. Furthermore, it provides the opportunity to use simulations to verify these approaches before the experimental test takes place.

The modeling of the considered beam structures uses the extended Hamilton's principle which relies on the analytically determined energy of the beams. For this purpose, the governing energies of a single Euler-Bernoulli beam are derived using the basic concepts of continuum mechanics taking the constitutive equations into account which describes the piezoelectric actuation. This states the origin of the modeling of the equations of motion of the coupled beam structures serving as proof of concept as well as benchmark studies for the considered wingsail structure and the associated control concepts.

Afterwards the equations of motion of the wingsail are introduced. Due to the complex structure and geometry of the wingsail, this is done by making use of the finite element method (FEM).

2.1. Equations of Motion of Single Cantilever Beams and Coupled Beams Structures

In the field of engineering it is common practice to approximate a complex process to obtain a simple but sufficient description focusing on the core effects. Most of the time further analysis of the core effects results in the solution of the original issue. This is why the classic beam theory remains a common tool for the domains of mechanical and civil engineering even today. Many structures consist of assemblies of beams. Furthermore, a large number of machine parts can be described by beams, like lever arms or shafts, wings, and fuselages. Also the interaction between loads applied by moving objects on a structure or the damage of a structure can be analyzed by beam theory [117, 119]. Even smaller structures like nanotubes [25] can be modeled using the beam theory.

Here, the considered elastic and interconnected beam structures in terms of a vertical beam configuration and delta beam configuration denote proof of concept studies for the subsequently analyzed wingsail structure, see Section 2.2.

As mentioned before the objective of this section is the determination of the equations of motion for interconnected beam structure. The section is organized as follows. At first the commonly appearing energies of a single beam are deduced on the basis of continuum mechanics considering the constitutive equations describing the material properties including the piezoelectric actuation. Thereafter, the mechanical configuration of the considered vertical and delta beam structure is presented. Based on the presented configurations the associated equations of motion of the displacement are deduced using the extended Hamilton's principle.

2.1.1. Modeling of an In-Domain Actuated Beam

In general, the determination of the energy stored in a single beam with embedded actuation can be found, e.g., in [98, 9]. However, for the sake of self-containedness and completeness it is presented below.

The governing effects which are responsible for the beam's displacement are described by the concepts of continuum mechanics which explain the deformation of a structure in response to forces and moments, see, e.g., [76, 23, 109]. In the following, the kinematics of a single beam with embedded actuation is deduced by the assumption of the Euler-Bernoulli beam theory to provide a deeper understanding of the underlying physics. Furthermore, the necessary constitutive equations are introduced. Also the acting dissipative effects namely damping are discussed. Taking all of these information into account the governing energies of a single beam are finally deduced.

2.1.1.1. Kinematics of an Euler-Bernoulli Beam

The kinematics are introduced considering the Euler-Bernoulli beam theory and the underlying assumption.

Assumption 2.1 *Taking Euler-Bernoulli beam theory into account the beam's deformation is small compared to its thickness. In addition, perpendicular plane sections w.r.t. the neutral axis (see dashed black line of Fig. 2.1) in the undeformed state stay plane, undeformed, and perpendicular to the neutral axis during deformation.*

Fig. 2.1 displays the schematic of a beam in its deformed and undeformed state. The governing kinematics are deduced taking into account the depicted geometry and its changes caused by the acting external force or bending moment.

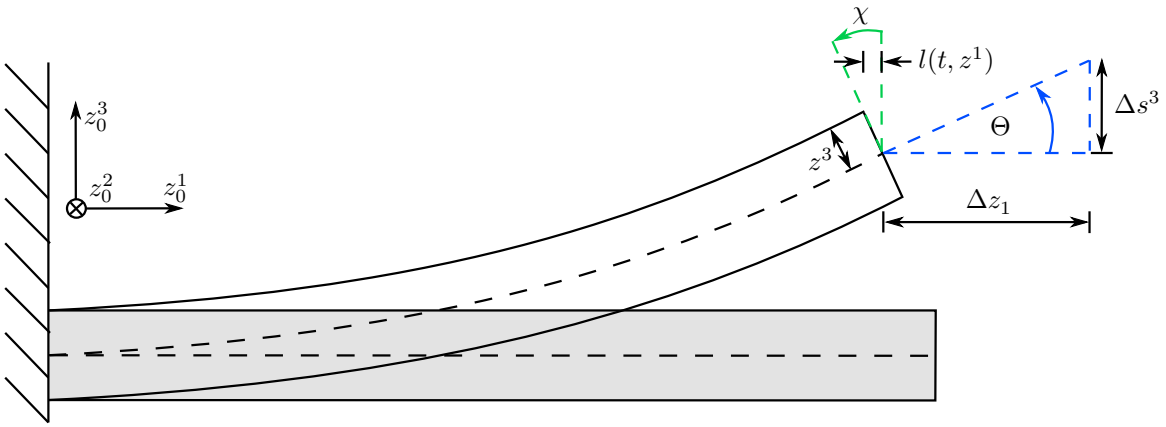

Figure 2.1.: Schematic of an undeformed and deformed beam (transversal displacement).

The transversal acting force or bending moment results in an out-of-plane or transversal displacement $\bar{s}_3(t, z^1) = s_3(t, z^1)$ causing an additional small longitudinal displacement of the beam $\bar{s}_1(t, z^1)$. From Fig. 2.1 the longitudinal displacement can be deduced as

$$\bar{s}_1(t, z^1) = s_1(t, z^1) - l(t, z^1). \tag{2.1}$$

The longitudinal displacement is split into a translatory part denoted by $s_1(t, z^1)$ and a rotatory part of the cross section $l(t, z^1)$.

The supplementary displacement $l(t, z^1)$ can be determined considering the trigonometric relations depicted in Fig. 2.1. In addition, Assumption 2.1 applies and results in the small angle approximation

$$\sin(\chi) = \frac{l(t, z^1)}{z^3} \quad \Rightarrow \quad \chi = \frac{l(t, z^1)}{z^3} \quad \Rightarrow \quad l(t, z^1) = z^3 \chi. \tag{2.2}$$

Furthermore, $\chi = \Theta$ holds true, where Θ is defined as

$$\tan(\Theta) = \frac{\Delta s_3(t, z^1)}{\Delta z^1} \quad \Rightarrow \quad \Theta = \frac{\Delta s_3(t, z^1)}{\Delta z^1} = \partial_{z^1} s_3(t, z^1). \tag{2.3}$$

This implies

$$l(t, z^1) = z^3 \partial_{z^1} s_3(t, z^1). \tag{2.4}$$

As a consequence the components of the beam's displacement vector are given by

$$\begin{aligned} \bar{s}_1(t, z^1) &= s_1(t, z^1) - z^3 \partial_{z^1} s_3(t, z^1), \\ \bar{s}_2(t, z^1) &= 0, \\ \bar{s}_3(t, z^1) &= s_3(t, z^1), \end{aligned} \tag{2.5}$$

2.1.1.2. Mechanical Constitutive Equation

The mechanical constitutive equation describes the relation between the strain and stress tensor $\underline{\epsilon}(\boldsymbol{s})$, $\underline{\sigma}(\boldsymbol{s})$, respectively. Considering [23] the symmetric strain tensor's elements are defined as

$$\epsilon_{im} = \partial_{z^i} \bar{s}_m(t, z^1) = \frac{1}{2}\left(\partial_{z^i} \bar{s}_m(t, z^1) + \partial_{z^m} \bar{s}_i(t, z^1)\right) \quad \forall \quad i, m \in \{1, 2, 3\}. \tag{2.6}$$

Taking the displacement vector of the beam (2.5) into account the non-zero elements of the strain tensor of the beam are given by

$$\epsilon_{11} = \partial_{z^1} s_1(t, z^1) - z^3 \partial_{z^1}^2 s_3(t, z^1), \quad \epsilon_{33} = \partial_{z^3} s_3(t, z^1) = 0. \tag{2.7}$$

Hooke's law [23, chap. 9],[111] provides the relation between the elements of the strain and stress tensor, usually this is denoted considering Einstein's summation convention

$$\sigma^{im} = E^{imkl} \epsilon_{kl}, \tag{2.8}$$

with E^{imkl} denoting Young's modulus also known as elastic modulus describing the material characteristics for which the following assumption holds.

Assumption 2.2 *All materials used for the construction of the beam are isotropic and homogeneous meaning they act in the same manner in all directions and are characterized by a uniform distribution of density and therefore mass. For Young's modulus this means*

$$E^{imkl} = E^{mikl}, \quad E^{imkl} = E^{imlk}.$$

In addition, considering Assumption 2.1 there is no lateral contraction acting which means that $E^{1111} = E$ is the only relevant element of the tensor leading to

$$\sigma^{11} = E\big(\partial_{z^1} s_1(t, z^1) - z^3 \partial_{z^1}^2 s_3(t, z^1)\big). \tag{2.9}$$

2.1.1.3. Piezoelectric Constitutive Equations and Actuation Concepts

The second set of constitutive equations provides the relation between the electric field strength, electrical flux density, the mechanical stress, and strain. This applies only in the spatial domain of the embedded piezoelectric macro-fiber composite (MFC) patches, which are used as actuators for the interconnected beam and wingsail structure. The MFC-patches consist of piezoceramic fibers aligned with the z^1-axis which are embedded in an epoxy carrier structure. Above and underneath of the embedded fibers are interdigitated electrode patterns arranged perpendicular to the fibers, see Fig. 2.2. This structure exploits the indirect piezoelectric effect in which voltage is converted to mechanical strain between the electrodes, which results into a bending moment due to the geometry and the mounting, see [9].

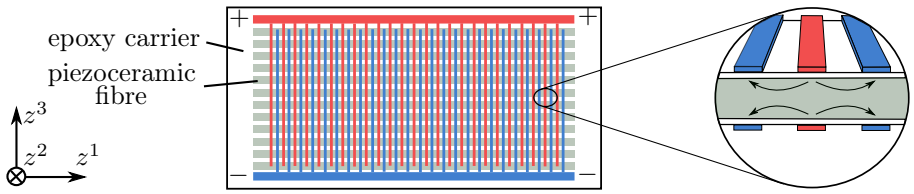

Figure 2.2.: Schematics of an MFC-actuator.

Taking [78, 10] into account the indirect and direct piezoelectric effect are represented by the electric constitutive equations

$$\begin{aligned} \sigma_{\mathrm{a}_k}^{im} &= E_{\mathrm{a}_k}^{imkl} \epsilon_{kl,\mathrm{a}_k} - a_{k,\mathrm{a}_k}^{im} D_{\mathrm{a}_k}^{k}, \\ E_{i,\mathrm{a}_k}^{\mathrm{el}} &= -a_{i,\mathrm{a}_k}^{mk} \epsilon_{mk,\mathrm{a}_k} + \beta_{im,\mathrm{a}_k} D_{\mathrm{a}_k}^{m}, \end{aligned} \tag{2.10}$$

where a_{i,a_k}^{mk} and β_{im,a_k} denote the piezoelectric material parameter and the dielectric constant, respectively. In addition $E_{i,\mathrm{a}_k}^{\mathrm{el}}$ and $D_{\mathrm{a}_k}^{i}$ represent the electric field strength and the electric flux density in $i \in \{1, 2, 3\}$ direction. To distinguish between the material constants of the carbon made carrier and the MFC-actuators, the actuators' parameters are marked by the index a_k. Hereby $k \in \{1, \ldots, p\}$ denotes a counting index of the p single actuators or patch pairs mounted on the beam. The counting starts at clamped position of the structure and ends at its free tip.

Due to the considered kinematics (2.5), the Assumption 2.1 and the fact that the electric field can be approximated by an exclusive homogeneous field component $E_{1,\mathrm{a}_k}^{\mathrm{el}}$ which leads to an exclusive field component of the flux density $D_{\mathrm{a}_k}^{1}$ the electric constitutive equations simplify to

$$\begin{aligned} \sigma_{\mathrm{a}_k}^{11} &= E_{\mathrm{a}_k}^{1111} \epsilon_{11,\mathrm{a}_k} - a_{1,\mathrm{a}_k}^{11} D_{\mathrm{a}_k}^{1}, \\ E_{1,\mathrm{a}_k}^{\mathrm{el}} &= -a_{1,\mathrm{a}_k}^{11} \epsilon_{11,\mathrm{a}_k} + \beta_{11,\mathrm{a}_k} D_{\mathrm{a}_k}^{1}. \end{aligned} \tag{2.11}$$

In fact, the MFC-actuators are controlled by the electric voltage $U_{\mathrm{a}_k}^{\mathrm{MFC}}$ and describe the physical system input. Hence, the flux density is substituted by the voltage

$$U_{\mathrm{a}_k}^{\mathrm{MFC}} = \int_{e_s}^{0} E_{i,}^{\mathrm{el}}\, \mathrm{d}z^1 = \beta_{11,\mathrm{a}_k} e_s D_{\mathrm{a}_k}^1 \quad \Rightarrow \quad D_{\mathrm{a}_k}^1 = \frac{U_{j,\mathrm{a}_k}^{\mathrm{MFC}}}{\beta_{11,\mathrm{a}_k} e_s}, \tag{2.12}$$

where e_s denotes the distance between two neighboring electrodes of an MFC-patch, see the magnifying glass of Fig. 2.3.

Remark 2.1 *The voltage range of the used MFC-patch is given by* $U_{a_k}^{MFC} \in [-500, 1500]\,\mathrm{V}$ *[105]. To obtain a symmetric input range the constant supply voltage or bias* $U_0 = 500\,\mathrm{V}$ *is applied*

$$U_{a_k}^{MFC} = U_0 + U_{a_k}, \tag{2.13}$$

leading to a symmetric voltage range $U_{a_k} \in [-1000, 1000]\,\mathrm{V}$ *which is subsequently used as control input.*

This work discusses two different actuation concepts considering MFC-patches. The construction designs are presented by the schematics of Fig. 2.3. The single patch actuation concept is used in the surface interconnected structure of beams forming a delta configuration, see Section 2.1.3. In addition, the pairwise actuation concept applies in the pointwise interconnected structure of vertically aligned beams, see Section 2.1.2.4.

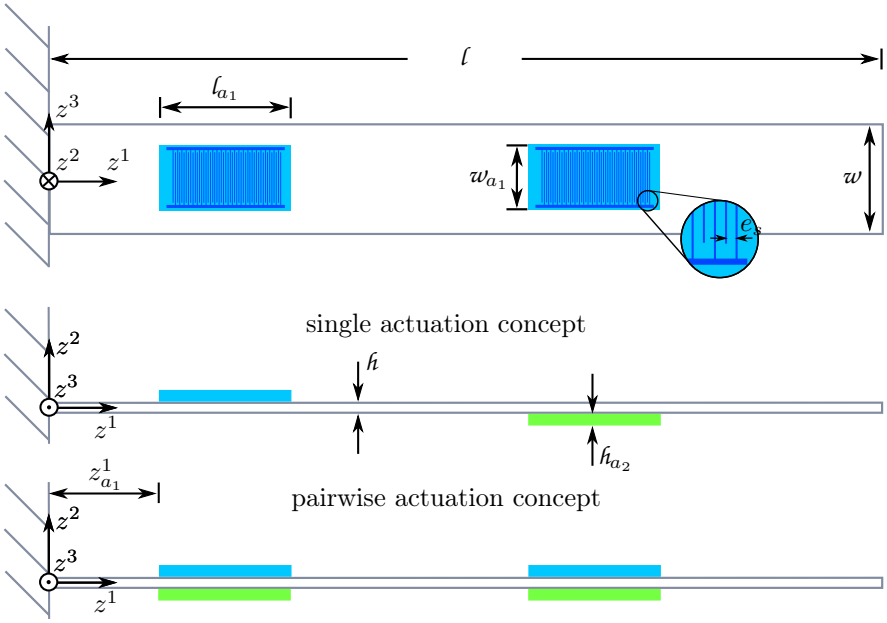

Figure 2.3.: Schematic of a single beam in a clamped-free configuration equipped considering single and pairwise actuation by MFC-actuators.

In the pairwise actuation concept two MFC-patches are placed symmetrically on the carrier structure to enhance the effect by an asymmetric voltage signal leading to an agonist-antagonist behavior like a pair of muscles. In other words, the patch placed on the front is supplied by a positive voltage leading to an enlargement of the MFC-patch, where the negative voltage of the MFC-patch on the back results in a shortening of the patch or vice versa which doubles the acting bending moment.

It has to be mentioned that this kind of modeling of the piezoelectric actuation is based on the following assumption.

Assumption 2.3 *The MFC-patches act linearly, due to an integrated hysteresis and creeping compensation [62, 100] counterbalancing the intrinsic creeping behavior and hysteresis effects.*

Fig. 2.4 displays the results of the compensation. The presented measurements are based on a single beam using $p = 1$ MFC-patch pairs, see [94]. The left subplot illustrates the displacement of a single beam considering an acting feedforward control. In the uncompensated case (blue curve) the displacement at the considered points of interest $s_{\mathrm{u},3}(t, z_{\mathrm{pi}}^1)$, here the beam's tip, shows a large deviation compared to the desired displacement

$s_3^*(t, z_{\mathrm{pi}}^1)$. This error is caused by the hysteresis corrupting the voltage to stress relation. Furthermore, this plots illustrates the creeping effect in the uncompensated case. During the steady state which should be reached after $t = 3\,\mathrm{s}$ the measured displacement "creeps" from $s_{\mathrm{u},3}(t, z_{\mathrm{pi}}^1) = 6 \times 10^3\,\mathrm{m}$ to $s_{\mathrm{u},3}(t, z_{\mathrm{pi}}^1) = 9 \times 10^3\,\mathrm{m}$. The behavior considering a compensation $s_{\mathrm{c},3}(t, z_{\mathrm{pi}}^1)$ (green curve) displays a strong reduction of both effects. Nevertheless, there are still some residual effects left which have to be addressed by a control approach.

The right subplot of Fig. 2.4 illustrates the hysteresis by comparing the applied voltage against the achieved displacement. Here, the uncompensated mode $s_{\mathrm{u},3}(z_{\mathrm{pi}}^1, U_{\mathrm{a}_1})$ (blue curve) displays the characteristic hysteresis' shape. In contrast the compensated behavior $s_{\mathrm{c},3}(z_{\mathrm{pi}}^1, U_{\mathrm{a}_1})$ shows a nearly linear relation between voltage and displacement. Concluding these experimental analysis Assumption 2.3 is valid.

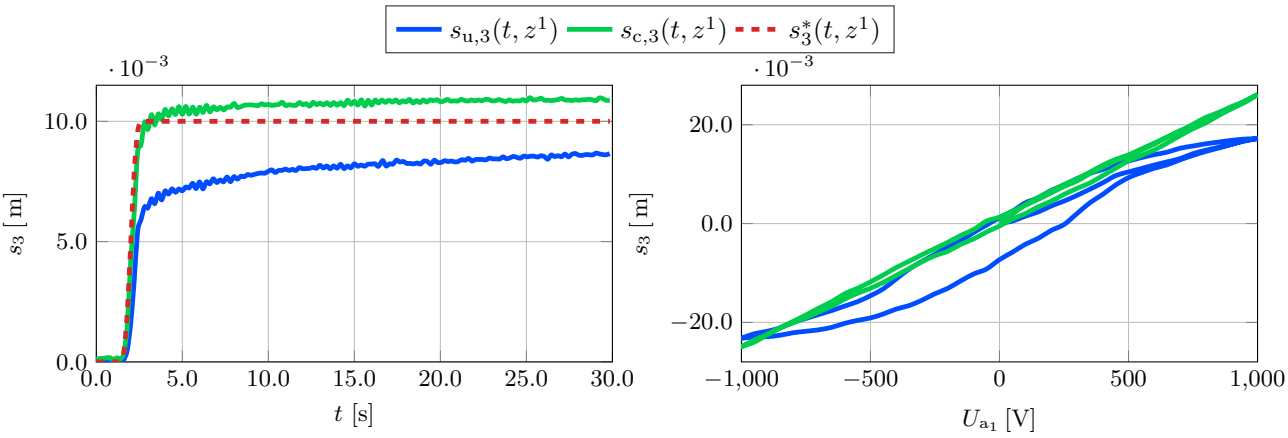

Figure 2.4.: *Left:* Illustration of the creeping and hysteresis' compensation on the example of a feedforward controled single beam, where $s_3^*(t, z^1)$ denotes the reference trajectory.
Right: Illustration of the reduction of the hysteresis effect due to the applied compensation. The uncompensated displacement is presented by $s_{\mathrm{u},3}(t, z^1)$, where $s_{\mathrm{c},3}(t, z^1)$ denotes the voltage dependent displacement considering compensation.

The following section determines the stored energy of the system considering single and pairwise actuation concepts to provide a framework for the subsequent modeling of the interconnected beam structures.

2.1.1.4. Stored Energies and Virtual Work of the Non-conservative Forces

In this section the potential and kinetic energy as well as the work of the non-conservative forces of the single beam are deduced. These terms are crucial to determine the equations of motion of the structures by applying the extended Hamilton's principle.

The energy terms as well as the virtual work rely on the spatial characteristics of the beam. Taking Assumption 2.2 into account the beam's components are made by isotropic and homogeneous materials. With this the spatial characteristics have only to provide the longitudinal positions of the covered areas at which the MFC-patches are mounted. This information enables the differentiation if only the material parameters of the carbon made carrier apply or additionally the parameters of the actuator have to be considered. As a mathematical description a notch function can be constructed by Heaviside functions $h(z^1)$

$$\Omega_{\mathrm{a}_k}(z^1) = h(z^1 - z_{\mathrm{a}_k}^1) - h(z^1 - z_{\mathrm{a}_k}^1 + \ell_{\mathrm{a}_k}), \tag{2.14}$$

where ℓ_{a_k} denotes the length of the k^{th} patch and $z_{\mathrm{a}_k}^1$ the associated mounting point, see Fig. 2.3. With this the beam's kinetic and potential energy as well as the virtual work of the non-conservative forces are determined.

Kinetic Energy In general, the kinetic energy is given by

$$W_{\mathrm{kin}} = \frac{1}{2} \int_{\Omega} \rho(z^1) \partial_t \bar{\boldsymbol{s}}^T \partial_t \bar{\boldsymbol{s}} \, \mathrm{d}\Omega, \tag{2.15}$$

where $\rho(z^1)$ denotes the spatially varying density per unit length and Ω reflects the spatial domain of the beam or in other words its volume. Due to the fact, that the magnitude of the longitudinal displacement is negligible

$s_1(t,z^1) \approx 0$ the kinetic energy results in

$$W_{\text{kin}} = \frac{1}{2}\int\limits_{\Omega} \rho(z^1)\big(\partial_t \bar{s}_3(t,z^1)\big)^2 \,\mathrm{d}\Omega = \frac{1}{2}\int\limits_{\Omega} \rho(z^1)\big(\partial_t s_3(t,z^1)\big)^2 \,\mathrm{d}\Omega. \tag{2.16}$$

Taking the geometry of the beam into account considering single MFC-patch actuation marked by the superscript s and evaluating the domain integral in z^2- and z^3-direction the kinetic energy results in

$$W_{\text{kin}}^{\text{s}} = \frac{1}{2}\int\limits_{0}^{\ell} \mu^{\text{s}}(z^1)\big(\partial_t s_3(t,z^1)\big)^2 \,\mathrm{d}z^1 \quad \text{with} \quad \mu^{\text{s}}(z^1) = \rho A + \sum_{k=1}^{p_j} \rho_{\text{a}_k} A_{\text{a}_k} \Omega_{\text{a}_k}(z^1), \tag{2.17}$$

where $A = \hbar w,\ A_{\text{a}_k} = \hbar_{\text{a}_k} w_{\text{a}_k}$ denotes the cross section of the carrier and MFC-patches, respectively. In addition, the densities are described by ρ and ρ_{a_k}.

The kinetic energy of the pairwise actuation concept is obtained similarly marked by the superscript p and is given by

$$W_{\text{kin}}^{\text{p}} = \frac{1}{2}\int\limits_{0}^{\ell} \mu^{\text{p}}(z^1)\big(\partial_t s_3(t,z^1)\big)^2 \,\mathrm{d}z^1 \quad \text{with} \quad \mu^{\text{p}}(z^1) = \rho A + \sum_{k=1}^{p_j} 2\rho_{\text{a}_k} A_{\text{a}_k} \Omega_{\text{a}_k}(z^1). \tag{2.18}$$

Potential Energy In general, the potential energy of the single beam with embedded actuation is given by

$$W_{\text{pot}} = W_{\text{g}} + W_{\text{st}} + W_{\text{el}}, \tag{2.19}$$

with W_{g}, W_{st}, W_{el} denoting the energy terms introduced by gravity, strain, and electricity, respectively.

Taking the orientation of the considered beam structures into account gravity does not affect the structure $W_{\text{g}} = 0$, because it only acts in z^2 direction in which the beam provides the highest stiffness caused by its geometry and mounting.

According to [78] the residual energy terms are defined as

$$W_{\text{st}} = \int\limits_{\Omega} \sum_{i=1}^{3}\sum_{m=1}^{3} \sigma^{im}\epsilon_{im} \,\mathrm{d}\Omega, \quad W_{\text{el}} = \int\limits_{\Omega} \sum_{i=1}^{3} E_{i,}^{\text{el}} D^i \,\mathrm{d}\Omega. \tag{2.20}$$

Considering the stress tensor (2.9) and the fact that the longitudinal displacement can be neglected the remaining energy terms simplify to

$$W_{\text{st}} = \int\limits_{\Omega} E^{1111}\big(z^3\partial_{z^1}^2 s_3(t,z^1)\big)^2 \,\mathrm{d}\Omega, \quad W_{\text{el}} = \sum_{k=1}^{p_j}\int\limits_{\Omega} 2a_{1,\text{a}_k}^{11} D_{\text{a}_k}^1 z^3 \partial_{z^1}^2 s_3(t,z^1) + \beta_{11,\text{a}_k}\big(D_{\text{a}_k}^1\big)^2 \,\mathrm{d}\Omega. \tag{2.21}$$

The evaluation of W_{st} considering the beam's geometry using the single MFC-patch actuation results in

$$W_{\text{st}}^{\text{s}} = \frac{1}{2}\int\limits_{0}^{\ell} \Lambda^{\text{s}}(z^1)\big(\partial_{z^1}^2 s_1(t,z^1)\big)^2 \,\mathrm{d}z^1, \quad \text{with} \quad \Lambda^{\text{s}}(z^1) = E^{1111} I + \sum_{k=1}^{p_j} E_{\text{a}_k}^{1111} I_{\text{a}_k} \Omega_{\text{a}_k}(z^1), \tag{2.22}$$

where $I = w\hbar^3/12$, $I_{\text{a}_k} = w_{\text{a}_k}[(\hbar/2 + \hbar_{\text{a}_k})^3 - (\hbar/2)^3]$ describe the area momentum of inertia of the carrier and the MFC-patches.

Evaluating the integral for the beam geometry actuated by pairwise MFC-patches leads to

$$W_{\text{st}}^{\text{p}} = \frac{1}{2}\int\limits_{0}^{\ell} \Lambda^{\text{p}}(z^1)\big(\partial_{z^1}^2 s_1(t,z^1)\big)^2 \,\mathrm{d}z^1, \quad \text{with} \quad \Lambda^{\text{p}}(z^1) = E^{1111} I + \sum_{k=1}^{p_j} 2E_{\text{a}_k}^{1111} I_{\text{a}_k} \Omega_{\text{a}_k}(z^1) \tag{2.23}$$

Analog, the electrical energy is determined. Evaluating the volume integral taking the geometry of the beam into account and substituting the flux density by the voltage considering (2.12) leads to the electric energy. In

case of the single MFC-patch actuated beam the location of the patches, either on the front ($z^2_{\mathrm{a}_k} > 0$) or the back ($z^2_{\mathrm{a}_k} < 0$) of the beam, affects the sign of the evaluation result

$$\begin{aligned} W^{\mathrm{s}}_{\mathrm{el}} &= \frac{1}{2}\int_0^{\ell}\sum_{k=1}^{p_j} \operatorname{sign}(z^2_{\mathrm{a}_k})\Gamma^{\mathrm{s}}_{\mathrm{a}_k}(z^1)U^{\mathrm{MFC}}_{\mathrm{a}_k}(t)\partial^2_{z^1}s_j(t,z^1)\,\mathrm{d}z^1, \quad \text{with} \\ \Gamma^{\mathrm{s}}_{\mathrm{a}_k}(z^1) &= \frac{A_{\mathrm{a}_k}a^{11}_{1,\mathrm{a}_k}(\hbar+\hbar_{\mathrm{a}_k})}{2\beta_{11,\mathrm{a}_k}e_s}\Omega_{\mathrm{a}_k}(z^1). \end{aligned} \tag{2.24}$$

Here, $A_{\mathrm{a}_k} = \hbar_{\mathrm{a}_k} w_{\mathrm{a}_k}$ denotes the area of the cross section of the patch. The constant voltage bias U_0, which is part of the applied voltage $U^{\mathrm{MFC}}_{\mathrm{a}_k}$ introduces a static tension on the carrier, which is discussed in Section 2.1.3.

The evaluation considering the beam's geometry using the pairwise MFC-patches requires to distinguish between different cases depending on the applied voltage. As mentioned before the MFC-patch pairs work as one unique actuator. Therefore, two scenarios regarding the applied patch's voltage signal mounted on the beam's front $U^{\mathrm{f}}_{\mathrm{a}_k}$ and back $U^{\mathrm{b}}_{\mathrm{a}_k}$ can be considered

- symmetric actuation $U^{\mathrm{f}}_{\mathrm{a}_k} = U^{\mathrm{b}}_{\mathrm{a}_k} = U_0 \pm U_{\mathrm{a}_k}$,
- asymmetric actuation $U^{\mathrm{f}}_{\mathrm{a}_k} = U_0 \pm U_{\mathrm{a}_k},\ U^{\mathrm{b}}_{\mathrm{a}_k} = U_0 \mp U_{\mathrm{a}_k}$.

The symmetric actuation leads to a longitudinal displacement, because both patches shrink or enlarge together. However, the stiffness acting in the longitudinal direction which results from the beam's geometry is high so that the achieved displacement is hardly measurable. In contrast, the asymmetric actuation provides the desired agonist-antagonist behavior leading to a bending moment aligned with the z^2-axis causing the required transversal displacement. Here, the constant bias U_0 results in a negligible longitudinal displacement which can be ignored $s_1(t,z^1) \approx 0$, see (2.5).

Due to this, only the asymmetric actuation is considered leading to

$$W^{\mathrm{p}}_{\mathrm{el}} = \frac{1}{2}\int_0^{\ell}\sum_{k=1}^{p_j}\Gamma^{\mathrm{p}}_{\mathrm{a}_k}(z^1)U_{\mathrm{a}_k}(t)\partial^2_{z^1}s_j(t,z^1)\,\mathrm{d}z^1, \quad \Gamma^{\mathrm{p}}_{\mathrm{a}_k}(z^1) = \frac{A_{\mathrm{a}_k}a^{11}_{1,\mathrm{a}_k}(\hbar+\hbar_{\mathrm{a}_k})}{\beta_{11,\mathrm{a}_k}e_s}\Omega_{\mathrm{a}_k}(z^1). \tag{2.25}$$

Taking (2.19), (2.22) and (2.24) into account the potential energy of the beam equipped with single MFC-patches results in

$$W^{\mathrm{s}}_{\mathrm{pot}} = \frac{1}{2}\int_0^{\ell}\Lambda^{\mathrm{s}}(z^1)\big(\partial^2_{z^1}s_1(t,z^1)\big)^2\,\mathrm{d}z^1 + \frac{1}{2}\int_0^{\ell}\sum_{k=1}^{p_j}\operatorname{sign}(z^2_{\mathrm{a}_k})\Gamma^{\mathrm{s}}_{\mathrm{a}_k}(z^1)U^{\mathrm{MFC}}_{\mathrm{a}_k}(t)\partial^2_{z^1}s_j(t,z^1)\,\mathrm{d}z^1. \tag{2.26}$$

In contrast, the potential energy of the pairwise actuated beam follows from (2.19), (2.23) and (2.25) in form of

$$W^{\mathrm{p}}_{\mathrm{pot}} = \frac{1}{2}\int_0^{\ell}\Lambda^{\mathrm{p}}(z^1)\big(\partial^2_{z^1}s_3(t,z^1)\big)^2\,\mathrm{d}z^1 + \frac{1}{2}\int_0^{\ell}\sum_{k=1}^{p_j}\Gamma^{\mathrm{p}}_{\mathrm{a}_k}(z^1)U_{\mathrm{a}_k}(t)\partial^2_{z^1}s_3(t,z^1)\,\mathrm{d}z^1. \tag{2.27}$$

Damping Models The mechatronic system is as usual affected by damping. These damping effects can be interpreted as external and internal friction detracting or more precisely converting the energy of the system leading to a dissipative behavior. Experimental analyses have shown that damping can only be described by a combination of viscous or external damping [77] and an additional internal damping effect, e.g., Kelvin-Voigt damping [77, 78] and structural damping [96, 24, 13].

Considering [77] the damping forces (sometimes referred to as virtual work) of the external damping acts proportional to the transversal velocity

$$f_{\mathrm{v}}(t,z^1) = \gamma^{\mathrm{v}}(z^1)\partial_t s_3(t,z^1), \tag{2.28}$$

where

$$\gamma^{\mathrm{v}}(z^1) = \begin{cases} \gamma^{\mathrm{v}}_{\mathrm{c}}(z^1) + \sum_{k=1}^{p_j}\gamma^{\mathrm{v}}_{\mathrm{a}_k}(z^1)\Omega_{\mathrm{a}_k}(z^1) & \text{single patch actuation} \\ \gamma^{\mathrm{v}}_{\mathrm{c}}(z^1) + \sum_{k=1}^{p_j}2\gamma^{\mathrm{v}}_{\mathrm{a}_k}(z^1)\Omega_{\mathrm{a}_k}(z^1) & \text{pairwise actuation} \end{cases} \tag{2.29}$$

defines the spatially varying viscous damping function considering the damping coefficients $\gamma_{\mathrm{c}}^{\mathrm{v}}(z^1)$, $\gamma_{\mathrm{a}_k}^{\mathrm{v}}(z^1)$ of the carrier and MFC-patch, respectively.

The Kelvin-Voigt damping can be interpreted as spring damper system which appends the stress tensor [77, 78]

$$\sigma^{im} = E^{imkl}\big(\epsilon_{kl} + \gamma^{\mathrm{kv}}(z^1)\partial_t\epsilon_{kl}\big) = E^{imkl}\big(\partial_{z^k}\bar{s}_l(t,z^1) + \gamma^{\mathrm{kv}}(z^1)\partial_t\partial_{z^k}\bar{s}_l(t,z^1)\big), \tag{2.30}$$

with the spatially varying Kelvin-Voigt damping function

$$\gamma^{\mathrm{kv}}(z^1) = \begin{cases} \gamma_{\mathrm{c}}^{\mathrm{kv}}(z^1) + \sum_{k=1}^{p_j} \gamma_{\mathrm{a}_k}^{\mathrm{kv}}(z^1)\Omega_{\mathrm{a}_k}(z^1) & \text{single patch actuation} \\ \gamma_{\mathrm{c}}^{\mathrm{kv}}(z^1) + \sum_{k=1}^{p_j} 2\gamma_{\mathrm{a}_k}^{\mathrm{kv}}(z^1)\Omega_{\mathrm{a}_k}(z^1) & \text{pairwise actuation} \end{cases} \tag{2.31}$$

considering the Kelvin-Voigt damping coefficients $\gamma_{\mathrm{c}}^{\mathrm{kv}}(z^1)$, $\gamma_{\mathrm{a}_k}^{\mathrm{kv}}(z^1)$ of the carrier and MFC-patch, respectively.

Taking Assumption 2.1 into account as well as the asymmetric actuation resulting in a translatory longitudinal displacement $s_1(t,z^1) \approx 0$ the stress tensor of the beam is given by

$$\sigma^{11} = -E\big(z^3\partial_{z^1}^2 s_3(t,z^1) + \gamma^{\mathrm{kv}}(z^1)z^3\partial_t\partial_{z^1}^2 s_3(t,z^1)\big). \tag{2.32}$$

The associated force is

$$f_{\mathrm{kv}}(t,z^1) = \gamma^{\mathrm{kv}}(z^1)z^3\partial_t\partial_{z^1}^2 s_3(t,z^1). \tag{2.33}$$

In case of a system defined by a 3-d body described by linear elasticity the combination of viscous and Kelvin-Voigt damping is a common choice, because the resulting damping force can be efficiently described especially in the framework of FEM, see Section 2.2.2.

The virtual or damping force of the second internal damping model acts proportional to the strain velocity $\partial_t\partial_{z^1}s_3(t,z^1)$, see, e.g., [96, 24, 13]

$$f_{\mathrm{sv}}(t,z^1) = \gamma^{\mathrm{sv}}(z^1)\partial_t\partial_{z^1}s_3(t,z^1), \tag{2.34}$$

where $\gamma^{\mathrm{sv}}(z^1)$ denotes the spatially varying structural damping function defined as

$$\gamma^{\mathrm{sv}}(z^1) = \begin{cases} \gamma_{\mathrm{c}}^{\mathrm{sv}}(z^1) + \sum_{k=1}^{p_j} \gamma_{\mathrm{a}_k}^{\mathrm{sv}}(z^1)\Omega_{\mathrm{a}_k}(z^1) & \text{single patch actuation} \\ \gamma_{\mathrm{c}}^{\mathrm{sv}}(z^1) + \sum_{k=1}^{p_j} 2\gamma_{\mathrm{a}_k}^{\mathrm{sv}}(z^1)\Omega_{\mathrm{a}_k}(z^1) & \text{pairwise actuation} \end{cases} \tag{2.35}$$

with the associated damping coefficients $\gamma_{\mathrm{c}}^{\mathrm{sv}}(z^1)$, $\gamma_{\mathrm{a}_k}^{\mathrm{sv}}(z^1)$ of the carrier structure and the MFC-patch, respectively.

The sum of these forces states a holonomic (integrable) constraint of the mechanical system. Applying the variational calculus, see, e.g., [91, chap. 4] considering the variational operator δ (related to the Gâteaux derivative) often interpreted as virtual displacement in this context finally leads to the virtual work of non-conservative forces

$$\begin{aligned} \delta W_{\mathrm{nc}} = -\int_0^{\ell} \Big(&\gamma^{\mathrm{v}}(z^1)\partial_t s_3(t,z^1)\delta s_3(t,z^1) + \gamma^{\mathrm{kv}}(z^1)\partial_t\partial_{z^1}^2 s_3(t,z^1)\delta\partial_{z^1}^2 s_3(t,z^1) \\ &+ \gamma^{\mathrm{sv}}(z^1)\partial_t\partial_{z^1}s_3(t,z^1)\delta\partial_{z^1}s_3(t,z^1)\Big)\,\mathrm{d}z^1. \end{aligned} \tag{2.36}$$

These energies are used in the following sections to determine the equations of motion of the interconnected beam structures considering the extended Hamilton's principle.

2.1.2. Modeling of a Pointwise Interconnected Beam Structure

As a proof of concept as well as a benchmark test for the model based control approach a pointwise interconnected structure of vertical aligned beams is introduced.

Below, the mechanical configuration of the system is presented. Thereafter, the energies of the vertical beam configuration are determined based on the previously discussed results of the single Euler-Bernoulli beam. Taking the extended Hamilton's principle into account the equations of motion are derived. Finally, a finite dimensional description is provided by the use of the Galerkin approximation.

2.1.2.1. Mechanical Configuration

In general, the vertical beam configuration is composed of $r \in \mathbb{N}$ carbon made beams clamped at $z^1 = 0\,\mathrm{m}$ and free at $z^1 = \ell_j$. Each beam j is actuated by $p_j \in \mathbb{N}$ MFC-patch pairs, where a patch pair consists of two actuators symmetrically mounted at the longitudinal position z^1_{j,a_k} on the front and back of the associated beam j, see pairwise actuation concept of Section 2.1.1.2 and Fig. 2.3. To provide a symmetric input range $U_{j,\mathrm{a}_k} \in [-1000, 1000]\,\mathrm{V}$ a voltage bias $U_0 = 500\,\mathrm{V}$ is applied on both patches, see Remark 2.1. Furthermore each beam is equipped with an additional tip mass m_j at $z^1 = \ell_j$. These aluminum made tip masses are used to connect neighboring beams with each other by a string modeled as spring characterized by the spring constant $k_{i,m}$ with $\{i, m\} = \{\{1, 2\}, \ldots, \{r-1, r\}\}$. As a visualization of the vertical beam configuration Fig. 2.5 displays the schematics as well as a photo of the experimental setup. The experimental setup is based on $r = 3$ beams, where the first and the last beam are equipped with one MFC-patch pair and the second beam is actuated by two pairs. Table 2.1 lists the dimensions of the used beams and MFC-actuators (type Smart Materials GmbH M 8528 P1 see [105]) as well as the longitudinal position z_{j,a_k} of the patch pairs on the beam surface and the distance between neighboring electrodes e_s.

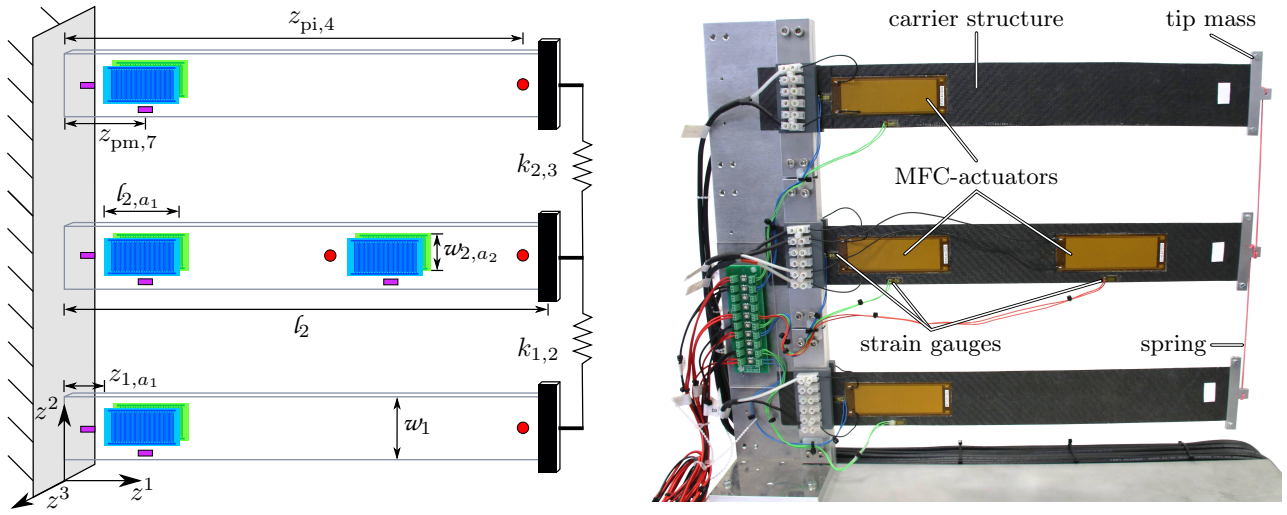

Figure 2.5.: *Left:* Schematics of the system of pointwise connected and vertical aligned beams. The red dots mark the points considered for the motion planning and tracking control approach (subsequently called points of interest). Furthermore the purple rectangles mark the location of the strain gauges used as measurement devices (subsequently called points of measurement), see also [58].
Right: Photo of the experimental setup, see also [58].

In addition to the embedded actuation, the beams are equipped with embedded sensors. The schematics in Fig. 2.5 visualizes these sensors as purple rectangles. The used sensors for the experimental setup are strain gauges (type HBM 1-Ly48-6/350) mounted on the carrier structure like the MFC-patches by using epoxy resin. Table 2.2 lists the sensor locations of the experimental setup as so-called points of measurement. The table also contains the points of interest at which the transversal deflection should be controlled, see also the red dot in the schematics of Fig. 2.5.

The notation is simplified to improve the readability. Variables and parameters associated with a specific beam are marked by the index $j \in \{1, \ldots, r\}$. The MFC-actuators are addressed by the indices j and a_k, where $k \in \{1, \ldots, p_j\}$ denotes MFC-patch pair mounted the considered beam j, where the counting starts at the clamping and ends at the free end. For simplification of the notation the direction tag of the independent spatial coordinate is discarded, i.e., $z = z^1$. Furthermore the notation of the beam's deflection is simplified as $s_j(t, z) = s_{3,j}(t, z)$, where neglecting of the moving sense is justified by the fact that the actuation only results in a transversal deflection (aligned with the z^3 axis) as mentioned before. In addition to the assumptions of Section 2.1.1 the considered length of all beams is identical $\ell_j = \ell$.

2.1.2.2. Stored Energies and Virtual Work of the Non-conservative Forces

As mentioned before the determination of the equations of motion of the transversal displacement by the extended Hamilton's principle relies on the associated energies. The vertical beam configuration consists of Euler-Bernoulli

Table 2.1.: Dimensions and actuator locations of the vertical beam configuration in mm for $j \in \{1,2,3\}$ beams, where the index a refers to the MFC-actuators, see also Fig. 2.5.

dimension						
ℓ_j	w_j	h_j	ℓ_{j,a_k}	w_{j,a_k}	h_{j,a_k}	e_s
400.0	55.0	0.8	85.0	25.0	0.3	0.5

MFC-actuator positions with $\mathrm{a}_k = \mathrm{a}_1$ for $j \in \{1,3\}$, $\mathrm{a}_k \in \{\mathrm{a}_1, \mathrm{a}_2\}$ for $j = 2$			
z_{1,a_1}	z_{2,a_1}	z_{2,a_2}	z_{3,a_1}
23.0	23.0	225.0	23.0

Table 2.2.: Positions of the points of interest and measurement of the vertical beam configuration in mm for $r = 3$ beams.

points of interest and measurement					
beam $j = 1$			beam $j = 3$		
$z_{\mathrm{pm},1}$	$z_{\mathrm{pm},2}$	$z_{\mathrm{pi},1}$	$z_{\mathrm{pm},6}$	$z_{\mathrm{pm},7}$	$z_{\mathrm{pi},4}$
7.0	68.0	370.0	10.0	68.0	370.0

beam $j = 2$				
$z_{\mathrm{pm},3}$	$z_{\mathrm{pm},4}$	$z_{\mathrm{pm},5}$	$z_{\mathrm{pi},2}$	$z_{\mathrm{pi},3}$
10.0	68.0	268.0	200.0	370.0

beams, therefore the stored kinetic and potential energy as well as the work of the non-conservative forces are based on the energies and forces of the single beam introduced in Section 2.1.1. However, the tip mass and the connecting spring have to be considered as well.

Kinetic Energy The effect of the tip mass on the kinetic energy is given by the translational and rotatory energy terms, i.e., the quadratic products of mass m_j times velocity $\partial_t s_j(\ell, t)$ and inertia J_j times angular velocity $\partial_t \partial_z s_j(\ell, t)$, where both velocity terms have to be evaluated at the position of the mass $z = \ell$. Hence the kinetic energy results in

$$W_{\mathrm{kin}}(t) = \sum_{j=1}^{r} \left(W_{\mathrm{kin},j}^{\mathrm{p}}(t) + \frac{m_j}{2} \big(\partial_t s_j(t,\ell)\big)^2 + \frac{J_j}{2} \big(\partial_t \partial_z s_j(t,\ell)\big)^2 \right). \tag{2.37}$$

According to (2.18) the kinetic energy term of the single beam considering pairwise actuation $W_{\mathrm{kin},j}^{\mathrm{p}}(t)$ is given by

$$W_{\mathrm{kin},j}^{\mathrm{p}}(t) = \frac{1}{2} \int_0^{\ell} \mu_j^{\mathrm{p}}(z) \big(\partial_t s_j(t,z)\big)^2 \,\mathrm{d}z \quad \text{with} \quad \mu_j^{\mathrm{p}}(z) = \rho_j A_j + \sum_{k=1}^{p_j} 2\rho_{j,\mathrm{a}_k} A_{j,\mathrm{a}_k} \Omega_{j,\mathrm{a}_k}(z) \tag{2.38}$$

where $A_j = hw$, $A_{j,\mathrm{a}_k} = h_{\mathrm{a}_k} w_{\mathrm{a}_k}$, ρ, and ρ_{a_k} denote the cross sections and densities of the carrier and MFC-patches, respectively. Furthermore, $\Omega_{j,\mathrm{a}_k}(z)$ describes the notch function (2.14) per beam, which provides the spatial characteristic of the MFC-patches or in other words it adds the additional effects of the actuators within their covered surface $z \in [z_{j,\mathrm{a}_k}, z_{j,\mathrm{a}_k} + \ell_{\mathrm{a}_k}]$.

Potential Energy Similar to the tip mass affecting the kinetic energy, the coupling springs at the beams' tips provide an additional term to the potential energy considering Hooke's law. This term is defined by the quadratic difference of the transversal deflection between neighboring beams multiplied with the associated spring constant $k_{i,m}$. Hence, the potential energy is given by

$$W_{\mathrm{pot}}(t) = \sum_{j=1}^{r} W_{\mathrm{pot},j}^{\mathrm{p}}(t) + \sum_{j=1}^{r-1} \frac{k_{j,j+1}}{2} \big(s_j(t,\ell) - s_{j+1}(t,\ell)\big)^2. \tag{2.39}$$

Taking (2.23), (2.25) and (2.27) into account the potential energy of a uncoupled single beam is defined by

$$W_{\mathrm{pot},j}^{\mathrm{p}}(t) = \frac{1}{2} \int_0^{\ell} \Lambda_j^{\mathrm{p}}(z) \big(\partial_z^2 s_j(t,z)\big)^2 \,\mathrm{d}z + \frac{1}{2} \int_0^{\ell} \sum_{k=1}^{p_j} \Gamma_{j,\mathrm{a}_k}^{\mathrm{p}}(z) U_{\mathrm{a}_k}(t) \partial_z^2 s_j(t,z) \,\mathrm{d}z \tag{2.40}$$

with

$$\Lambda_j^{\mathrm{p}}(z) = E_j^{1111} I_j + \sum_{k=1}^{p_j} 2E_{j,\mathrm{a}_k}^{1111} I_{j,\mathrm{a}_k} \Omega_{j,\mathrm{a}_k}(z), \quad \Gamma_{j,\mathrm{a}_k}^{\mathrm{p}}(z) = \frac{A_{j,\mathrm{a}_k} a_{1,j,\mathrm{a}_k}^{11} (\hbar_j + \hbar_{j,\mathrm{a}_k})}{\beta_{11,j,\mathrm{a}_k} e_s} \Omega_{j,\mathrm{a}_k}(z). \tag{2.41}$$

These substitutions are derived under the assumption of an asymmetric voltage supply, the piezoelectric constitutive law and the underlying geometry, see Section 2.1.1. Recall that herein E_j^{1111} and $E_{j,\mathrm{a}_k}^{1111}$ denote the elasticity modulus of the carrier structure and the MFC-patches and $I_j = w_j \hbar_j^3/12$ as well as $I_{j,\mathrm{a}_k} = w_{j,\mathrm{a}_k}[(\hbar_j/2 + \hbar_{j,\mathrm{a}_k})^3 - (\hbar_j/2)^3]$ describe the area moment of inertia of the carrier and MFC-actuators. The parameters $a_{j,\mathrm{a}_k,1}^{11}$, $\beta_{j,\mathrm{a}_k,11}$ and e_s represent the piezoelectric parameter, the dielectric constant of the k^{th} MFC-patch pair and the distance between neighboring electrodes on an MFC-patch.

Remark 2.2 *Considering the mechanical setup of the vertical beam configuration, taking only the pairwise actuation into account, the notation is therefore simplified as follows* $\mu_j(z) = \mu_j^p(z)$, $\Lambda_j(z) = \Lambda_j^p(z)$, *and* $\Gamma_{j,a_k}(z) = \Gamma_{j,a_k}^p(z)$.

Damping Models For the vertical beam configuration the introduced damping models can be considered, see Section 2.1.1. Taking (2.36) into account the work of the non-conservative forces is given by

$$\begin{aligned}\delta W_{\mathrm{nc}}(t) = -\sum_{j=1}^{r} \int_0^{\ell} \Big(&\gamma_j^{\mathrm{v}}(z) \partial_t s_j(t,z) \delta s_j(t,z) + \gamma_j^{\mathrm{kv}}(z) \partial_t \partial_z^2 s_j(t,z) \delta \partial_z^2 s_j(t,z) \\ &+ \gamma_j^{\mathrm{sv}}(z) \partial_t \partial_z s_j(t,z) \delta \partial_z s_j(t,z) \Big) \, \mathrm{d}z.\end{aligned} \tag{2.42}$$

Considering the pairwise actuation the damping functions of (2.29), (2.31) and (2.35) yield

$$\gamma_j^{\mathrm{v}}(z) = \gamma_{j,\mathrm{c}}^{\mathrm{v}}(z) + \sum_{k=1}^{p_j} 2\gamma_{j,\mathrm{a}_k}^{\mathrm{v}}(z) \Omega_{j,\mathrm{a}_k}(z), \tag{2.43}$$

$$\gamma_j^{\mathrm{kv}}(z) = \gamma_{j,\mathrm{c}}^{\mathrm{kv}}(z) + \sum_{k=1}^{p_j} 2\gamma_{j,\mathrm{a}_k}^{\mathrm{kv}}(z) \Omega_{j,\mathrm{a}_k}(z), \tag{2.44}$$

$$\gamma_j^{\mathrm{sv}}(z) = \gamma_{j,\mathrm{c}}^{\mathrm{sv}}(z) + \sum_{k=1}^{p_j} 2\gamma_{j,\mathrm{a}_k}^{\mathrm{sv}}(z) \Omega_{j,\mathrm{a}_k}(z). \tag{2.45}$$

As discussed in Section 2.1.1 the parameters $\gamma_{j,\mathrm{c}}^{\mathrm{v}}(z)$, $\gamma_{j,\mathrm{a}_k}^{\mathrm{v}}(z)$, $\gamma_{j,\mathrm{c}}^{\mathrm{kv}}(z)$, $\gamma_{j,\mathrm{a}_k}^{\mathrm{kv}}(z)$, $\gamma_{j,\mathrm{c}}^{\mathrm{sv}}(z)$, and $\gamma_{j,\mathrm{a}_k}^{\mathrm{sv}}(z)$ denote the viscous, Kelvin-Voigt, and structural damping coefficient of the of the carrier and MFC actuators, respectively.

2.1.2.3. Equations of Motion

The determination of the equations of motion governing the transversal deflection of the vertical beam configuration's relies on the so-called extended Hamilton's principle. The extended Hamilton's principle uses the variational calculus to derive the dynamics of systems of particles, rigid bodies, and deformable or elastic solids. It states a generalization of the principle of virtual displacements which can be used to model the static equilibrium of solid structures.

Hamilton's principle characterizes the considered system by its kinetic and potential energy $W_{\mathrm{pot}}(t)$, $W_{\mathrm{kin}}(t)$ [91]. The extension of the principle also takes the dissipative effects in terms of the virtual work of non-conservative forces $\delta W_{\mathrm{nc}}(t)$ into account. The energies as well as the virtual work are based on either a finite number of generalized coordinates for so-called discrete systems or for continuous systems by dependent variables which are functions of the position or the displacement, see [91, 77, 102] for further details.

The main idea of the principle, see, e.g., [91, chap. 5], states that the true path $s(t,z)$ of a material particle or the displacement of a flexible structure within an admissible set of paths or trajectories results in an extremum of the the functional

$$J(t) = \int_{t_0}^{t_1} \big(W_{\mathrm{kin}}(t) - W_{\mathrm{pot}}(t) + W_{\mathrm{nc}}(t) \big) \, \mathrm{d}t \quad \text{with} \quad t_0 < t_1, \ t_0, t_1 \in \mathbb{R}. \tag{2.46}$$

An admissible path means a spatial and temporal displacement profile which can be reached and fulfills additional conditions, e.g., a clamping condition or an initial velocity profile that is compatible with the geometry and its boundary constraints.

The determination of the true path is done by identifying the extremum of the functional $J(t)$. This can be done by the Gâteaux derivative or first variation [91, chap. 4] which is given for an arbitrary function $F(x)$ as

$$\delta F(x) = \lim_{\chi \to 0} \frac{\partial F(x + \chi \delta x)}{\partial \chi} = \frac{\partial F(x + \chi \delta x)}{\partial \chi}\Big|_{\chi=0}, \tag{2.47}$$

where δ is also known as the variational operator. The extremum of a functional is reached, if $\delta F(x) = 0$ holds true (necessary condition).

Considering the functional $J(t)$ the Gâteaux derivative can be split

$$\delta J(t) = \int_{t_0}^{t_1} \big(\delta W_{\mathrm{kin}}(t) - \delta W_{\mathrm{pot}}(t) + \delta W_{\mathrm{nc}}(t)\big)\,\mathrm{d}t = 0, \tag{2.48}$$

where the variation of the path at $t = t_2$ and $t = t_1$ is given by $\delta s(t_0, z) = \delta s(t_1, z) = 0$.

Below, the extended Hamilton's principle is evaluated considering the vertical beam configuration. Therefore, to enhance the readability the spatial and temporal arguments of the transversal displacement $s_j = s_j(t, z)$ are omitted as long as no special evaluation of the displacement is required.

At the beginning of the evaluation of the extended Hamilton's principle the variation of the kinetic and potential energy are required. Taking (2.37) to (2.40) into account they result in

$$\delta W_{\mathrm{kin}}(t) = \sum_{j=1}^{r} \Bigg(\int_0^{\ell} \mu_j(z) \partial_t s_j \delta \partial_t s_j \,\mathrm{d}z + m_j \partial_t s_j(t,\ell) \delta \partial_t s_j(t,\ell) + J_j \partial_t \partial_z s_j(t,\ell) \delta \partial_t \partial_z s_j(t,\ell) \Bigg), \tag{2.49}$$

$$\begin{aligned} \delta W_{\mathrm{pot}}(t) = {} & \sum_{j=1}^{r} \Bigg(\int_0^{\ell} \Lambda_j(z) \partial_z^2 s_j \delta \partial_z^2 s_j \,\mathrm{d}z + \int_0^{\ell} \sum_{k=1}^{p_j} \Gamma_{j,\mathrm{a}_k}(z) U_{\mathrm{a}_k}(t) \delta \partial_z^2 s_j \,\mathrm{d}z \Bigg) \\ & + \sum_{j=1}^{r-1} k_{j,j+1}\big(s_j(t,\ell) - s_{j+1}(t,\ell)\big)\delta\big(s_j(t,\ell) - s_{j+1}(t,\ell)\big). \end{aligned} \tag{2.50}$$

Hence, considering (2.42) the first variation or Gâteaux derivative reads

$$\begin{aligned} \delta J(t) = \int_{t_0}^{t_1} \sum_{j=1}^{r} \Bigg(& \int_0^{\ell} \mu_j(z) \partial_t s_j \delta \partial_t s_j - \Lambda_j(z) \partial_z^2 s_j \delta \partial_z^2 s_j - \sum_{k=1}^{p_j} \Gamma_{j,\mathrm{a}_k}(z) U_{\mathrm{a}_k}(t) \delta \partial_z^2 s_j \\ & - \gamma_j^{\mathrm{v}}(z) \partial_t s_j \delta s_j - \gamma_j^{\mathrm{kv}}(z) \partial_t \partial_z^2 s_j \delta \partial_z^2 s_j - \gamma_j^{\mathrm{sv}}(z) \partial_t \partial_z s_j \delta \partial_z s_j \,\mathrm{d}z \\ & + m_j \partial_t s_j(t,\ell) \delta \partial_t s_j(t,\ell) + J_j \partial_t \partial_z s_j(t,\ell) \delta \partial_t \partial_z s_j(t,\ell) \Bigg) \\ & - \sum_{j=1}^{r-1} k_{j,j+1}\big(s_j(t,\ell) - s_{j+1}(t,\ell)\big)\delta\big(s_j(t,\ell) - s_{j+1}(t,\ell)\big)\,\mathrm{d}t. \end{aligned} \tag{2.51}$$

Applying partial integration to standardize the variational operator to $\delta s_j(t, z^1)$, $\delta s_j(t, \ell)$ and considering the fundamental lemma of variational calculus [91, 77] leads to

$$
\begin{aligned}
\delta J(t) = \int_{t_0}^{t_1} \sum_{j=1}^{r} \Bigg(\int_0^{\ell} \Big\{ & -\mu_j(z)\partial_t^2 s_j - \partial_z^2\big[\Lambda_j(z)\partial_z^2 s_j\big] - \sum_{k=1}^{p_j} \partial_z^2\big[\Gamma_{j,\mathrm{a}_k}(z)U_{\mathrm{a}_k}(t)\big] \\
& - \gamma_j^{\mathrm{v}}(z)\partial_t s_j - \partial_z^2\big[\gamma_j^{\mathrm{kv}}(z)\partial_t\partial_z^2 s_j\big] + \partial_z\big(\gamma_j^{\mathrm{sv}}(z)\partial_t\partial_z s_j\big)\Big\}\delta s_j \,\mathrm{d}z \\
& + \Big\{\partial_z\big[\Lambda_j(\ell)\partial_z^2 s_j(t,\ell)\big] + \sum_{k=1}^{p_j}\partial_z\Gamma_{j,\mathrm{a}_k}(\ell)U_{\mathrm{a}_k}(t) + \partial_z\big[\gamma_j^{\mathrm{kv}}(\ell)\partial_t\partial_z^2 s_j(t,\ell)\big] \\
& - \gamma_j^{\mathrm{sv}}(\ell)\partial_t\partial_z s_j(t,\ell) - m_j\partial_t^2 s_j(t,\ell)\Big\}\delta s_j(t,\ell) \\
& + \Big\{ -\Lambda_j(\ell)\partial_z^2 s_j(t,\ell) - \sum_{k=1}^{p_j}\Gamma_{j,\mathrm{a}_k}(\ell)U_{\mathrm{a}_k}(t) - \gamma_j^{\mathrm{kv}}(\ell)\partial_t\partial_z^2 s_j(t,\ell) \\
& - J_j\partial_t^2\partial_z s_j(t,\ell)\Big\}\delta\partial_z s_j(t,\ell)\Bigg) \\
& - \sum_{j=1}^{r-1} k_{j,j+1}\big(s_j(t,\ell) - s_{j+1}(t,\ell)\big)\delta\big(s_j(t,\ell) - s_{j+1}(t,\ell)\big)\,\mathrm{d}t.
\end{aligned}
\tag{2.52}
$$

The last summation term can be substituted by

$$
\sum_{j=1}^{r-1} k_{j,j+1}\big(s_j(\ell,t) - s_{j+1}(\ell,t)\big)\delta\big(s_j(\ell,t) - s_{j+1}(\ell,t)\big) = \sum_{j=1}^{r} \mathcal{k}_j(\boldsymbol{s})\delta s_j(t,\ell) \tag{2.53}
$$

with

$$
\mathcal{k}_j\big(\boldsymbol{s}(t,\ell)\big) = \begin{cases} k_{j,j+1}\big(s_j(t,\ell) - s_{j+1}(t,\ell)\big), & j = 1 \\ k_{j,j+1}\big(s_j(t,\ell) - s_{j+1}(t,\ell)\big) \\ -k_{j-1,j}\big(s_{j-1}(t,\ell) - s_j(t,\ell)\big) \end{cases}, \quad j \in \{2,...,r-1\}, \quad \text{and} \quad \boldsymbol{s}(t,\ell) = \begin{bmatrix} s_1(t,\ell) \\ \vdots \\ s_r(t,\ell) \end{bmatrix} \tag{2.54}
$$

$$
-k_{r-1,r}\big(s_{r-1}(t,\ell) - s_r(t,\ell)\big), \quad j = r,
$$

Considering the extended Hamilton's principle the true trajectory is found if $\delta J(t) = 0$ holds true. Hence, the equations of motion are obtained from (2.52) with (2.53) in terms of the partial differential equation (PDE) for the j^{th} beam

$$
0 = \mu_j(z)\partial_t^2 s_j + \gamma_j^{\mathrm{v}}(z)\partial_t s_j - \partial_z\big[\gamma_j^{\mathrm{sv}}(z)\partial_t\partial_z s_j\big] + \partial_z^2\big[\Lambda_j(z)\partial_z^2 s_j + \gamma_j^{\mathrm{kv}}(z)\partial_t\partial_z^2 s_j\big] + \sum_{k=1}^{p_j}\partial_z^2\Gamma_{j,\mathrm{a}_k}(z)U_{j,\mathrm{a}_k}, \tag{2.55a}
$$

for $z \in (0,\ell)$ and $t > 0$. The geometric boundary conditions according to Fig. 2.5 read,

$$
s_j = 0, \quad \partial_z s_j = 0, \tag{2.55b}
$$

for $t > 0$ at the clamped beam tip $z = 0$ and

$$
\begin{aligned}
m_j\partial_t^2 s_j + \mathcal{k}_j(\boldsymbol{s}) &= \partial_z\big[\Lambda_j(z)\partial_z^2 s_j + \gamma_j^{\mathrm{kv}}(z)\partial_t\partial_z^2 s_j\big] - \gamma_j^{\mathrm{sv}}(z)\partial_t\partial_z s_j + \sum_{k=1}^{p_j}\partial_z\Gamma_{j,\mathrm{a}_k}(\ell)U_{\mathrm{a}_k}(t) \\
J_j\partial_t^2\partial_z s_j &= -\Lambda_j(z)\partial_z^2 s_j - \gamma_j^{\mathrm{kv}}(z)\partial_t\partial_z^2 s_j - \sum_{k=1}^{p_j}\Gamma_{j,\mathrm{a}_k}(\ell)U_{\mathrm{a}_k}(t)
\end{aligned}
\tag{2.55c}
$$

at the free but coupled beam tip $z = \ell$.

Assumption 2.4 *The terms in the free boundary conditions* (2.55c) *depending on* $U_{a_k}(t)$ *describe the effect of actuators extending the beam tip. Usually there are no MFC-actuators placed at the beam's tips because this position describes the lowest impact of the actuators on the transversal deflection taking their lever into account. Therefore, it is assumed that no MFC-actuators is placed at a beam tip leading to*

$$
\Gamma_{j,a_k}(\ell)U_{a_k}(t) = \partial_z\big(\Gamma_{j,a_k}(\ell)U_{a_k}(t)\big) = 0, \quad \forall \quad j,k.
$$

Hence, below the simplified boundary conditions are considered.

The initial condition of the system at $t = 0$ can be chosen arbitrarily

$$s_j = s_{j,0}, \quad \partial_t s_j = s_{j,1}. \tag{2.55d}$$

Subsequently, the in-domain measurement achieved by strain gauges has to be described in the same framework as the equations of motion. These sensors provide the longitudinal strain averaged over the covered area which can be described in terms of (2.6) as

$$\epsilon_{j,1}(t, z_{\mathrm{pm},g}) = \frac{\hbar_j}{2} \partial_z^2 s_j(t, z_{\mathrm{pm},g}), \tag{2.56}$$

where $z_{\mathrm{pm},g}$ with $g \in \{1, \ldots, 7\}$ denotes the longitudinal position of the strain gauges on the vertical beam configuration as depicted in the schematics of Fig. 2.5, where the numeric values are given by Table 2.2.

Due to the spatial characteristics $\Omega_{j,\mathrm{a}_k}(z)$ of the MFC-patches defined in (2.14) based on Heaviside functions, for which the second spatial derivation is not defined, the system (2.55) has to be interpreted in a distributional sense. This leads to the introduction of the weak formulation, see also [10, 115, 101]. In addition the weak form is required by the Galerkin approximation which is used as finite dimensional approximation of the equations of motion required for the implementation on a real time control device.

At this point all three damping models are considered. However, as mentioned in Remark 3.1 a combination of external (viscous) and one of the internal damping models (Kelvin-Voigt or structural damping) is adequate to describe the experimental measured dynamic, compare [56] and [58]. Taking experimental results into account there is no significant distinction between these two damping setups. Nevertheless, there is a difference between the setups w.r.t. the resulting infinite eigenvalue distribution, see Appendix B.2.

Remark 2.3 *In addition, the inertia of the tip mass J_j is neglected since it does not show significant effect either in the static or in the transient behavior of the experimental setup.*

2.1.2.4. Finite Dimensional Approximation of the Equations of Motion of the Pointwise Interconnected Beam Structure

As mentioned before the finite dimensional approximation is a necessary action enabling the implementation of a controller on a real time control device which is not capable to project the infinite dimensional system. In addition, the distributed parameters description of the equations of motion is often complex even for simple geometries and therefore hard to solve, if at all possible.

The implementation of a control approach relies always on such an approximation. The literature [78] distinguishes between "early lumping" and "late lumping" approaches. An early lumping approach introduces at first the finite dimensional approximation. Thereafter the control approach is designed taking the discretized system description into account. Late lumping approaches on the other hand design the control algorithm based on the infinite description and discretized the result for the implementation.

If the control design is based on the finite dimensional or early lumped system so-called "spillover effects" may disturb the performance. Also if the design or the system description relies on parameters which are identified considering experimental measurements spillover effects may occur, because most of the time the identification compares a spatial discretized simulation with the experimental measurements. Spillover effects describe the differences or errors made by the approximation of the PDE, e.g., eigenfrequencies which are not included in the approximated ordinary differential equation (ODEs). This can cause problems if such a frequency is excited in the experimental setup, because the control algorithm can not anticipate the resulting behavior. A late lumping approach as presented in Appendix B.3 deals with the infinite system leading to an infinite control algorithm which will be discretized immediately before the implementation.

However, the finite dimensional approximation is a necessary step and is described below. For the beam structures the Galerkin approximation is used which is based on the weak formulation of (2.55).

Weak Formulation of the Equations of Motion The weak formulation also known as variational formulation of the equations of motion (2.55) enables us to apply a Galerkin approximation. It is deduced by the multiplication of the governing PDE (2.55a) with a test function $\phi_j(z) \in H_0^2(0, \ell)$, where $H_0^2(0, \ell) = \{\phi \in H^2(0, \ell) | \phi(0) = \partial_z \phi(0) = 0\}$ denotes a Hilbert space[1].

[1]The space $H^2(0, \ell)$ is a so-called Sobolev space and is defined as $H^2(0, \ell) = \left\{\phi \in L^2(0, \ell) | \frac{d^\alpha \phi}{dz^\alpha} \in L^2(0, \ell), \alpha \in \{0, 1, 2\}\right\}$ equipped with the norm $\|\phi\|_{H^2} = \left(\sum_\alpha \| \frac{d^\alpha}{dz^\alpha} \phi \|_{L^2}^2\right)^{\frac{1}{2}}$.

This yields

$$\begin{aligned}&\mu_j(z)\partial_t^2 s_j\phi_j(z)+\gamma_j^{\mathrm{v}}(z)\partial_t s_j\phi_j(z)-\partial_z\left[\gamma_j^{\mathrm{sv}}(z)\partial_t\partial_z s_j\right]\phi_j(z)\\&\quad+\partial_z^2\left[\Lambda_j(z)\partial_z^2 s_j+\gamma_j^{\mathrm{kv}}(z)\partial_t\partial_z^2 s_j\right]\phi_j(z)=-\sum_{k=1}^{p_j}\partial_z^2\Gamma_{j,\mathrm{a}_k}(z)U_{j,\mathrm{a}_k}\phi_j(z).\end{aligned}\tag{2.57}$$

For the vertical beam configuration the test function is chosen as an eigenfunction of the undamped system, see Appendix B.2. The product allows us to apply an integration by parts to shift the two times spatial derivative of $\Lambda_j(z)$, $\gamma_j^{\mathrm{kv}}(z)$, and $\Gamma_{j,\mathrm{a}_k}(z)$ to $\phi_j(z)$ to the test function. Taking the boundary conditions (2.55b) and (2.55c) into account this result in the weak form

$$\begin{aligned}&\langle\mu_j(z)\partial_t^2 s_j,\phi_j(z)\rangle+\langle\Lambda_j(z)\partial_z^2 s_j,\partial_z^2\phi_j(z)\rangle+\langle\gamma_j^{\mathrm{v}}(z)\partial_t s_j,\phi_j(z)\rangle+\langle\gamma_j^{\mathrm{kv}}(z)\partial_t\partial_z^2 s_j,\partial_z^2\phi_j(z)\rangle\\&+\langle\gamma_j^{\mathrm{sv}}(z)\partial_t\partial_z s_j,\partial_z\phi_j(z)\rangle+m_j\partial_t^2 s_j(\ell)\phi_j(\ell)+\mathcal{k}_j(\boldsymbol{s})\phi_j(\ell)=-\sum_{k=1}^{p_j}\langle\Gamma_{j,\mathrm{a}_k}(z)U_{j,\mathrm{a}_k},\partial_z^2\phi_j(z)\rangle,\end{aligned}\tag{2.58}$$

where $\langle\,\cdot\,,\,\cdot\,\rangle$ denotes the $L^2(0,\ell)$ inner product.

Definition 2.1 *Taking [17] into account the inner or scalar product of $L^2(0,\ell)$ is defined as*

$$\langle a,b\rangle=\langle a,b\rangle_{L^2(0,\ell)}=\int_0^\ell a\bar{b}\,\mathrm{d}z\tag{2.59}$$

where $\bar{b}$ denotes the complex conjugate of function b.

Galerkin Approximation Weighted residual and thus Galerkin's method are based on the separation of the temporal and spatial dependencies of the deflection $s_j(t,z)$, i.e.,

$$s_j(t,z)\approx\sum_{i=1}^{N_j}q_{j,i}(t)\phi_{j,i}(z),\tag{2.60}$$

which is why these belong to the class of series discretization methods, where remaining error is defined as weighted residual, further details are provided by [77]. Here, $\{q_{j,i}(t)\}_{i=1}^{N_j}$ defines the set of finite ($N_j\in\mathbb{N}$) time dependent functions or coefficients often called generalized coordinates. In addition, $\{\psi_{j,i}\}_{i=1}^{N_j}$ denotes an arbitrary set of linear independent trail function of beam $j\in\{1,\ldots,r\}$ fulfilling the same boundary condition as the original problem (2.55b) and (2.55c). Galerkin's method assumes that the trail function and the test function in the weak formulation are identical $\psi_{j,i}=\phi_{j,i}$, see Appendix B.2.

Substituting this approximation into (2.58)

$$\begin{aligned}&\sum_{m=1}^{N_j}\sum_{i=1}^{N_j}\Big(\langle\mu_j(z)\phi_{j,i}(z),\phi_{j,m}(z)\rangle\partial_t^2 q_{j,i}(t)+\langle\Lambda_j(z)\partial_z^2\phi_{j,i}(z),\partial_z^2\phi_{j,m}(z)\rangle q_{j,i}(t)\\&\qquad+\langle\gamma_j^{\mathrm{v}}(z)\phi_{j,i}(z),\phi_{j,m}(z)\rangle\partial_t q_{j,i}(t)+\langle\gamma_j^{\mathrm{kv}}(z)\partial_z^2\phi_{j,i}(z),\partial_z^2\phi_{j,m}(z)\rangle\partial_t q_{j,i}(t)\\&\qquad+\langle\gamma_j^{\mathrm{sv}}(z)\partial_z\phi_{j,i}(z),\partial_z\phi_{j,m}(z)\rangle\partial_t q_{j,i}(t)+m_j\phi_{j,i}(\ell)\partial_t^2 q_{j,i}(t)+\widetilde{\mathcal{k}}_{j,i}\boldsymbol{q}(t)\phi_{j,i}(\ell)\Big)\\&\qquad=-\sum_{i=1}^{N_j}\Big(\sum_{k=1}^{p_j}\langle\Gamma_{j,\mathrm{a}_k}(z)U_{j,\mathrm{a}_k},\partial_z^2\phi_{j,m}(z)\rangle\Big)\end{aligned}\tag{2.61}$$

with

$$\widetilde{\mathcal{k}}_{j,i}\boldsymbol{q}(t)=\begin{cases}k_{j,j+1}\big(\phi_{j,i}(\ell)q_{j,i}(t)-\phi_{j+1,i}(\ell)q_{j+1,i}(t)\big), & j=1\\k_{j,j+1}\big(\phi_{j,i}(\ell)q_{j,i}(t)-\phi_{j+1,i}(\ell)q_{j+1,i}(t)\big)\\-k_{j-1,j}\big(\phi_{j-1,i}(\ell)q_{j-1,i}(t)-\phi_{j,i}(\ell)q_{j,i}(t)\big)\end{cases},\quad j\in\{2,...,r-1\}\,,\\\begin{cases}-k_{r-1,r}\big(\phi_{j-1,i}(\ell)q_{j-1,i}(t)-\phi_{j,i}(\ell)q_{j,i}(t)\big), & j=r,\end{cases}\end{cases}\tag{2.62}$$

and $\boldsymbol{q}(t) = [q_{1,1}(t) \quad \dots \quad q_{1,N}(t) \quad \dots \quad q_{r,1}(t) \quad \dots \quad q_{r,N}(t)]^T \in \mathbb{R}^{rN}$ the vector of generalized coordinates. The evaluation of the arising integrals leads to the classic formulation of the equations of motion of a mechanic multi-body system

$$M\ddot{\boldsymbol{q}}(t) + C\dot{\boldsymbol{q}}(t) + K\boldsymbol{q}(t) = L\boldsymbol{u}(t), \tag{2.63}$$

with $\boldsymbol{u}(t) = [U_{1,\mathrm{a}_1}(t) \quad \dots \quad U_{1,\mathrm{a}_{p_1}}(t) \quad \dots \quad U_{r,1}(t) \quad \dots \quad U_{r,\mathrm{a}_{p_r}}(t)]^T \in \mathbb{R}^{n_u}$ denotes the vector of generalized inputs, where the number of inputs is defined by $n_u = \sum_{j=1}^{r} p_j$. The elements of the mass matrix M, the damping matrix C, the stiffness matrix K, and the input matrix L are summarized in Appendix C.1.

By introducing the state vector $\boldsymbol{x}(t) = [\boldsymbol{q}^T(t) \quad \dot{\boldsymbol{q}}^T(t)]^T \in \mathbb{R}^{2rN}$ system (2.63) can be rewritten as

$$\dot{\boldsymbol{x}}(t) = A\boldsymbol{x}(t) + B\boldsymbol{u}(t), \quad t > 0, \quad \boldsymbol{x}(0) = \boldsymbol{x}_0, \text{ with} \tag{2.64}$$

$$A = \begin{bmatrix} 0 & I \\ -M^{-1}K & -M^{-1}C \end{bmatrix}, \quad B = \begin{bmatrix} 0 \\ M^{-1}L \end{bmatrix}, \tag{2.65}$$

where $I \in \mathbb{R}^{rN \times rN}$ denotes the identity matrix. In addition, the system is characterized by the two output vectors

$$\boldsymbol{y}_{\mathrm{pi}}(t) = H_{\mathrm{pi}}\boldsymbol{x}(t), \quad \boldsymbol{y}_{\mathrm{pm}}(t) = H_{\mathrm{pm}}\boldsymbol{x}(t), \tag{2.66}$$

where $\boldsymbol{y}_{\mathrm{pi}} \in \mathbb{R}^{n_{\mathrm{pi}}}$ denotes the deflection at the points of interest of the structure $\boldsymbol{z}_{\mathrm{pi}} \in \mathbb{R}^{n_{\mathrm{pi}}}$ stating the target of the motion planning and tracking control approach. Subsequently $\boldsymbol{y}_{\mathrm{pm}} \in \mathbb{R}^{n_{\mathrm{pm}}}$ denotes the measured strain (2.56) at the points of measurement $\boldsymbol{z}_{\mathrm{pm}} \in \mathbb{R}^{n_{\mathrm{pm}}}$, see also Fig. 2.5 and Table 2.2. Taking (2.56) and (2.60) into account the output matrices are given by

$$H_{\mathrm{pi}} = \begin{bmatrix} \boldsymbol{h}_{1,\mathrm{pi}}^T & 0 & 0 & \boldsymbol{0}^T \\ 0 & \ddots & 0 & \vdots \\ 0 & 0 & \boldsymbol{h}_{n_{\mathrm{pi}},\mathrm{pi}}^T & \boldsymbol{0}^T \end{bmatrix}, \quad H_{\mathrm{pm}} = \begin{bmatrix} \boldsymbol{h}_{1,\mathrm{pm}}^T & 0 & 0 & \boldsymbol{0}^T \\ 0 & \ddots & 0 & \vdots \\ 0 & 0 & \boldsymbol{h}_{n_{\mathrm{pm}},\mathrm{pm}}^T & \boldsymbol{0}^T \end{bmatrix}, \tag{2.67}$$

with $n_{\mathrm{pi}} = \sum_{j=1}^{r} n_{j,\mathrm{pi}}$ as well as $n_{\mathrm{pm}} = \sum_{j=1}^{r} n_{j,\mathrm{pm}}$ and

$$\boldsymbol{h}_{f,\mathrm{pi}}^T = \begin{bmatrix} \phi_{j,1}(z_{\mathrm{pi},f}) & \dots & \phi_{j,N}(z_{\mathrm{pi},f}) \end{bmatrix}, \quad \boldsymbol{h}_{g,\mathrm{pm}}^T = \frac{\ell_j}{2} \begin{bmatrix} \partial_z^2\phi_{j,1}(z_{\mathrm{pm},g}) & \dots & \partial_z^2\phi_{j,N}(z_{\mathrm{pm},g}) \end{bmatrix}. \tag{2.68}$$

2.1.3. Modeling of a Surface Interconnected Beam Structure

The surface interconnected beam structure is used as a proof of concept study of the actual wingsail structure introduced in Section 2.2. The setup consists of two single beams touching each other at their free tip, therefore they can be imagined as a segment of the wingsail. Considering the top view the structure forms a triangle, due to this the structure is also referred to as delta beam configuration.

Below, the mechanical configuration of the system is introduced. Subsequently, the kinetic and potential energy as well as the work of the non-conservative forces based on the results of the single Euler-Bernoulli beam are determined. This states the origin for the spatial varying description taking the extended Hamilton's principle into account analog to Section 2.1.2.3, where for the delta beam configuration the coupling of the beams has to be considered as an additional constraint. This touching constraint is addressed by the usage of a Lagrange multiplier resulting in a system of differential algebraic equations (DAEs). Finally, Galerkin's approximation provides a finite dimensional description of the equations of motion.

2.1.3.1. Mechanical Configuration

As depicted in the schematics and the photo of the experimental setup in Fig. 2.6 the delta beam configuration is composed of $r = 2$ carbon made beams. Both beams are clamped at $z = 0\,\mathrm{m}$ and are free but interconnected at $z = \ell$, where the same simplified notation is used as introduced in Section 2.1.2.1, i.e., $z = z^1$ and $s_j(t, z) = s_{3,j}(t, z)$. The connection at the free tip is established by the considered pretension of the configuration and ensured by an elastic clip allowing a longitudinal motion, i.e., the beams can slide along the respective contact surface.

Furthermore both beams are equipped with one MFC-patch (type Smart Materials GmbH M 8528 P1 see [105]) mounted on the inward side of the structure at $z_{1,\mathrm{a}_k} = z_{2,\mathrm{a}_k}$, see Fig. 2.6 and Table 2.3, facing each other in accordance with the single actuation concept, see Fig. 2.3. To provide a symmetric input range $U_{j,\mathrm{a}_k} \in$

$[-1000, 1000]$ V, see also Remark 2.1, the voltage bias $U_0 = 500$ V is applied which leads to a static tension as mentioned in Section 2.1.1.4. This effect is counter balanced by the previously discussed mechanical pretension. The initial tension is introduced by the geometric setting of the beam structure ensuring an undeformed state of the interconnected beams, if the voltage bias U_0 is applied. Due to this so-called "neutral state", the actual acting voltage results in $U_{\mathrm{a}_k}^{\mathrm{MFC}} = U_{\mathrm{a}_k}$. The common notation is further simplified by the fact that each beam is only equipped with a single MFC-actuator ($k = 1$), therefore below it is sufficient to label actuator parameters by the index $\mathrm{a} = \mathrm{a}_k$.

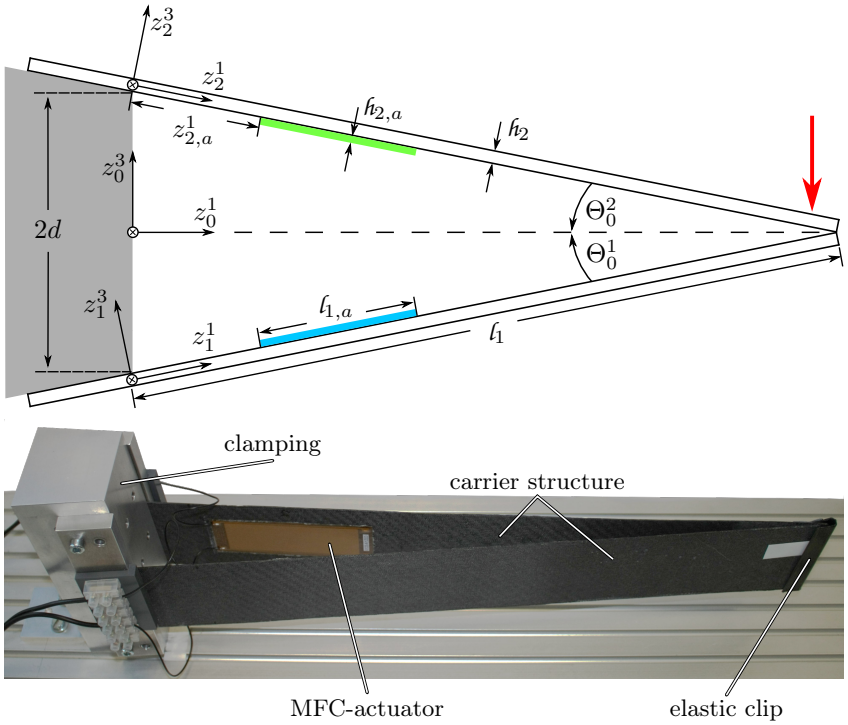

Figure 2.6.: *Top:* Schematic of the system of surface connected and horizontal aligned beams. The red arrow marks the point of interest of the motion planning and tracking control approach, see also [57]. *Bottom:* Photo of the experimental setup, see also [57].

Taking the identical geometry of both beams into account their length is given by $l = l_j$, see Table 2.3. The setup is further characterized by the constant lateral distance $2d$ between the clamping points. The beams' orientation is given by the constant angular displacement $\Theta_0^2 = -\Theta_0^1 = \Theta$ around the z^2-axis of the beam fixed coordinate system compared to the inertial coordinate system, see Fig. 2.6. Hence, the position of an arbitrary point on the inward surface of the carrier structure in the inertial coordinate system, or to be precise its z_0^3-coordinate, is determined by taking the Euler-Bernoulli beam assumptions introduced in Section 2.1.1 into account and neglecting the insignificant longitudinal deflection. This results in

$$p_{0,j}^3(z1) = \mathrm{s}_\Theta\left((-1)^{j+1}z - \frac{h_j}{2}\partial_z s_j\right) + \mathrm{c}_\Theta s_j + (-1)^j d, \tag{2.69}$$

with $\mathrm{c}_\Theta = \cos(\Theta)$ and $\mathrm{s}_\Theta = \sin(\Theta)$. The transversal displacement of beam j is denoted by s_j and h_j describes the height of the carrier layer. This formulation is used to define the touching constraint later on.

In the end, it has to be mentioned that the point of interest coincides with the point of measurement. Its location is highlighted by the red arrow in the schematic of Fig. 2.6 and its precise longitudinal position is listed in Table 2.3. As measurement device a laser sensor (Welotec GmbH type OWLF 4030 FA S1) based on the triangulation principle is used.

2.1.3.2. Touching Constraint, Stored Energies, and Virtual Work of the Non-conservative Forces

As mentioned before, the extended Hamilton's principle relies on the associated energies stating the basis of the determination of the equations of motion of the transversal displacement. The delta beam configuration is governed by an additional constraint defined by the touching of both beams at their tips. Such constraints can

Table 2.3.: Dimensions and locations of the actuator, point of measurement and interest of the delta beam configuration in mm, where $j \in \{1, 2\}$ refers to the associated beam. Furthermore, the index a marks characteristics of the MFC-actuators, see also Fig. 2.6.

dimension					
ℓ_j	w_j	h_j	ℓ_{j,a_k}	w_{j,a_k}	h_{j,a_k}
420.0	69.0	0.98	85.0	25.0	0.3

e_s	d	Θ_0^1	Θ_0^2
0.5	25.0	$-4.0°$	$4.0°$

MFC-actuator positions		point of interest and measurement	
$z_{1,\mathrm{a}}$	$z_{2,\mathrm{a}}$	$z_{\mathrm{pi},j}$	$z_{\mathrm{pm},j}$
23.0	23.0	401	401

be included in the modeling process by the use of a so-called Lagrange multiplier. Below the touching constraint as well as the energies of the interconnected beam system are introduced.

The touching constraint states that the transversal positions of the inward facing beams' surfaces have to be identical. Taking (2.69) into account the constraint is defined as

$$G(t) = p_{0,1}^3(\ell) - p_{0,2}^3(\ell) = \mathrm{s}_\Theta \frac{h_j}{2}\big(\partial_z s_2(t,\ell) - \partial_z s_1(t,\ell)\big) + \mathrm{c}_\Theta\big(s_1 - s_2(t,\ell)\big) + 2\ell\mathrm{s}_\Theta - 2d = 0. \tag{2.70}$$

By geometric construction of the setup the last term evaluates to $2\ell\mathrm{s}_\Theta - 2d = 0$ simplifying the constraint to

$$G(t) = \mathrm{s}_\Theta \frac{h_j}{2}\big(\partial_z s_2(t,\ell) - \partial_z s_1(t,\ell)\big) + \mathrm{c}_\Theta\big(s_1(t,\ell) - s_2(t,\ell)\big) = 0. \tag{2.71}$$

The stored energies and the virtual work of non-conservative forces of the delta beam configuration are given by the sum of the energies and virtual work of the single Euler-Bernoulli beam introduced in Section 2.1.1. In contrast to the vertical beam configuration the single actuation concept has to considered resulting in a dependency of the actuator placement mainly of the potential energy.

Kinetic Energy Considering (2.16) the kinetic energy of the delta beam configuration yields

$$W_{\mathrm{kin}}(t) = W_{\mathrm{kin},1}^{\mathrm{s}}(t) + W_{\mathrm{kin},2}^{\mathrm{s}}(t) = \frac{1}{2}\int_0^\ell \mu_1^{\mathrm{s}}(z)\big(\partial_t s_1\big)^2 + \mu_2^{\mathrm{s}}(z)\big(\partial_t s_2\big)^2\,\mathrm{d}z, \tag{2.72}$$

with

$$\mu_j^{\mathrm{s}}(z) = \rho_j A_j + \rho_{j,\mathrm{a}} A_{j,\mathrm{a}} \Omega_{j,\mathrm{a}}(z) \tag{2.73}$$

where $A_j = h w$, $A_{j,\mathrm{a}_k} = h_{\mathrm{a}_k} w_{\mathrm{a}_k}$, ρ, and ρ_{a_k} denote the the cross sections and densities of the carrier and MFC-patches, respectively. Furthermore, $\Omega_{j,\mathrm{a}_k}(z)$ describes the notch function (2.14) per beam, which provides the spatial characteristic of the MFC-patches or in other words it adds the additional effects of the actuators within their covered surface $z \in [z_{j,\mathrm{a}}, z_{j,\mathrm{a}} + \ell_{\mathrm{a}}]$.

Potential Energy Taking (2.26) into account the potential energy of the delta beam configuration results in

$$W_{\mathrm{pot}}(t) = W_{\mathrm{pot},1}^{\mathrm{s}}(t) + W_{\mathrm{pot},2}^{\mathrm{s}}(t) = \frac{1}{2}\int_0^\ell \Lambda_1^{\mathrm{s}}(z)\big(\partial_z^2 s_1\big)^2 + \Lambda_2^{\mathrm{s}}(z)\big(\partial_z^2 s_2\big)^2 + \Gamma_2^{\mathrm{s}}(z) U_2 \partial_z^2 s_2 - \Gamma_1^{\mathrm{s}}(z) U_1 \partial_z^2 s_1\,\mathrm{d}z \tag{2.74}$$

with

$$\Lambda_j^{\mathrm{s}}(z) = E_j^{1111} I_j + E_{j,\mathrm{a}}^{1111} I_{j,\mathrm{a}} \Omega_{j,\mathrm{a}}(z), \quad \Gamma_{j,\mathrm{a}}^{\mathrm{s}}(z) = \frac{A_{j,\mathrm{a}} a_{1,j,\mathrm{a}}^{11}(h_j + h_{j,\mathrm{a}})}{2\beta_{11,j,\mathrm{a}} e_s} \Omega_{j,\mathrm{a}}(z). \tag{2.75}$$

Considering Section 2.1.1 these substitutions are derived under the assumption of an asymmetric voltage supply taking the single actuation concept into account, the piezoelectric constitutive law and the underlying geometry.

The elasticity modulus of the carrier structure and the MFC-patches are denoted by E_j^{1111} and $E_{j,\mathrm{a}_k}^{1111}$ and the area moment of inertia of the carrier and MFC-actuators are given by $I_j = w_j \hbar_j^3/12$ as well as $I_{j,\mathrm{a}} = w_{j,\mathrm{a}}[(\hbar_j/2 + \hbar_{j,\mathrm{a}})^3 - (\hbar_j/2)^3]$. The parameters $a_{j,\mathrm{a},1}^{11}$, $\beta_{j,\mathrm{a},11}$ and e_s represent the piezoelectric parameter, the dielectric constant of the MFC-patch and the distance between neighboring electrodes on an MFC-patch.

Remark 2.4 *Considering the mechanical setup of the delta beam configuration taking only the single actuation into account, the notation is therefore simplified as follows* $\mu_j(z) = \mu_j^s(z)$, $\Lambda_j(z) = \Lambda_j^s(z)$, *and* $\Gamma_j(z) = \Gamma_{j,a}^s(z)$.

Damping Models The virtual work of the non-conservative forces is provided by the sum of the virtual work of the single beam, as introduced in Section 2.1.1. In contrast to the vertical beam configuration, for the delta beam configuration only structural damping is considered as internal damping model. Hence, the work of the non-conservative forces is given by the sum of discussed forces of single beams (2.36) with $\gamma^{\mathrm{kv}}(z) = 0$, resulting in

$$\begin{aligned}\delta W_{\mathrm{nc}}(t) = -\int_0^\ell \Big(&\gamma_1^{\mathrm{v}}(z)\partial_t s_1(t,z^1)\delta s_1(t,z^1) + \gamma_2^{\mathrm{v}}(z)\partial_t s_2(t,z^1)\delta s_2(t,z^1) \\ &+ \gamma_1^{\mathrm{sv}}(z)\partial_t\partial_z s_1(t,z^1)\delta\partial_z s_1(t,z^1) + \gamma_2^{\mathrm{sv}}(z)\partial_t\partial_z s_2(t,z^1)\delta\partial_z s_2(t,z^1)\Big)\,\mathrm{d}z.\end{aligned} \tag{2.76}$$

The damping functions are given by (see (2.29) and (2.35))

$$\gamma_j^{\mathrm{v}}(z) = \gamma_{j,\mathrm{c}}^{\mathrm{v}}(z) + \gamma_{j,\mathrm{a}}^{\mathrm{v}}(z)\Omega_{j,\mathrm{a}}(z), \tag{2.77}$$

$$\gamma_j^{\mathrm{sv}}(z) = \gamma_{j,\mathrm{c}}^{\mathrm{sv}}(z) + \gamma_{j,\mathrm{a}}^{\mathrm{sv}}(z)\Omega_{j,\mathrm{a}}(z). \tag{2.78}$$

The parameters $\gamma_{\mathrm{c}}^{\mathrm{v}}(z)$, $\gamma_{\mathrm{a}}^{\mathrm{v}}(z)$, $\gamma_{\mathrm{c}}^{\mathrm{sv}}(z)$, and $\gamma_{\mathrm{a}}^{\mathrm{sv}}(z)$ denote the viscous and structural damping coefficient of the of the carrier and MFC actuators, respectively as discussed in Section 2.1.1.

2.1.3.3. Equations of Motion

Analog to the vertical beam configuration the extended Hamilton's principle is applied to obtain the equations of motion of the delta beam configuration. However, the process has to be extended to consider the touching constraint (2.83) governing the dynamic of the structure. Equality constraints can be addressed in the framework of Hamilton's principle by so-called Lagrange multipliers $p(t)$ [91]. In the context of physics the Lagrange multiplier can be interpreted as a constraining force which ensures that the underlying constraint is fulfilled. With this the extended functional reads

$$J(t) = \int_{t_0}^{t_1} \big(W_{\mathrm{kin}}(t) - W_{\mathrm{pot}}(t) + W_{\mathrm{nc}}(t) + p(t)G(t)\big)\,\mathrm{d}t \tag{2.79}$$

with $t_0 < t_1,\ t_0, t_1 \in \mathbb{R}$. To determine the equations of motion the Gâteaux derivative of $J(t)$ is introduced

$$\delta J(t) = \int_{t_0}^{t_1} \big(\delta W_{\mathrm{kin}}(t) - \delta W_{\mathrm{pot}}(t) + \delta W_{\mathrm{nc}}(t) + \delta p(t)G(t) + p(t)\delta G(t)\big)\,\mathrm{d}t, \tag{2.80}$$

with $\delta s(t_0, z) = \delta s(t_1, z) = 0$, where δ denotes the variational operator. As mentioned before the governing equations of motion result from the extremum of the functional $J(t)$.

For the evaluation of the extended Hamilton's principle the variations of the energies (2.72) and (2.74) as well as of the touching constraint (2.83) are required which are given by

$$\delta W_{\mathrm{kin}}(t) = \sum_{j=1}^{2} \int_0^\ell \mu_j(z)\partial_t s_j \delta\partial_t s_j\,\mathrm{d}z, \tag{2.81}$$

$$\delta W_{\mathrm{pot}}(t) = \sum_{j=1}^{2} \int_0^\ell \Lambda_j(z)\partial_z^2 s_j \delta\partial_z^2 s_j + (-1)^j \Gamma_{j,\mathrm{a}}(z)U_j(t)\delta\partial_z^2 s_j\,\mathrm{d}z, \tag{2.82}$$

$$\delta G(t) = \mathrm{s}_\Theta \frac{\hbar_j}{2}\big(\delta\partial_z s_2(t,\ell) - \delta\partial_z s_1(t,\ell)\big) + \mathrm{c}_\Theta\big(\delta s_1(t,\ell) - \delta s_2(t,\ell)\big). \tag{2.83}$$

Hence, considering (2.76) $\delta J(t)$ evaluates to

$$\begin{aligned}\delta J(t) = \int_{t_0}^{t_1} \sum_{j=1}^{2} \Bigg(\int_0^{\ell} & \mu_j(z)\partial_t s_j \delta\partial_t s_j - \Lambda_j(z)\partial_z^2 s_j \delta\partial_z^2 s_j - (-1)^j \Gamma_{j,\mathrm{a}}(z) U_j(t) \delta\partial_z^2 s_j \\ & - \gamma_j^{\mathrm{v}}(z)\partial_t s_j \delta s_j - \gamma_j^{\mathrm{sv}}(z)\partial_t\partial_z s_j \delta\partial_z s_j \,\mathrm{d}z \Bigg) \\ & + \delta p(t)\Big(\mathrm{s}_\Theta \frac{\hbar_j}{2}\big(\partial_z s_2(t,\ell) - \partial_z s_1(t,\ell)\big) + \mathrm{c}_\Theta\big(s_1(t,\ell) - s_2(t,\ell)\big)\Big) \\ & + p(t)\Big(\mathrm{s}_\Theta \frac{\hbar_j}{2}\big(\delta\partial_z s_2(t,\ell) - \delta\partial_z s_1(t,\ell)\big) + \mathrm{c}_\Theta\big(\delta s_1(t,\ell) - \delta s_2(t,\ell)\big)\Big)\,\mathrm{d}t.\end{aligned} \tag{2.84}$$

Applying partial integration to standardize the variational operator to $\delta s_j(t,z^1)$, $\delta s_j(t,\ell)$ and considering the fundamental lemma of variational calculus [91, 77] leads to

$$\begin{aligned}\delta J(t) = \int_{t_0}^{t_1} \sum_{j=1}^{2} \Bigg(\int_0^{\ell} & \Big\{ -\mu_j(z)\partial_t^2 s_j - \partial_z^2\big[\Lambda_j(z)\partial_z^2 s_j\big] - (-1)^j \partial_z^2 \Gamma_{j,\mathrm{a}}(z) U_j(t) \\ & - \gamma_j^{\mathrm{v}}(z)\partial_t s_j + \partial_z\big[\gamma_j^{\mathrm{sv}}(z)\partial_t\partial_z s_j\big]\Big\}\delta s_j \,\mathrm{d}z \\ & + \Big\{\partial_z\big[\Lambda_j(\ell)\partial_z^2 s_j(t,\ell)\big] + (-1)^j \partial_z \Gamma_{j,\mathrm{a}}(\ell) U_j(t) - \gamma_j^{\mathrm{sv}}(\ell)\partial_t\partial_z s_j(t,\ell)\Big\}\delta s_j(t,\ell) \\ & - \Big\{\Lambda_j(\ell)\partial_z^2 s_j(t,\ell) + (-1)^j \Gamma_{j,\mathrm{a}}(\ell) U_j(t)\Big\}\delta\partial_z s_j(t,\ell)\Bigg) \\ & + \delta p(t)\Big(\mathrm{s}_\Theta \frac{\hbar_j}{2}\big(\partial_z s_2(t,\ell) - \partial_z s_1(t,\ell)\big) + \mathrm{c}_\Theta\big(s_1(t,\ell) - s_2(t,\ell)\big)\Big) \\ & + p(t)\Big(\mathrm{s}_\Theta \frac{\hbar_j}{2}\big(\delta\partial_z s_2(t,\ell) - \delta\partial_z s_1(t,\ell)\big) + \mathrm{c}_\Theta\big(\delta s_1(t,\ell) - \delta s_2(t,\ell)\big)\Big)\,\mathrm{d}t.\end{aligned} \tag{2.85}$$

Considering the extended Hamilton's principle the true trajectory is found if the necessary condition $\delta J(t) = 0$ is fulfilled. Hence, the equations of motion can be read out or gathered from (2.85) leading to the PDE for the j^{th} beam

$$0 = -\mu_j(z)\partial_t^2 s_j - \gamma_j^{\mathrm{v}}(z)\partial_t s_j + \partial_z\big[\gamma_j^{\mathrm{sv}}(z)\partial_t\partial_z s_j\big] - \partial_z^2\big[\Lambda_j(z)\partial_z^2 s_j\big] - (-1)^j\partial_z^2\Gamma_{j,\mathrm{a}}(z)U_j(t), \tag{2.86a}$$

for $z \in (0,\ell)$ and $t > 0$. Taking the boundary conditions into account

$$s_j = 0, \quad \partial_z s_j = 0, \tag{2.86b}$$

for $t > 0$ at the clamped beam tip $z = 0$ and

$$\begin{aligned}0 &= \partial_z\Lambda_j(z)\partial_z^2 s_j - \gamma_j^{\mathrm{sv}}(z)\partial_t\partial_z s_j + (-1)^j\partial_z\Gamma_{j,\mathrm{a}}(\ell)U_j(t)\delta s_j(t,\ell) + (-1)^{j+1}p(t)\mathrm{c}_\Theta, \\ 0 &= -\Lambda_j(z)\partial_z^2 s_j - (-1)^j\Gamma_{j,\mathrm{a}}(\ell)U_j(t)\delta\partial_z s_j(t,\ell) + (-1)^j p(t)\mathrm{s}_\Theta\frac{\hbar_j}{2}\end{aligned} \tag{2.86c}$$

at the free but coupled beam tip $z = \ell$. Since no MFC-actuator extends to the beam tips (see Assumption 2.4) it follows that

$$\Gamma_{j,\mathrm{a}}(\ell)U_j(t)\delta\partial_z s_j(t,\ell) = \partial_z\Gamma_{j,\mathrm{a}}(\ell)U_j(t)\delta s_j(t,\ell) = 0, \quad \forall j.$$

The term $\delta p(t)G(t)$ has no direct effect in the functional because the touching constraint has to be fulfilled at any time $G(t) = 0$. Even though the term can not be neglected at all, because the Lagrange multiplier or constraining force $p(t)$ states an essential part of the boundary conditions, ensuring that the touching constraint (2.70) is fulfilled. In other words the constraint defines the origin of the determination of the constraining force $p(t)$, see Section 2.1.3.4. Hence, the equations of motion are given by a system of partial differential algebraic equations (PDAEs).

As mentioned in the context of the vertical beam configuration introduced in Section 2.1.2 the second order derivation of the spatial characteristics $\Omega_{j,\mathrm{a}}(z)$ of the MFC-patches defined in (2.14) requires an interpretation of the system in a distributional sense, e.g., in terms of the weak formulation.

2.1.3.4. Finite Dimensional Approximation of the Equations of Motion of the Surface Interconnected Beam Structure

The applied strategy for the delta beam configuration is the same as for the vertical beam configuration, see Section 2.1.2.4. However, due to the equations of motion based on PDAEs additional actions are necessary compared to the previously discussed process. Nevertheless, the approach utilizes the weak formulation of the equations of motion followed by the Galerkin approximation leading to a system of DAEs. Hereinafter, the constraining force has to be determined and integrated in a ODEs system.

Weak Formulation of the Equations of Motion The arising differentiations in the equations of motion of the spatial characteristics $\Omega_{j,\mathrm{a}}(z)$ in terms of the Heaviside function require to analyze the weak form of the equations of motion (2.86). Therefore, an arbitrary test function $\phi_j(z) \in H_0^2(0,\ell)$ is multiplied with the governing PDE (2.86a) resulting in

$$\begin{aligned}\mu_j(z)\partial_t^2 s_j\phi_j(z) + \gamma_j^{\mathrm{v}}(z)\partial_t s_j\phi_j(z) - \partial_z\big[\gamma_j^{\mathrm{sv}}(z)\partial_t\partial_z s_j\big]\phi_j(z)\\ + \partial_z^2\big[\Lambda_j(z)\partial_z^2 s_j\big]\phi_j(z) = -(-1)^j\partial_z^2\Gamma_{j,\mathrm{a}}(z)U_{j,\mathrm{a}_k}\phi_j(z),\end{aligned} \tag{2.87}$$

where $H_0^2(0,\ell) = \{\phi \in H^2(0,\ell) | \phi(0) = \partial_z\phi(0) = 0\}$.

Analog to the vertical beam configuration, the eigenfunctions of the undamped system (see Appendix B.2) are chosen as test functions $\phi_1(z) = \phi_2(z)$. The application of integration by parts shifts the two times derivative of $\Lambda_j(z)$ and $\Gamma_{j,\mathrm{a}_k}(z)$ to $\phi_j(z)$ taking the boundary conditions (2.55c) and (2.86b) into account. This yields

$$\begin{aligned}\langle\mu_j(z)\partial_t^2 s_j, \phi_j(z)\rangle + \langle\Lambda_j(z)\partial_z^2 s_j, \partial_z^2\phi_j(z)\rangle + \langle\gamma_j^{\mathrm{v}}(z)\partial_t s_j, \phi_j(z)\rangle + \langle\gamma_j^{\mathrm{sv}}(z)\partial_t\partial_z s_j, \partial_z\phi_j(z)\rangle\\ + (-1)^j\big(\mathrm{c}_\Theta - (\hbar_j/2)\mathrm{s}_\Theta\partial_{z1}\big)p(t) = -(-1)^j\langle\Gamma_{j,\mathrm{a}_k}(z)U_{j,\mathrm{a}_k}, \partial_z^2\phi_j(z)\rangle.\end{aligned} \tag{2.88}$$

Galerkin Approximation Considering the weak formulation the Galerkin approximation introduced in Section 2.1.2.4 is given by

$$s_j(z,t) \approx \sum_{i=1}^{N_j} q_{j,i}(t)\psi_{j,i}(z), \tag{2.89}$$

where the test function of the weak form is chosen as trail function $\psi_{j,i} = \phi_{j,i}$. In addition, as mentioned before $\{q_{j,i}(t)\}_{i=1}^{N_j}$ defines the set of time dependent coefficients or generalized coordinates. Applying the Galerkin approximation to the weak form (2.88)

$$\begin{aligned}&\sum_{m=1}^{N_j}\sum_{i=1}^{N_j}\Big(\langle\mu_j(z)\phi_{j,i}(z), \phi_{j,m}(z)\rangle\partial_t^2 q_{j,i}(t) + \langle\Lambda_j(z)\partial_z^2\phi_{j,i}(z), \partial_z^2\phi_{j,m}(z)\rangle q_{j,i}(t)\\ &+ \langle\gamma_j^{\mathrm{v}}(z)\phi_{j,i}(z), \phi_{j,m}(z)\rangle\partial_t q_{j,i}(t) + \langle\gamma_j^{\mathrm{sv}}(z)\partial_z\phi_{j,i}(z), \partial_z\phi_{j,m}(z)\rangle\partial_t q_{j,i}(t)\Big)\\ &= -\sum_{i=1}^{N_j}\Big(\langle\Gamma_{j,\mathrm{a}_k}(z)U_{j,\mathrm{a}_k}, \partial_z^2\phi_{j,i}(z)\rangle + (-1)^j\big(\mathrm{c}_\Theta\phi_{j,i}(\ell) - (\hbar_j/2)\mathrm{s}_\Theta\partial_{z1}\phi_{j,m}(\ell)\big)p(t)\Big)\end{aligned} \tag{2.90}$$

results in the required separation of the variables in time t and space z with $\boldsymbol{q}_j = [q_{j,1}(t) \quad \dots \quad q_{j,N}(t)]^T \in \mathbb{R}^N$ the vector of generalized coordinates of the j^{th} beam and the associated input signal U_j. This leads to

$$M_j\ddot{\boldsymbol{q}}_j(t) + C_j\dot{\boldsymbol{q}}_j(t) + K_j\boldsymbol{q}_j(t) = -\boldsymbol{l}_j U_j + \boldsymbol{f}_j p(t). \tag{2.91}$$

The elements of the mass matrix M_j, the damping matrix C_j, the stiffness matrix K_j, the input vector $\boldsymbol{l}_j$, and the constraining vector $\boldsymbol{f}_j$ are summerized in Appendix C.2. The second part of the DAE system describing the equations of motion is the algebraic touching constraints (2.83).

By differentiation of the underlying constraint the DAE system can be converted to an ODEs system [37]. In this context the index of the DAE system is defined as the number of time derivatives of the constraint until $\dot{p}(t)$ appears. For this purpose, the Galerkin approximation has to be applied to the touching constraint

$$G(t) = \boldsymbol{g}_1^T\boldsymbol{q}_1 + \boldsymbol{g}_2^T\boldsymbol{q}_2. \tag{2.92}$$

Twofold time differentiation yields

$$\partial_t^2 G(t) = \boldsymbol{g}_1^T \ddot{\boldsymbol{q}}_1(t) + \boldsymbol{g}_2^T \ddot{\boldsymbol{q}}_2(t). \tag{2.93}$$

Solving (2.91) for the acceleration $\ddot{\boldsymbol{q}}_j(t)$

$$\ddot{\boldsymbol{q}}_j(t) = -M_j^{-1} C_j \dot{\boldsymbol{q}}_j(t) - M_j^{-1} K_j \boldsymbol{q}_j(t) - M_j^{-1} \boldsymbol{l}_j U_j + M_j^{-1} \boldsymbol{f}_j p(t). \tag{2.94}$$

and substituting the result into (2.93) yields

$$\begin{aligned} \partial_t^2 G(t) = &- \boldsymbol{g}_1^T M_1^{-1} C_1 \dot{\boldsymbol{q}}_1(t) - \boldsymbol{g}_1^T M_1^{-1} K_1 \boldsymbol{q}_1(t) - \boldsymbol{g}_1^T M_1^{-1} \boldsymbol{l}_1 U_1 && (2.95)\\ &- \boldsymbol{g}_2^T M_2^{-1} C_2 \dot{\boldsymbol{q}}_2(t) - \boldsymbol{g}_2^T M_2^{-1} K_2 \boldsymbol{q}_2(t) - \boldsymbol{g}_2^T M_2^{-1} \boldsymbol{l}_2 U_2 + \kappa_p p(t). && (2.96) \end{aligned}$$

with $\kappa_p = \boldsymbol{g}_1^T M_1^{-1} \boldsymbol{f}_1 + \boldsymbol{g}_2^T M_2^{-1} \boldsymbol{f}_2$. Performing again a temporal differentiation and solving the result for $\dot{p}(t)$ leads to the desired ODE characterizing the constraining force

$$\dot{p} = \boldsymbol{c}_{p_1}^T \dot{\boldsymbol{q}}_1 - \boldsymbol{k}_{p_1}^T \boldsymbol{q}_1 - b_{p_1} U_1 + b_{dp_1} \dot{U}_1 + \boldsymbol{c}_{p_2}^T \dot{\boldsymbol{q}}_2 - \boldsymbol{k}_{p_2}^T \boldsymbol{q}_2 - b_{p_2} U_2 + b_{dp_2} \dot{U}_2 + \eta_p p, \tag{2.97}$$

where the substitutions are described in Appendix C.2.

The conversion of the index 3 DAE system into an ODE system imposes three (artificial) zero eigenvalues $\lambda_z = 0$. It has to be noted that the used high voltage amplifiers impose a prescribed voltage almost immediately compared to the reaction time of the mechanical parts. Hence, $\dot{U}_1$ and $\dot{U}_2$ can be neglected in formulation (2.97).

Reformulating (2.91) into a first order ODE system and adding (2.97) considering the discussed simplification, yields

$$\begin{aligned} \dot{\boldsymbol{x}}_j &= \boldsymbol{x}_{j+2}, && (2.98a)\\ \dot{\boldsymbol{x}}_{j+2} &= -M_j^{-1} C_j \boldsymbol{x}_{j+2} - M_j^{-1} K_j \boldsymbol{x}_j + M_j^{-1} \boldsymbol{f}_j p - M_j^{-1} \boldsymbol{l}_j u_j, && (2.98b)\\ \dot{p} &= \boldsymbol{c}_{p_1}^T \boldsymbol{x}_3 - \boldsymbol{k}_{p_1}^T \boldsymbol{x}_1 - b_{p_1} u_1 + \boldsymbol{c}_{p_2}^T \boldsymbol{x}_4 - \boldsymbol{k}_{p_2}^T \boldsymbol{x}_2 - b_{p_2} u_2 + \eta_p p, && (2.98c) \end{aligned}$$

considering the state vector $\boldsymbol{x}^T = [\boldsymbol{x}_1 \quad \boldsymbol{x}_2 \quad \boldsymbol{x}_3 \quad \boldsymbol{x}_4] = [\boldsymbol{q}_1 \quad \boldsymbol{q}_2 \quad \dot{\boldsymbol{q}}_1 \quad \dot{\boldsymbol{q}}_2] \in \mathbb{R}^{4N}$ and the input vector $\boldsymbol{u}^T = [U_1 \quad U_2] \in \mathbb{R}^2$. Introducing the matrix formulation of (2.98) leads to

$$\begin{bmatrix} \dot{\boldsymbol{x}} \\ \dot{p} \end{bmatrix} = \begin{bmatrix} A_x & \boldsymbol{\alpha}_{xp} \\ \boldsymbol{\alpha}_{px}^T & \eta_p \end{bmatrix} \begin{bmatrix} \boldsymbol{x} \\ p \end{bmatrix} + \begin{bmatrix} B_x \\ \boldsymbol{b}_p^T \end{bmatrix} \boldsymbol{u}. \tag{2.99}$$

where $\boldsymbol{x} \in \mathbb{R}^{4N}$ and $\boldsymbol{u} \in \mathbb{R}^2$ denote the state- and input vector, respectively. The definitions of the matrix elements are listed in the Appendix C.2.

Remark 2.5 *Beside the considered method to analyze DAE systems arising in multi-body dynamics several other approaches exist, e.g., the Weierstraß canonical form [65], which is also suitable for over- and underdetermined systems.*

The fact that the touching constraint has to be fulfilled at any time leads to the following assumption.

Assumption 2.5 *The constraining force $p(t)$ acts instantaneous. Hence, $\dot{p}(t) = 0$ holds true which leads to*

$$p = -\frac{\boldsymbol{\alpha}_{px}^T}{\eta_p} \boldsymbol{x} - \frac{\boldsymbol{b}_p^T}{\eta_p} \boldsymbol{u} \tag{2.100}$$

denoting the stationary description of the constraining force.

The substitution of the stationary force description into (2.99) yields

$$\begin{aligned} &\dot{\boldsymbol{x}} = A\boldsymbol{x} + B\boldsymbol{u}, \quad \text{with} \\ &A = A_x - \frac{\boldsymbol{\alpha}_{xp} \boldsymbol{\alpha}_{px}^T}{\eta_p}, \; B = B_x - \frac{\boldsymbol{\alpha}_{xp} \boldsymbol{b}_p^T}{\eta_p}, \end{aligned} \tag{2.101}$$

whereby the set of eigenvalues of the matrix A results in $\{\lambda_z, \lambda_k\} \in \mathbb{C}, \; k \in \mathbb{K} = \{2, \cdots, 4N\}$ with $\Re\{\lambda_k\} < 0$ together with the corresponding eigenvectors $\boldsymbol{v}_z$, $\boldsymbol{v}_k$.

In addition the system is characterized by the two output vectors

$$\boldsymbol{y}_{\mathrm{pi}}(t) = H_{\mathrm{pi}}\boldsymbol{x}(t), \quad \boldsymbol{y}_{\mathrm{pm}}(t) = H_{\mathrm{pm}}\boldsymbol{x}(t), \tag{2.102}$$

where $\boldsymbol{y}_{\mathrm{pi}} \in \mathbb{R}^{n_{\mathrm{pi}}}$ denotes the deflection at the points of interest of the structure $\boldsymbol{z}_{\mathrm{pi}} \in \mathbb{R}^{n_{\mathrm{pi}}}$ stating the target of the motion planning and tracking control approach. Subsequently $\boldsymbol{y}_{\mathrm{pm}} \in \mathbb{R}^{n_{\mathrm{pm}}}$ denotes the measured deflection at the points of measurement $\boldsymbol{z}_{\mathrm{pm}} \in \mathbb{R}^{n_{\mathrm{pm}}}$ considering the used laser sensors. For the delta beam configuration the points of interest and points of measurement coincide and are located near the beams' tips, see Fig. 2.5 and Table 2.2 for the precise location.

Hence, the output matrices yield

$$H_{\mathrm{pi}} = H_{\mathrm{pm}} = \begin{bmatrix} \boldsymbol{h}_1^T & 0 & \boldsymbol{0}^T \\ 0 & \boldsymbol{h}_2^T & \boldsymbol{0}^T \end{bmatrix}, \quad \text{with} \quad \boldsymbol{h}_j^T = \begin{bmatrix} \phi_{j,1}(z_{\mathrm{pi},j}) & \dots & \phi_{j,N}(z_{\mathrm{pi},j}) \end{bmatrix}. \tag{2.103}$$

2.2. Equations of Motion of the Elastic Wingsail

In general, the derivation process of the equations of motion of the wingsail displays similarities to the previously discussed beam structures. However, the complexity of the structure mainly induced by the curvature of the wingsail area requires a different approximation process. This is why instead of an analytic approach the finite element method (FEM) is applied.

The section is organized as follows. At first the mechanical design of the considered wingsail structure is discussed. Thereafter, the theory of linear elasticity is briefly reviewed which states the basis of the modeling process and describes the underlying physical effects of the elastic deformation of the structure. The theory of linear elasticity directly provides the equations of motion of a flexible structure considering different sets of boundary conditions. Finally, the finite dimensional approximation of the PDE based description in terms of a spatial discretization by the FEM is briefly discussed.

2.2.1. Mechanical Configuration

The considered wingsail is characterized by two unitary carbon sailing areas mounted on a narrowing mast of the boat. The mast tapers linear from bottom to top. Its thickness at ground level is given by $h_{\mathrm{m}}(0\,\mathrm{m}) = 0.05\,\mathrm{m}$ and $h_{\mathrm{m}}(1.77\,\mathrm{m}) = 0.025\,\mathrm{m}$ at the mast's top. The opposite edge is characterized by the touching of both sailing areas similar to the previously discussed delta beam configuration of Section 2.1.3. Moreover, the top and bottom edges are free.

Fig. 2.7 illustrates the setting of the wingsail by a 3-d explosion drawing and a schematic of the side view of the right structure providing the measurements and positions of the considered components. The numeric values of these geometric measurements are summarized in Table 2.4. In addition Table 2.5 lists the location of the points of measurement. For the wingsail structure the points of measurement are identical to the points of interest.

Beside their mounting and geometry, the sailing areas are characterized by four carbon supply beams mounted on the "inside" surfaces of the wingsail facing each other. The horizontal installation of the supply beams strengthens the sail, where all beams are mounted flush with the mast as depicted in the schematics on the right of Fig. 2.7. Furthermore, they end in a constant distance $z_{\mathrm{f}}^1 = 0.03$ m to the touching edge. The resulting non-strengthened area on the touching tip allows the gliding of the sailing areas on each other. Due to the integrated supply beams the stiffness of the complete structure is partially increased. This increases the effect and therefore the efficiency of the embedded MFC-actuators to the flexible and weakly damped structure. All actuators are placed in a constant distance $z_{\mathrm{m}}^1 = 0.02\,\mathrm{m}$ to the mast, providing a lever capable to generate significant deflections of the sail in z^1-direction.

In contrast to Section 2.1, where the embedded MFC-actuators are modeled by two counter-rotating bending moments, the induced deformation is modeled by two tractions $\boldsymbol{f}_{\Gamma,\mathrm{a}_k}^{\mathrm{f}}(t, \boldsymbol{z}_{\mathrm{a}_k})$, $\boldsymbol{f}_{\Gamma,\mathrm{a}_k}^{\mathrm{r}}(t, \boldsymbol{z}_{\mathrm{a}_k})$ per MFC-patch. The modeling by forces is required by the used FEM software tools. The tractions act on the boundaries of the MFC-patch which are aligned with the z^3-axis. Both forces point either inwards of the concerning actuator or outwards leading to the typical shorting / stretching of the MFC-actuator. Taking the mounting of the actuator on the sail's surface into account the actuator deformation results in a bending of the wingsail structure. The tractions are defined as follows

$$\boldsymbol{f}_{\Gamma,\mathrm{a}_k}^{\mathrm{f}}(t, \boldsymbol{z}_{\mathrm{a}_k}) = -\boldsymbol{f}_{\Gamma,\mathrm{a}_k}^{\mathrm{r}}(t, \boldsymbol{z}_{\mathrm{a}_k}) = \beta U_{\mathrm{a}_k} \boldsymbol{n}(\boldsymbol{z}_{\mathrm{a}_k}), \quad k \in \{1, \dots, 4\} \tag{2.104}$$

with β denoting the conversion factor between the applied voltage and the generated force. In addition, $\boldsymbol{n}(\boldsymbol{z}_{\mathrm{a}_k})$ defines the outward pointing normal vector of the associated boundary surface Γ of the k^{th} MFC-actuator.

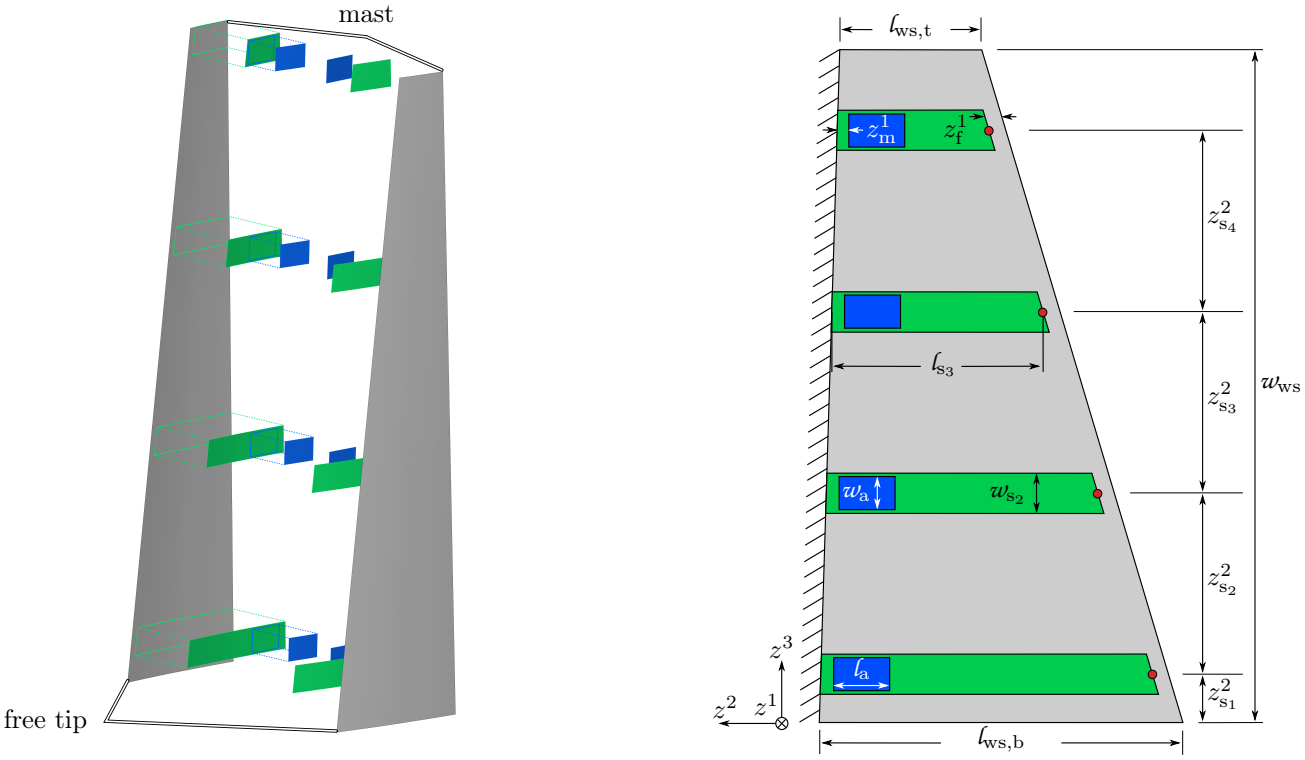

Figure 2.7.: *Left:* Explosion drawing (generated with *FreeCAD* [35]) of the assembled wingsail consisting of the sail areas (in gray), the supply beams (in green) and the embedded actuators (in blue), see also [59]. *Right:* Schematics of the right wingsail structure (side view) considering all elements, see also [59]. The red points mark the considered points of interest of transversal deflection $s^1(t, \boldsymbol{z}_{\mathrm{pi},f})$ $f \in [1, \cdots, 4]$. Table 2.5 lists the exact location. The numeric values of the depicted dimensions and positions are listed in Table 2.4.

Table 2.4.: List of dimensions in mm of the components wingsail area, supply beam and actuator referred by the indices ws, s and a, respectively.

lengths		widths		heights		positions	
$l_{ws,b}$	150.0	w_{ws}	1770.0	h_{ws}	0.20	z^1_m	30.0
$l_{ws,t}$	420.0					z^1_f	20.0
l_{s_1}	372.0	w_{s_1}	75.0	h_{s_1}	0.50	$z^2_{s_1}$	120.0
l_{s_2}	302.0	w_{s_2}	75.0	h_{s_2}	0.50	$z^2_{s_2}$	460.0
l_{s_3}	232.0	w_{s_3}	75.0	h_{s_3}	0.50	$z^2_{s_3}$	460.0
l_{s_4}	162.0	w_{s_4}	75.0	h_{s_4}	0.50	$z^2_{s_4}$	460.0
l_a	62.0	w_a	64.0	h_a	0.30		

Table 2.5.: Location of the points of measurement which are identical to the points of interest $\boldsymbol{z}_{\mathrm{pm},g} = \boldsymbol{z}_{\mathrm{pi},g}$ with $g \in [1, \ldots, 4]$.

in mm	$\boldsymbol{z}_{\mathrm{pm},1}$	$\boldsymbol{z}_{\mathrm{pm},2}$	$\boldsymbol{z}_{\mathrm{pm},3}$	$\boldsymbol{z}_{\mathrm{pm},4}$
z^1	3.04	3.01	2.96	2.94
z^2	-388.75	-364.43	-287.39	-236.02
z^3	117.22	656.58	1195.95	1736.21

Compared to the beam structures the mounted MFC-patches of the wingsail (type Smart Materials GmbH M 8557 P1, see [105]) are larger and therefore more powerful. However, their electrical characteristics are the same. The input voltage range is given by $U_{\mathrm{MFC}} \in [-500,\ 1500]\,\mathrm{V}$. Analog to the beam structures a linear behavior of the MFC-actuators is assumed, see Assumption 2.3. Also a constant bias $U_0 = 500\,\mathrm{V}$ (see Remark 2.1) is applied to ensure a "neutral state" of the wingsail by counter balancing the initial mechanical tension (pretension) introduced by the geometric setting of the voltage-free structure (analog to the delta beam configuration, see Section 2.1.3.1)

$$U_{\mathrm{a}_k}^{\mathrm{l}} = U_0 + U_{\mathrm{a}_k}, \quad U_{\mathrm{a}_k}^{\mathrm{r}} = U_0 - U_{\mathrm{a}_k}. \tag{2.105}$$

The superscripts l and r denote the location of the single MFC-patches mounted either on the left or on right part of the wingsail, respectively. Furthermore this leads to a symmetric input voltage range $U_{\mathrm{a}_k} \in [-1000,\ 1000]\,\mathrm{V}$. As in the delta beam configuration the MFC-actuators of both sailing areas are asymmetrically exited resulting in the desired agonist-antagonist behavior and also defines the system inputs in terms of the voltages U_{a_k} with $k \in \{1, \ldots, 4\}$.

Remark 2.6 *The dimensions and positions listed in Table 2.4 are used in the design of the computer aided design (CAD) model. However, the actual wingsail differs slightly from the CAD model due to the tolerances of the manufacturing process. Especially the height or thickness of the carbon made components varies as a result of the processing of the epoxy resin which is used in all carbon structures. Furthermore the thickness of the large elements is difficult to measure precisely considering its magnitude of a few 100 μm. Hence, an uncertainty remains which is further discussed in Section 3.2.2.3.*

2.2.2. Theory of Linear Elasticity

The linear elasticity is a subclass of the classical theory of elasticity and belongs to the field of continuum mechanics. It deals with the deformable continua of so-called linear elastic solids and describes their displacements subject to forces. Thereby, the term linear elastic solid refers to a solid body which deforms when a force is applied but returns to its original shape if the force is removed [23, chap. 9]. The equations of motion of the single Euler-Bernoulli beam as well as the systems of Euler-Bernoulli beams presented in Section 2.1 denote a subset of this theory. In contrast to this spatially 1-d system the equations of motion of the wingsail deals with 3-d displacement field of the structure which requires a different notation. Due to this, the necessary equations describing the deformation of the elastic wingsail structure are reintroduced in their tensor based representation. These equations consider assumptions for the wingsail which does not holds true for each solid in general. A detailed description of the linear elasticity is provided in textbooks, e.g., [23, 109].

The common equations of motion provided by the theory of linear elasticity (see [23, 109]) are given by

$$\rho \partial_t^2 \boldsymbol{s}(t, \boldsymbol{z}) - \boldsymbol{f}_\Omega(t, \boldsymbol{z}) - \nabla \cdot \big(\underline{\sigma}(\boldsymbol{s})\big) = \boldsymbol{0}, \quad t \in (0, T],\ \boldsymbol{z} \in \Omega. \tag{2.106a}$$

These consist of the product of the density ρ with the acceleration field $\partial_t^2 \boldsymbol{s}(t, \boldsymbol{z})$, the applied body force $\boldsymbol{f}_\Omega(\boldsymbol{z})$ (e.g., gravity) which acts on the whole domain Ω, and the divergence of the stress tensor $\underline{\sigma}(\boldsymbol{s})$. Whereby, the divergence operator of a continuously differentiable vector field is defined as

$$\nabla \cdot \big(\boldsymbol{s}(\boldsymbol{z})\big) = \begin{bmatrix} \partial_{z^1} & \partial_{z^2} & \partial_{z^3} \end{bmatrix} \cdot \begin{bmatrix} s^1(\boldsymbol{z}) & s^2(\boldsymbol{z}) & s^3(\boldsymbol{z}) \end{bmatrix},$$

with $\cdot$ denoting an arbitrary tensor product, which leads to a tensor contraction.

In addition, the boundary and initial conditions are required to describe the temporal displacement of a solid. For the wingsail structure the following conditions have to be considered

$$\text{BC (clamped):} \qquad \boldsymbol{s}(t, \boldsymbol{z}) = \boldsymbol{0}, \quad \boldsymbol{z} \in \Gamma_1,\ t \geq 0 \tag{2.106b}$$

$$\text{BC (actuation):} \qquad \underline{\sigma}(\boldsymbol{s}) \cdot \boldsymbol{n}(\boldsymbol{z}) = \boldsymbol{f}_\Gamma(t, \boldsymbol{z}), \quad \boldsymbol{z} \in \Gamma_2,\ t \geq 0, \tag{2.106c}$$

$$\text{BC (free):} \qquad \underline{\sigma}(\boldsymbol{s}) \cdot \boldsymbol{n}(\boldsymbol{z}) = \boldsymbol{0}, \quad \boldsymbol{z} \in \Gamma_3,\ t \geq 0, \tag{2.106d}$$

$$\text{IC:} \qquad \boldsymbol{s}(t, \boldsymbol{z}) = \partial_t \boldsymbol{s}(t, \boldsymbol{z}) = \boldsymbol{0}, \quad t = 0, \tag{2.106e}$$

where $\boldsymbol{f}_\Gamma(\boldsymbol{z})$ is defined as traction (also refereed to as surface force) acting on the boundary surface Γ_2 and $\boldsymbol{n}(\boldsymbol{z})$ describes the outward pointing normal vector of each boundary surface in $\Gamma = \Gamma_1 \cup \Gamma_2 \cup \Gamma_3$ at a specific point $\boldsymbol{z}$.

Remark 2.7 *Taking the wingsail geometry into account all surfaces of the sailing areas and the supply beams connected to the mast define the clamped boundary surfaces Γ_1. Such a boundary condition is often refereed to*

as Dirichlet condition. In addition, the surfaces on which the tractions $\boldsymbol{f}^{f}_{\Gamma,a_k}(t,\boldsymbol{z}_{a_k})$, $\boldsymbol{f}^{r}_{\Gamma,a_k}(t,\boldsymbol{z}_{a_k})$ *act define the actuated boundary surfaces* Γ_2 *also known as Neumann or natural condition. Considering the wingsail structure these are the surfaces of the MFC-actuators which are aligned with the* z^3*-axis. Finally, all other surfaces denote the set of free boundaries* Γ_3*.*

Furthermore, it has to be mentioned that the impact of gravity can be neglected due to the high amount of stiffness of the structure in the z^3-axis induced by the shape and clamping. Hence, the acting body forces yield $\boldsymbol{f}_\Omega(\boldsymbol{z}) = \boldsymbol{0}\,\mathrm{N}$.

Recalling from Section 2.1.1 the stress tensor (2.106a) is given by the constitutive law (Hooke's law) [23, chap. 9],[111] providing a relation between the stress and the strain

$$\underline{\sigma}(\boldsymbol{s}) = \underline{E} \cdot \underline{\epsilon}(\boldsymbol{s}). \tag{2.107}$$

Here, $\cdot$ denotes the tensor product of the 4^{th} order elasticity tensor $\underline{E}$ with the symmetric second order strain tensor

$$\underline{\epsilon}(\boldsymbol{s}) = \frac{1}{2}\Big(\nabla \boldsymbol{s} + \big(\nabla \boldsymbol{s}\big)^T\Big) \tag{2.108}$$

with ∇ denoting the gradient of an continuous displacement field $\boldsymbol{s}$. This is a compact notation of the commonly used and previously discussed component form considering Einstein's sum convention

$$\sigma^{im} = E^{imkl}\epsilon_{kl}.$$

Assuming isotropic and homogeneous material, Hookes's law simplifies to

$$\underline{\sigma}(\boldsymbol{s}) = \lambda \mathrm{Tr}\big(\underline{\epsilon}\big) I + 2\mu\underline{\epsilon}, \tag{2.109}$$

where I denotes the identity matrix (second order identity tensor), see Assumption 2.2 and [23, chap. 9]. The stiffness of the considered material is specified by the Lamé parameters λ, μ. Both parameters can be determined by Young's modulus E and the Poisson's ratio ν as follows [23, chap. 9]

$$\lambda = \frac{\nu E}{(1+\nu)(1-2\nu)}, \quad \mu = \frac{E}{2(1+\nu)}. \tag{2.110}$$

Considering the symmetric strain tensor $\underline{\epsilon}(\boldsymbol{s})$ the stress tensor $\underline{\sigma}(\boldsymbol{s})$ can be reformulated as

$$\underline{\sigma}(\boldsymbol{s}) = \lambda \mathrm{Tr}\big(\nabla \boldsymbol{s}\big) I + \mu\Big(\nabla \boldsymbol{s} + \big(\nabla \boldsymbol{s}\big)^T\Big). \tag{2.111}$$

The formulation (2.106a) of the equations of motion describes an energy conserving system which is not capable to cover the non-conservative dynamics of the wingsail. Therefore, the system has to be extended by a damping function to achieve a realistic behavior. Commonly this is done by the usage of the so-called Rayleigh damping. This damping model results in a spatially discretized formulation in a damping matrix, which is proportional to the mass and stiffness matrix $C = \gamma^{\mathrm{v}} M + \gamma^{\mathrm{kv}} K$ leading to a damping force $\boldsymbol{f}_{\mathrm{d}} = -C\partial_t \boldsymbol{s}(\boldsymbol{z})$. Considering [77, chap. 7] and [120, chap. 16] the mass proportional term represents viscous damping and the stiffness proportional term depicts Kelvin-Voigt damping, with the corresponding damping parameter γ^{v} and γ^{kv}, respectively. To achieve this damping effect in the continuous strong formulation the damping force is introduced as a vector field

$$\boldsymbol{f}_{\mathrm{d}} = -\Big(\gamma^{\mathrm{v}}\rho\partial_t \boldsymbol{s} - \gamma^{\mathrm{kv}}\nabla\cdot\big(\underline{\sigma}(\partial_t \boldsymbol{s})\big)\Big). \tag{2.112}$$

Taking the FEM into account this formulation directly leads to the damping matrix of [77, chap. 7] without further expensive computation by the sum of the already determined mass and stiffness matrix. Furthermore, this formulation enables an operator based representation, which states the basis of the implementation in the used FEM framework, see also Appendix A. This "external" damping force appears as a general force which leads to the residual formulation of the damped linear elasticity equation and the related boundary as well as initial conditions

$$\text{PDE:} \quad \rho\partial_t^2 \boldsymbol{s}(t,\boldsymbol{z}) - \boldsymbol{f}_\Omega(t,\boldsymbol{z}) - \nabla\cdot\big(\underline{\sigma}(\boldsymbol{s})\big) + \gamma^{\mathrm{v}}\rho\partial_t \boldsymbol{s} - \gamma^{\mathrm{kv}}\nabla\cdot\big(\underline{\sigma}(\partial_t \boldsymbol{s})\big) = \boldsymbol{0}, \quad \boldsymbol{z}\in\Omega,\ t\in(0,T], \tag{2.113a}$$

$$\text{BC (clamped):} \quad \boldsymbol{s}(t,\boldsymbol{z}) = \boldsymbol{0}, \quad \boldsymbol{z}\in\Gamma_1,\ t\geq 0 \tag{2.113b}$$

$$\text{BC (actuation):} \quad \underline{\sigma}(\boldsymbol{s})\cdot\boldsymbol{n}(\boldsymbol{z}) = \boldsymbol{f}_\Gamma(t,\boldsymbol{z}), \quad \boldsymbol{z}\in\Gamma_2,\ t\geq 0, \tag{2.113c}$$

$$\text{BC (free):} \quad \underline{\sigma}(\boldsymbol{s})\cdot\boldsymbol{n}(\boldsymbol{z}) = \boldsymbol{0}, \quad \boldsymbol{z}\in\Gamma_3,\ t\geq 0, \tag{2.113d}$$

$$\text{IC:} \quad \boldsymbol{s}(t,\boldsymbol{z}) = \partial_t \boldsymbol{s}(t,\boldsymbol{z}) = \boldsymbol{0}, \quad t=0. \tag{2.113e}$$

2.2.3. Finite Dimensional Approximation of the Equations of Motion Using the Finite Element Method

Similar to the Galerkin approximation used for the beam models before, the FEM is introduced to obtain a finite dimensional approximation of the infinite dimensional model. In fact, Galerkin's approximation is part of the presented FEM algorithm. Due to this the weak formulation of the associated equations of motion states again the origin of the approximation. The main difference to the previous approach is displayed by the choice of the trail and test function.

Below the divergence theorem (also known as Gauss's theorem) or a multi-dimensional integration by parts is recalled which is frequently used in the following subsections.

Definition 2.2 *Taking an arbitrary vector* $\boldsymbol{u}$ *and tensor* $\underline{T}$ *into account the divergence theorem ([111], [49, chap. 1, 8]) is defined as*

$$\int_{\Omega} \nabla \boldsymbol{u} : \underline{T} \, \mathrm{d}\Omega = \int_{\Gamma} \boldsymbol{u} \cdot (\boldsymbol{n}(\boldsymbol{z}) \cdot \underline{T}) \, \mathrm{d}\Gamma - \int_{\Omega} \boldsymbol{u} \cdot (\nabla \cdot (\underline{T})) \, \mathrm{d}\Omega, \tag{2.114}$$

where : *denotes the double tensor contraction* $\underline{h} : \underline{k} = \operatorname{trace}(\underline{h}^T \underline{k}) = \operatorname{trace}(\underline{k}\,\underline{h}^T)$ *[49, chap. 1].*

2.2.3.1. Weak Formulation

The application of the FEM requires the weak form of the governing PDE and the related boundary condition. As before, the weak form is constructed by the product of the PDE with an arbitrary vector of continuous test functions $\boldsymbol{\phi}$. The test function has to fulfill the same boundary conditions as the original problem [120, chap. 3]. For the considered problem formulation this yields

$$\int_0^T \int_{\Omega} \rho \boldsymbol{\phi} \cdot \partial_t^2 \boldsymbol{s}(t,\boldsymbol{z}) - \boldsymbol{\phi} \cdot \boldsymbol{f}_{\Omega}(t,\boldsymbol{z}) - \boldsymbol{\phi} \cdot \nabla \cdot \big(\underline{\sigma}(\boldsymbol{s})\big) + \gamma^{\mathrm{v}} \rho \boldsymbol{\phi} \cdot \partial_t \boldsymbol{s} - \gamma^{\mathrm{kv}} \boldsymbol{\phi} \cdot \nabla \cdot \big(\underline{\sigma}(\partial_t \boldsymbol{s})\big) \, \mathrm{d}\Omega \, \mathrm{d}t = 0. \tag{2.115}$$

Applying the divergence theorem (2.114) results in

$$\begin{aligned} 0 = &\int_0^T \int_{\Omega} \rho \boldsymbol{\phi} \cdot \partial_t^2 \boldsymbol{s}(t,\boldsymbol{z}) - \boldsymbol{\phi} \cdot \boldsymbol{f}_{\Omega}(t,\boldsymbol{z}) + \nabla \boldsymbol{\phi} : \underline{\sigma}(\boldsymbol{s}) + \gamma^{\mathrm{v}} \rho \boldsymbol{\phi} \cdot \partial_t \boldsymbol{s} + \gamma^{\mathrm{kv}} \nabla \boldsymbol{\phi} : \underline{\sigma}(\partial_t \boldsymbol{s}) \, \mathrm{d}\Omega \, \mathrm{d}t \\ &- \int_0^T \int_{\Gamma} \boldsymbol{\phi} \cdot \big(\boldsymbol{n}(\boldsymbol{z}) \cdot \underline{\sigma}(\boldsymbol{s})\big) + \gamma^{\mathrm{kv}} \boldsymbol{\phi} \cdot \big(\boldsymbol{n}(\boldsymbol{z}) \cdot \underline{\sigma}(\partial_t \boldsymbol{s})\big) \, \mathrm{d}\Gamma \, \mathrm{d}t. \end{aligned} \tag{2.116}$$

Considering the definition of the stress tensor (2.111) the time derivative yields

$$\underline{\sigma}(\partial_t \boldsymbol{s}) = \partial_t \underline{\sigma}(\boldsymbol{s}). \tag{2.117}$$

In view of the boundary condition (2.113b) to (2.113d) as well as the absence of body forces $\boldsymbol{f}_{\Omega}(t,\boldsymbol{z}) = \boldsymbol{0}\,\mathrm{N}$, the weak form (2.116) can be simplified to

$$\begin{aligned} 0 = &\int_0^T \int_{\Omega} \rho \boldsymbol{\phi} \cdot \partial_t^2 \boldsymbol{s}(t,\boldsymbol{z}) + \nabla \boldsymbol{\phi} : \underline{\sigma}(\boldsymbol{s}) + \gamma^{\mathrm{v}} \rho \boldsymbol{\phi} \cdot \partial_t \boldsymbol{s} + \gamma^{\mathrm{kv}} \nabla \boldsymbol{\phi} : \underline{\sigma}(\partial_t \boldsymbol{s}) \, \mathrm{d}\Omega \, \mathrm{d}t \\ &- \int_0^T \int_{\Gamma_2} \boldsymbol{\phi} \cdot \boldsymbol{f}_{\Gamma}(t,\boldsymbol{z}) + \gamma^{\mathrm{kv}} \boldsymbol{\phi} \cdot \partial_t \boldsymbol{f}_{\Gamma}(t,\boldsymbol{z}) \, \mathrm{d}\Gamma_2 \, \mathrm{d}t, \end{aligned} \tag{2.118}$$

where the traction $\boldsymbol{f}_{\Gamma}(t,\boldsymbol{z})$ denotes the control input.

2.2.3.2. Galerkin Approximation

The Galerkin approximation is applied by making use of

$$\boldsymbol{s}(t,\boldsymbol{z}) \approx \boldsymbol{s}_{\mathrm{h}}(t,\boldsymbol{z}) = \sum_{i=1}^{N} \phi_i(z) q_i(t), \tag{2.119}$$

where $\boldsymbol{s}_\mathrm{h} \in S^\mathrm{h} \subset H_0^1(\Omega)$ denotes the approximated displacement field. Here, S^h defines a finite dimensional space with the basis denoted as $\{\phi_i(z)\}_{i=1}^N$, also known as trail functions, where $N = \dim(S^\mathrm{h})$ which is later on called the number of degrees of freedom (DoFs). The time dependent coefficient or generalized coordinates are given by $\{q_i(t)\}_{i=1}^N$.

Until now only the notation changed slightly compared to the previously discussed approach. As mentioned before the choice of the test and trail functions causes the major difference compared to the analytic modeling process used for the beam structures. For the beam structures a set of eigenfunctions of the undamped single beam is used fulfilling the same boundary condition as the original problem. This is not suitable any more, due to the increased complexity of the structure. An analytic solution would require the application of the theory of shells considering tapered shell elements of non trivial geometries.

This motivates the use of the FEM. The main idea of the FEM is the subdivision of a complex domain into many simple geometries which can easily be described. With this and taking the Galerkin approximation into account the original problem (2.113) described by the PDE and its boundary conditions can be reformulated as a large system of ODEs which can be efficiently solved. Below, a brief introduction of the FEM is provided, which is mainly based on [120] providing an engineering perspective and [17] focusing on the mathematical background.

2.2.3.3. Spatial Discretization

The test and trail functions are defined by the spatial discretization which subdivides the complex domain into small and simple subdomains the so-called finite elements.

Remark 2.8 *Taking the exposition in [120] into account it is common practice to reduce the number of DoFs by only considering one half of a symmetric domain. In other words, redundant information can be skipped, i.e., it is sufficient to consider only the right part of the wingsail structure for the finite element (FE) analysis.*

The spatial discretization subdivides the complex structure into FEs characterized by a simple geometry. This enables the description of the displacement of the complete domain by the superposition of the displacement of single FEs which are easily determined compared to the original domain. Independent of the FE type each FE can be characterized as follows.

Definition 2.3 *The triple $(\mathcal{K}, \Phi, \mathcal{N})$ denotes a FE if*

- *the finite domain $\mathcal{K} \subseteq \mathbb{R}^n$ be a bounded and closed domain with nonempty interior and piecewise smooth boundary,*
- *the shape functions Φ describe the finite dimensional space of function on $\mathcal{K}$, and*
- *the nodal variables $\mathcal{N} = \{N_1, \ldots, N_k\}$ stating a basis of Φ', where it is assumed for a FE $(\mathcal{K}, \Phi, \mathcal{N})$ that the nodal variables N_i lie in a dual space, e.g., a Sobolev space. Hence, a basis $\{\phi_1, \ldots, \phi_k\}$ of Φ dual to $\mathcal{N}\big(N_i(\phi_m)\big) = \delta_{im}$ is called nodal basis for Φ,*

see [17, chap. 3.1].

In the definition above the symbol δ_{im} describes the Kronecker delta for which $\delta_{im} = 1$, if and only if $i = m$ else $\delta_{im} = 0$ holds true.

The FEs interact on their nodal variables with each other. Hence, the displacement at these position results directly by the FE solution. To obtain the description of the whole displacement field shape functions $\{\Phi_j\}_{j=1}^r$ are used, which approximate the displacement defined at the nodes within the FE domain $\{\mathcal{K}_j\}_{j=1}^r$. A common choice for shape functions are polynomials, where the order of the polynomial may affect the performance of the approximation in terms of the discretization error [120, chap. 2]. In case of the equations of motion (2.113) based on the theory of linear elasticity at least second order polynomials are recommended to cover the effects of the stress tensor $\underline{\sigma}(\boldsymbol{s})$.

As a result the displacement within the j^th FE can be determined by

$$\boldsymbol{s}_{\mathrm{h},j}(t) = \Phi_j(z)\boldsymbol{q}_j(t), \tag{2.120}$$

where $\boldsymbol{q}_j(t)$ denotes the nodal values of the displacement. Furthermore, the shape function $\Phi_j(z)$ of the j^th FE is characterized by the conditions

- $\Phi_j(z_j) = I$ if evaluated on the position z_j of its FE nodal variables,

- $\Phi_j(z_m) = 0$ if evaluated on the position z_m of the nodal variables of another FE, and
- $\Phi_j(z) = 0$ if evaluated outside the associated FE domain, i.e., $z \notin \mathcal{K}_j$.

Hence, the global approximation is given by the superposition of the shape function of each element

$$\boldsymbol{s}_{\mathrm{h}}(t, \boldsymbol{z}) = \begin{bmatrix} \Phi_1(z) & \dots & \Phi_r(z) \end{bmatrix} \begin{bmatrix} \boldsymbol{q}_1(t) \\ \vdots \\ \boldsymbol{q}_r(t) \end{bmatrix}, \tag{2.121}$$

where r denotes the number of considered FEs. Simultaneously the global approximation defines a mapping between local and global coordinates. Further information about different types of FEs and their associated shape functions are provided in [120, chap. 4] and [17, chap. 3].

As a result of (2.121), the local gradient of the m-d displacement field is given by

$$\nabla \boldsymbol{s}_{\mathrm{h},j}(t) = \partial_z \Phi_j(z) \boldsymbol{q}_j(t), \quad \text{with} \quad \partial_z \Phi_j(z) = \begin{bmatrix} \partial_{z^1} \Phi_{j,z^1} & 0 & 0 \\ 0 & \ddots & 0 \\ 0 & 0 & \partial_{z^m} \Phi_{j,z^m} \end{bmatrix} \tag{2.122}$$

and the global gradient reads

$$\nabla \boldsymbol{s}_{\mathrm{h}}(t, \boldsymbol{z}) = \begin{bmatrix} \partial_z \Phi_1(z) & \dots & \partial_z \Phi_r(z) \end{bmatrix} \begin{bmatrix} \boldsymbol{q}_1(t) \\ \vdots \\ \boldsymbol{q}_r(t) \end{bmatrix}. \tag{2.123}$$

This enables the determination of the strain and stress tensor defined by (2.108) and (2.109), see also [120, chap. 6].

The subdivision process of the domain, also known as meshing, is described in detail by [17, chap 3.3], where the main facts can be summarized as follows.

Definition 2.4 *A subdivision of a domain Ω is a finite collection of FE domains $\{\mathcal{K}_j\}_{j=1}^r$ such that*

- *the intersection of two distinct interiors denotes the empty set $\mathcal{K}_i^\circ \cap \mathcal{K}_m^\circ = \emptyset$ and*
- *the union of all boundaries results in the boundary of the domain $\bar{\mathcal{K}_j} = \bar{\Omega}$.*

Furthermore, it is import that the subdivision is characterized by some continuity properties which ensure that the elements interact properly with each other. In case of a 2-d domain discretized by triangular FE this can be assured by the definition of triangulation. This can analogously be formulated for higher dimensions and other types of FE, i.e., tetrahedrons and hexagons based meshes or even mixed meshes which are frequently used on 3-d domains.

Definition 2.5 *A subdivision of a polygonal domain Ω considering triangular FE is called a triangulation, if no vertex of any triangle lies in the interior of an edge on another triangle also known as "hanging node".*

Normally the subdividing process is performed by a meshing software, e.g., *Gmsh*, *T3D Mesh Generator*, *Trelis*, etc. providing the desired mesh. Depending on the software different types of FEs are supported. Furthermore most of these tools assist the user by different modi like automatic meshing or component-wise meshing. They also enable to choose between fine or a coarse meshes which directly effects the number of DoFs denoted by the number of nodal variables, or in other words the number of nodes times their free moving (displacement) directions. In addition these tools provide an automatic validation of the mesh to check if the resolution of the spatial discretization is fine enough and no "hanging" nodes arise, see Definition 2.5.

2.2.3.4. Assembly of the Finite Dimensional System

The last step of the FEM is the so-called assembling, where the weak form of the equations of motion (2.118) is evaluated taking the Galerkin approximation (2.119) into account. This yields the desired separation of the variables in the time dependent coefficients and the previously discussed spatial dependent test and trail function in terms of the FEs' shape functions.

For linear elastic systems this results in the well known formulation

$$M\ddot{\boldsymbol{q}}(t) + C\dot{\boldsymbol{q}}(t) + K\boldsymbol{q}(t) = L\boldsymbol{u}(t), \tag{2.124}$$

where the construction of the mass, damping and stiffness matrix as well as the input vector based on the shape functions $\{\Phi_j\}_{j=1}^r$ are presented in Appendix C.3. In addition, $\boldsymbol{q}(t) \in \mathbb{R}^N$ denotes the vector of time dependent coefficients of the DoFs, where N defines the total number of the considered DoFs. Furthermore, $\boldsymbol{u}(t) = [U_{\mathrm{a}_1}(t) \quad \dots \quad U_{\mathrm{a}_p}(t)] \in \mathbb{R}^p$ describes the input vector of the system composed of the applied voltages to MFC-actuators. The state vector $\boldsymbol{x}(t) = [\boldsymbol{q}^T(t) \quad \dot{\boldsymbol{q}}^T(t)]^T \in \mathbb{R}^{2N}$ can be introduced to obtain a first order system description

$$\dot{\boldsymbol{x}}(t) = A\boldsymbol{x}(t) + B\boldsymbol{u}(t), \quad t > 0, \quad \boldsymbol{x}(0) = \boldsymbol{x}_0, \text{ with} \tag{2.125}$$

$$A = \begin{bmatrix} 0 & I \\ -M^{-1}K & -M^{-1}C \end{bmatrix}, \quad B = \begin{bmatrix} 0 \\ M^{-1}L \end{bmatrix}, \tag{2.126}$$

where $I \in \mathbb{R}^{N \times N}$ denotes the identity matrix. In addition, the system is characterized by the two output vectors

$$\boldsymbol{y}_{\mathrm{pi}}(t) = H_{\mathrm{pi}}\boldsymbol{x}(t), \quad \boldsymbol{y}_{\mathrm{pm}}(t) = H_{\mathrm{pm}}\boldsymbol{x}(t), \tag{2.127}$$

where $\boldsymbol{y}_{\mathrm{pi}} \in \mathbb{R}^{n_{\mathrm{pi}}}$ denotes the displacement at the points of interest of the structure $\boldsymbol{z}_{\mathrm{pi}} \in \mathbb{R}^{n_{\mathrm{pi}}}$ which states the target of the motion planning and tracking control approach. In addition, $\boldsymbol{y}_{\mathrm{pm}} \in \mathbb{R}^{n_{\mathrm{pm}}}$ denotes the displacement of the structure at the points of measurement.

In most practical applications the sensors only provided pointwise measurement information instead of the complete displacement field of the structure modeled by the FEM. The considered laser sensors of the wingsail setup provide only the displacement of the structure in one direction in terms of the distance between the wingsail and the sensor (the line of sight). This characteristic can be addressed in the FEM framework by a projection of the solution space or a Gauss function. However, considering the finite dimensional system it is sufficient to evaluate the shape functions while neglecting the unmeasured dimensions. In case of the wingsail structure the points of interest and measurement coincide, so the system output matrices yield

$$H_{\mathrm{pi}} = H_{\mathrm{pm}} = \begin{bmatrix} \boldsymbol{h}^T & \boldsymbol{0}^T \end{bmatrix}, \quad \text{with} \quad \boldsymbol{h}^T = \begin{bmatrix} \phi_{j,1}(\boldsymbol{z}_{\mathrm{pi}}) & \dots & \phi_{j,N}(\boldsymbol{z}_{\mathrm{pi}}) \end{bmatrix}. \tag{2.128}$$

2.2.3.5. Tool Chain and Results for the Wingsail Structure

The mesh of the wingsail structure is generated by the meshing software *Trelis* and consists of 16545 tetrahedral FEs resulting in a total number of $N = 93255$ DoFs. As mentioned above the shape functions used for problems regarding linear elasticity should be polynomials of at least second order. Numeric experiments for the wingsail with tetrahedral FEs show that polynomials of higher order (> 2) do not show significant improvements regarding the displacement field solution. Hence, in this work quadratic polynomials are chosen as shape functions. Fig. 2.8 displays the resulting tetrahedral mesh of the wingsail structure.

Tetrahedral elements are considered due to the limitation of the used FE framework, where this decision does not affect the resulting performance. The chosen framework is the *Python* and *PETSc* [8] based open source project *Firedrake* [89, 50, 46], which denotes an extremely powerful and efficient tool especially due to the implemented *PETSc* algorithms. Furthermore, this framework can be extended by the user code providing the potential to write and include own functionalities. In contrast to other proprietary tools which only provide the second order system matrices of the finite dimensional system (2.124) and classic tools of FE-analysis like visualizations of different solution aspects, eigenvalue studies, etc., this denotes a great benefit. This potential is used in the context of the parameter identification process in Section 3.2.

Remark 2.9 *The ratio of the thickness and the area of the wingsail structure yields a challenging geometry for the meshing process, due to the fact that the thickness limits the size of the FE domain of the used FEs. The application of the theory of shells within the FE framework as presented in [59] using the FE software COMSOL [26] reduces the necessary number DoFs to 8461 considering the same structure of the wingsail. However, due to the previously discussed benefits of the used tool chain consisting of the FE framework Firedrake and the powerful methods of model order reduction (discussed in Chapter 4) the larger tetrahedral mesh is used for the modeling as well as for the control design.*

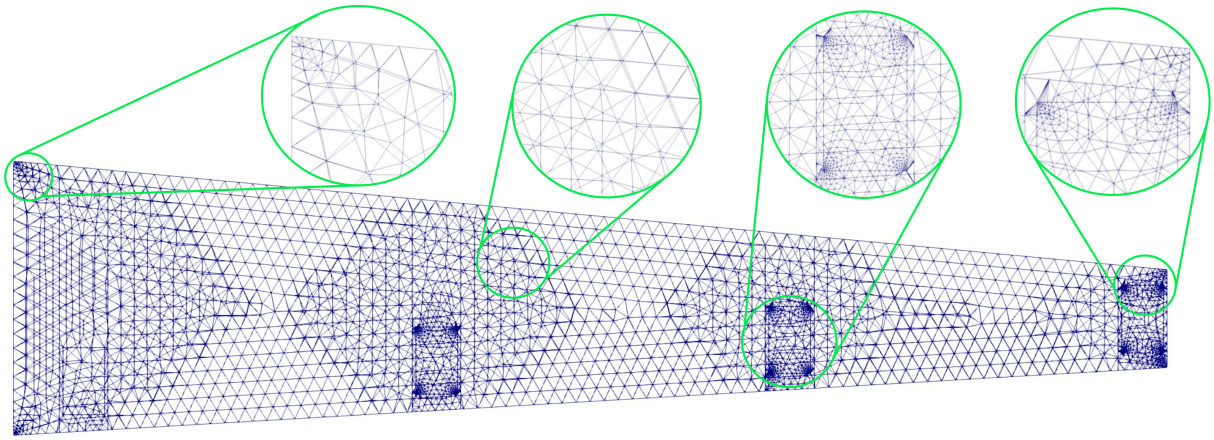

Figure 2.8.: Tetrahedral mesh of the wingsail structure generated by *Trelis* and visualized by *ParaView* [52, 7].

3. Parameter Identification

The previously deduced mathematical models provide the basis for the control design. Additionally, they allow to set up a simulation environment which can be used to validate different controllers or even different system configurations in general. The equations of motion determined in Chapter 2 rely on the knowledge of geometric and material parameters. While the dimensions can be measured exactly, it is hard or even impossible to measure the material parameters which are not provided in a datasheet by the manufacturer.

In order to determine all necessary parameters, a systematic method is required which is given by the so-called parameter identification also known as parameter estimation. The main objective is the fitting of the provided mathematical model or more precisely its simulation results to the measured signals of the experimental setup. This is done by adjusting the considered system parameters.

Considering the wide range of applications there is a variety of identification methods. In the following, two methods and their results are presented. The first method relies on the physical understanding of the considered setup and can only be used for small systems. It is used for the beam structures, which are characterized by the need of identify only a small number of parameters. Furthermore, these interconnected beam structures can be analyzed in an uncoupled state. This procedure splits the complex dynamic into several simpler processes, reducing the cross coupling effects of the parameters. Secondly, an adjoint based optimization process is introduced and used to identify the parameter of the wingsail. This method is capable of dealing with the complex system of the wingsail with its high number of parameters to be identified. In addition, this method can be efficiently implemented in the *Python* and *PETSc* based simulation environment enabling the benefits of working directly with the full order system in a fast manner. The use of the full system description during the identification process instead of a reduced model description preserve the physical meaning and effects of the parameters which may be lost by the model reduction process. The adjoint method makes use of the sensitivity analysis [93], where sensitivity functions (also called gradients of the objective function) are derived using the equations of motion and the variational calculus. In this sense sensitivity functions describe the effect of a parameter variation regarding the objective function which can be used to speed up the optimization process.

3.1. Manual Parameter Identification for the Beam Structures

The parameter identification for the presented beam structures relies on the physical understanding of the system. Due to the construction, both structures can be split into independent beams. This procedure offers the separation of the coupling effect from the single bending beam dynamics. The resulting single beam dynamics is characterized by only nine parameters consisting of the density, the damping, and the stiffness of the carrier structure and the MFC-actuators, as well as the tip mass and the conversion factor between voltage and bending moment. In addition, these parameters do not display a strong interference with each other. Hence, the introduced distributed parameter systems (equations of motion) of the vertical beam configuration (2.55) and of the delta beam configuration (2.86) or rather their finite dimensional approximations (2.98) and (C.1) can be analyzed manually.

For the vertical beam configuration, the separation means that the rubber band connecting neighboring beams has to be detached from the experimental setup. To reflect this change in the equations of motion the associated spring constants are set to $k_{i,m} = 0\,\mathrm{N/m^2}$. After the identification of the parameters of uncoupled beams the coupling spring constant can be identified by comparing the static deflection of the coupled and uncoupled configuration.

The uncoupling of the delta beam configuration means that only one beam is mounted when the measurement of the single beams is taken. Setting the coupling vector $\boldsymbol{\alpha}_{xp} = \mathbf{0}$ implies the decoupled behavior. For the neglected constraining force no further identification steps are needed because it relies only on the geometric constraint of the touching of the beam tips. Therefore, the coupling vector is composed of the material parameters of both beams.

For the measurement a voltage step is used to reveal the full dynamics of the single beam which has to be covered by the system model. The same step signal is used as input for the simulation. The fitting of the resulting step responses is done by adjusting the material parameters:

- The steady state deflection is given by the relation between Young's modulus E_j^{1111}, $E_{j,\mathrm{a}_k}^{1111}$ and the conversion factor of the MFC-patches $a_{j,\mathrm{a}_k,1}^{11}/\beta_{j,\mathrm{a}_k,11}$. Hence, these parameters can be determined by adjusting the parameters in the solution of the steady state equations, which can be computed without significant effort.
- The densities of the beam and the MFC-patches as well as the tip mass of the beam (for the vertical beam configuration) have a major impact on the frequency of the oscillation in the step response. The tip mass can only be adjusted within a small range around the initial guess which is provided by a weighing scale. This scale measurement differs slightly caused by the low weight of the aluminum of the tip mass and the uncertainties of the mass of the covered carbon of the carrier. Nevertheless, the initial guess is trustworthy and so only adjustments within a very small range are necessary, therefore the densities are the main parameters considering the identification.
- The main effect of the damping models becomes visible on the amplitude of the oscillations. In addition the Kelvin-Voigt as well as the structural damping have a minor effect on the frequency.

Taken into account these impacts on the static and dynamic behavior it is possible to tune the parameter for only one beam at a time. Subsequently, a least squares objective function can be formulated and solved by *MATLAB*'s `fmincon()`-function. This optimization is very slow, therefore the manual tuning is necessary to speed up the process and to bypass local minimums. The results of this mainly manual process and the previous mentioned static comparison to determine the spring constants are listed in Table 3.1 for the vertical beam configuration and in Table 3.2 for the delta beam configuration.

Table 3.1.: Set of identified system/material parameters of the vertical beam configuration with $r = 3$ beams and up to $p_j = 2$ equipped MFC-actuators per beam considering Remark 3.1.

beam	$j=1$	$j=2$		$j=3$		
actuator	$k=1$	$k=1$	$k=2$	$k=1$	unit	
ρ_j	1.134	1.008		1.050	$\times 10^3$	$\mathrm{kg/m^3}$
ρ_{j,a_k}	4.932			5.711	$\times 10^3$	$\mathrm{kg/m^3}$
E_j^{1111}	2.406				$\times 10^{10}$	$\mathrm{N/m^2}$
$E_{j,\mathrm{a}_k}^{1111}$	7.499				$\times 10^9$	$\mathrm{N/m^2}$
$\gamma^{\mathrm{v}}(z^1)$	1.399			1.679	$\times 10^{-2}$	kg/sm
$\gamma_{\mathrm{a}_k}^{\mathrm{v}}(z^1)$	8.892	0.445	0.356	8.892	$\times 10^{-2}$	kg/sm
$\gamma^{\mathrm{kv}}(z^1)$	9.521	9.790		9.521	$\times 10^{-5}$	$\mathrm{kgm^3/s}$
$\gamma_{\mathrm{a}_k}^{\mathrm{kv}}(z^1)$	2.503	2.482	2.497	2.512	$\times 10^{-5}$	$\mathrm{kgm^3/s}$
$\gamma^{\mathrm{sv}}(z^1)$	1.000				$\times 10^{-3}$	$\mathrm{kgm^2/s}$
$\gamma_{\mathrm{a}_k}^{\mathrm{sv}}(z^1)$	1.000		0.800	1.200	$\times 10^{-3}$	$\mathrm{kgm^2/s}$
$k_{1,2}, k_{2,3}$	2.399		3.516			$\mathrm{N/m^2}$
m_j	9.000	9.000		8.800	$\times 10^{-3}$	kg
$\frac{a_{j,\mathrm{a}_k,1}^{11}}{\beta_{j,\mathrm{a}_k,11}}$	1.961	2.069	2.055	2.027		$\mathrm{As/m^2}$

Remark 3.1 *It has to be mentioned that the combination of viscous and either Kelvin-Voigt or structural damping is required to match the behavior observed in experiments. In the following, the combination of viscous and structural damping is used.*

As an example the measured step response and the simulation result for the identified parameters of the first beam of the vertical beam configuration evaluated at the point of measurement is displayed in Fig. 3.1. The comparison shows that the amplitudes of the oscillation in the beginning are slightly too high and decay too fast in the end. However, this deviation is small and the overall matching between the measurement and the simulation shows a nearly exact synchronization. The related voltage step $u_1(t) = 700\,\mathrm{V}h(t - 0.5\,\mathrm{s})$ is also used as system excitation in the identification process.

Table 3.2.: Set of identified system / material parameters of the delta beam configuration where $j \in \{1, 2\}$ refers to the beams and the index a marks the MFC-actuators.

beam	$j = 1$	$j = 2$	unit	
ρ_j	7.24	8.60	$\times 10^2$	kg/m^3
$\rho_{j,\mathrm{a}}$	3.36	3.47	$\times 10^3$	kg/m^3
E_j^{1111}	9.74	11.52	$\times 10^9$	N/m^2
$E_{j,\mathrm{a}}^{1111}$	8.84	9.67	$\times 10^9$	N/m^2
$\gamma^{\mathrm{v}}(z^1)$	3.50	3.50	$\times 10^{-4}$	kg/sm
$\gamma_{\mathrm{a}}^{\mathrm{v}}(z^1)$	1.80	1.80	$\times 10^{-3}$	kg/sm
$\gamma^{\mathrm{sv}}(z^1)$	8.00	9.00	$\times 10^{-4}$	kgm^2/s
$\gamma_{\mathrm{a}}^{\mathrm{sv}}(z^1)$	7.60	7.60	$\times 10^{-3}$	kgm^2/s
$\frac{a_{j,\mathrm{a},1}^{11}}{\beta_{j,\mathrm{a},11}}$	2.54	2.54	$\times 10^0$	As/m^2

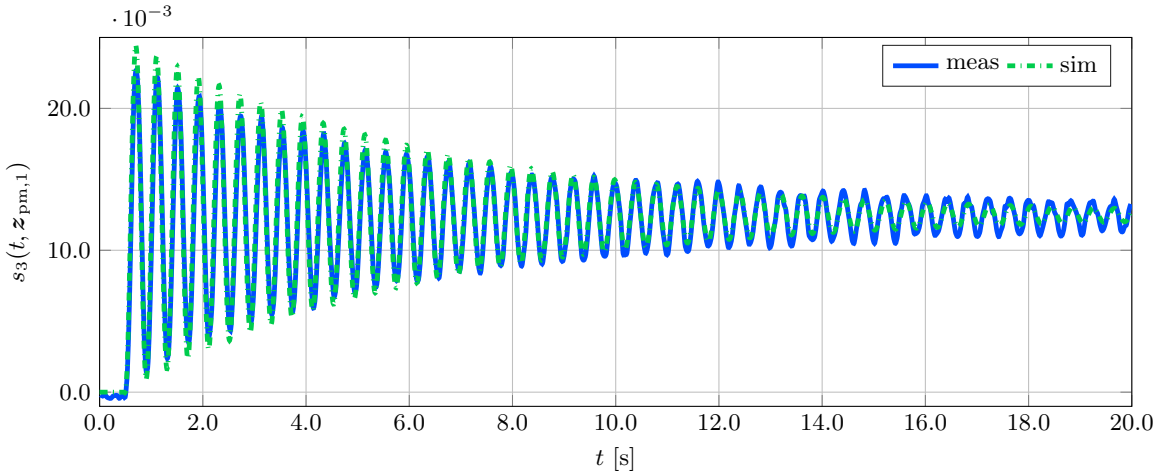

Figure 3.1.: Comparison of the measurement of the first beam of the vertical beam configuration with the related simulation results considering the identified parameters.

3.2. Parameter Identification for the Wingsail Structure Using the Adjoint Method

The wingsail is more complex than the previously discussed beam structures. It is impossible to separate its components for an independent identification. Therefore, the number of objective parameters and the associated cross coupling effects can not be reduced. They can only be split based on their temporal impact. One set of parameters affects only the transient behavior of the system. Hence, this set can only be identified considering the temporal solution of the displacement field. The second set on the other hand displays its impact on the steady state, so that it is sufficient to analyze the static displacement field reducing the computational effort. Due to the high system order of $N = 93255$ DoFs resulting from the FE-approximation the computational effort is much higher compared to the beam structures which deal with only up to 30 DoFs.

The main idea of the subsequent considered optimization based identification process is to reduce a quadratic cost or objective function (least squares problem formulation). This can be done by determining the impact of the desired parameters on the objective function. The impacts, also called gradients, can be deduced in different ways. The simplest one is the so-called finite difference method, where the optimization first varies the considered parameter, solves the system and evaluates the objective function. This is done in each iteration for each parameter to determine their impacts and directions in which the parameters have to be changed. Considering the equations of motion the stiffness and damping as well as the densities of each component of the wingsail has to be identified which results in 30 objective parameters. Taking the finite difference method into account this amount of parameters leads to a high computational effort which is too time consuming. However, the gradients can also be determined analytically by the sensitivity analysis [93]. One way to do this is the

so-called adjoint method, which applies the variational calculus to the equations of motion or in other words it introduces a Lagrange multiplier. The method is distinguish in the continuous adjoint based method which is based on the distributed parameter equations of motion and the discrete adjoint method relying on the spatial discretization of the equations of motion.

In this work the continuous adjoint method is used. However, both approaches are widely used, e.g., they are common in the field of aerospace engineering to optimize the profiles of airfoils, see, e.g., [86, 107] or [39]. Nearly at the same time the method became popular in the field of seismology [111, 32, 72], where it is used for 3-d analysis of the soil. It is also used in the field of medical engineering for tomography e.g. [30, 66] and flow control [43].

The main advantage of the adjoint method is the analytical sensitivity function (gradient) which relies on the solution of the adjoint state. Compared to the finite difference method, which requires at least one solution of the equations of motion per objective parameter, the adjoint method only requires one solution of the equations of motion and one of the adjoint equations independent of the number of objective parameters. This enables the usage of the full order system during the identification process. Therefore, further errors introduced by a reduced order model, which would blur the influence of the parameters (sensitivities), can be avoided.

In the following, the sensitivity functions are derived by the solution of the adjoint state of the equations of the linear static and transient elasticity. Afterwards, the optimization schema is presented and in the end results of a benchmark example (bending beam) as well as of the wingsail are presented.

3.2.1. Derivation of the Adjoint Equations and the Sensitivity Functions

For the case of linear elasticity, there are three classes of unknown material parameters

1. stiffness,
2. density,
3. and damping.

Additionally the input parameter of each MFC-actuator likewise affects the dynamics of the mechanical structure, but only acts at a constant ratio with the stiffness parameters. Therefore, it is sufficient to predefine this parameter set within a meaningful and physical parameter range and only identify the parameters affecting the stiffness.

The remaining parameter classes can be split into two sets. The first one, containing the stiffness, affects the solution of the steady state equations. The effect of the second set of parameters only appears in the dynamical behavior of the structure. Due to this separation, the identification process can be split as well, providing the benefit of reduced computational effort for the identification of the stiffness parameters by solving only the static equation. Density and damping parameters can only be identified by a process solving the transient equations of linear elasticity requiring a higher amount of computational time and storage.

In the following, the derivation of the static and transient sensitivity functions for the material parameters are presented. These functions can be constructed by the related adjoint state, which has to be introduced first.

3.2.1.1. Identification Process of the Static Case - the Stiffness Parameters

The static displacement of a flexible structure can be described by the equations of elastostatics which deals with the conditions of equilibrium of linear elasticity. It can be derived taking into account that all transient processes have settled, i.e., $\partial_t^2 \boldsymbol{s}(t,\boldsymbol{z}) = \partial_t \boldsymbol{s}(t,\boldsymbol{z}) = \boldsymbol{0}$, so that the equations of linear elasticity (2.106) simplify to (see also [23, 109])

$$\begin{aligned}
&\text{PDE:} && \boldsymbol{R}(\boldsymbol{z}) = -\boldsymbol{f}_\Omega(\boldsymbol{z}) - \nabla\cdot\big(\underline{\sigma}(\boldsymbol{s})\big) = \boldsymbol{0}, \quad \boldsymbol{z}\in\Omega, && (3.1a)\\
&\text{BC (clamped):} && \boldsymbol{s}(\boldsymbol{z}) = \boldsymbol{0}, \quad \boldsymbol{z}\in\Gamma_1, && (3.1b)\\
&\text{BC (actuation):} && \underline{\sigma}(\boldsymbol{s})\cdot\boldsymbol{n}(\boldsymbol{z}) = \boldsymbol{f}_\Gamma(\boldsymbol{z}), \quad \boldsymbol{z}\in\Gamma_2, && (3.1c)\\
&\text{BC (free):} && \underline{\sigma}(\boldsymbol{s})\cdot\boldsymbol{n}(\boldsymbol{z}) = \boldsymbol{0}, \quad \boldsymbol{z}\in\Gamma_3. && (3.1d)
\end{aligned}$$

In the static case the objective parameters are the Lamé parameters and the quadratic objective function can be defined as

$$J(\lambda,\mu) = \frac{\alpha}{2}\|\boldsymbol{s}^*(\boldsymbol{z}) - \boldsymbol{s}(\boldsymbol{z},\lambda,\mu)\|_{L^2}^2. \tag{3.2}$$

This function maps the quadratic deviation (multidimensional least squares) between a desired spatial displacement profile $\boldsymbol{s}^*(\boldsymbol{z})$ and the actual profile $\boldsymbol{s}(\boldsymbol{z}, \lambda, \mu)$ depending on a specific set of Lamé parameters into a real scalar cost in terms of the L^2 norm of the deviation profile. For numerical reasons a weighting parameter α is introduced.

Definition 3.1 *The L^2 norm of a vector-valued function $\boldsymbol{u} : \Omega \to \mathbb{R}^n$ is given by*

$$\|\boldsymbol{u}\|_{L^2} = \Big(\langle \boldsymbol{u}, \boldsymbol{u} \rangle_{L^2}\Big)^{\frac{1}{2}} = \Big(\int_\Omega \boldsymbol{u}^T \bar{\boldsymbol{u}} \, \mathrm{d}\Omega\Big)^{\frac{1}{2}} = \Big(\int_\Omega \boldsymbol{u} \cdot \boldsymbol{u} \, \mathrm{d}\Omega\Big)^{\frac{1}{2}}, \tag{3.3}$$

where $\langle \boldsymbol{u}, \boldsymbol{u} \rangle_{L^2}$ denotes the $L^2(\Omega)$ inner or scalar product [17] with $\bar{\boldsymbol{u}}$ denoting the complex conjugate of $\boldsymbol{u}$, see also Definition 2.1. If $\Omega \in \mathbb{R}^n$ holds true a vector field $\boldsymbol{v} : \Omega \to \mathbb{R}^n$, like the displacement field, is represented by a vector-valued function.

For the case of parameter identification the term "desired" means measured. In most practical applications the measurement is only provided pointwise. Hence, the desired deflection profile reduces to measurement information located at specific positions $\boldsymbol{z}_{\mathrm{pm}}$ on the domain. For the displacement field this means that only the DoFs (nodes of the mesh) located at $\boldsymbol{z}_{\mathrm{pm},g}$ provide the measured displacement. Regarding the used measurement method, the profile information of a 3-d vector field reduces to a vector field of lower order, e.g., a stationary laser measurement of a 3-d displacement field returns only a scalar value in terms of the distance between the device and the structure (line of sight).

Such profiles can be constructed considering the product of the displacement fields with an approximation of the Dirac function

$$\boldsymbol{s}_{\mathrm{pm}}(\boldsymbol{z}, \boldsymbol{z}_{\mathrm{pm}}, \lambda, \mu) = \boldsymbol{s}(\boldsymbol{z}, \lambda, \mu)\gamma(\boldsymbol{z}, \boldsymbol{z}_{\mathrm{pm}}), \quad \boldsymbol{s}^*_{\mathrm{pm}}(\boldsymbol{z}, \boldsymbol{z}_{\mathrm{pm}}) = \boldsymbol{s}^*(\boldsymbol{z})\gamma(\boldsymbol{z}, \boldsymbol{z}_{\mathrm{pm}}). \tag{3.4}$$

As a consequence, the modified objective function reads

$$J_{\mathrm{pm}}(\lambda, \mu) = \frac{\alpha}{2} \|\boldsymbol{s}^*_{\mathrm{pm}} - \boldsymbol{s}_{\mathrm{pm}}\|^2_{L^2}, \tag{3.5}$$

where as approximation for the Dirac a Gauss function or a projection of the solution space can be used. In fact, the implementation of this Dirac approximation defines a trail function which roughly speaking locates the nearest vertices of the mesh to the points of measurement and and constrains the motion to a single dimension only, see Fig. 3.2.

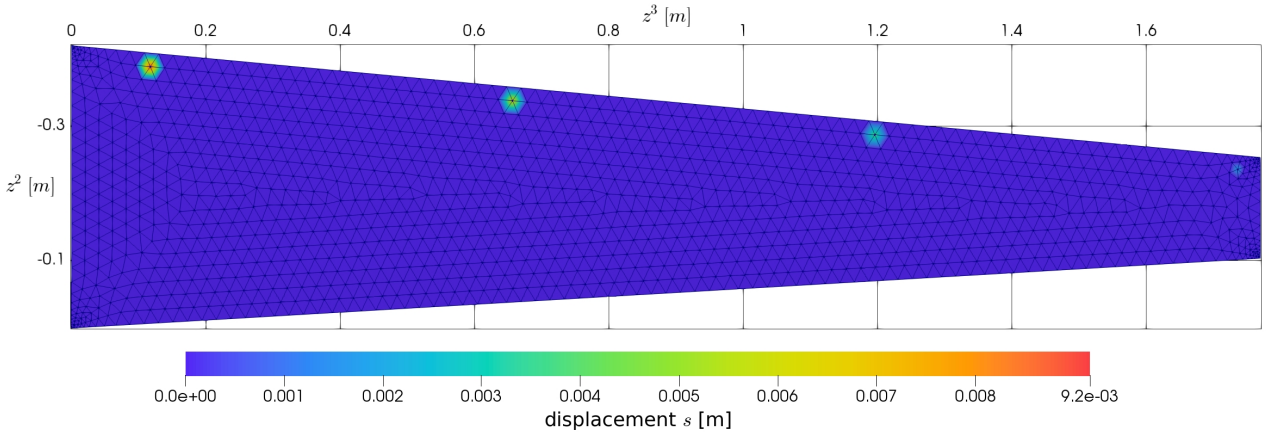

Figure 3.2.: Example of a desired / measured displacement profile $\boldsymbol{s}^*_{\mathrm{pm}}(\boldsymbol{z}_{\mathrm{pm}})$ of the wingsail structure using four laser sensors.

To determine the sensitivity function the objective function is extended by the product of the adjoint state (or Lagrange multiplier) $\boldsymbol{p}(\boldsymbol{z})$ and an auxiliary constraint. For the wingsail the constraint is given by the residual $\boldsymbol{R}(\boldsymbol{z})$ (3.1a). As a result the so-called Lagrangian yields

$$\mathcal{L} = J_{\mathrm{pm}} - \int_\Omega \boldsymbol{p} \cdot \boldsymbol{R} \, \mathrm{d}\Omega = \frac{\alpha}{2} \int_\Omega (\boldsymbol{s}^*_{\mathrm{pm}} - \boldsymbol{s}_{\mathrm{pm}}) \cdot (\boldsymbol{s}^*_{\mathrm{pm}} - \boldsymbol{s}_{\mathrm{pm}}) \, \mathrm{d}\Omega + \int_\Omega \boldsymbol{p} \cdot \big(\nabla \cdot \big(\underline{\sigma}(\boldsymbol{s})\big) + \boldsymbol{f}_\Omega\big) \, \mathrm{d}\Omega. \tag{3.6}$$

Applying the divergence theorem (2.114) with $\boldsymbol{u} = \boldsymbol{p}$ and $\underline{T} = \underline{\sigma}(\boldsymbol{s})$ and taking into account the boundary conditions (3.1b) to (3.1d) results in

$$\begin{aligned}
\mathcal{L} &= \frac{\alpha}{2} \int_{\Omega} (\boldsymbol{s}^*_{\mathrm{pm}} - \boldsymbol{s}_{\mathrm{pm}}) \cdot (\boldsymbol{s}^*_{\mathrm{pm}} - \boldsymbol{s}_{\mathrm{pm}}) \, \mathrm{d}\Omega + \int_{\Gamma} \boldsymbol{p}(\boldsymbol{z}) \cdot (\boldsymbol{n}(\boldsymbol{z}) \cdot \underline{\sigma}(\boldsymbol{s})) \, \mathrm{d}\Gamma \\
&\quad - \int_{\Omega} \nabla \boldsymbol{p}(\boldsymbol{z}) : \underline{\sigma}(\boldsymbol{s}) \, \mathrm{d}\Omega + \int_{\Omega} \boldsymbol{p}(\boldsymbol{z}) \cdot \boldsymbol{f}_{\Omega}(\boldsymbol{z}) \, \mathrm{d}\Omega \\
&= \frac{\alpha}{2} \int_{\Omega} (\boldsymbol{s}^*_{\mathrm{pm}} - \boldsymbol{s}_{\mathrm{pm}}) \cdot (\boldsymbol{s}^*_{\mathrm{pm}} - \boldsymbol{s}_{\mathrm{pm}}) \, \mathrm{d}\Omega + \int_{\Gamma_2} \boldsymbol{p}(\boldsymbol{z}) \cdot \boldsymbol{f}_{\Gamma}(\boldsymbol{z}) \, \mathrm{d}\Gamma_2 \\
&\quad - \int_{\Omega} \nabla \boldsymbol{p}(\boldsymbol{z}) : \underline{\sigma}(\boldsymbol{s}) \, \mathrm{d}\Omega + \int_{\Omega} \boldsymbol{p}(\boldsymbol{z}) \cdot \boldsymbol{f}_{\Omega}(\boldsymbol{z}) \, \mathrm{d}\Omega.
\end{aligned} \tag{3.7}$$

To determine the static sensitivity functions the variation of the Lagrangian $\mathcal{L}(\lambda, \mu, \boldsymbol{s}_{\mathrm{pm}}(\boldsymbol{z}, \boldsymbol{z}_{\mathrm{pm}}, \lambda, \mu))$ subject to the Lamé parameters is introduced

$$\begin{aligned}
\delta\mathcal{L} =& \frac{\partial \mathcal{L}(\lambda + \chi\delta\lambda, \mu + \chi\delta\mu, \boldsymbol{s}_{\mathrm{pm}}(\boldsymbol{z}, \boldsymbol{z}_{\mathrm{pm}}, \lambda + \chi\delta\lambda, \mu + \chi\delta\mu))}{\partial \chi}\Big|_{\chi=0} \\
=& \underbrace{\alpha \int_{\Omega} \big(\boldsymbol{s}^*_{\mathrm{pm}} - \boldsymbol{s}_{\mathrm{pm}}\big) \cdot \left(- \frac{\partial \boldsymbol{s}_{\mathrm{pm}}(\boldsymbol{z}, \boldsymbol{z}_{\mathrm{pm}}, \lambda + \chi\delta\lambda, \mu + \chi\delta\mu)}{\partial \chi} \right) \mathrm{d}\Omega \Big|_{\chi=0}}_{\mathcal{A}} \\
& - \int_{\Omega} \nabla \boldsymbol{p}(\boldsymbol{z}) : \underbrace{\Big(\delta\lambda \mathrm{Tr}\big(\nabla \boldsymbol{s}\big) I + \delta\mu \big(\nabla \boldsymbol{s} + (\nabla \boldsymbol{s})^T\big)\Big)}_{\text{see (2.108) and (2.109)}} \mathrm{d}\Omega \\
& \underbrace{- \int_{\Omega} \nabla \boldsymbol{p}(\boldsymbol{z}) : \Big(\lambda \mathrm{Tr}\big(\nabla \delta\boldsymbol{s}\big) I + \mu \big(\nabla \delta\boldsymbol{s} + (\nabla \delta\boldsymbol{s})^T\big)\Big) \mathrm{d}\Omega}_{\mathcal{B}} .
\end{aligned} \tag{3.8}$$

Taking (3.4) into account $\mathcal{A}$ can be rewritten

$$\begin{aligned}
\mathcal{A} =& \alpha \int_{\Omega} \big(\boldsymbol{s}^*_{\mathrm{pm}} - \boldsymbol{s}_{\mathrm{pm}}\big) \cdot \left(- \gamma(\boldsymbol{z}, \boldsymbol{z}_{\mathrm{pm}}) \frac{\partial \boldsymbol{s}(\boldsymbol{z}, \boldsymbol{z}_{\mathrm{pm}}, \lambda + \chi\delta\lambda, \mu + \chi\delta\mu)}{\partial \chi} \right) \mathrm{d}\Omega \Big|_{\chi=0} \\
=& - \alpha \int_{\Omega} \big(\boldsymbol{s}^*_{\mathrm{pm}} - \boldsymbol{s}_{\mathrm{pm}}\big) \gamma(\boldsymbol{z}, \boldsymbol{z}_{\mathrm{pm}}) \cdot \underbrace{\left(\frac{\partial \boldsymbol{s}(\boldsymbol{z}, \boldsymbol{z}_{\mathrm{pm}}, \lambda + \chi\delta\lambda, \mu + \chi\delta\mu)}{\partial \chi} \right)\Big|_{\chi=0}}_{\delta \boldsymbol{s}(\boldsymbol{z})} \mathrm{d}\Omega.
\end{aligned} \tag{3.9}$$

Considering the substitutions (3.4) the approximated Dirac function is used for $\boldsymbol{s}^*_{\mathrm{pm}}$ and $\boldsymbol{s}_{\mathrm{pm}}$. Therefore, the second application of the Dirac has no effect due to its characteristic such that $\mathcal{A}$ simplifies to

$$\mathcal{A} = -\alpha \int_{\Omega} \big(\boldsymbol{s}^*_{\mathrm{pm}} - \boldsymbol{s}_{\mathrm{pm}}\big) \cdot \delta \boldsymbol{s}(\boldsymbol{z}) \, \mathrm{d}\Omega. \tag{3.10}$$

In addition, reformulating $\mathcal{B}$ yields

$$\mathcal{B} = \underbrace{\int_{\Omega} \nabla \boldsymbol{p}(\boldsymbol{z}) : \lambda \mathrm{Tr}\big(\nabla \delta\boldsymbol{s}\big) I \, \mathrm{d}\Omega}_{a} + \underbrace{\int_{\Omega} \nabla \boldsymbol{p}(\boldsymbol{z}) : \mu \nabla \delta\boldsymbol{s} \, \mathrm{d}\Omega}_{b} + \underbrace{\int_{\Omega} \nabla \boldsymbol{p}(\boldsymbol{z}) : \mu (\nabla \delta\boldsymbol{s})^T \, \mathrm{d}\Omega}_{c} . \tag{3.11}$$

In the next step the variational operator $\delta\boldsymbol{s}$ has to be standardize to obtain the equation of the adjoint state, its auxiliary conditions, and the sensitivity functions. Hence, partial integration is required using the divergence theorem (2.114). In order to do this, the term $\mathcal{B}$ is split and the properties of the double contraction of two

second order tensors $\underline{h} : \underline{k} = \mathrm{trace}(\underline{h}^T \underline{k}) = \mathrm{trace}(\underline{k}\,\underline{h}^T)$ have to be considered, see Definition 2.2) . For term a yields

$$a = \int_\Omega \lambda \mathrm{Tr}\big(\nabla \delta \boldsymbol{s}\big)\big(I : \nabla \boldsymbol{p}(\boldsymbol{z})\big)\ \mathrm{d}\Omega = \int_\Omega \lambda \mathrm{Tr}\big(\nabla \delta \boldsymbol{s}\big)\mathrm{Tr}\big(I \nabla \boldsymbol{p}(\boldsymbol{z})\big)\ \mathrm{d}\Omega = \int_\Omega \lambda \big(\nabla \delta \boldsymbol{s} : I\big)\mathrm{Tr}\big(\nabla \boldsymbol{p}(\boldsymbol{z})\big)\ \mathrm{d}\Omega. \tag{3.12}$$

Applying (2.114) with $\boldsymbol{u} = \delta \boldsymbol{s}$ and $\underline{T} = \mathrm{Tr}\big(\nabla \boldsymbol{p}(\boldsymbol{z})\big) I$ results in

$$a = \lambda \int_\Gamma \delta \boldsymbol{s} \cdot \big(\boldsymbol{n}(\boldsymbol{z}) \cdot \mathrm{Tr}\big(\nabla \boldsymbol{p}(\boldsymbol{z})\big) I\big)\ \mathrm{d}\Gamma - \lambda \int_\Omega \delta \boldsymbol{s} \cdot \Big(\nabla \cdot \big(\mathrm{Tr}\big(\nabla \boldsymbol{p}(\boldsymbol{z})\big) I\big)\Big)\ \mathrm{d}\Omega. \tag{3.13}$$

The terms b and c can be rewritten directly, taking (2.114) into account with $\boldsymbol{u} = \delta \boldsymbol{s}$ and $\underline{T} = \nabla \boldsymbol{p}$ as well as $\underline{T} = (\nabla \boldsymbol{p})^T$

$$b = \mu \int_\Omega \nabla \delta \boldsymbol{s} : \nabla \boldsymbol{p}(\boldsymbol{z})\ \mathrm{d}\Omega = \mu \int_\Gamma \delta \boldsymbol{s} \cdot \big(\boldsymbol{n}(\boldsymbol{z}) \cdot \nabla \boldsymbol{p}\big)\ \mathrm{d}\Gamma - \mu \int_\Omega \delta \boldsymbol{s} \cdot \big(\nabla \cdot \big(\nabla \boldsymbol{p}\big)\big)\ \mathrm{d}\Omega \tag{3.14}$$

$$c = \mu \int_\Omega \nabla \delta \boldsymbol{s} : (\nabla \boldsymbol{p}(\boldsymbol{z}))^T\ \mathrm{d}\Omega = \mu \int_\Gamma \delta \boldsymbol{s} \cdot \big(\boldsymbol{n}(\boldsymbol{z}) \cdot (\nabla \boldsymbol{p})^T\big)\ \mathrm{d}\Gamma - \mu \int_\Omega \delta \boldsymbol{s} \cdot \big(\nabla \cdot \big((\nabla \boldsymbol{p})^T\big)\big)\ \mathrm{d}\Omega \tag{3.15}$$

Reassembly of the individual parts provides

$$\begin{aligned} \mathcal{B} &= \int_\Gamma \delta \boldsymbol{s} \cdot \Big(\boldsymbol{n}(\boldsymbol{z}) \cdot \big[\lambda I \mathrm{Tr}\big(\nabla \boldsymbol{p}(\boldsymbol{z})\big) + \mu\big(\nabla \boldsymbol{p}(\boldsymbol{z}) + (\nabla \boldsymbol{p}(\boldsymbol{z}))^T\big)\big]\Big)\ \mathrm{d}\Gamma \\ &\quad - \int_\Omega \delta \boldsymbol{s} \cdot \Big(\nabla \cdot \big[\lambda I \mathrm{Tr}\big(\nabla \boldsymbol{p}(\boldsymbol{z})\big) + \mu\big(\nabla \boldsymbol{p}(\boldsymbol{z}) + (\nabla \boldsymbol{p}(\boldsymbol{z}))^T\big)\big]\Big)\ \mathrm{d}\Omega \\ &= \int_\Gamma \delta \boldsymbol{s} \cdot \big(\boldsymbol{n}(\boldsymbol{z}) \cdot \underline{\sigma}(\boldsymbol{p})\big)\ \mathrm{d}\Gamma - \int_\Omega \delta \boldsymbol{s} \cdot \big(\nabla \cdot \underline{\sigma}(\boldsymbol{p})\big)\ \mathrm{d}\Omega. \end{aligned} \tag{3.16}$$

In summary the variation of the Lagrangian is obtained as

$$\begin{aligned} \delta \mathcal{L} = &- \int_\Omega \alpha\big(\boldsymbol{s}^*_{\mathrm{pm}} - \boldsymbol{s}_{\mathrm{pm}}\big) \cdot \delta \boldsymbol{s}\ \mathrm{d}\Omega - \int_\Omega \delta \boldsymbol{s} \cdot \big(\nabla \cdot \underline{\sigma}(\boldsymbol{p})\big)\ \mathrm{d}\Omega + \int_\Gamma \delta \boldsymbol{s} \cdot \big(\boldsymbol{n}(\boldsymbol{z}) \cdot \underline{\sigma}(\boldsymbol{p})\big)\ \mathrm{d}\Gamma \\ &- \int_\Omega \nabla \boldsymbol{p}(\boldsymbol{z}) : \Big(\delta\lambda \mathrm{Tr}\big(\nabla \boldsymbol{s}\big) I + \delta\mu\big(\nabla \boldsymbol{s} + (\nabla \boldsymbol{s})^T\big)\Big)\ \mathrm{d}\Omega = 0. \end{aligned} \tag{3.17}$$

The parameter set minimizing (3.5) subject to the constraint (3.1a) is found, when the necessary condition $\delta \mathcal{L} = 0$ is fulfilled. Considering the fundamental lemma of variational calculus [91, 77] the adjoint state equation and its boundary conditions are given by

$$\text{PDE:} \qquad \nabla \cdot \underline{\sigma}\big(\boldsymbol{p}(\boldsymbol{z})\big) + \alpha\big(\boldsymbol{s}_{\mathrm{pm}} - \boldsymbol{s}^*_{\mathrm{pm}}\big) = \boldsymbol{0}, \quad \boldsymbol{z} \in \Omega, \tag{3.18a}$$

$$\text{BC (clamped):} \qquad \boldsymbol{p}(\boldsymbol{z}) = \boldsymbol{0}, \quad \boldsymbol{z} \in \Gamma_1, \tag{3.18b}$$

$$\text{BC (free):} \qquad \boldsymbol{n}(\boldsymbol{z}) \cdot \underline{\sigma}\big(\boldsymbol{p}(\boldsymbol{z})\big) = \boldsymbol{0}, \quad \boldsymbol{z} \in \Gamma_2 \cup \Gamma_3, \tag{3.18c}$$

where the adjoint state's clamping condition acting at Γ_1 results directly from the Dirichlet boundary condition of the original problem formulation (3.1b). The static sensitivity functions or gradients w.r.t. the Lamé parameters follows as

$$\begin{bmatrix} \partial_{\delta\lambda} \delta \mathcal{L} \\ \partial_{\delta\mu} \delta \mathcal{L} \end{bmatrix} = \begin{bmatrix} -\int_\Omega \nabla \boldsymbol{p}(\boldsymbol{z}) : \mathrm{Tr}\big(\nabla \boldsymbol{s}\big) I\ \mathrm{d}\Omega \\ -\int_\Omega \nabla \boldsymbol{p}(\boldsymbol{z}) : \big(\nabla \boldsymbol{s} + (\nabla \boldsymbol{s})^T\big)\ \mathrm{d}\Omega \end{bmatrix}. \tag{3.19}$$

These functions provide the information of the influence of the Lamé parameters on the Lagrangian and therefore on the objective function. Due to this, they can directly be used as gradients to minimize the objective function. These gradients only require the solution of the displacement field $\boldsymbol{s}(\boldsymbol{z})$ and of the adjoint state $\boldsymbol{p}(\boldsymbol{z})$. The solution of the adjoint state can be computed using the same FEM framework as is used for the displacement

field. As a consequence the weak formulation of the adjoint state equation (3.18) is needed which can be derived completely analogously to the weak formulation of the displacement field (2.118). Taking into account the divergence theorem (2.114) as well as the boundary condition (3.18b) and (3.18c) the weak formulation results in

$$\mathbf{0} = \int_\Omega \boldsymbol{\phi} \cdot \nabla \cdot \underline{\sigma}\big(\boldsymbol{p}(\boldsymbol{z})\big) + \alpha \boldsymbol{\phi} \cdot \big(\boldsymbol{s}_{\mathrm{pm}} - \boldsymbol{s}^*_{\mathrm{pm}}\big)\ \mathrm{d}\Omega = \int_\Omega -\nabla\boldsymbol{\phi} : \underline{\sigma}\big(\boldsymbol{p}(\boldsymbol{z})\big) + \alpha \boldsymbol{\phi} \cdot \big(\boldsymbol{s}_{\mathrm{pm}} - \boldsymbol{s}^*_{\mathrm{pm}}\big)\ \mathrm{d}\Omega. \tag{3.20}$$

Remark 3.2 *As can be seen, the adjoint based gradients* (3.19) *only require the solution of the boundary value problem consisting of elastostatic equations* (3.1a) *in terms of the displacement field* $\boldsymbol{s}(\boldsymbol{z})$ *and of the related adjoint state* $\boldsymbol{p}(\boldsymbol{z})$ *governed by* (3.18a)*. This requirement is independent of the number of objective parameters. In other words the computational effort, which is mainly caused by the solution process of the boundary value problem, stays the same. In contrast to the finite-difference (FD) method, which require one basic evaluation of the linear elastostatic PDE and in addition per demanded parameter one (forward or backward FD) or more (e.g., central FD) evaluations. As a consequence the usage of the adjoint based sensitivity function is beneficial regarding computational effort especially for complex structures.*

3.2.1.2. Identification Process of the Transient Case - the Density and Damping Parameters

In the transient scenario the dynamics of the system are described by (2.113) to improve the readability the PDE, its boundary and initial conditions are recapitulated

$$\text{PDE:} \qquad \boldsymbol{R}(t,\boldsymbol{z}) = \rho\partial_t^2\boldsymbol{s}(t,\boldsymbol{z}) - \boldsymbol{f}_\Omega(t,\boldsymbol{z}) - \nabla\cdot\big(\underline{\sigma}(\boldsymbol{s})\big) + \gamma^{\mathrm{v}}\rho\partial_t\boldsymbol{s} - \gamma^{\mathrm{kv}}\nabla\cdot\big(\underline{\sigma}(\partial_t\boldsymbol{s})\big) = \mathbf{0}, \quad \boldsymbol{z}\in\Omega,\ t\in(0,T], \tag{3.21a}$$

$$\text{BC (clamped):} \qquad \boldsymbol{s}(t,\boldsymbol{z}) = \mathbf{0}, \quad \boldsymbol{z}\in\Gamma_1,\ t\geq 0, \tag{3.21b}$$

$$\text{BC (actuation):} \qquad \underline{\sigma}(\boldsymbol{s})\cdot\boldsymbol{n}(\boldsymbol{z}) = \boldsymbol{f}_\Gamma(t,\boldsymbol{z}), \quad \boldsymbol{z}\in\Gamma_2,\ t\geq 0, \tag{3.21c}$$

$$\text{BC (free):} \qquad \underline{\sigma}(\boldsymbol{s})\cdot\boldsymbol{n}(\boldsymbol{z}) = \mathbf{0}, \quad \boldsymbol{z}\in\Gamma_3,\ t\geq 0, \tag{3.21d}$$

$$\text{IC:} \qquad \boldsymbol{s}(t,\boldsymbol{z}) = \partial_t\boldsymbol{s}(t,\boldsymbol{z}) = \mathbf{0}, \quad t=0. \tag{3.21e}$$

Similar to the static case a quadratic objective function is constructed to estimate the density ρ and the damping parameters $\gamma^{\mathrm{v}},\ \gamma^{\mathrm{kv}}$. In particular

$$J(\rho,\gamma^{\mathrm{v}},\gamma^{\mathrm{kv}}) = \int_0^T \frac{1}{2}\alpha(t)\|\boldsymbol{s}^*(t,\boldsymbol{z}) - \boldsymbol{s}(t,\boldsymbol{z},\rho,\gamma^{\mathrm{v}},\gamma^{\mathrm{kv}})\|^2_{L^2}\ \mathrm{d}t \tag{3.22}$$

is considered, where the weighting term $\alpha(t)$ may change over time. This feature allows more flexibility during the identification process and is discussed in Section 3.2.2 in greater detail.

In the case of a pointwise measurement the objective has to be reformulated as discussed previously

$$J_{\mathrm{pm}}(\rho,\gamma^{\mathrm{v}},\gamma^{\mathrm{kv}}) = \int_0^T \frac{1}{2}\alpha(t)\|\boldsymbol{s}^*_{\mathrm{pm}} - \boldsymbol{s}_{\mathrm{pm}}\|^2_{L^2}\ \mathrm{d}t, \tag{3.23}$$

with

$$\boldsymbol{s}_{\mathrm{pm}}(t,\boldsymbol{z},\boldsymbol{z}_{\mathrm{pm}},\rho,\gamma^{\mathrm{v}},\gamma^{\mathrm{kv}}) = \boldsymbol{s}(t,\boldsymbol{z},\rho,\gamma^{\mathrm{v}},\gamma^{\mathrm{kv}})\gamma(\boldsymbol{z},\boldsymbol{z}_{\mathrm{pm}}), \quad \boldsymbol{s}^*_{\mathrm{pm}}(t,\boldsymbol{z},\boldsymbol{z}_{\mathrm{pm}}) = \boldsymbol{s}^*(\boldsymbol{z})\gamma(\boldsymbol{z},\boldsymbol{z}_{\mathrm{pm}}). \tag{3.24}$$

The time dependent weighting term $\alpha(t)$ provides the opportunity to increase the impact of the deviation during the optimization process at crucial instants of time.

As in the static case, the Lagrangian has to be defined to derive the transient adjoint based sensitivity functions

$$\begin{aligned}
\mathcal{L} &= J_{\mathrm{pm}}(\rho,\gamma^{\mathrm{v}},\gamma^{\mathrm{kv}}) - \int_0^T\int_\Omega \boldsymbol{p}(t,\boldsymbol{z})\cdot\boldsymbol{R}(t,\boldsymbol{z})\ \mathrm{d}\Omega\ \mathrm{d}t \\
&= \int_0^T\int_\Omega \frac{1}{2}\alpha(t)(\boldsymbol{s}^*_{\mathrm{pm}} - \boldsymbol{s}_{\mathrm{pm}})\cdot(\boldsymbol{s}^*_{\mathrm{pm}} - \boldsymbol{s}_{\mathrm{pm}})\ \mathrm{d}\Omega\ \mathrm{d}t \\
&\quad + \int_0^T\int_\Omega \boldsymbol{p}\cdot\Big(-\rho\partial_t^2\boldsymbol{s} + \boldsymbol{f}_\Omega + \nabla\cdot\big(\underline{\sigma}(\boldsymbol{s})\big) - \gamma^{\mathrm{v}}\rho\partial_t\boldsymbol{s} + \gamma^{\mathrm{kv}}\nabla\cdot\big(\underline{\sigma}(\partial_t\boldsymbol{s})\big)\Big)\ \mathrm{d}\Omega\ \mathrm{d}t.
\end{aligned} \tag{3.25}$$

Applying the divergence theorem (2.114) with $\boldsymbol{u} = \boldsymbol{p}$, $\underline{T} = \underline{\sigma}(\boldsymbol{s})$ and $\boldsymbol{u} = \boldsymbol{p}$, $\underline{T} = \underline{\sigma}(\partial_t \boldsymbol{s})$ and taking the boundary conditions (3.21b) to (3.21d) into account results in

$$\begin{aligned}\mathcal{L} = &\int_0^T \int_\Omega \frac{1}{2}\alpha(t)(\boldsymbol{s}^*_{\mathrm{pm}} - \boldsymbol{s}_{\mathrm{pm}}) \cdot (\boldsymbol{s}^*_{\mathrm{pm}} - \boldsymbol{s}_{\mathrm{pm}}) \,\mathrm{d}\Omega \,\mathrm{d}t + \int_0^T \int_\Omega \boldsymbol{p} \cdot \Big(-\rho \partial_t^2 \boldsymbol{s} + \boldsymbol{f}_\Omega - \gamma^{\mathrm{v}} \rho \partial_t \boldsymbol{s} \Big) \,\mathrm{d}\Omega \,\mathrm{d}t \\ &- \int_0^T \int_\Omega \nabla \boldsymbol{p} : \underline{\sigma}(\boldsymbol{s}) + \gamma^{\mathrm{kv}} \nabla \boldsymbol{p} : \underline{\sigma}(\partial_t \boldsymbol{s}) \,\mathrm{d}\Omega \,\mathrm{d}t + \int_0^T \int_{\Gamma_2} \boldsymbol{p} \cdot \boldsymbol{f}_\Gamma \,\mathrm{d}\Gamma_2 \,\mathrm{d}t \\ &+ \int_0^T \int_\Gamma \gamma^{\mathrm{kv}} \nabla \cdot (\boldsymbol{p}) : \underline{\sigma}(\partial_t \boldsymbol{s}) \,\mathrm{d}\Gamma \,\mathrm{d}t\end{aligned} \tag{3.26}$$

The first variation of $\mathcal{L}$ can be computed as

$$\delta\mathcal{L} = \frac{\partial \mathcal{L}(\rho + \chi\delta\rho, \gamma^{\mathrm{v}} + \chi\delta\gamma^{\mathrm{v}}, \gamma^{\mathrm{kv}} + \chi\delta\gamma^{\mathrm{kv}}, \boldsymbol{s}_{\mathrm{pm}}(t, \boldsymbol{z}, \boldsymbol{z}_{\mathrm{pm}}, \rho + \chi\delta\rho, \gamma^{\mathrm{v}} + \chi\delta\gamma^{\mathrm{v}}, \gamma^{\mathrm{kv}} + \chi\delta\gamma^{\mathrm{kv}}))}{\partial \chi}\Big|_{\chi=0},$$

considering (3.24). Similar to the static part the parameter set minimizing (3.23) subject to the constraint (3.21a) is found, when the necessary condition $\delta\mathcal{L} = 0$ is fulfilled. Its evaluation results in

$$\begin{aligned}\delta\mathcal{L} = &\underbrace{\int_0^T \int_\Omega \alpha(t)\big(\boldsymbol{s}^*_{\mathrm{pm}} - \boldsymbol{s}_{\mathrm{pm}}\big) \cdot \Big(- \frac{\partial \boldsymbol{s}_{\mathrm{pm}}(t, \boldsymbol{z}, \boldsymbol{z}_{\mathrm{pm}}, \lambda + \chi\delta\lambda, \mu + \chi\delta\mu)}{\partial \chi} \Big) \,\mathrm{d}\Omega \,\mathrm{d}t\Big|_{\chi=0}}_{\mathcal{A}} \\ &- \int_0^T \int_\Omega \boldsymbol{p} \cdot \partial_t^2 \boldsymbol{s} \delta\rho \,\mathrm{d}\Omega \,\mathrm{d}t - \int_0^T \int_\Omega \rho \boldsymbol{p} \cdot \delta\partial_t^2 \boldsymbol{s} \,\mathrm{d}\Omega \,\mathrm{d}t - \int_0^T \int_\Omega \rho \boldsymbol{p} \cdot \partial_t \boldsymbol{s} \delta\gamma^{\mathrm{v}} \,\mathrm{d}\Omega \,\mathrm{d}t \\ &- \int_0^T \int_\Omega \gamma^{\mathrm{v}} \boldsymbol{p} \cdot \partial_t \boldsymbol{s} \delta\rho \,\mathrm{d}\Omega \,\mathrm{d}t - \int_0^T \int_\Omega \gamma^{\mathrm{v}} \rho \boldsymbol{p} \cdot \delta\partial_t \boldsymbol{s} \,\mathrm{d}\Omega \,\mathrm{d}t \\ &- \int_0^T \int_\Omega \nabla \boldsymbol{p} : \Big(\lambda \mathrm{Tr}\big(\nabla \partial_t \boldsymbol{s}\big) I + \mu \Big(\nabla \partial_t \boldsymbol{s} + \big(\nabla \partial_t \boldsymbol{s}\big)^T\Big)\Big) \delta\gamma^{\mathrm{kv}} \,\mathrm{d}\Omega \,\mathrm{d}t \\ &- \int_0^T \int_\Omega \nabla \boldsymbol{p} : \Big(\lambda \mathrm{Tr}\big(\nabla \delta\boldsymbol{s}\big) I + \mu \Big(\nabla \delta\boldsymbol{s} + \big(\nabla \delta\boldsymbol{s}\big)^T\Big)\Big) \,\mathrm{d}\Omega \,\mathrm{d}t \\ &- \int_0^T \int_\Omega \gamma^{\mathrm{kv}} \nabla \boldsymbol{p} : \Big(\lambda \mathrm{Tr}\big(\nabla \delta\partial_t \boldsymbol{s}\big) I + \mu \Big(\nabla \delta\partial_t \boldsymbol{s} + \big(\nabla \delta\partial_t \boldsymbol{s}\big)^T\Big)\Big) \,\mathrm{d}\Omega \,\mathrm{d}t \\ &+ \int_0^T \int_\Gamma \boldsymbol{p} \cdot \Big(\boldsymbol{n} \cdot \underline{\sigma}(\partial_t \boldsymbol{s})\Big) \delta\gamma^{\mathrm{kv}} \,\mathrm{d}\Gamma \,\mathrm{d}t + \int_0^T \int_\Gamma \gamma^{\mathrm{kv}} \boldsymbol{p} \cdot \Big(\boldsymbol{n} \cdot \underline{\sigma}(\delta\partial_t \boldsymbol{s})\Big) \,\mathrm{d}\Gamma \,\mathrm{d}t = 0.\end{aligned} \tag{3.27}$$

As in the static case the term $\mathcal{A}$ is reformulated considering (3.24)

$$\begin{aligned}\mathcal{A} &= \int_0^T \int_\Omega \alpha(t)\big(\boldsymbol{s}^*_{\mathrm{pm}} - \boldsymbol{s}_{\mathrm{pm}}\big) \cdot \Big(- \gamma(\boldsymbol{z}, \boldsymbol{z}_{\mathrm{pm}}) \frac{\partial \boldsymbol{s}(t, \boldsymbol{z}, \boldsymbol{z}_{\mathrm{pm}}, \lambda + \chi\delta\lambda, \mu + \chi\delta\mu)}{\partial \chi} \Big) \,\mathrm{d}\Omega \,\mathrm{d}t\Big|_{\chi=0} \\ &= - \int_0^T \int_\Omega \alpha(t)\big(\boldsymbol{s}^*_{\mathrm{pm}} - \boldsymbol{s}_{\mathrm{pm}}\big)\gamma(\boldsymbol{z}, \boldsymbol{z}_{\mathrm{pm}}) \cdot \underbrace{\Big(\frac{\partial \boldsymbol{s}(t, \boldsymbol{z}, \boldsymbol{z}_{\mathrm{pm}}, \lambda + \chi\delta\lambda, \mu + \chi\delta\mu)}{\partial \chi} \Big)\Big|_{\chi=0}}_{\delta \boldsymbol{s}(\boldsymbol{z})} \,\mathrm{d}\Omega \,\mathrm{d}t.\end{aligned} \tag{3.28}$$

Recalling that the approximated Dirac function is already used for $\boldsymbol{s}^*_{\mathrm{pm}}$ and $\boldsymbol{s}_{\mathrm{pm}}$, see (3.24), and a second application has no effect $\mathcal{A}$ simplifies to

$$\mathcal{A} = -\int_0^T \int_\Omega \alpha(t)\big(\boldsymbol{s}^*_{\mathrm{pm}} - \boldsymbol{s}_{\mathrm{pm}}\big)\delta\boldsymbol{s} \ \mathrm{d}\Omega \ \mathrm{d}t. \tag{3.29}$$

In addition, the variational operators have to be standardized. This is accomplished by the multiple usage of partial integration. Initially, the divergence theorem (2.114) is applied upon five terms. Here, $\boldsymbol{u} = \nabla\boldsymbol{p}$ is fix, where $\underline{T}$ alters in each application $\underline{T} = I$, $\underline{T} = \nabla\delta\boldsymbol{s}$, $\underline{T} = \big(\nabla\delta\boldsymbol{s}\big)^T$, $\underline{T} = \nabla\delta\partial_t\boldsymbol{s}$ and $\underline{T} = \big(\nabla\delta\partial_t\boldsymbol{s}\big)^T$, resulting in

$$\begin{aligned}
\delta\mathcal{L} = &-\int_0^T \int_\Omega \alpha(t)\big(\boldsymbol{s}^*_{\mathrm{pm}} - \boldsymbol{s}_{\mathrm{pm}}\big)\cdot\delta\boldsymbol{s} \ \mathrm{d}\Omega \ \mathrm{d}t - \int_0^T \int_\Omega \boldsymbol{p}\cdot\partial_t^2\boldsymbol{s}\delta\rho \ \mathrm{d}\Omega \ \mathrm{d}t - \int_0^T \int_\Omega \rho\boldsymbol{p}\cdot\delta\partial_t^2\boldsymbol{s} \ \mathrm{d}\Omega \ \mathrm{d}t \\
&- \int_0^T \int_\Omega \rho\boldsymbol{p}\cdot\partial_t\boldsymbol{s}\delta\gamma^{\mathrm{v}} \ \mathrm{d}\Omega \ \mathrm{d}t - \int_0^T \int_\Omega \gamma^{\mathrm{v}}\boldsymbol{p}\cdot\partial_t\boldsymbol{s}\delta\rho \ \mathrm{d}\Omega \ \mathrm{d}t - \int_0^T \int_\Omega \gamma^{\mathrm{v}}\rho\boldsymbol{p}\cdot\delta\partial_t\boldsymbol{s} \ \mathrm{d}\Omega \ \mathrm{d}t \\
&- \int_0^T \int_\Omega \nabla\boldsymbol{p} : \Big(\lambda\mathrm{Tr}\big(\nabla\partial_t\boldsymbol{s}\big)I + \mu\Big(\nabla\partial_t\boldsymbol{s} + \big(\nabla\partial_t\boldsymbol{s}\big)^T\Big)\Big)\delta\gamma^{\mathrm{kv}} \ \mathrm{d}\Omega \ \mathrm{d}t \\
&+ \int_0^T \int_\Omega \nabla\cdot\big(\underline{\sigma}(\boldsymbol{p})\big)\cdot\delta\boldsymbol{s} \ \mathrm{d}\Omega \ \mathrm{d}t + \int_0^T \int_\Omega \gamma^{\mathrm{kv}}\nabla\cdot\big(\underline{\sigma}(\boldsymbol{p})\big)\cdot\delta\partial_t\boldsymbol{s} \ \mathrm{d}\Omega \ \mathrm{d}t \\
&- \int_0^T \int_\Gamma \Big(\boldsymbol{n}\cdot\underline{\sigma}(\boldsymbol{p})\Big)\cdot\delta\boldsymbol{s} \ \mathrm{d}\Gamma \ \mathrm{d}t - \int_0^T \int_\Gamma \gamma^{\mathrm{kv}}\Big(\boldsymbol{n}\cdot\underline{\sigma}(\boldsymbol{p})\Big)\cdot\delta\partial_t\boldsymbol{s} \ \mathrm{d}\Gamma \ \mathrm{d}t \\
&+ \int_0^T \int_\Gamma \boldsymbol{p}\cdot\Big(\boldsymbol{n}\cdot\underline{\sigma}(\partial_t\boldsymbol{s})\Big)\delta\gamma^{\mathrm{kv}} \ \mathrm{d}\Gamma \ \mathrm{d}t + \int_0^T \int_\Gamma \gamma^{\mathrm{kv}}\boldsymbol{p}\cdot\Big(\boldsymbol{n}\cdot\underline{\sigma}(\delta\partial_t\boldsymbol{s})\Big) \ \mathrm{d}\Gamma \ \mathrm{d}t = 0.
\end{aligned} \tag{3.30}$$

To reduce the complexity the kernels of two boundary integrals terms can be eliminated by the choice $\boldsymbol{n}\cdot\underline{\sigma}(\boldsymbol{p}) = \boldsymbol{0}$ as the first boundary condition of the transient adjoint. Introducing this into the variational from of the Lagrangian reduces the effort of the next step. Furthermore, to simplify the notation the term in front of $\delta\gamma^{\mathrm{kv}}$ can be rewritten as $\underline{\sigma}(\partial_t\boldsymbol{s})$ using (2.111).

A standardized variational operator is received by three temporal partial integrations leading to

$$
\begin{aligned}
\delta\mathcal{L} = &- \int_0^T \int_\Omega \alpha(t)\big(\boldsymbol{s}^*_{\mathrm{pm}} - \boldsymbol{s}_{\mathrm{pm}}\big)\cdot\delta\boldsymbol{s}\ \mathrm{d}\Omega\ \mathrm{d}t - \int_0^T \int_\Omega \boldsymbol{p}\cdot\partial_t^2\boldsymbol{s}\delta\rho\ \mathrm{d}\Omega\ \mathrm{d}t - \int_0^T \int_\Omega \rho\partial_t^2\boldsymbol{p}\cdot\delta\boldsymbol{s}\ \mathrm{d}\Omega\ \mathrm{d}t \\
&- \Big[\int_\Omega \rho\boldsymbol{p}\cdot\delta\partial_t\boldsymbol{s}\ \mathrm{d}\Omega\Big]_0^T + \Big[\int_\Omega \rho\partial_t\boldsymbol{p}\cdot\delta\boldsymbol{s}\ \mathrm{d}\Omega\Big]_0^T - \int_0^T \int_\Omega \rho\boldsymbol{p}\cdot\partial_t\boldsymbol{s}\delta\gamma^{\mathrm{v}}\ \mathrm{d}\Omega\ \mathrm{d}t \\
&- \int_0^T \int_\Omega \gamma^{\mathrm{v}}\boldsymbol{p}\cdot\partial_t\boldsymbol{s}\delta\rho\ \mathrm{d}\Omega\ \mathrm{d}t + \int_0^T \int_\Omega \gamma^{\mathrm{v}}\rho\partial_t\boldsymbol{p}\cdot\delta\boldsymbol{s}\ \mathrm{d}\Omega\ \mathrm{d}t - \Big[\int_\Omega \gamma^{\mathrm{v}}\rho\boldsymbol{p}\delta\boldsymbol{s}\ \mathrm{d}\Omega\Big]_0^T \\
&+ \int_0^T \int_\Omega \nabla\boldsymbol{p} : \underline{\sigma}(\partial_t\boldsymbol{s})\delta\gamma^{\mathrm{kv}}\ \mathrm{d}\Omega\ \mathrm{d}t + \int_0^T \int_\Omega \nabla\cdot\big(\underline{\sigma}(\boldsymbol{p})\big)\cdot\delta\boldsymbol{s}\ \mathrm{d}\Omega\ \mathrm{d}t - \int_0^T \int_\Omega \gamma^{\mathrm{kv}}\nabla\cdot\big(\underline{\sigma}(\partial_t\boldsymbol{p})\big)\cdot\delta\boldsymbol{s}\ \mathrm{d}\Omega\ \mathrm{d}t \qquad (3.31) \\
&+ \Big[\int_\Omega \nabla\cdot\big(\underline{\sigma}(\partial_t\boldsymbol{p})\big)\cdot\delta\boldsymbol{s}\ \mathrm{d}\Omega\Big]_0^T - \int_0^T \int_\Gamma \partial_t\boldsymbol{p}\cdot\Big(\boldsymbol{n}\cdot\underline{\sigma}(\boldsymbol{s})\Big)\delta\gamma^{\mathrm{kv}}\ \mathrm{d}\Gamma\ \mathrm{d}t \\
&- \int_0^T \int_\Gamma \gamma^{\mathrm{kv}}\partial_t\boldsymbol{p}\cdot\Big(\boldsymbol{n}\cdot\underline{\sigma}(\delta\boldsymbol{s})\Big)\ \mathrm{d}\Gamma\ \mathrm{d}t + \Big[\int_\Gamma \boldsymbol{p}\cdot\Big(\boldsymbol{n}\cdot\underline{\sigma}(\boldsymbol{s})\Big)\delta\gamma^{\mathrm{kv}}\ \mathrm{d}\Gamma\Big]_0^T \\
&+ \Big[\int_\Gamma \gamma^{\mathrm{kv}}\boldsymbol{p}\cdot\Big(\boldsymbol{n}\cdot\underline{\sigma}(\delta\boldsymbol{s})\Big)\ \mathrm{d}\Gamma\Big]_0^T = 0.
\end{aligned}
$$

At first, the analysis is focused on the integration concerning the boundaries and taking the boundary condition of the displacement field (3.1b) to (3.1d) into account which yields

$$
\begin{aligned}
\mathcal{B} = &- \int_0^T \int_\Gamma \partial_t\boldsymbol{p}\cdot\Big(\boldsymbol{n}\cdot\underline{\sigma}(\boldsymbol{s})\Big)\delta\gamma^{\mathrm{kv}}\ \mathrm{d}\Gamma\ \mathrm{d}t - \int_0^T \int_\Gamma \gamma^{\mathrm{kv}}\partial_t\boldsymbol{p}\cdot\Big(\boldsymbol{n}\cdot\underline{\sigma}(\delta\boldsymbol{s})\Big)\ \mathrm{d}\Gamma\ \mathrm{d}t \\
&+ \Big[\int_\Gamma \boldsymbol{p}\cdot\Big(\boldsymbol{n}\cdot\underline{\sigma}(\boldsymbol{s})\Big)\delta\gamma^{\mathrm{kv}}\ \mathrm{d}\Gamma\Big]_0^T + \Big[\int_\Gamma \gamma^{\mathrm{kv}}\boldsymbol{p}\cdot\Big(\boldsymbol{n}\cdot\underline{\sigma}(\delta\boldsymbol{s})\Big)\ \mathrm{d}\Gamma\Big]_0^T \\
= &- \int_0^T \int_{\Gamma_2} \partial_t\boldsymbol{p}\cdot\boldsymbol{f}_\Gamma\delta\gamma^{\mathrm{kv}}\ \mathrm{d}\Gamma_2\ \mathrm{d}t - \int_0^T \int_\Gamma \gamma^{\mathrm{kv}}\partial_t\boldsymbol{p}\cdot\Big(\boldsymbol{n}\cdot\underline{\sigma}(\delta\boldsymbol{s})\Big)\ \mathrm{d}\Gamma\ \mathrm{d}t \\
&+ \Big[\int_{\Gamma_2} \boldsymbol{p}\cdot\boldsymbol{f}_\Gamma\delta\gamma^{\mathrm{kv}}\ \mathrm{d}\Gamma_2\Big]_0^T + \Big[\int_\Gamma \gamma^{\mathrm{kv}}\boldsymbol{p}\cdot\Big(\boldsymbol{n}\cdot\underline{\sigma}(\delta\boldsymbol{s})\Big)\ \mathrm{d}\Gamma\Big]_0^T.
\end{aligned}
$$

The variation of the displacement field at the boundary surface Γ_1 vanishes ($\delta\boldsymbol{s} = \boldsymbol{0}$) because the field has to satisfy its boundary conditions, see [91, chap. 4]. The actuated and free Neumann boundary condition leads to

$$
\underline{\sigma}(\delta\boldsymbol{s})\cdot\boldsymbol{n}(\boldsymbol{z}) = \delta\boldsymbol{f}_\Gamma(t,\boldsymbol{z}), \quad \boldsymbol{z}\in\Gamma_2,\ t\geq 0, \qquad \underline{\sigma}(\delta\boldsymbol{s})\cdot\boldsymbol{n}(\boldsymbol{z}) = \boldsymbol{0}, \quad \boldsymbol{z}\in\Gamma_3,\ t\geq 0.
$$

The applied traction (surface force) is assumed to be constant, which means that the variation of the traction vanishes $\delta\boldsymbol{f}_\Gamma(t,\boldsymbol{z}) = \boldsymbol{0}$.

Temporal partial integration of the remaining integral of $\mathcal{B}$ leads to

$$
\mathcal{B} = \int_0^T \int_{\Gamma_2} \boldsymbol{p}\partial_t\boldsymbol{f}_\Gamma\delta\gamma^{\mathrm{kv}}\ \mathrm{d}\Gamma_2\ \mathrm{d}t.
$$

During the identification process the same constant traction function is used as in the measurement scenario,

so that $\mathcal{B} = 0$ holds. Hence, the variation of the Lagrangian simplifies to

$$\begin{aligned}
\delta\mathcal{L} = &- \int_0^T \int_\Omega \alpha(t)\big(\boldsymbol{s}^*_{\mathrm{pm}} - \boldsymbol{s}_{\mathrm{pm}}\big)\cdot\delta\boldsymbol{s}\ \mathrm{d}\Omega\ \mathrm{d}t - \int_0^T \int_\Omega \boldsymbol{p}\cdot\partial_t^2\boldsymbol{s}\delta\rho\ \mathrm{d}\Omega\ \mathrm{d}t - \int_0^T \int_\Omega \rho\partial_t^2\boldsymbol{p}\cdot\delta\boldsymbol{s}\ \mathrm{d}\Omega\ \mathrm{d}t \\
&- \Big[\int_\Omega \rho\boldsymbol{p}\cdot\delta\partial_t\boldsymbol{s}\ \mathrm{d}\Omega\Big]_0^T + \Big[\int_\Omega \rho\partial_t\boldsymbol{p}\cdot\delta\boldsymbol{s}\ \mathrm{d}\Omega\Big]_0^T - \int_0^T \int_\Omega \rho\boldsymbol{p}\cdot\partial_t\boldsymbol{s}\delta\gamma^{\mathrm{v}}\ \mathrm{d}\Omega\ \mathrm{d}t \\
&- \int_0^T \int_\Omega \gamma^{\mathrm{v}}\boldsymbol{p}\cdot\partial_t\boldsymbol{s}\delta\rho\ \mathrm{d}\Omega\ \mathrm{d}t + \int_0^T \int_\Omega \gamma^{\mathrm{v}}\rho\partial_t\boldsymbol{p}\cdot\delta\boldsymbol{s}\ \mathrm{d}\Omega\ \mathrm{d}t - \Big[\int_\Omega \gamma^{\mathrm{v}}\rho\boldsymbol{p}\delta\boldsymbol{s}\ \mathrm{d}\Omega\Big]_0^T \\
&+ \int_0^T \int_\Omega \nabla\boldsymbol{p} : \underline{\sigma}(\partial_t\boldsymbol{s})\delta\gamma^{\mathrm{kv}}\ \mathrm{d}\Omega\ \mathrm{d}t + \int_0^T \int_\Omega \nabla\cdot\big(\underline{\sigma}(\boldsymbol{p})\big)\cdot\delta\boldsymbol{s}\ \mathrm{d}\Omega\ \mathrm{d}t - \int_0^T \int_\Omega \gamma^{\mathrm{kv}}\nabla\cdot\big(\underline{\sigma}(\partial_t\boldsymbol{p})\big)\cdot\delta\boldsymbol{s}\ \mathrm{d}\Omega\ \mathrm{d}t \\
&+ \Big[\int_\Omega \nabla\cdot\big(\underline{\sigma}(\partial_t\boldsymbol{p})\big)\cdot\delta\boldsymbol{s}\ \mathrm{d}\Omega\Big]_0^T = 0.
\end{aligned} \tag{3.32}$$

As in the static case, the adjoint state as well as the sensitivity functions are given, if the necessary condition $\delta\mathcal{L} = 0$ is fulfilled. Taking the initial condition of the displacement field (2.113e) into account and considering the fundamental lemma of variational calculus [91, 77] the adjoint state equation, boundary and terminal conditions are given by

$$\text{PDE:} \qquad -\alpha(t)\big(\boldsymbol{s}^*_{\mathrm{pm}} - \boldsymbol{s}_{\mathrm{pm}}\big) - \rho\partial_t^2\boldsymbol{p} + \nabla\cdot\big(\underline{\sigma}(\boldsymbol{p})\big) + \gamma^{\mathrm{v}}\rho\partial_t\boldsymbol{p} - \gamma^{\mathrm{kv}}\nabla\cdot\big(\underline{\sigma}(\partial_t\boldsymbol{p})\big) = \boldsymbol{0} \tag{3.33a}$$

$$\boldsymbol{z}\in\Omega,\ t\in(0,T], \tag{3.33b}$$

$$\text{BC (clamped):} \qquad \boldsymbol{p}(t,\boldsymbol{z}) = \boldsymbol{0}, \quad \boldsymbol{z}\in\Gamma_1,\ t\geq 0, \tag{3.33c}$$

$$\text{BC (free):} \qquad \underline{\sigma}(\boldsymbol{p})\cdot\boldsymbol{n}(\boldsymbol{z}) = \boldsymbol{0}, \quad \boldsymbol{z}\in\Gamma_2\cup\Gamma_3,\ t\geq 0, \tag{3.33d}$$

$$\text{TC:} \qquad \boldsymbol{p}(t,\boldsymbol{z}) = \partial_t\boldsymbol{p}(\boldsymbol{z}) = \boldsymbol{0}, \quad t = T. \tag{3.33e}$$

The sensitivity functions or gradients w.r.t. density and damping parameters follows as

$$\begin{bmatrix} \partial_{\delta\rho}\delta\mathcal{L} \\ \partial_{\delta\gamma^{\mathrm{v}}}\delta\mathcal{L} \\ \partial_{\delta\gamma^{\mathrm{kv}}}\delta\mathcal{L} \end{bmatrix} = \begin{bmatrix} -\int_0^T \int_\Omega \boldsymbol{p}\partial_t^2\boldsymbol{s} + \gamma^{\mathrm{v}}\boldsymbol{p}\partial_t\boldsymbol{s}\ \mathrm{d}\Omega\ \mathrm{d}t \\ -\int_0^T \int_\Omega \rho\boldsymbol{p}\partial_t\boldsymbol{s}\ \mathrm{d}\Omega\ \mathrm{d}t \\ -\int_0^T \int_\Omega \nabla\boldsymbol{p} : \underline{\sigma}(\partial_t\boldsymbol{s})\ \mathrm{d}\Omega\ \mathrm{d}t \end{bmatrix}. \tag{3.34}$$

These functions provide information about the influence of the density and damping parameters on the Lagrangian and therefore on the objective function. To determine these sensitivity functions only the solutions of the displacement field $\boldsymbol{s}(t,\boldsymbol{z})$ and of the adjoint state $\boldsymbol{p}(t,\boldsymbol{z})$ are required. The solution of the adjoint state can be computed using the same FEM framework as is used for the displacement field. As a consequence the weak formulation of the adjoint state equation (3.33) is needed which can be derived analog to the weak formulation of the displacement field (2.118). Taking into account the divergence theorem (2.114) as well as the boundary condition (3.33c) and (3.33d) the weak formulation results in

$$\begin{aligned}
\boldsymbol{0} &= \int_\Omega -\alpha(t)\boldsymbol{\phi}\cdot\big(\boldsymbol{s}^*_{\mathrm{pm}} - \boldsymbol{s}_{\mathrm{pm}}\big) - \rho\boldsymbol{\phi}\cdot\partial_t^2\boldsymbol{p} + \boldsymbol{\phi}\cdot\nabla\cdot\big(\underline{\sigma}(\boldsymbol{p})\big) + \gamma^{\mathrm{v}}\boldsymbol{\phi}\cdot\rho\partial_t\boldsymbol{p} - \gamma^{\mathrm{kv}}\boldsymbol{\phi}\cdot\nabla\cdot\big(\underline{\sigma}(\partial_t\boldsymbol{p})\big)\ \mathrm{d}\Omega \\
&= \int_\Omega -\alpha(t)\boldsymbol{\phi}\cdot\big(\boldsymbol{s}^*_{\mathrm{pm}} - \boldsymbol{s}_{\mathrm{pm}}\big) - \rho\boldsymbol{\phi}\cdot\partial_t^2\boldsymbol{p} - \nabla\boldsymbol{\phi} : \underline{\sigma}(\boldsymbol{p}) + \gamma^{\mathrm{v}}\boldsymbol{\phi}\cdot\rho\partial_t\boldsymbol{p} + \gamma^{\mathrm{kv}}\nabla\boldsymbol{\phi} : \underline{\sigma}(\partial_t\boldsymbol{p})\ \mathrm{d}\Omega.
\end{aligned} \tag{3.35}$$

Remark 3.3 *It can be seen that the advantage of the adjoint based sensitivity function considering the static part regarding computational effort still holds, see Remark 3.2. In fact the advantage increases, due to the fact that each gradient evaluation requires the complete time solution including the evaluation of the PDEs in each*

time step, which significantly increases the computational effort. The adjoint based sensitivity functions only require the temporal solution of the displacement field and of the adjoint state instead of the multiple temporal solutions needed by the finite difference method. Furthermore, the impact increases even more caused by the rising of the number of objective parameters per domain.

3.2.2. Results of the Adjoint Based Parameter Identification

Below, the applied optimization scheme is briefly discussed and the results of the parameter identification process are presented. At first, a simple model is designed to validate the process itself through simulations. Secondly the parameter identification process of the wingsail using pointwise laser measurements is presented, whereby special usage of the weighting term $\alpha(t)$ is discussed. The resulting material parameters as well as the displacement field are presented and analyzed.

3.2.2.1. Optimization Scheme

Conveying an insight of the complete identification process, the process flow is briefly discussed. Fig. 3.3 displays the process schematic in a condensed form.

Based on the governing mathematical problem description and an initial guess of the parameters of interest $\boldsymbol{\theta}_0$ a numerical solution $\boldsymbol{s}_0$ is computed. This step will be referred to as "forward solve", because for the general case $\boldsymbol{s}_0(t)$ is solved forward in time. Starting the actual optimization cycle, the objective function J has to be evaluated. This requires the solution $\boldsymbol{s}_i$ of the current iteration step i as well as the desired solution (measured data) $\boldsymbol{s}^*$. In the next step the numerical solution of the sensitivity functions (gradients) of the parameters of interest $\partial_{\delta\boldsymbol{\theta}}\delta\mathcal{L}$ has to be computed. As mentioned before, this can be done efficiently by using the adjoint state $\boldsymbol{p}_i$. Hence, the solution of the adjoint state is computed, which has to be done "backward" in time considering the general time dependent case w.r.t. the terminal condition of the adjoint state (3.33e). In the last step of the cycle, the optimization routine receives the numeric values of the function and the gradients. The selected algorithm computes the new set of parameters $\boldsymbol{\theta}_{i+1}$ and starts the process once more or terminates the process based on its absolute and relative convergence tolerance ϵ_a, ϵ_r. Depending on the choice of the used optimization algorithm additional constraints can be included, e.g., bounded parameters.

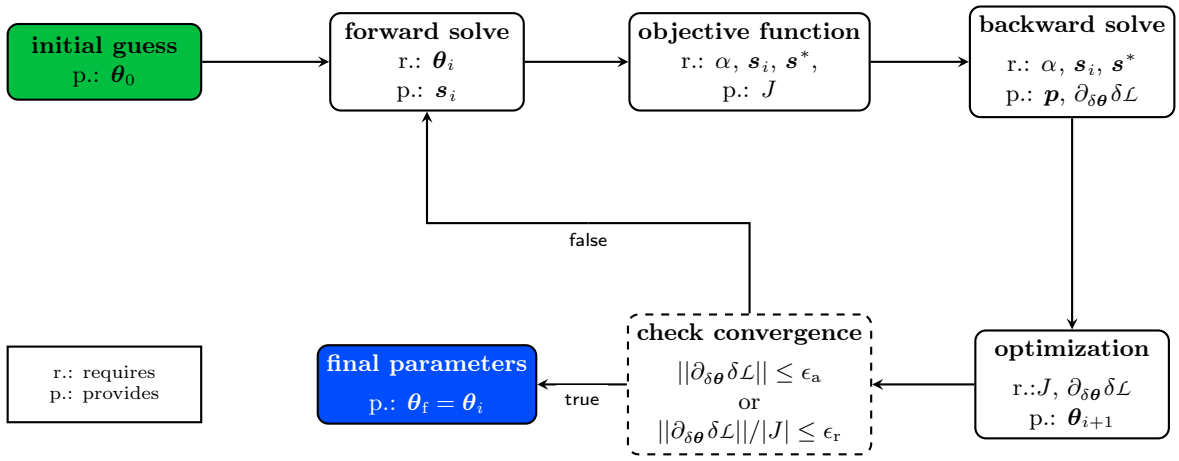

Figure 3.3.: Schematics of the parameter identification process.

3.2.2.2. Proof of Concept Study

To validate the introduced adjoint based parameter identification method, a 3-d cantilever beam is considered as a proof of concept study. The beam is modeled by the equations of linear elasticity. The beam is clamped $\boldsymbol{s}(t,\boldsymbol{z}) = \boldsymbol{0}$ at $z^1 = 0\,\mathrm{m}$ and free $\underline{\sigma}(\boldsymbol{s})\cdot\boldsymbol{n}(\boldsymbol{z}) = \boldsymbol{0}$ on all other boundaries. Its displacement and velocity at $t = 0\,\mathrm{s}$ are set to $\boldsymbol{s}(t,\boldsymbol{z}) = \partial_t\boldsymbol{s}(t,\boldsymbol{z}) = \boldsymbol{0}$. The only acting force is given by the body force $\boldsymbol{f}_\Omega(t,\boldsymbol{z}) = [0.0 \quad 9.81 \quad 0.0]^T h(t) \times 10^{-3}\,\mathrm{N}$, with $h(t)$ denoting the Heaviside function. Table 3.3 displays the length ℓ, width w, and thickness or height h as well as the chosen set of material parameters. It has to be mentioned that non-physical parameters are used for this concept validation.

Table 3.3.: Geometric dimensions and choosen set of material parameters.

dimension in m			material parameters				
ℓ	w	h	λ^*	μ^*	ρ^*	$\gamma^{\mathrm{v}*}$	$\gamma^{\mathrm{kv}*}$
0.40	0.10	0.01	$1.00\,\mathrm{N/m^2}$	$0.20\,\mathrm{N/m^2}$	$1.00\,\mathrm{kg/m^3}$	$0.10\,1/\mathrm{s}$	$0.10\,\mathrm{s}$

The simulation is implemented in the open source FE framework *Firedrake* [89, 50] based on *Python* and *PETSc* [8]. The mesh of the beam is generated by tetrahedral finite elements considering second order continuous Galerkin shape functions, see Section 2.2.3.3. This leads to a small system described by 6765 DoFs. Fig. 3.4 displays the mesh and the resulting steady state displacement field of the selected scenario.

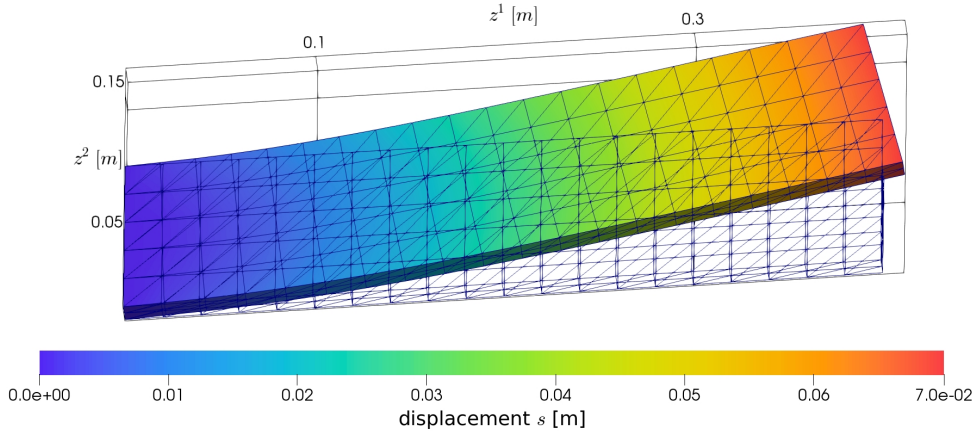

Figure 3.4.: Static solution of the 3-d displacement field of the considered beam scenario (colorized surface plot) compared with the not actuated profile (blue grid).

For the optimization *PETSc* provides the so-called toolkit for advanced optimization (*tao*) [83] containing different optimization routines. As depicted in Fig. 3.3 *tao* obtains the numeric values of the objective function J and the sensitivity functions (gradients) $\partial_{\delta\boldsymbol{\theta}_i}\delta\mathcal{L}$ and determines the new parameter set $\boldsymbol{\theta}_{i+1}$. This is done by the bound-constrained limited-memory variable-metric method (*BLMVM*) (see [83]) considering the Moré-Thuente line search method [82].

For the validation the "measured" data $\boldsymbol{s}^*$ is generated by a forward solve of the displacement field, which takes place before the actual identification process starts. The selected parameters used in this numerical solution display the optimal parameter set and are listed in Table 3.3. Due to the split identification process, the parameter set of interest also splits up. For the static case $\boldsymbol{\theta}_{\mathrm{s}}^* = [\lambda^* \quad \mu^*]^T$ has to be identified and for the transient case $\boldsymbol{\theta}_{\mathrm{t}}^* = [\rho^* \quad \gamma^{\mathrm{v}*} \quad \gamma^{\mathrm{kv}*}]^T$ is required.

The validation of the beam's parameters considers two separate scenarios. At first, it is assumed that the complete displacement field is known (implying measurability) and can be used for the parameter identification. This scenario will be abbreviated as "full profile information". The second scenario considers a pointwise measurement at eight locations on the beam surface and will be referred as "pointwise information" below. These measurements provide only displacement information in z^2- and / or z^3-direction. Table 3.4 lists the locations of the points of measurements and Fig. 3.5 visualizes the resulting measured displacement field $\boldsymbol{s}_{\mathrm{pm}}(\boldsymbol{z}_{\mathrm{pm}})$.

Table 3.4.: Location of the points of measurement.

in m	$\boldsymbol{z}_{\mathrm{pm},1}$	$\boldsymbol{z}_{\mathrm{pm},2}$	$\boldsymbol{z}_{\mathrm{pm},3}$	$\boldsymbol{z}_{\mathrm{pm},4}$	$\boldsymbol{z}_{\mathrm{pm},5}$	$\boldsymbol{z}_{\mathrm{pm},6}$	$\boldsymbol{z}_{\mathrm{pm},7}$	$\boldsymbol{z}_{\mathrm{pm},8}$
z^1	0.40	0.30	0.40	0.30	0.40	0.30	0.40	0.30
z^2	0.00	0.00	0.10	0.10	0.00	0.00	0.10	0.10
z^3	0.01	0.01	0.01	0.01	0.00	0.00	0.00	0.00

Static Case – "Full Profile Information" The process starts with an initial guess using a erroneous parameter set, where each parameter is adulterated by the constant factor $\boldsymbol{\theta} = 100.0\,\boldsymbol{\theta}^*$. Table 3.5 lists the results from

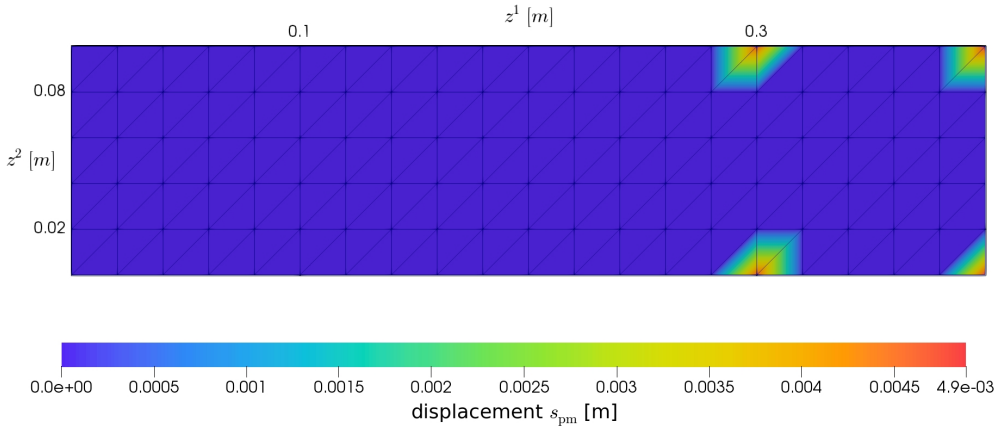

Figure 3.5.: Solution of the pointwise 3-d displacement field of the considered beam scenario (front view).

every 5^{th} iteration i of the identification process. In addition, the value of the objective function $J(\lambda_i, \mu_i)$, taken into account a global weighting term $\alpha = 1.0 \times 10^7$, the values of the parameter related sensitivity functions (gradients) and errors are presented. In particular, the weighting term is used to normalize the value of the objective function to increase the efficiency of the optimization method provided by *tao*. Good results were accomplished if the initial value of the objective function is within the range $[0.1, 10]$.

The parameter errors of each iteration i are defined as

$$\tilde{\lambda}_i = \lambda^* - \lambda_i, \quad \tilde{\mu}_i = \mu^* - \mu_i, \tag{3.36}$$

where the superscript $*$ declares the optimal parameter as discussed before and listed in Table 3.3.

During the identification process the objective function displays a monotonically decreasing behavior, see Table 3.5, where the gradients are characterized by an overall decreasing trend but sometimes rise for a short period. This effect is related to the interaction of the parameters among themselves, meaning that the improvement of the objective by the adjustment of one parameter may lead to a stronger impact of the other parameters. The more parameters are considered in the process, the stronger and more frequent this effect becomes. In this example the effect is marginal.

The complete optimization process takes only $i = 26$ iterations and the converged parameter set is nearly equal to the optimal set with errors less than 3.83×10^{-8}. This result is generated considering *tao*'s default convergence tolerances $\epsilon_{\text{a}} = \epsilon_{\text{r}} = 1 \times 10^{-8}$.

Table 3.5.: Optimization results of the static beam converged within $i = 26$ iterations. The final parameter set yields $\lambda_{26} = 1.00000003832\,\text{N/m}^2$ and $\mu_{26} = 0.199999999509\,\text{N/m}^2$.

i	$J(\lambda_i, \mu_i)$	$\tilde{\lambda}_i$ [N/m^2]	$\partial_{\delta\lambda_i}\delta\mathcal{L}$	$\tilde{\mu}_i$ [N/m^2]	$\partial_{\delta\mu_i}\delta\mathcal{L}$
0	$+2.56 \cdot 10^{0}$	$-9.90 \cdot 10^{1}$	$+3.08 \cdot 10^{-5}$	$-1.98 \cdot 10^{1}$	$+2.44 \cdot 10^{-3}$
5	$+1.67 \cdot 10^{-3}$	$-5.92 \cdot 10^{0}$	$-3.98 \cdot 10^{-6}$	$+1.58 \cdot 10^{-2}$	$-4.43 \cdot 10^{-1}$
10	$+1.17 \cdot 10^{-4}$	$-1.08 \cdot 10^{0}$	$-9.72 \cdot 10^{-5}$	$+7.71 \cdot 10^{-3}$	$-7.23 \cdot 10^{-2}$
15	$+7.57 \cdot 10^{-6}$	$-2.71 \cdot 10^{-1}$	$+4.52 \cdot 10^{-6}$	$+2.83 \cdot 10^{-3}$	$-5.84 \cdot 10^{-3}$
25	$+7.55 \cdot 10^{-17}$	$-7.72 \cdot 10^{-7}$	$-6.03 \cdot 10^{-10}$	$+1.03 \cdot 10^{-8}$	$-6.04 \cdot 10^{-8}$
26	$+3.90 \cdot 10^{-20}$	$-3.83 \cdot 10^{-8}$	$-6.26 \cdot 10^{-12}$	$+4.91 \cdot 10^{-10}$	$-7.89 \cdot 10^{-10}$

Static Case – "Pointwise Information" In this scenario the initial guess uses a erroneous parameter set, where each parameter is adulterated by the constant factor $\boldsymbol{\theta} = 10.0\,\boldsymbol{\theta}^*$. Analog to the "full profile information" scenario Table 3.5 lists the results from every 5^{th} iteration i of the identification process. It presents the objective function $J_{\text{pm}}(\lambda_i, \mu_i)$, considering a global weighting term $\alpha = 1.0 \times 10^9$. The numeric value of the weighting term is increased compared to the "full profile information" scenario. This is done to compensate the decreased numeric value of the objective function which relies only on the eight measurement points containing only displacement information in z^2- and z^3-direction. Furthermore, the values of the parameter related sensitivity functions (gradients) and errors (3.36) are shown. The resulting parameter set $\lambda_{24} = 1.00000138941\,\text{N/m}^2$, $\mu_{24} = 0.199999983725\,\text{N/m}^2$ reached in $i = 24$ iterations displays a high accuracy.

Comparable results can be achieved by discarding the displacement information in z^3-direction. Such a setup results in a parameter set of $\lambda_{242} = 1.0032518623\,\mathrm{N/m^2}$, $\mu_{242} = 0.199959266788\,\mathrm{N/m^2}$ within $i = 242$ iterations. The reduced accuracy and the increased number of iterations can be interpreted by the physical meaning of the parameter set. The Lamé parameters are composed of Young's modulus and the Poisson ratio or in other words they correlate with the longitudinal and lateral strain. Therefore, the difficulty of the identification rises by omitting the lateral displacement information (z^3-direction). Nevertheless, the identification process provides a sufficiently accurate parameter set with a relative error of less than 0.36 % compared to an initial error of 990 %.

Table 3.6.: Optimization results of the static beam converged within $i = 24$ iterations. The final parameter set yields $\lambda_{24} = 1.00000138941\,\mathrm{N/m^2}$ and $\mu_{24} = 0.199999983725\,\mathrm{N/m^2}$.

i	$J_{\mathrm{pm}}(\lambda_i, \mu_i)$	$\tilde{\lambda}_i$ [N/m^2]	$\partial_{\delta\lambda_i}\delta\mathcal{L}$	$\tilde{\mu}_i$ [N/m^2]	$\partial_{\delta\mu_i}\delta\mathcal{L}$
0	$+2.15 \cdot 10^{-1}$	$-9.00 \cdot 10^{0}$	$+9.68 \cdot 10^{-4}$	$-1.80 \cdot 10^{0}$	$+7.71 \cdot 10^{-2}$
5	$+9.67 \cdot 10^{-5}$	$-4.96 \cdot 10^{0}$	$+1.88 \cdot 10^{-5}$	$+1.38 \cdot 10^{-2}$	$-7.90 \cdot 10^{-2}$
10	$+7.74 \cdot 10^{-6}$	$-9.30 \cdot 10^{-1}$	$-2.23 \cdot 10^{-5}$	$+6.91 \cdot 10^{-3}$	$-1.70 \cdot 10^{-2}$
15	$+4.44 \cdot 10^{-7}$	$-1.76 \cdot 10^{-1}$	$-5.18 \cdot 10^{-5}$	$+2.08 \cdot 10^{-3}$	$-6.65 \cdot 10^{-3}$
20	$+7.53 \cdot 10^{-10}$	$-8.47 \cdot 10^{-3}$	$-1.09 \cdot 10^{-6}$	$+1.09 \cdot 10^{-4}$	$-1.33 \cdot 10^{-4}$
24	$+3.02 \cdot 10^{-17}$	$-1.39 \cdot 10^{-6}$	$+1.70 \cdot 10^{-10}$	$+1.63 \cdot 10^{-8}$	$+7.18 \cdot 10^{-9}$

Transient Case – "Full Profile Information" The temporal solution of the beam displacement field $\boldsymbol{s}(t, \boldsymbol{z})$ is computed with a Newmark solver, see Appendix A.3 and [84], considering a fixed sample time $t_{\mathrm{s}} = 50.0 \times 10^{-3}\,\mathrm{s}$ for the time interval $t \in [0, 1.0]\,\mathrm{s}$. Analog to the static case, Table 3.7 presents the results from every 5^{th} iteration, where the parameter errors of each optimization iteration i are defined as

$$\tilde{\rho}_i = \rho^* - \rho_i, \quad \tilde{\gamma}_i^{\mathrm{v}} = \gamma^{\mathrm{v}*} - \gamma_i^{\mathrm{v}}, \quad \tilde{\gamma}_i^{\mathrm{kv}} = \gamma^{\mathrm{kv}*} - \gamma_i^{\mathrm{kv}}. \tag{3.37}$$

As before the optimal parameters, denoted by *, are listed in Table 3.3, where the set of the initial guess is adulterated by $\boldsymbol{\theta}_0 = 100.0\,\boldsymbol{\theta}^*$

Table 3.7.: Optimization results of the transient beam converged within $i = 16$ iterations. The final parameter set yields $\rho_{16} = 1.00000000103\,\mathrm{kg/m^3}$, $\gamma_{16}^{\mathrm{v}} = 0.0999999957185\,1/\mathrm{s}$ and $\gamma_{16}^{\mathrm{kv}} = 0.100000000232\,\mathrm{s}$.

i	$J(\rho_i, \gamma_i^{\mathrm{v}}, \gamma_i^{\mathrm{kv}})$	$\tilde{\rho}_i$ [kg/m^3]	$\partial_{\delta\rho_i}\delta\mathcal{L}$	$\tilde{\gamma}_i^{\mathrm{v}}$ [1/s]	$\partial_{\delta\gamma_i^{\mathrm{v}}}\delta\mathcal{L}$	$\tilde{\gamma}_i^{\mathrm{kv}}$ [s]	$\partial_{\delta\gamma_i^{\mathrm{kv}}}\delta\mathcal{L}$
0	$+4.84 \cdot 10^{0}$	$-9.90 \cdot 10^{1}$	$+2.43 \cdot 10^{-4}$	$-9.90 \cdot 10^{0}$	$+2.04 \cdot 10^{-3}$	$-9.90 \cdot 10^{0}$	$+3.11 \cdot 10^{-5}$
5	$+6.50 \cdot 10^{-3}$	$+7.64 \cdot 10^{-2}$	$-6.97 \cdot 10^{-2}$	$-3.39 \cdot 10^{-1}$	$-1.70 \cdot 10^{-2}$	$+8.50 \cdot 10^{-2}$	$-1.85 \cdot 10^{-1}$
10	$+3.94 \cdot 10^{-8}$	$+3.52 \cdot 10^{-4}$	$-4.25 \cdot 10^{-4}$	$-1.09 \cdot 10^{-3}$	$-7.73 \cdot 10^{-5}$	$-7.60 \cdot 10^{-5}$	$+1.80 \cdot 10^{-4}$
15	$+1.87 \cdot 10^{-15}$	$+9.93 \cdot 10^{-8}$	$-1.04 \cdot 10^{-7}$	$-3.31 \cdot 10^{-7}$	$-1.98 \cdot 10^{-8}$	$+6.17 \cdot 10^{-9}$	$+6.00 \cdot 10^{-9}$
16	$+2.12 \cdot 10^{-19}$	$-1.03 \cdot 10^{-9}$	$-6.72 \cdot 10^{-10}$	$+4.28 \cdot 10^{-9}$	$-2.67 \cdot 10^{-10}$	$-2.32 \cdot 10^{-10}$	$-1.22 \cdot 10^{-10}$

To improve the results of the line search the weighting term is chosen as $\alpha(t) = 1 \times 10^{10}$, so that the initial objective function value lays in the vicinity of 1. Furthermore the convergence tolerances are set to $\epsilon_{\mathrm{a}} = 1 \times 10^{-8}$, $\epsilon_{\mathrm{r}} = 1 \times 10^{-8}$.

Fig. 3.6 shows the displacement over time of the beam tip $\boldsymbol{s}(t, \boldsymbol{z}_{\mathrm{pm},1})$. The gray line denotes the optimal movement based on the "measured" data. The dashed lines display the displacement corresponding to the parameter sets of the current iteration i. Within seven iterations the optimal displacement over time seems to be reached. Considering the numerics there are still slightly differences. The objective function results in $J(\rho_7, \gamma_7^{\mathrm{v}}, \gamma_7^{\mathrm{kv}}) \approx 2.22 \times 10^{-4}$, which can be further improved compared to the value of the 16^{th} iteration of $J(\rho_{16}, \gamma_{16}^{\mathrm{v}}, \gamma_{16}^{\mathrm{kv}}) \approx 2.12 \times 10^{-19}$. Also the absolute errors in the 7^{th} iteration are $\tilde{\rho} = 2.01 \times 10^{-2}\,\mathrm{kg/m^3}$, $\tilde{\gamma}^{\mathrm{v}} = 1.76 \times 10^{-1}\,1/\mathrm{s}$ and $\tilde{\gamma}^{\mathrm{kv}} = 1.59 \times 10^{-2}\,\mathrm{s}$, which is still high compared with the nearly perfect result of the 16^{th} iteration.

Transient Case – "Pointwise Information" Like in the "full profile information" scenario the parameters of the initial guess are adulterated by $\boldsymbol{\theta}_0 = 10.0\,\boldsymbol{\theta}^*$. Furthermore the same settings are chosen, only the weighting term is set to $\alpha(t) = 1 \times 10^{14}$. As before only eight measurement points are used, where the displacement information is restricted to the z^2-direction.

Table 3.8 displays every 5^{th} iteration result of the identification process in terms of the objective function $J_{\mathrm{pm}}(\rho_i, \gamma_i^{\mathrm{v}}, \gamma_i^{\mathrm{kv}})$, the sensitivity functions (gradients) and the parameter errors defined by (3.37). The result

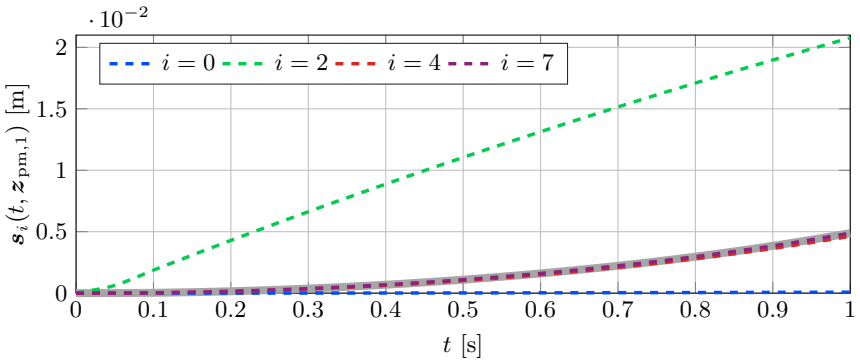

Figure 3.6.: Beam tip's z^2 displacement over time $s_i(t, z_{\mathrm{pm},1})$ with $z_{\mathrm{pm},1} = [0.40 \quad 0.00 \quad 0.01]^T$ m during the optimization process. The gray line marks the trajectory of the solution considering the correct parameter set and index i denotes current iteration of the optimization.

display a comparable behavior to the "full profile information" scenario. Convergence is reached within $i = 25$ iterations but it has to be kept in mind that the initial error is about a factor 10 smaller as in the "full profile information" scenario. Nevertheless, this initial error is large and the adjoint based identification still shows a good performance even if only pointwise measurement data is available.

Table 3.8.: Optimization results of the transient beam converged within $i = 25$ iterations. The final parameter set yields $\rho_{25} = 1.00000000007\,\mathrm{kg/m^3}$, $\gamma_{25}^{\mathrm{v}} = 0.0999999998925\,1/\mathrm{s}$ and $\gamma_{25}^{\mathrm{kv}} = 0.100000000038\,\mathrm{s}$.

i	$J_{\mathrm{pm}}(\rho_i, \gamma_i^{\mathrm{v}}, \gamma_i^{\mathrm{kv}})$	$\tilde{\rho}_i$ [kg/m^3]	$\partial_{\delta\rho_i}\delta\mathcal{L}$	$\tilde{\gamma}_i^{\mathrm{v}}$ [1/s]	$\partial_{\delta\gamma_i^{\mathrm{v}}}\delta\mathcal{L}$	$\tilde{\gamma}_i^{\mathrm{kv}}$ [s]	$\partial_{\delta\gamma_i^{\mathrm{kv}}}\delta\mathcal{L}$
0	$+2.75 \cdot 10^{1}$	$-9.00 \cdot 10^{0}$	$+1.66 \cdot 10^{0}$	$-9.00 \cdot 10^{-1}$	$+3.78 \cdot 10^{0}$	$-9.00 \cdot 10^{-1}$	$-1.95 \cdot 10^{-1}$
5	$+3.42 \cdot 10^{-1}$	$-7.03 \cdot 10^{-2}$	$+9.48 \cdot 10^{0}$	$-5.49 \cdot 10^{-2}$	$+2.87 \cdot 10^{0}$	$-7.44 \cdot 10^{-1}$	$+1.23 \cdot 10^{0}$
10	$+4.15 \cdot 10^{-3}$	$-1.34 \cdot 10^{-2}$	$+2.25 \cdot 10^{0}$	$+4.68 \cdot 10^{-3}$	$+5.96 \cdot 10^{-1}$	$-2.60 \cdot 10^{-2}$	$+5.97 \cdot 10^{-2}$
15	$+3.53 \cdot 10^{-5}$	$-6.45 \cdot 10^{-3}$	$+1.30 \cdot 10^{-2}$	$+2.46 \cdot 10^{-2}$	$-6.92 \cdot 10^{-3}$	$-9.18 \cdot 10^{-4}$	$-6.76 \cdot 10^{-3}$
20	$+2.24 \cdot 10^{-8}$	$+8.02 \cdot 10^{-5}$	$-3.29 \cdot 10^{-3}$	$-2.20 \cdot 10^{-4}$	$-8.01 \cdot 10^{-4}$	$+1.00 \cdot 10^{-4}$	$-6.35 \cdot 10^{-4}$
25	$+5.59 \cdot 10^{-20}$	$-7.10 \cdot 10^{-11}$	$+9.53 \cdot 10^{-9}$	$+1.08 \cdot 10^{-10}$	$+2.41 \cdot 10^{-9}$	$-3.80 \cdot 10^{-11}$	$-5.01 \cdot 10^{-10}$

Fig. 3.7 displays the transient behavior during the iterations i. Like before, the temporal displacement depicted over the different iterations of the beam tip displays a behaviour converging quickly towards the optimal trajectory shown in gray. Iteration $i = 9$ already presents a feasible solution, althought the objective function provides a high value of $J_{\mathrm{pm}}(\rho_9, \gamma_9^{\mathrm{v}}, \gamma_9^{\mathrm{kv}}) = 2.04 \times 10^{-2}$ compared to the final iteration. The parameter errors are given by $\tilde{\rho}_9 = -1.00 \times 10^{-3}$, $\tilde{\gamma}_9^{\mathrm{v}} = 3.178 \times 10^{-2}$ and $\tilde{\gamma}_9^{\mathrm{kv}} = 9.99 \times 10^{-2}$.

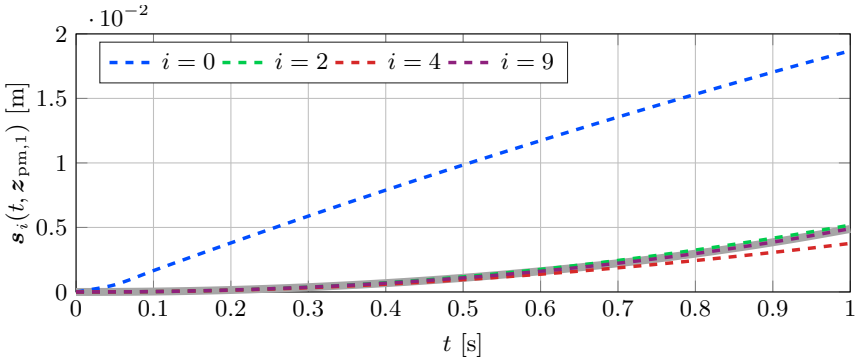

Figure 3.7.: Beam tip's z^2 displacement over time $s_i(t, z_{\mathrm{pm},1})$ with $z_{\mathrm{pm},1} = [0.40 \; 0.00 \; 0.01]^T$ m during the optimization process. The gray line marks the trajectory of the optimal solution and index i denotes current iteration of the optimization.

Concluding the results of beam structure the adjoint based parameter identification overall displays a good performance on the simple test case in both scenarios. It nearly reaches the optimal parameter values.

3.2.2.3. Parameter Identification of the Wingsail Structure

Below, the same procedure is used for the wingsail structure. The Lamé parameters are identified in the static case. Furthermore the densities and damping parameters are estimated using the transient case. In addition an analysis of the deviation between the experimental setup and the underlying CAD-model is provided.

Identification Setup Section 2.2.1 states that the wingsail is composed by two unitary parts. Hence, all parameters of the left and right side are identical. In this case it is adequate to identify only one side of the structure. However, during the construction and the first practical tests deviations between the experimental setup and the underlying CAD-model were noticed, which are discussed and analyzed below.

The main deviation is based on the geometric measures and the curvature of the sailing area itself. It reveals that the sailing area of the prototype is shorter compared to the underlying CAD model in the z^2-direction (width of the sail). The resulting error of the curvature can be fixed by the mounting of the supply beams, but the shortage of the structure leads to a gap of approximately 0.01 m between both sail areas on the free tip. To accomplish the touching behavior especially in the case of pretensioned actuators (2.105) the tips have to be elastically clamped to each other by rubber bands, see the magnifying glass of Fig. 3.8.

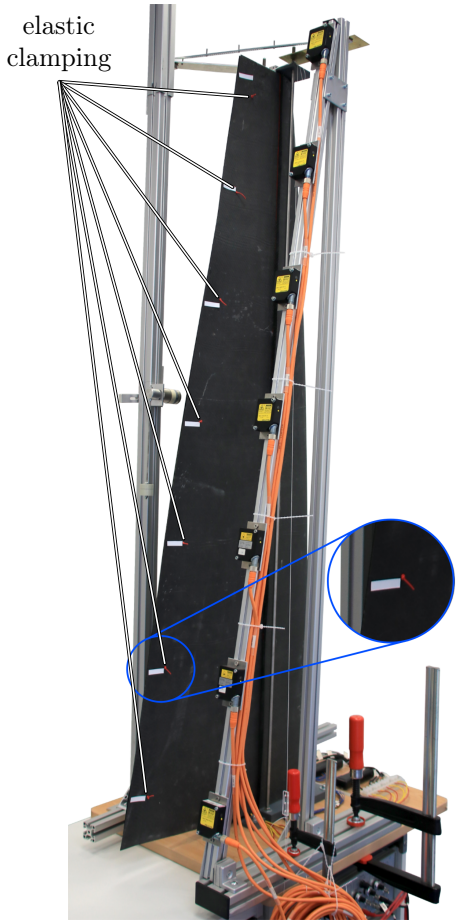

Figure 3.8.: Experimental setup of the wingsail structure including installed elastic clamping.

In addition, it can not be guaranteed that the material parameters of both parts are identical, due to the mounting process of the structure elements. The mounting is done by applying a mixture of epoxy resin and hardener on the surfaces which should be connected. This process has to be performed two times for each wingsail part to connect the sailing area with the supply beams and the supply beams with the actuators. As a result both parts can differ among themselves. The main effect for this deviation is given by the needed preparation time. The viscosity of the mixture is crucial regarding the amount of remaining epoxy glue on the resulting structure affecting its thickness, stiffness, damping, and density.

Considering these deviations, material parameters of the wingsail parts can not be identified separately in general. Furthermore the question arises, if the deviation between both parts among themselves leads to problems

in the FE-analysis. Due to the fact, that for the FE-analysis symmetric parts of a structure where neglected to reduce the number of DoFs, see Section 2.2.3 and Section 2.2.1.

Therefore, the open loop behavior of the transversal displacement of the unilateral wingsail and the coupled sails has to be analyzed. If both dynamics display a similar behavior it can be assumed that the additional clamping only introduces symmetric pretensions to both parts. Hence, the reduced FE-analysis stays valid.

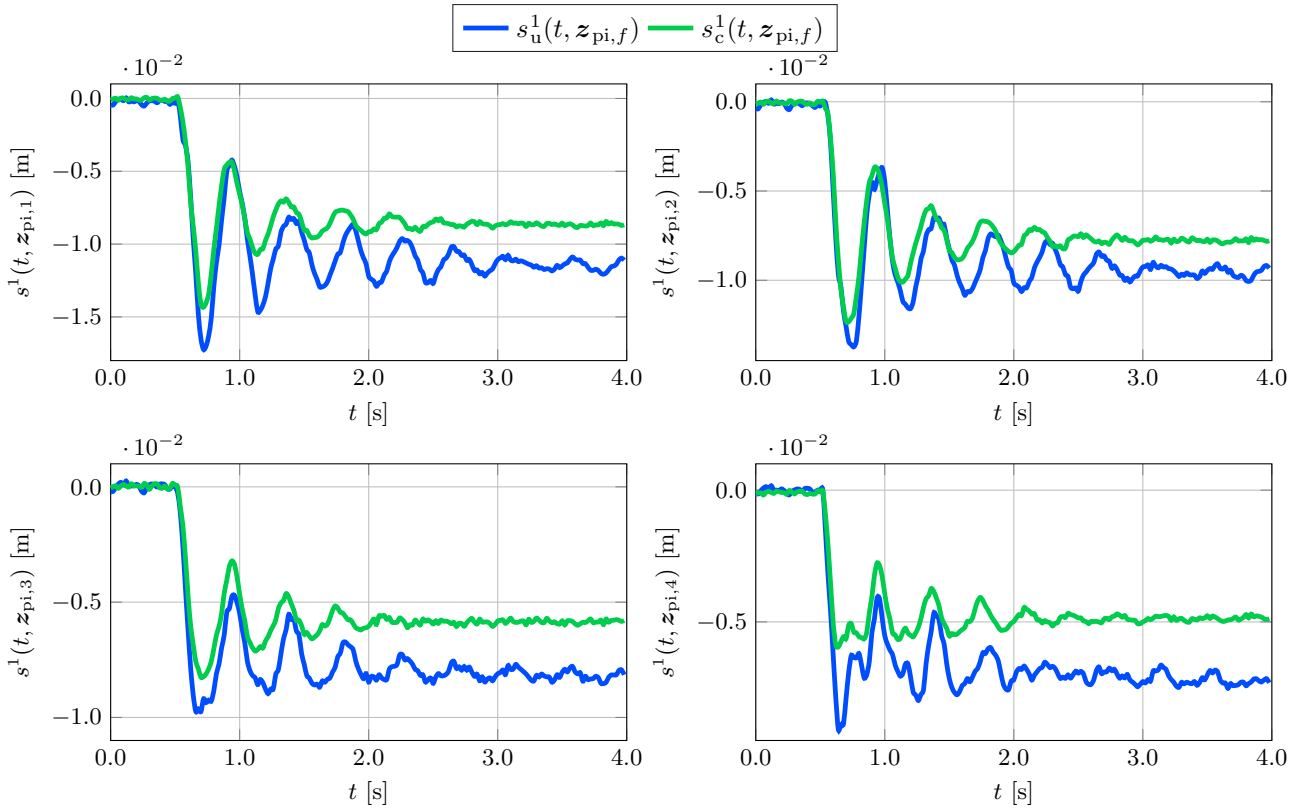

Figure 3.9.: Comparison between the step responses of the unilateral wingsail (right wingsail part only) and the coupled wingsail considering the input signals (3.38).

Fig. 3.10 displays the step response of the unilateral wingsail $s^1_{\mathrm{u}}(t, \boldsymbol{z}_{\mathrm{pi},f})$ and of the coupled wingsail $s^1_{\mathrm{c}}(t, \boldsymbol{z}_{\mathrm{pi},f})$ subject to the input signals

$$\boldsymbol{u}_{\mathrm{u}}(t) = \boldsymbol{u}_{\mathrm{c}}(t) = \begin{bmatrix} -700 & -700 & -700 & -700 \end{bmatrix} h(t - 0.5\,\mathrm{s}) \tag{3.38}$$

with $h(t)$ denoting the Heaviside function. These transversal deflections are measured by laser sensors (Welotec GmbH type OWLF 4030 FA S1) based on the triangulation principle. The measurements are taken on the points of interest at the end of the supply beams numbered from bottom to top, see Fig. 2.7. It has to be mentioned, that the signals are filtered by a first order low pass filter characterized by a cutoff frequency $f_{\mathrm{c}} = 100\,\mathrm{Hz}$ to reduce the noise.

Both measurements display a similar dynamical behavior. The frequency and the phase of the oscillation as well as the decaying process are nearly identical. Only the steady states differ from each other. Hence, it can be deduced that the pretension introduced by the coupling mainly effects the stiffness of the structure. This effect is symmetric which justifies the negligence of the left part of the wingsail structure in the FE-analysis. For the parameter identification this means that the material parameters of the right wingsail have to cover the additional effect of the elastic coupling. The resulting mathematical model is used as base for the controller design.

Static Case The objective parameters of the identification process in the static case are the Lamé parameters sets $\boldsymbol{\lambda}$ and $\boldsymbol{\mu}$. These sets contain the single parameters of the sailing areas, the four supply beams and the actuators marked by the indices ws, s, and a, respectively

$$\boldsymbol{\lambda} = \begin{bmatrix} \lambda_{\mathrm{ws}} & \lambda_{\mathrm{s}_1} & \dots & \lambda_{\mathrm{s}_4} & \lambda_{\mathrm{a}} \end{bmatrix}^T, \quad \boldsymbol{\mu} = \begin{bmatrix} \mu_{\mathrm{ws}} & \mu_{\mathrm{s}_1} & \dots & \mu_{\mathrm{s}_4} & \mu_{\mathrm{a}} \end{bmatrix}^T. \tag{3.39}$$

Each side of the wingsail is equipped with four MFC-actuators placed on the supply beams.

Assumption 3.1 *To reduce the number of desired parameters it is assumed that the material parameters of the MFC-actuators are equal. The actuators this assumption is justified, due to the marginal manufacturing tolerances of the patches. However, the mounting of the actuators is done with the previously explained epoxy resin resulting in the discussed potential uncertainties. The crucial preparation time of the MFC-actuators' mounting is much shorter compared to those of the mounting of the supply beams. This means that the viscosity of the epoxy mixture changes only slightly during the preparation phase, so that the uncertainties are reduced to a minimum.*

The static displacement is determined by a product of the Lamé parameters and the acting force. For the wingsail the acting force is the traction defined as $\boldsymbol{f}^{\mathrm{f}}_{\Gamma,\mathrm{a}_k}(t,\boldsymbol{z}_{\mathrm{a}_k}) = -\boldsymbol{f}^{\mathrm{r}}_{\Gamma,\mathrm{a}_k}(t,\boldsymbol{z}_{\mathrm{a}_k}) = \beta U_{\mathrm{a}_k}\boldsymbol{n}(\boldsymbol{z}_{\mathrm{a}_k})$ (see also (2.104)), where the conversion factor β is not exactly known. To identify the Lamé parameters and the conversion factor, two identification processes with different measurements are necessary. At first, an exactly known force has to be applied on a precise location on the wingsail surface. Hence, the identification can be concentrated on the Lamé parameters using the known force as input. In a second process, the MFC-actuators can be used as excitation of the structure, so that the conversion factor can be estimated.

Here the practical issue arises to apply an exactly known force to a precise location on the surface. Furthermore, the magnitude of this force has to be small due to the reaction of the lightweight wingsail structure. The force could be applied by an electric driven pulse hammer neglecting the friction of the rotating mounting of the hammer. However, this procedure would require a FE-analysis dealing with solid structure interaction, because the impact of the pulse hammer can not be modeled as simple force. Due to the fact, that the contact area of the lightweight structure and the hammer as well as the applied force varies over time.

To avoid these additional effort the conversion factor is chosen as $\beta = 5.0 \times 10^3\,\mathrm{N/V}$. Hence, the Lamé parameters fall into the expected parameter range.

Remark 3.4 *It has to be mentioned that due to the specification of the conversion factor β the resulting identified parameters are non-physical. This means that the mathematical model and its material parameters match the measurements although they are unrelated to the physical parameters. In fact, it is impossible to find a physical set of parameters for the underlying model, due to the previously discussed uncertainties. At least since the introduced elastic clamping with rubber bands the Lamé parameters have to cover additional effects and therefore are non-physical.*

Addressing the geometry of the wingsail (the magnitude of deflection declines significantly from bottom to top) the objective function (3.5) is adjusted to ensure an equal weighting of all measurements

$$J_{\mathrm{pm}}(\boldsymbol{\lambda}_i,\boldsymbol{\mu}_i) = \alpha\frac{1}{2}\int_{\Omega}\|\tilde{\boldsymbol{s}}^{\mathrm{rel}}_{\mathrm{pm}}(i)\|^2_{L^2}\,\mathrm{d}\Omega, \tag{3.40}$$

where $\tilde{\boldsymbol{s}}^{\mathrm{rel}}_{\mathrm{pi}}(i)$ denotes the projection of the relative error displacement field in the static case and is defined as

$$\tilde{\boldsymbol{s}}^{\mathrm{rel}}_{\mathrm{pm}}(i) = \sum_{g=1}^{n_{\mathrm{pm}}}\tilde{s}^{\mathrm{rel}}_{\mathrm{pm},g}(i)\gamma(\boldsymbol{z},\boldsymbol{z}_{\mathrm{pm}}), \quad \text{with} \quad \tilde{s}^{\mathrm{rel}}_{\mathrm{pm},g}(i) = \frac{s^{*,1}(\boldsymbol{z}_{\mathrm{pm},g}) - s^1(\boldsymbol{z}_{\mathrm{pm},g},\boldsymbol{\theta}_i)}{s^{*,1}(\boldsymbol{z}_{\mathrm{pm},g})}. \tag{3.41}$$

The measured deflection in z^1-direction on the points of measurement at $t = 4\,\mathrm{s}$ is given by $s^{*,1}(\boldsymbol{z}_{\mathrm{pm},g})$. In addition, the solution of static displacement profile evaluated on the same points is given by $s^1(\boldsymbol{z}_{\mathrm{pi},g},\boldsymbol{\theta}_i)$ and depends on the parameter set $\boldsymbol{\theta}_i = [\boldsymbol{\lambda}_i^T \quad \boldsymbol{\mu}_i^T]^T$, where i displays the number of iterations. Recalling from Section 2.2.1 (see Table 2.5) that the points of measurement of the wingsail are identical to the points of interest so that $\tilde{s}^{\mathrm{rel}}_{\mathrm{pm},g}(i) = \tilde{s}^{\mathrm{rel}}_{\mathrm{pi},f}(i)$ holds for the error.

The results of the parameter identification considering the adjusted objective function are given in Tables 3.9 and 3.10 taking a weighting parameter $\alpha = 1 \times 10^{13}$ into account. Both tables display the results of one optimization.

In addition to the numeric results Fig. 3.10 displays the decay of the function values (on the left) and the decay of the single relative errors (on the right). During the optimization the objective function displays a fast monotonically decreasing behavior starting at $J_{\mathrm{pm}}(\boldsymbol{\lambda}_0,\boldsymbol{\mu}_0) = 15840.42$ and resulting in $J_{\mathrm{pm}}(\boldsymbol{\lambda}_{23},\boldsymbol{\mu}_{23}) = 15.47$ as convergence is reached.

Moreover, all single relative errors tend towards zero starting with high values $\tilde{s}^{\mathrm{rel}}_{\mathrm{pi},1}(0) = 33.19\,\%$, $\tilde{s}^{\mathrm{rel}}_{\mathrm{pi},2}(0) = 42.62\,\%$, $\tilde{s}^{\mathrm{rel}}_{\mathrm{pi},3}(0) = 21.29\,\%$, and $\tilde{s}^{\mathrm{rel}}_{\mathrm{pi},4}(0) = -14.14\,\%$. The final errors remaining after convergence is reached are $\tilde{s}^{\mathrm{rel}}_{\mathrm{pi},1}(23) = 0.86\,\%$, $\tilde{s}^{\mathrm{rel}}_{\mathrm{pi},2}(23) = -1.18\,\%$, $\tilde{s}^{\mathrm{rel}}_{\mathrm{pi},3}(23) = 0.52\,\%$ and $\tilde{s}^{\mathrm{rel}}_{\mathrm{pi},4}(23) = -1.91\,\%$ which corresponds

Table 3.9.: Optimization results of $\boldsymbol{\lambda} = \begin{bmatrix}\lambda_{\mathrm{ws}} & \lambda_{\mathrm{s}_1} & \dots & \lambda_{\mathrm{s}_4} & \lambda_{\mathrm{a}}\end{bmatrix}^T$ of the static wingsail identification after $i = 23$ iterations (see Table 3.10 for the associated results of $\boldsymbol{\mu}$).

i	$J_{\mathrm{pm}}(\boldsymbol{\lambda}_i, \boldsymbol{\mu}_i)$	$\lambda_{\mathrm{ws},i}$ [N/m^2]	$\lambda_{\mathrm{s}_1,i}$ [N/m^2]	$\lambda_{\mathrm{s}_2,i}$ [N/m^2]	$\lambda_{\mathrm{s}_3,i}$ [N/m^2]	$\lambda_{\mathrm{s}_4,i}$ [N/m^2]	$\lambda_{\mathrm{a},i}$ [N/m^2]
0	$1.58 \cdot 10^4$	$1.07 \cdot 10^1$	$2.55 \cdot 10^1$	$2.55 \cdot 10^1$	$2.60 \cdot 10^1$	$1.11 \cdot 10^2$	$2.07 \cdot 10^0$
5	$1.01 \cdot 10^3$	$1.21 \cdot 10^1$	$2.56 \cdot 10^1$	$2.56 \cdot 10^1$	$2.61 \cdot 10^1$	$1.11 \cdot 10^2$	$3.03 \cdot 10^0$
10	$3.76 \cdot 10^2$	$1.12 \cdot 10^1$	$2.57 \cdot 10^1$	$2.56 \cdot 10^1$	$2.61 \cdot 10^1$	$1.11 \cdot 10^2$	$3.19 \cdot 10^0$
15	$2.73 \cdot 10^2$	$1.12 \cdot 10^1$	$2.57 \cdot 10^1$	$2.58 \cdot 10^1$	$2.62 \cdot 10^1$	$1.11 \cdot 10^2$	$3.73 \cdot 10^0$
20	$2.59 \cdot 10^1$	$1.15 \cdot 10^1$	$2.57 \cdot 10^1$	$2.80 \cdot 10^1$	$2.57 \cdot 10^1$	$1.10 \cdot 10^2$	$7.46 \cdot 10^0$
23	$1.55 \cdot 10^1$	$1.16 \cdot 10^1$	$2.57 \cdot 10^1$	$2.83 \cdot 10^1$	$2.56 \cdot 10^1$	$1.10 \cdot 10^2$	$7.90 \cdot 10^0$

Table 3.10.: Optimization results of $\boldsymbol{\mu} = \begin{bmatrix}\mu_{\mathrm{ws}} & \mu_{\mathrm{s}_1} & \dots & \mu_{\mathrm{s}_4} & \mu_{\mathrm{a}}\end{bmatrix}^T$ of the static wingsail identification converged after $i = 23$ iterations (see Table 3.9 for the associated results of $\boldsymbol{\lambda}$).

i	$J_{\mathrm{pm}}(\boldsymbol{\lambda}_i, \boldsymbol{\mu}_i)$	$\mu_{\mathrm{ws},i}$ [N/m^2]	$\mu_{\mathrm{s}_1,i}$ [N/m^2]	$\mu_{\mathrm{s}_2,i}$ [N/m^2]	$\mu_{\mathrm{s}_3,i}$ [N/m^2]	$\mu_{\mathrm{s}_4,i}$ [N/m^2]	$\mu_{\mathrm{a},i}$ [N/m^2]
0	$1.58 \cdot 10^4$	$2.19 \cdot 10^1$	$1.54 \cdot 10^{-1}$	$2.30 \cdot 10^{-1}$	$4.65 \cdot 10^0$	$3.04 \cdot 10^2$	$9.05 \cdot 10^0$
5	$1.01 \cdot 10^3$	$2.66 \cdot 10^1$	$2.86 \cdot 10^0$	$3.42 \cdot 10^0$	$5.80 \cdot 10^0$	$3.04 \cdot 10^2$	$1.17 \cdot 10^1$
10	$3.76 \cdot 10^2$	$2.22 \cdot 10^1$	$1.49 \cdot 10^{-3}$	$2.29 \cdot 10^1$	$6.03 \cdot 10^0$	$3.03 \cdot 10^2$	$1.26 \cdot 10^1$
15	$2.73 \cdot 10^2$	$2.05 \cdot 10^1$	$5.93 \cdot 10^{-3}$	$2.43 \cdot 10^1$	$8.88 \cdot 10^0$	$3.03 \cdot 10^2$	$1.45 \cdot 10^1$
20	$2.59 \cdot 10^1$	$1.45 \cdot 10^1$	$3.54 \cdot 10^{-2}$	$3.90 \cdot 10^1$	$1.23 \cdot 10^1$	$3.01 \cdot 10^2$	$2.59 \cdot 10^1$
23	$1.55 \cdot 10^1$	$1.38 \cdot 10^1$	$3.93 \cdot 10^{-2}$	$4.06 \cdot 10^1$	$1.24 \cdot 10^1$	$3.01 \cdot 10^2$	$2.72 \cdot 10^1$

to the absolute errors $\tilde{s}^{\mathrm{abs}}_{\mathrm{pi},1}(23) = 0.074 \times 10^{-3}\,\mathrm{m}$, $\tilde{s}^{\mathrm{abs}}_{\mathrm{pi},2}(23) = -0.069 \times 10^{-3}\,\mathrm{m}$, $\tilde{s}^{\mathrm{abs}}_{\mathrm{pi},3}(23) = 0.019 \times 10^{-3}\,\mathrm{m}$, and $\tilde{s}^{\mathrm{abs}}_{\mathrm{pi},4}(23) = -0.033 \times 10^{-3}\,\mathrm{m}$. The values of these absolute errors already fall into the range of the lasers' measurement noise. For this reason no further optimization processes are started and the identification process of the Lamé parameters is completed.

Overall the mathematical model for the resulting parameters matches the measurements. Furthermore, most of the values of the material parameter lay in the expected range. Table 3.11 provides the stiffness parameters in terms of Young's modulus E and Poisson's ratio ν considering the conversion (2.110) to provide a better comparability with the parameters of the beam structures, see Section 3.1. Tables 3.10 and 3.11 show that parameters of the first supply beam unexpectedly differ from the others. This is most likely caused by the deviation between the original CAD-file and the experimental setup which is the basis of the mesh used in the FE-analysis. Nevertheless, the result fits the measurement nearly perfectly so that it will be used in the next steps.

Table 3.11.: Stiffness parameters in terms of Young's modulus E_c and Poisson's ratio ν_c, where the index $c = \{\mathrm{ws},\ \mathrm{s}_1, \dots,\ \mathrm{s}_4,\ \mathrm{a}\}$ denotes the related part of the wingsail.

Part	ws	s_1	s_2	s_3	s_4	a
E_c [N/m^2]	33.873×10^9	0.118×10^9	97.805×10^9	33.265×10^9	682.091×10^9	60.484×10^9
ν_c	0.2282	0.4992	0.2053	0.3366	0.1337	0.1126

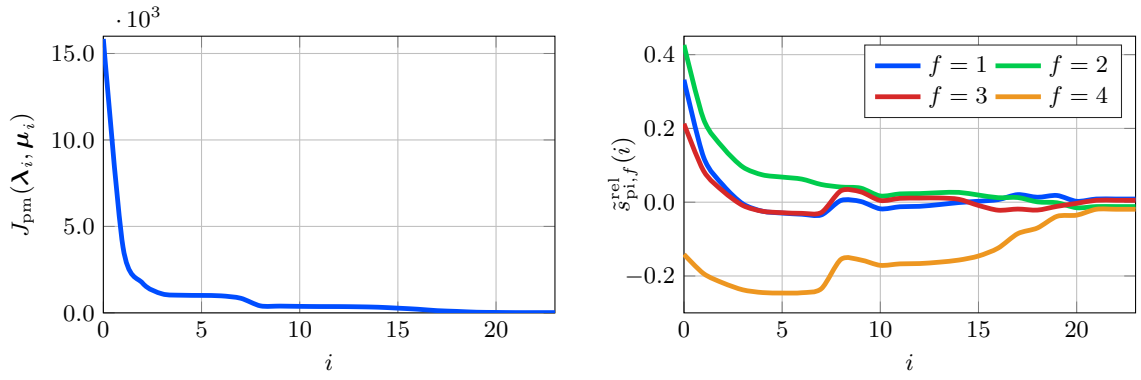

Figure 3.10.: *Left:* Behavior of the objective function $J_{\mathrm{pm}}(\boldsymbol{\lambda}_i, \boldsymbol{\mu}_i)$ during the optimization. Convergence is reached within $i = 23$ iteration, see also Tables 3.9 and 3.10.
Right: Associated behavior of the relative static errors $\tilde{s}^{\mathrm{rel}}_{\mathrm{pi},f}(i)$ during the optimization.

Transient Case Considering the identified stiffness parameters only the densities $\boldsymbol{\rho}$ and the viscous $\boldsymbol{\gamma}^{\mathrm{v}}$ as well as the Kelvin-Voigt damping parameters $\boldsymbol{\gamma}^{\mathrm{kv}}$ have to be estimated. As before each part of the wingsail is characterized by its own parameter set except for the MFC-actuators, see Assumption 3.1. Hence, the objective parameter sets are defined by

$$\boldsymbol{\rho} = \begin{bmatrix} \rho_{\mathrm{ws}} & \rho_{\mathrm{s}_1} & \dots & \rho_{\mathrm{s}_4} & \rho_{\mathrm{a}} \end{bmatrix}, \quad \boldsymbol{\gamma}^{\mathrm{v}} = \begin{bmatrix} \gamma^{\mathrm{v}}_{\mathrm{ws}} & \gamma^{\mathrm{v}}_{\mathrm{s}_1} & \dots & \gamma^{\mathrm{v}}_{\mathrm{s}_4} & \gamma^{\mathrm{v}}_{\mathrm{a}} \end{bmatrix}, \quad \boldsymbol{\gamma}^{\mathrm{kv}} = \begin{bmatrix} \gamma^{\mathrm{kv}}_{\mathrm{ws}} & \gamma^{\mathrm{kv}}_{\mathrm{s}_1} & \dots & \gamma^{\mathrm{kv}}_{\mathrm{s}_4} & \gamma^{\mathrm{kv}}_{\mathrm{a}} \end{bmatrix}. \tag{3.42}$$

The identification problem becomes more complex due to the fact that the number of desired parameters rise to 18 and that the problem is defined in a time span $t \in [0, T]$ taking into account the objective function (3.23). This is not a problem if the initial parameter guess is close to the ideal parameters. However, if the initial guess is not close enough, the following issues may appear:

- The number of desired parameters increases the cross coupling effect, especially by the combination of the densities and the Kelvin-Voigt damping. Both parameters affect the frequency of the oscillation of the transversal deflection resulting from the voltage step. This impact to the simulated dynamic can result in a kind of limit cycle.
- The considered time span also affects the optimization result. The temporal integration of the objective function shows a "low pass" behavior if the time span is not properly chosen, i.e., there is a local minimum for the optimization on the temporal averaged value most likely coinciding with the steady state. In this case the resulting parameters leads to an PT_1-behavior neglecting the oscillation at the beginning of the measurement.
- In addition, the previously discussed geometric weighting can not be used in the transient case due to the signal to noise ratio for the deflections which corrupts the relative error (3.41). Therefore, the optimization prioritizes the lower points of interest due to the larger magnitudes of their deflections.

If the initial guess is not close to the ideal parameter set a solution the wingsail is given by an iterative identification process. This means that the process is separated into the identification of the densities and the damping. This provides the opportunity to adjust the temporal weighting function $\alpha(t)$ as well as the considered time span (mainly the final time T) in the context of the objective parameter set.

In the following, the main idea of the time dependent weighting function and the separated or iterative identification process is explained. For a better understanding Fig. 3.11 illustrates the weighting. The main effect of the densities emerges in the frequency of the oscillation. Therefore, the weighting of the temporal region around the pivot points of the measurement signal has to be increased (green areas). Caused by the resulting increased error the optimization tries to fit the slope as well as the pivot points and leads to the correct frequency. To accelerate the optimization and to decrease the "low pass" behavior the considered final time is set to T_ρ, see Fig. 3.11.

In a second run both types of damping parameters have to be optimized. The main effect of the damping becomes clearly visible by the amplitude of the oscillation. Although the Kelvin-Voigt damping affects the frequency its impact is much smaller compared to the density. Hence, the weighting around the minima (yellow areas) and maxima (red areas) is increased. The chosen time span is also larger compared to the densities

$T_\gamma > T_\rho$. A "low pass" effect caused by the time dependent objective function has not to be concerned, due to the fact that a large error around the extreme points causes a high value of the objective function.

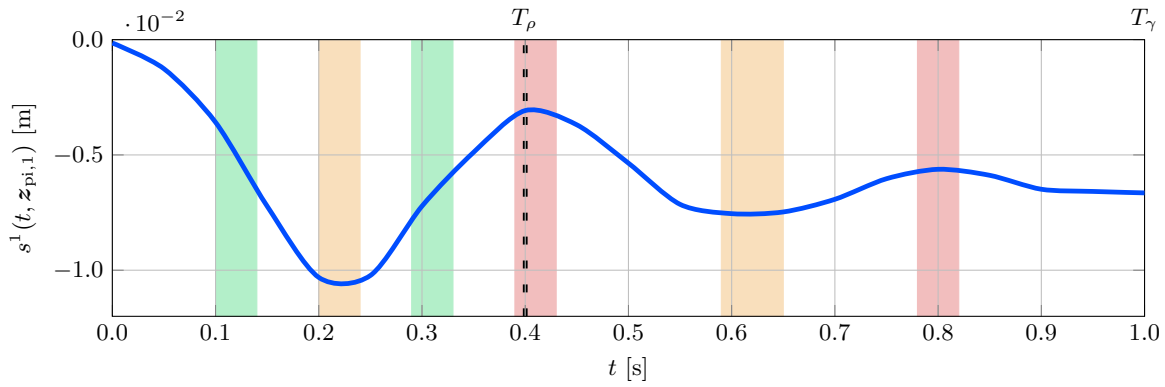

Figure 3.11.: Illustration the time dependent weighting of the objective function $J_{\mathrm{pm}}(\alpha(t), \boldsymbol{\rho}, \boldsymbol{\gamma}^{\mathrm{v}}, \boldsymbol{\gamma}^{\mathrm{kv}})$ by taking the example of the deflection of the first points of interest. The colored areas mark the time spans in which the weighting term $\alpha(t)$ is increased subject to the identification of the different parameters (green for the density, yellow and red for the damping parameters).

Fig. 3.12 illustrates the result of the presented iterated identification. The blue line displays the measurement of the displacement at the points of interest of the wingsail actuated by a voltage step of 700 Vof all actuators at $t = 0.0\,\mathrm{s}$. The simulation result of the initial guess is depicted by the green line. Compared to the measurement it can be clearly seen that this setting suffers from a high damping behavior. Also the frequency does not match, e.g., at the first point of interest at $t = 0.3\,\mathrm{s}$ and on the third point of interest. The red line shows the result of the first identification focused on the densities which fixes the frequencies as discussed before. In addition the yellow line displays the result of the second identification process taking the damping parameters into account. The oscillation of the first two points of interest display a good result. Likewise the third point of interest displays an acceptable match. Only the last point which refers to the top of the wingsail seems to be characterized by too high damping parameters. Nevertheless, the final result displays a good performance and will be used for the further motion planning process and the control design.

Table 3.12 lists the related material parameters of the wingsail structure. As mentioned before, these are non-physical parameters (see Remark 3.4) which only cover the measured dynamic but are not related to the expected value range. Especially the density of the supply beams attract attention due to their high magnitudes stating that the carbon composite material is denser than steel. This huge difference can be explained by the assumed thickness of the structure elements. As mentioned in Remark 2.6 and in the beginning of Section 3.2.2.3 the thickness of the structure elements is only a few 100 µm. Due to these small heights, even small deviations have a large impact to the volume. Considering the discussed deviation the decision was made to deal with non-physical parameter sets instead of rebuilding the complete prototype without any guarantee that these uncertainties will not appear again. Therefore, the parameter, especially the densities, cover these deviations. Instead of "adjusting" the related volume the numeric value of the density is used to match the measurements. Although, in the end it is essential that the mathematical model matches the measurement, which is proven by Fig. 3.12.

Table 3.12.: Densities ρ_c and viscous as well as Kelvin-Voigt damping parameters γ_c^{v}, γ_c^{kv} of the wingsail structure, where the index $c = \{\mathrm{ws},\ \mathrm{s}_1, \ldots,\ \mathrm{s}_4,\ \mathrm{a}\}$ denotes the related part of the wingsail.

Part	ws	s_1	s_2	s_3	s_4	a
ρ_c [kg/m^3]	5.547×10^3	61.894×10^3	161.423×10^3	533.515×10^3	153.463×10^3	192.069×10^3
γ_c^{v} [1/s]	4.572	0.201	0.846	5.647	21.475	18.241
γ_c^{kv} [s]	2.013×10^{-3}	649.057×10^{-3}	99.303×10^{-3}	26.178×10^{-3}	0.5215×10^{-3}	11.683×10^{-3}

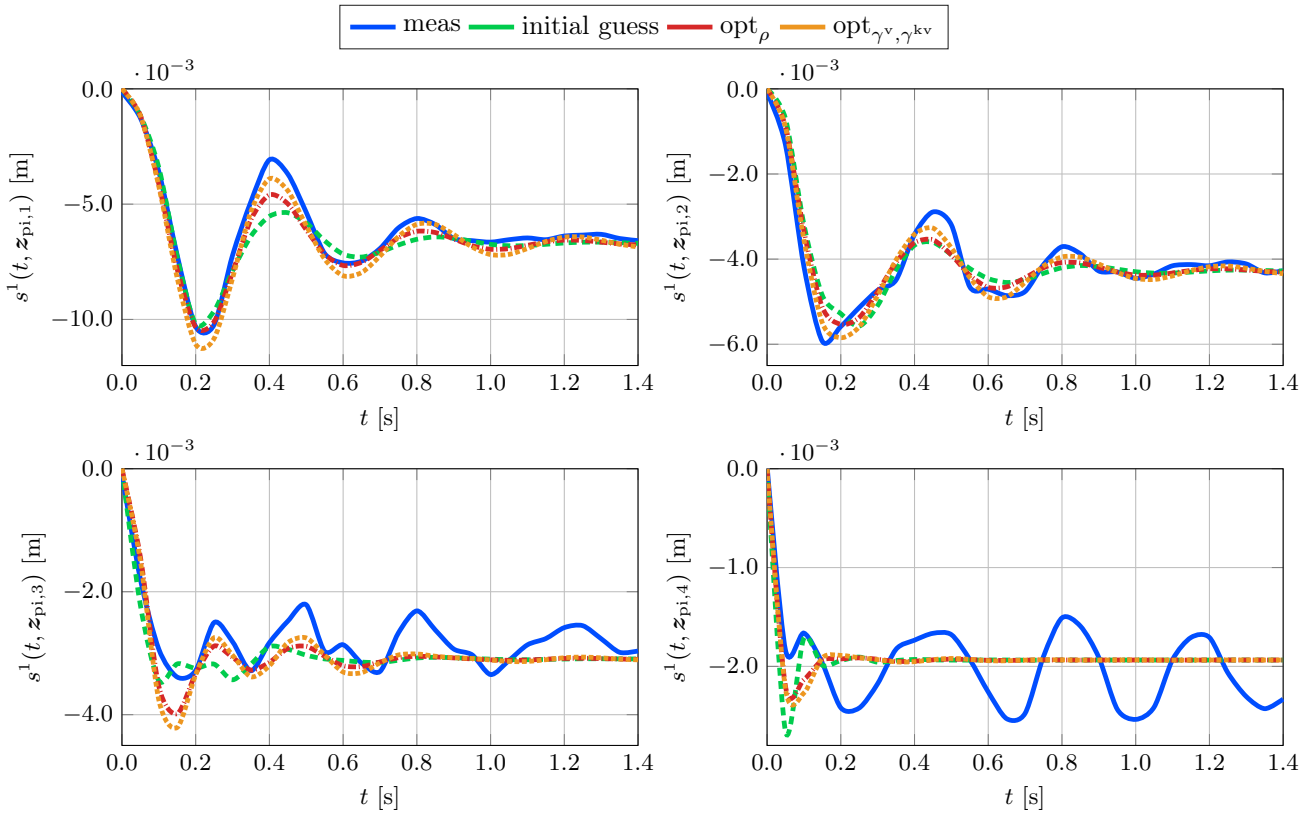

Figure 3.12.: Illustration of the optimization process compared to the measured deflection on the points of interest.

4. Model Order Reduction

For the purpose of simulation and control design an accurate mathematical description is required, though most of the time the accuracy goes hand in hand with the system's dimension and therefore the computational effort and the demanded storage space. As a result, the computation time increases so simulations get time consuming, especially if the process has to buffer its information. However, considering an online application in terms of the implementation of a control approach on a real time control device this increase of computational time may exceed the prescribed sample time. Therefore, reducing the computational effort is crucial and the reason for using the model order reduction (MOR) methods. The principle objective of MOR methods is to reduce the effort but to preserve as much accuracy as possible or required.

In general, most of the MOR methods can be assigned to one of the following groups

- singular value decomposition (SVD) based methods,
- Krylov based methods,
- or a combination of both.

An overview as well as detailed information about these different groups and the related methods are given in [5]. Subsequently, the following MOR methods

1. modal truncation,
2. second order balanced truncation,
3. and proper orthogonal decomposition (POD)

are introduced and discussed. All presented methods belong to the group of SVD based techniques. Each method is characterized by its pros and cons, which are discussed with regard to their considered application. The related numerical results are presented in Chapter 6.

As basis for the MOR the abstract full order model is either described by the second order equations of motion

$$M\ddot{\boldsymbol{q}}(t) + C\dot{\boldsymbol{q}}(t) + K\boldsymbol{q}(t) = L\boldsymbol{u}(t), \quad t > 0, \quad \boldsymbol{q}(0) = \boldsymbol{q}_0, \tag{4.1a}$$

$$\boldsymbol{y}_{\mathrm{pi}}(t) = P_{\mathrm{pi}}\boldsymbol{q}(t), \quad \boldsymbol{y}_{\mathrm{pm}}(t) = P_{\mathrm{pm}}\boldsymbol{q}(t), \quad t \geq 0 \tag{4.1b}$$

or the first order system description

$$\dot{\boldsymbol{x}}(t) = A\boldsymbol{x}(t) + B\boldsymbol{u}(t), \quad t > 0, \quad \boldsymbol{x}(0) = \boldsymbol{x}_0, \tag{4.2a}$$

$$\boldsymbol{y}_{\mathrm{pi}}(t) = H_{\mathrm{pi}}\boldsymbol{x}(t), \quad \boldsymbol{y}_{\mathrm{pm}}(t) = H_{\mathrm{pm}}\boldsymbol{x}(t), \quad t \geq 0, \text{ with} \tag{4.2b}$$

$$A = \begin{bmatrix} 0 & I \\ -M^{-1}K & -M^{-1}C \end{bmatrix}, \quad B = \begin{bmatrix} 0 \\ M^{-1}L \end{bmatrix}, \tag{4.2c}$$

considering the state vector $\boldsymbol{x}(t) = [\boldsymbol{q}^T(t)\ \dot{\boldsymbol{q}}^T(t)]^T \in \mathbb{R}^{2N}$, where N denotes the number of DoFs of the related second order system. Details are provided by (2.64) to (2.67) for the vertical beam configuration, (2.101) to (2.103) for the delta beam configuration, and (2.125) to (2.128) for the wingsail structure.

4.1. Modal Truncation

Modal truncation is a well studied MOR method especially in the field of mechanics. In the following, the main concept is discussed in view of its application to the presented flexible structures. Further details and varieties are provided in [5, chap. 9.2].

In general, modal truncation uses projection matrices based on the eigenvectors of the system matrix A of (4.2c) to generate a reduced order system. Considering the solution of the left and right eigenvalue problem

$$W^T A = A_\Delta W^T, \quad AV = VA_\Delta, \tag{4.3}$$

yields the eigenvalues λ_i, $i \in 1,\dots,2N$ and the associated matrices of left and right eigenvectors $W = [\boldsymbol{w}_1 \quad \dots \quad \boldsymbol{w}_{2N}]$, $V = [\boldsymbol{v}_1 \quad \dots \quad \boldsymbol{v}_{2N}]$, respectively. The matrix A_Δ denotes the sorted diagonal matrix $A_\Delta = \operatorname{diag}\{\lambda_1,\dots,\lambda_{2N}\}$ which displays the Jordan matrix. In addition, according to the applied damping model the eigenvalues occur in complex conjugated pairs with $\Re\{\lambda_i\} < 0$. The related frequency of such a pair is the so-called eigenfrequency or resonance frequency of the associated eigenmode. The higher the frequency the higher the damping effect becomes in a Kelvin-Voigt or structurally damped mechanical system. At a specific eigenfrequency the damping becomes overcritical and the associated eigenmode as well as all following eigenmodes become insignificant [120, chap 16]. The results of the asymptotic eigenvalue distribution of the vertical beam configuration supports this statement, see Appendix B.2. In other words the first eigenmodes contain the most of the system energy and are important for an accurate but reduced description.

Here, the MOR comes into play by truncating the eigenmodes and only considering the first $N_\mathrm{r} < N$ modes of the system. Hence, only the eigenvalues λ_l within the index set $l \in \mathbb{L} = \{1,\dots,2N_\mathrm{r}\}$ are considered with the reduced eigenvector matrices $W_\mathrm{r} = \begin{bmatrix}\boldsymbol{w}_1 & \dots & \boldsymbol{w}_{2N_\mathrm{r}}\end{bmatrix} \in \mathbb{R}^{2N\times 2N_\mathrm{r}}$, $V_\mathrm{r} = \begin{bmatrix}\boldsymbol{v}_1 & \dots & \boldsymbol{v}_{2N_\mathrm{r}}\end{bmatrix} \in \mathbb{R}^{2N\times 2N_\mathrm{r}}$. The reduced modal system state is given by $\boldsymbol{z}_\mathrm{r} = V_\mathrm{r}^\dagger \boldsymbol{x} \in \mathbb{R}^{2N_\mathrm{r}}$ where the full state can be constructed by $\boldsymbol{x} = V_\mathrm{r}\boldsymbol{z}_\mathrm{r}$.

Remark 4.1 *To simplify the notation the reduced modal state $\boldsymbol{z}_r$ is referred to as $\boldsymbol{z}$. This also applies to the associated system matrices, i.e., $A_\Delta = A_{\Delta,r}$.*

The reduced right eigenvector matrix V_r and its pseudoinverse $V_\mathrm{r}^\dagger$ are used as projection matrices, where the pseudoinverse can also be interpreted as a scaling of the eigenvector matrices for which $V_\mathrm{r}^\dagger V_\mathrm{r} = I \in \mathbb{R}^{N_\mathrm{r}\times N_\mathrm{r}}$ holds. The pseudoinverse is determined by expanding the right eigenvalue problem by W_r leading to

$$W_\mathrm{r}^T A V_\mathrm{r} = W_\mathrm{r}^T V_\mathrm{r} A_\Delta \quad \Rightarrow \quad A_\Delta = \left(W_\mathrm{r}^T V_\mathrm{r}\right)^{-1} W_\mathrm{r}^T A V_\mathrm{r} = V_\mathrm{r}^\dagger A V_\mathrm{r}, \quad \text{with} \quad V_\mathrm{r}^\dagger = \left(W_\mathrm{r}^T V_\mathrm{r}\right)^{-1} W_\mathrm{r}^T. \tag{4.4}$$

As long as the left and right eigenvectors are perfectly known $W_\mathrm{r}^T V_\mathrm{r} = I$ holds true so the pseudoinverse matrix is given by $V_\mathrm{r}^\dagger = W_\mathrm{r}^T$. However, for an ill-conditioned matrix A, e.g., in case of the wingsail, the inverse $\left(W_\mathrm{r}^T V_\mathrm{r}\right)^{-1}$ compensates the numeric artifacts of the eigenvector determination and ensures that $V_\mathrm{r}^\dagger V_\mathrm{r} = I$ holds true.

Considering the projection $\boldsymbol{x} = V_\mathrm{r}\boldsymbol{z}$ the system (4.2) reduces to

$$\begin{aligned} \dot{\boldsymbol{z}}(t) &= A_\Delta \boldsymbol{z}(t) + B_\Delta \boldsymbol{u}(t), \quad t > 0,\ \boldsymbol{z}(0) = \boldsymbol{z}_0, \\ \boldsymbol{y}_\mathrm{pi}(t) &= H_{\Delta,\mathrm{pi}} \boldsymbol{z}(t), \quad \boldsymbol{y}_\mathrm{pm}(t) = H_{\Delta,\mathrm{pm}} \boldsymbol{z}(t), \quad t \geq 0, \end{aligned} \tag{4.5}$$

with $A_\Delta = V_\mathrm{r}^\dagger A V_\mathrm{r}$, $B_\Delta = V_\mathrm{r}^\dagger B_\Delta$ and $H_{\Delta,\mathrm{pi|pm}} = H_{\mathrm{pi|pm}} V_\mathrm{r}$. In particular, the projected system matrix by construction results in $A_\Delta = \operatorname{diag}\{\lambda_l\}_{l=1}^{n_\mathrm{r}}$. This modal system description is also the basis of the flatness-based feedforward controls approach introduced in Section 5.1.

Modal truncation is used in an numeric pre-study of the wingsail structure [59, 116]. On the basis of the geometry presented by the CAD design of Fig. 2.7 the FEM model is developed using the proprietary FEM software *COMSOL* [26]. The complete structure is described by triangular finite shell elements with $N = 11688$ DoFs. Modal truncation leads to a reduced system described by $2N_\mathrm{r} = 68$ states ($\boldsymbol{z}(t) \in \mathbb{R}^{2N_\mathrm{r}}$) fulfilling the requirements of the feedforward control design.

Modal truncation is also used in a related project, where the flexible structure is an artificial fishtail modeled by the *Firedrake* framework [104, 103]. Here the original second order system is described by $N = 779232$ DoFs. Due to modal truncation the system can be reduced to $2N_\mathrm{r} = 10$ states ($\boldsymbol{z}(t) \in \mathbb{R}^{2N_\mathrm{r}}$). This reduced order system provides a high accuracy which is validated in simulations and therefore satisfies the requirements of the feedforward control approach.

In a way, the modeling of the beam structures also displays a kind of a modal truncation through the use of the finite dimensional Galerkin approximation. The resulting approximation of the Fourier series (2.60) and (2.89) considers only a finite number of eigenfunctions of an undamped Euler-Bernoulli beam. Therefore, it performs a truncation of higher modes of the infinite dimensional system. The results are discussed in Section 6.2.

In conclusion, it has to be mentioned that the modal truncation presents a stable MOR method. It can be used as long as at least a sufficient large number of eigenvalues and its left and right eigenvectors can be computed within a feasible tolerance. For the special case of a symmetric first order system (4.2) it is sufficient to determine only the right eigenvectors because $\boldsymbol{v}_l = \boldsymbol{w}_l$ holds true which reduces the computational effort of the method itself. Nevertheless, depending on the problem formulation there are more powerful MOR methods.

4.2. Second Order Balanced Truncation

The methods of this group are also based on projections but are based on a balanced form of the associated controllability and observability Gramians of the system [5, chap. 7.2].

Addressing the special structure of the input and system matrix (4.2) arising from the second order system (4.1a), the so-called second order balanced truncation is used to preserve the physical meaning of the reduced representation [22, 92]. At first, like in the general approach, the controllability and the observability Gramian have to be determined by solving the associated Lyapunov equations

$$A\mathcal{W}_{\mathrm{c}} + \mathcal{W}_{\mathrm{c}}A^T = -BB^T,\ A^T\mathcal{W}_{\mathrm{o}} + \mathcal{W}_{\mathrm{o}}A = -H^TH, \tag{4.6}$$

where the output matrix is chosen as $H = I$ to later enable the state observer design. Secondly, both symmetric and positive definite Gramians are partitioned into pairs of block matrices

$$\mathcal{W}_{\mathrm{c}} = \begin{bmatrix} \mathcal{W}_{\mathrm{c,p}} & \mathcal{W}_{\mathrm{c,12}} \\ \mathcal{W}_{\mathrm{c,21}} & \mathcal{W}_{\mathrm{c,v}} \end{bmatrix},\ \mathcal{W}_{\mathrm{o}} = \begin{bmatrix} \mathcal{W}_{\mathrm{o,p}} & \mathcal{W}_{\mathrm{o,12}} \\ \mathcal{W}_{\mathrm{o,21}} & \mathcal{W}_{\mathrm{o,v}} \end{bmatrix}, \tag{4.7}$$

whereby the second index p or v denotes the connection of the controllability and observability Gramian to the position or the velocity, respectively. This procedure is necessary to preserve the second order structure in the reduced system providing an interpretation in a physical manner. As long as both Gramians are regular the system is controllable and observable, i.e., there exists a matrix $\mathcal{T}$, that transforms the system into a balanced form where $\widetilde{\mathcal{W}}_{\mathrm{c,p}} = \widetilde{\mathcal{W}}_{\mathrm{o,p}}$ and $\widetilde{\mathcal{W}}_{\mathrm{c,v}} = \widetilde{\mathcal{W}}_{\mathrm{o,v}}$ holds true [92]. The construction of $\mathcal{T}$ requires at first the decomposition of the sub-Gramians by the Cholesky factorization

$$\mathcal{W}_{\mathrm{c,p}} = \mathcal{P}_{\mathrm{c,p}}\mathcal{P}_{\mathrm{c,p}}^T, \quad \mathcal{W}_{\mathrm{c,v}} = \mathcal{P}_{\mathrm{c,v}}\mathcal{P}_{\mathrm{c,v}}^T, \quad \mathcal{W}_{\mathrm{o,p}} = \mathcal{P}_{\mathrm{o,p}}\mathcal{P}_{\mathrm{o,p}}^T, \quad \mathcal{W}_{\mathrm{o,v}} = \mathcal{P}_{\mathrm{o,v}}\mathcal{P}_{\mathrm{o,v}}^T. \tag{4.8}$$

The associated lower triangular matrices are multiplied and a singular value decomposition [85, Theorem 8.34] is applied so that

$$\mathcal{P}_{\mathrm{o,p}}^T\mathcal{P}_{\mathrm{c,p}} = U_{\mathrm{p}}\Sigma_{\mathrm{p}}V_{\mathrm{p}}^T, \quad \mathcal{P}_{\mathrm{o,v}}^T\mathcal{P}_{\mathrm{c,v}} = U_{\mathrm{v}}\Sigma_{\mathrm{v}}V_{\mathrm{v}}^T. \tag{4.9}$$

This decomposition provides directly the Hankel singular values $\zeta_{\mathrm{p|v},i}$ in terms of the elements of the diagonal matrix $\Sigma_{\mathrm{p|v}}$ associated to the position or the velocity. With these preparations the transformation matrix and its inverse are given by

$$\mathcal{T} = \begin{bmatrix} \mathcal{T}_{\mathrm{p}} & 0 \\ 0 & \mathcal{T}_{\mathrm{v}} \end{bmatrix}, \quad \mathcal{T}^{-1} = \begin{bmatrix} \mathcal{T}_{\mathrm{p}}^{-1} & 0 \\ 0 & \mathcal{T}_{\mathrm{v}}^{-1} \end{bmatrix} \tag{4.10}$$

with

$$\begin{aligned} \mathcal{T}_{\mathrm{p}} &= \mathcal{P}_{\mathrm{c,p}}V_{\mathrm{p}}\Sigma_{\mathrm{p}}^{-\frac{1}{2}}, & \mathcal{T}_{\mathrm{p}}^{-1} &= \Sigma_{\mathrm{p}}^{-\frac{1}{2}}U_{\mathrm{p}}^T\mathcal{P}_{\mathrm{o,p}}^T, \\ \mathcal{T}_{\mathrm{v}} &= \mathcal{P}_{\mathrm{c,v}}V_{\mathrm{v}}\Sigma_{\mathrm{v}}^{-\frac{1}{2}}, & \mathcal{T}_{\mathrm{v}}^{-1} &= \Sigma_{\mathrm{v}}^{-\frac{1}{2}}U_{\mathrm{v}}^T\mathcal{P}_{\mathrm{o,v}}^T. \end{aligned} \tag{4.11}$$

The reduction is achieved by considering only the N_{r} position and velocity states with the highest associated Hankel singular values from $\zeta_{\mathrm{p|v},1}$ to $\zeta_{\mathrm{p|v},N_{\mathrm{r}}}$ and neglecting all other states. This can be done by partitioning of the transformation sub-matrices

$$\mathcal{T}_{\mathrm{p|v}} = \begin{bmatrix} \mathcal{T}_{\mathrm{p|v},1} & \mathcal{T}_{\mathrm{p|v},2} \end{bmatrix}, \quad \mathcal{T}_{\mathrm{p|v}}^{-1} = \begin{bmatrix} \mathcal{T}_{\mathrm{p|v},1}^{-1} \\ \mathcal{T}_{\mathrm{p|v},2}^{-1} \end{bmatrix}, \tag{4.12}$$

where $\widetilde{\mathcal{T}}_{\mathrm{p|v}} = \mathcal{T}_{\mathrm{p|v},1} \in \mathbb{R}^{N\times N_{\mathrm{r}}}$ and $\widetilde{\mathcal{T}}_{\mathrm{p|v}}^{-1} = \mathcal{T}_{\mathrm{p|v},1}^{-1} \in \mathbb{R}^{N_{\mathrm{r}}\times N}$ are chosen. Introducing $\widetilde{\mathcal{T}} = \mathrm{diag}\{\widetilde{\mathcal{T}}_{\mathrm{p}}, \widetilde{\mathcal{T}}_{\mathrm{v}}\}$ and $\widetilde{\mathcal{T}}^{-1} = \mathrm{diag}\{\widetilde{\mathcal{T}}_{\mathrm{p}}^{-1}, \widetilde{\mathcal{T}}_{\mathrm{v}}^{-1}\}$ the reduced order system is obtained as

$$\begin{aligned} \dot{\boldsymbol{x}}_{\mathrm{r}}(t) &= A_{\mathrm{r}}\boldsymbol{x}_{\mathrm{r}}(t) + B_{\mathrm{r}}\boldsymbol{u}(t), \quad t > 0, \quad \boldsymbol{x}_{\mathrm{r}}(0) = \boldsymbol{x}_{\mathrm{r},0}, \\ \boldsymbol{y}_{\mathrm{pi}}(t) &= H_{\mathrm{r,pi}}\boldsymbol{x}_{\mathrm{r}}(t), \quad \boldsymbol{y}_{\mathrm{pm}}(t) = H_{\mathrm{r,pm}}\boldsymbol{x}_{\mathrm{r}}(t), \quad t \geq 0, \end{aligned} \tag{4.13}$$

with the reduced state given by $\boldsymbol{x}_{\mathrm{r}} = \widetilde{\mathcal{T}}^{-1}\boldsymbol{x} \in \mathbb{R}^{2N_{\mathrm{r}}}$ and the associated system matrices

$$A_{\mathrm{r}} = \widetilde{\mathcal{T}}^{-1}A\widetilde{\mathcal{T}}, \quad B_{\mathrm{r}} = \widetilde{\mathcal{T}}^{-1}B, \quad H_{\mathrm{r,pi|pm}} = H_{\mathrm{pi|pm}}\widetilde{\mathcal{T}}. \tag{4.14}$$

As mentioned in Section 4.1 the application of a damping model leads to pairs of complex conjugate eigenvalues of the full system $\lambda_i \in \mathbb{C}$ with $i = \{1, \ldots, 2N\}$ and $\Re(\lambda_i) < 0$. As stated in [92, Corollary 3.2] the applied second order balance truncation preserves the stability in the case of a symmetric second order system (4.1a) with a positive definite mass matrix M, damping matrix C, and stiffness matrix K as it is given here.

To summerize, second order balanced truncation is a powerfull MOR method if the Gramians of the system can be determined. This imposes a restriction in particular for large scale systems with many DoFs. The Hankel singular values offer a measure of the impact of the states regarding the system's observability and controllability. Thereby the Hankel singular values provide the relative amount of energy of the reduced system compared to the energy of the full system by

$$\varepsilon(N_\mathrm{r}) = \frac{\sum_{m=1}^{N_\mathrm{r}} \left(\zeta_{\mathrm{p},m} + \zeta_{\mathrm{v},m}\right)}{\sum_{i=1}^{N} \left(\zeta_{\mathrm{p},i} + \zeta_{\mathrm{v},i}\right)}. \tag{4.15}$$

This can be used by the design of the state observer and controller.

The quality of the resulting reduced order system is evaluated in Section 6.1.1.1 considering the vertical beam configuration.

4.3. Proper Orthogonal Decomposition (POD)

The last presented method is the proper orthogonal decomposition (POD) also referred to as principal component analysis (PCA). This technique applies projection matrices based on simulated or sometimes measured data, so-called snapshots. The derivation of these matrices is based on the solution of a constrained optimization problem applying a Lagrangian framework, which results in an eigenvalue problem for the taken snapshots. Below, a brief derivation is presented to convey an understanding for the principal concept. Further details about the POD method are provided by [112, 113].

The main idea is to find a proper orthonormal basis (POD basis) capable to approximate the snapshots and therefore the behavior of the considered system. The snapshots are solutions of the considered problem, e.g., the displacement profile $y = \boldsymbol{q} \in \mathbb{R}^N$ for $t \in [0, T]$. It is crucial that these snapshots cover the dominating dynamics of the system. Hence, n_s snapshots within the time span $[0, T]$ are taken and stored in the data matrix

$$Y = \begin{bmatrix} y_1 & \dots & y_{n_s} \end{bmatrix} \in \mathbb{R}^{N \times n_s}, \tag{4.16}$$

where most of the time $N > n_s$ holds true. The basis is spanned by $\{\boldsymbol{\psi}_i\}_i^l$, where the rank of the basis is given by $l \leq \min(N, n_s)$.

Taking [113] into account the first order necessary optimality conditions are strongly related to the SVD of the data matrix. The SVD states that the rectangular data matrix Y can be described in the form

$$Y = \Psi \Sigma \Phi^T \quad \text{with} \quad \Sigma = \begin{bmatrix} D & 0 \\ 0 & 0 \end{bmatrix}, \tag{4.17}$$

where $D = \mathrm{diag}(\sigma_1 \geq \dots \geq \sigma_d) \in \mathbb{R}^{d \times d}$ is a matrix of positive real numbers also known as singular values of Y. In addition, Ψ and Φ denote the orthogonal matrices given by

$$\Psi = \begin{bmatrix} \boldsymbol{\psi}_1 & \dots & \boldsymbol{\psi}_N \end{bmatrix} \in \mathbb{R}^{N \times N}, \quad \Phi = \begin{bmatrix} \boldsymbol{\phi}_1 & \dots & \boldsymbol{\phi}_N \end{bmatrix} \in \mathbb{R}^{n_s \times n_s}. \tag{4.18}$$

The first d columns of the orthogonal matrices satisfy

$$Y \boldsymbol{\phi}_i = \sigma_i \boldsymbol{\psi}_i, \quad Y^T \boldsymbol{\psi}_i = \sigma_i \boldsymbol{\phi}_i, \quad \text{with} \quad i = 1, \dots, d. \tag{4.19}$$

In other words they define the eigenvectors of YY^T and Y^TY, respectively. The associated eigenvalues are given by $\lambda_i = \sigma_i^2 > 0$.

Taking the special form of Σ into account (4.17) can be rewritten as

$$Y = \Psi_d D \Phi_d^T, \quad \text{with} \quad \Psi = \begin{bmatrix} \Psi_d & \Psi_\alpha \\ \Psi_\beta & \Psi_\gamma \end{bmatrix}, \quad \Phi = \begin{bmatrix} \Phi_d & \Phi_\alpha \\ \Phi_\beta & \Phi_\gamma \end{bmatrix}, \tag{4.20}$$

where $\Psi_d \in \mathbb{R}^{N \times d}$ and $\Psi_d \in \mathbb{R}^{n_s \times d}$ are chosen. This formulation omits the zero singular values which have no effect on Y. Hence, considering [113] the m^{th} snapshot y_m is given by

$$\begin{aligned} y_m &= \sum_{i=1}^{d} [D\Phi_d^T]_{i,m} \boldsymbol{\psi}_i = \sum_{i=1}^{d} [\underbrace{\Psi_d^T \overbrace{\Psi_d D \Phi_d^T}^{Y}}_{I}]_{i,m} \boldsymbol{\psi}_i = \sum_{i=1}^{d} [\Psi_d^T Y]_{i,m} \boldsymbol{\psi}_i \\ &= \sum_{i=1}^{d} \left(\boldsymbol{\psi}_i^T y_m\right) \boldsymbol{\psi}_i = \sum_{i=1}^{d} \langle y_m, \boldsymbol{\psi}_i \rangle_{\mathbb{R}^N} \boldsymbol{\psi}_i, \quad \forall \quad m = 1, \dots, n_s \end{aligned} \tag{4.21}$$

where $\langle \cdot, \cdot \rangle_{\mathbb{R}^N}$ denotes the scalar product in $\mathbb{R}^N$. According to the SVD each snapshot can be displayed by d basis vectors.

The objective of POD is to reduce the number of considered basis vectors to express the essential information of the snapshots with a minimum of basis vectors. For POD this can be formulated as an iterative optimization problem. In the first step, the maximum of possible information from the data matrix should be gathered by a single normalized vector

$$\max_{\boldsymbol{\psi}_1} \sum_{m=1}^{n_s} (\langle y_m, \boldsymbol{\psi}_1 \rangle_{\mathbb{R}^N})^2, \tag{4.22a}$$

considering the constraint

$$\|\boldsymbol{\psi}_1\|_{\mathbb{R}^N}^2 = 1. \tag{4.22b}$$

To solve this problem the associated Lagrangian $\mathcal{L}$ with the Lagrange multiplier $\lambda_1 \in \mathbb{R}$ is formulated

$$\mathcal{L}(\boldsymbol{\psi}_1, \lambda_1) = \sum_{m=1}^{n_s} (\langle y_m, \boldsymbol{\psi}_1 \rangle_{\mathbb{R}^N})^2 + \lambda_1 (1 - \|\boldsymbol{\psi}_1\|_{\mathbb{R}^N}^2). \tag{4.23}$$

Considering [113] the necessary optimality condition $\partial_{\boldsymbol{\psi}_1} \mathcal{L} = 0$ results in

$$\begin{aligned} \partial_{\boldsymbol{\psi}_1} \mathcal{L} =& \partial_{\boldsymbol{\psi}_1} \left(\sum_{m=1}^{n_s} \left(\sum_{k=1}^{N} Y_{k,m} \boldsymbol{\psi}_1 \right)^2 + \lambda_1 (1 - \|\boldsymbol{\psi}_1\|_{\mathbb{R}^N}^2) \right) = 2 \sum_{m=1}^{n_s} \left(\sum_{k=1}^{N} Y_{k,m} \boldsymbol{\psi}_1 \right) Y_{k,m} + 2\lambda_1 \boldsymbol{\psi}_1 \Big) \\ =& 2\big(YY^T \boldsymbol{\psi}_1 - \lambda_1 \boldsymbol{\psi}_1\big) = \mathbf{0}, \end{aligned} \tag{4.24}$$

which can be reformulated as the eigenvalue problem

$$YY^T \boldsymbol{\psi}_1 = \lambda_1 \boldsymbol{\psi}_1, \tag{4.25}$$

where the symmetric matrix $YY^T \in \mathbb{R}^{N \times N}$ is positive semi-definite. The non-negative eigenvalues are denoted as λ_i with $i \in 1, \ldots, N$. To check if a maximum is reached the sufficient optimality condition is used

$$\partial_{\boldsymbol{\psi}_1}^2 \mathcal{L} = YY^T - \lambda_1 I = 0. \tag{4.26}$$

The basis can be extended to improve the performance by the previously mentioned iterative process. Therefore, an extended optimization problem can be stated

$$\max_{\boldsymbol{\psi}_1, \ldots, \boldsymbol{\psi}_{N_\mathrm{r}}} \sum_{i=1}^{N_\mathrm{r}} \sum_{m=1}^{n_s} (\langle y_m, \boldsymbol{\psi}_i \rangle_{\mathbb{R}^N})^2, \tag{4.27}$$

where $N_\mathrm{r} \in \{1, \ldots, d\}$ denotes the number of considered POD bases or in other words the number of reduced states. In addition, the constraint is extended to

$$\langle \boldsymbol{\psi}_i, \boldsymbol{\psi}_m \rangle_{\mathbb{R}^N} = \delta_{im} \quad 1 \leq i, m \leq N_\mathrm{r}, \tag{4.28}$$

demanding that the eigenvectors or bases $\{\boldsymbol{\psi}_i\}_{i=1}^{N_\mathrm{r}}$ are pairwise orthonormal. The symbol δ_{im} denotes the Kronecker delta for which $\delta_{im} = 1$ if and only if $i = m$ else $\delta_{im} = 0$ holds true.

This optimization leads to the eigenvalue problem

$$YY^T \boldsymbol{\psi}_i = \lambda_i \boldsymbol{\psi}_i, \quad i = 1, \ldots, N_\mathrm{r}, \tag{4.29}$$

where only the first $N_\mathrm{r} \leq d \leq N$ are considered revealing a truncation like in the other presented MOR methods. Taking [43, Sec. 5.2.1] into account the decay rate of the eigenvalues can be interpreted as a measure of the snapshots where a slow decay rate indicates a bad choice of snapshots.

For practical reasons, it is common to reformulate the eigenvalue problem (4.29), where the eigenvalues and eigenvectors of $YY^T \in \mathbb{R}^{N \times N}$ have to be calculated leading to a significant effort for a numerical solver depending on the size of the data set. Instead the method of snapshots [113, chap. 2] states that

$$Y^T Y \boldsymbol{\phi}_i = \lambda_i \boldsymbol{\phi}_i, \quad i = 1, \ldots, N_\mathrm{r}, \tag{4.30}$$

can be solved taking the relation

$$\boldsymbol{\psi}_i = \frac{1}{\sqrt{\lambda_i}} Y \boldsymbol{\phi}_i, \quad i = 1, \dots, N_\mathrm{r} \tag{4.31}$$

into account. This reduces the effort, due to the fact that the eigenvalue problem of $Y^T Y \in \mathbb{R}^{n_s \times n_s}$ is considered where usually $n_s < N$ holds true.

Similar to the balanced truncation (4.15) POD provides a relative measure of the considered energy of the reduced system compared to the energy of the full system

$$\varepsilon = \frac{\sum_{m=1}^{N_\mathrm{r}} \lambda_m}{\sum_{i=1}^{N} \lambda_i}, \tag{4.32}$$

where the denominator is also given by $\sum_{i=1}^{N} \lambda_i = \mathrm{trace}(YY^T) = \mathrm{trace}(Y^T Y)$.

One last modification is introduced in order to deal with heterogeneous local distributions meaning meshes consisting of FE characterized by significantly varying volumes. Such distributions usually emerge in meshes of complex structures. The inner product of (4.21) is substituted by the weighted inner product

$$\langle y_m, \boldsymbol{\psi}_i \rangle_W = \langle W y_m, \boldsymbol{\psi}_i \rangle_{\mathbb{R}^N} = \langle y_m, W \boldsymbol{\psi}_i \rangle_{\mathbb{R}^N} \tag{4.33}$$

considering the symmetric and positive definite weighting matrix W, see also [113, chap. 3]. Analog to the unweighted case the solution of the constraint optimization results in the eigenvalue problem

$$\bar{Y}^T \bar{Y} \bar{\boldsymbol{\phi}}_i = \lambda_i \bar{\boldsymbol{\phi}}_i, \quad i = 1, \dots, N_\mathrm{r}, \tag{4.34}$$

with $\bar{Y} = W^{\frac{1}{2}} Y$. The relation between the unweighted and weighted basis is given by

$$\boldsymbol{\psi}_i = W^{\frac{1}{2}} \bar{\boldsymbol{\psi}}_i = \frac{1}{\sqrt{\lambda_i}} Y \bar{\boldsymbol{\phi}}_i. \tag{4.35}$$

For systems generated by the FEM a suitable choice of the weighting matrix is usually the special kind of mass matrix, where the densities of all components are set to $\rho = 1$. The resulting matrix can be interpreted as a weighting of the geometry or the mesh.

The resulting basis vectors $\bar{\Psi} = [\bar{\boldsymbol{\psi}}_1 \quad \dots \quad \bar{\boldsymbol{\psi}}_{N_\mathrm{r}}]$ are used as the projection matrix leading to $\boldsymbol{q}(t) = \bar{\Psi} \boldsymbol{q}_\mathrm{r}(t)$. Hence, the reduced second order system is given by

$$M_\mathrm{r} \ddot{\boldsymbol{q}}_\mathrm{r}(t) + C_\mathrm{r} \dot{\boldsymbol{q}}_\mathrm{r}(t) + K_\mathrm{r} \boldsymbol{q}_\mathrm{r}(t) = L_\mathrm{r} \boldsymbol{u}(t), \quad \text{with} \quad t > 0, \quad \boldsymbol{q}_\mathrm{r}(0) = \bar{\Psi} \boldsymbol{q}_0 \tag{4.36}$$

where the reduced matrices are given by

$$M_\mathrm{r} = \bar{\Psi}^T M \bar{\Psi}, \quad C_\mathrm{r} = \bar{\Psi}^T C \bar{\Psi}, \quad K_\mathrm{r} = \bar{\Psi}^T K \bar{\Psi}, \quad L_\mathrm{r} = \bar{\Psi}^T L. \tag{4.37}$$

The corresponding first order system reads

$$\dot{\boldsymbol{x}}(t) = A_\mathrm{r} \boldsymbol{x}(t) + B_\mathrm{r} \boldsymbol{u}(t), \quad t > 0, \quad \boldsymbol{x}_\mathrm{r}(0) = \begin{bmatrix} \boldsymbol{q}_\mathrm{r}^T(0) & \dot{\boldsymbol{q}}_\mathrm{r}^T(0) \end{bmatrix}^T \in \mathbb{R}^{2N_\mathrm{r}}, \tag{4.38}$$

$$\boldsymbol{y}_\mathrm{pi}(t) = H_\mathrm{r,pi} \boldsymbol{x}(t), \quad \boldsymbol{y}_\mathrm{pm}(t) = H_\mathrm{r,pm} \boldsymbol{x}(t), \quad t \geq 0, \text{ with} \tag{4.39}$$

$$A_\mathrm{r} = \begin{bmatrix} 0 & I \\ -M_\mathrm{r}^{-1} K_\mathrm{r} & -M_\mathrm{r}^{-1} C_\mathrm{r} \end{bmatrix}, \quad B_\mathrm{r} = \begin{bmatrix} 0 \\ M_\mathrm{r}^{-1} L_\mathrm{r} \end{bmatrix}, \quad H_\mathrm{r,pi|pm} = H_\mathrm{pi|pm} \bar{\Psi}. \tag{4.40}$$

The implementation of the POD method for the wingsail structure is done by the MOR-projector [4] which is a part of the *Firedrake* FEM framework. The MOR-projector is a shared work of J. Andrej, D. Siebelts and the author. The presented wingsail setup is used as a test case for this project. The result of this POD method are displayed in Section 6.3.1.1.

5. Motion Planning and Control Design

The control of flexible structures often aims to deflect the initial shape of the considered structure to a desired displacement profile. Such a transition has to be planed subject to the constraints of the elastic structure. This is done by the so-called motion planning. In this work, the motion planning problem is given by a rest-to-rest motion which realize a smooth transition between an initial and a final displacement profile within a finite time of the previously discussed interconnected beam structures and the wingsail.

To achieve such a rest-to-rest motion two different control designs are introduced. At first the so-called two-degrees-of-freedom control approach is taken into account. Fig. 5.1 displays the associated control scheme composed by a feedforward control Σ^* and a feedback controller Σ_{fb}. The flatness-based feedforward control solves the motion planning problem, where the design is focused to avoid or at least reduce oscillations of light weight and weakly damped structures. In addition, the feedforward control contributes the main amount to the input signal $\boldsymbol{u}(t)$ and provides the desired reference trajectories of the system states $\boldsymbol{x}_{\mathrm{r}}^*(t)$ and outputs $\boldsymbol{y}_{\mathrm{pi}}^*(t)$ for the subsequent feedback control. The present states and outputs at the points of interest are estimated by a state observer Σ_{ob}. Due to the measuring noise of the laser sensors or the strain gauges, a Kalman filter is used to improve the signal to noise ratio of the measured outputs $\boldsymbol{y}_{\mathrm{pm}}(t)$ and to estimate the system states $\widehat{\boldsymbol{x}}_{\mathrm{r}}(t)$ and the deflections on the points of interest $\widehat{\boldsymbol{y}}_{\mathrm{pi}}(t)$. The feedback control ensures that the dynamic of the tracking error ($\tilde{\boldsymbol{x}}_{\mathrm{c}}$ or $\tilde{\boldsymbol{y}}_{\mathrm{pi}}$) is stabilized, where different control approaches are introduced, starting with classic output and state feedback controls and ending with a Lyapunov-based approach.

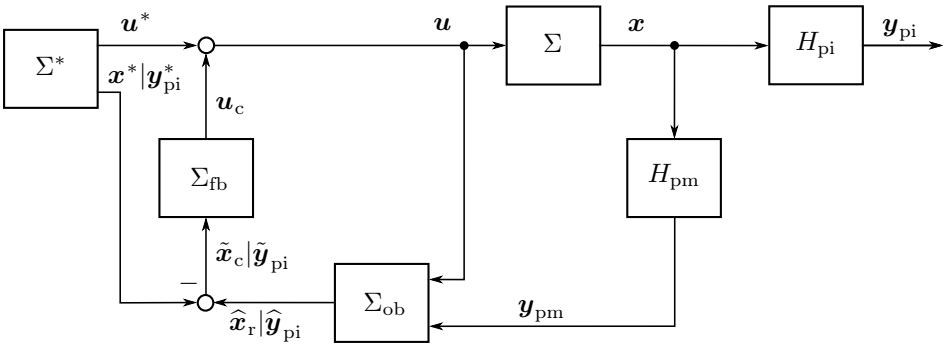

Figure 5.1.: Block diagram of the two-degrees-of-freedom control scheme, composed of a flatness-based trajectory generation and feedforward control Σ^*, an output or state feedback controller Σ_{fb}, and a state observer Σ_{ob}.

Secondly, the model predictive control (MPC) concept is introduced as an alternative control approach. The main idea of the concept is based on an optimization on a prediction horizon of the system's trajectories. The control input is determined by minimization of a cost functional. The first time step of the predicted input minimizing the cost functional yields the actual control input. This procedure is applied in each subsequent time step. Furthermore, the optimization process allows us to consider additional constraints, e.g., limited actuator behavior.

In order to introduce the control approaches in a general manner the following system description is applied as origin

$$\Sigma: \begin{cases} \dot{\boldsymbol{x}}_{\mathrm{r}}(t) = A_{\mathrm{r}}\boldsymbol{x}_{\mathrm{r}}(t) + B_{\mathrm{r}}\boldsymbol{u}(t), & t > 0, \quad \boldsymbol{x}_{\mathrm{r}}(0) = \boldsymbol{x}_{\mathrm{r},0} \in \mathbb{R}^{2N_{\mathrm{r}}}, \\ \boldsymbol{y}_{\mathrm{pi|pm}}(t) = H_{\mathrm{r,pi|pm}}\boldsymbol{x}_{\mathrm{r}}(t), & t \geq 0. \end{cases} \tag{5.1}$$

The chapter is organized as follows. At first, the design elements of the two-degrees-of-freedom control approach are discussed starting with the flatness-based motion planning and feedforward control is introduced. Afterwards, the state estimation and the different feedback control approaches are discussed. Secondly, the MPC approach is introduced. The performance of the presented control approaches are discussed in Chapter 6 by numeric as well as experimental results considering the setups of the interconnected beam structures and the wingsail.

5.1. Flatness-Based Motion Planning and Feedforward Control

As mentioned before, the objective of the motion planning process in this work is the design of a transition between an initial and a desired displacement profile of the elastic structures. Therefore the process has to consider the equations of motion of the considered structure as well as additional constraints. For the considered weakly damped structures a design constraint is given by the requirement to accomplish the desired rest-to-rest motion within a finite time T. Furthermore, oscillations should be reduced to a minimum.

For this purpose, a flatness-based approach is chosen that enables us to systematically solve the motion planning problem. This approach exploits the spectral representation of the system to determine the so-called flat output. This flat output denotes an auxiliary variable on which the control law and the desired reference trajectories are based. The sections below introduce the complete approach where further details are provided by [78].

5.1.1. Spectral Representation

The spectral system representation (also known as modal representation) defines the basis of the considered flatness-based motion planning and feedforward control approach. In general, the spectral representation is obtained by the similarity transformation $\boldsymbol{x}_\mathrm{r}(t) = V\boldsymbol{z}(t)$ with $V = [\boldsymbol{v}_1, \ldots, \boldsymbol{v}_{2N_\mathrm{r}}]$ the matrix of eigenvectors of A_r. Hence, (5.1) reduces to

$$\begin{aligned} \dot{\boldsymbol{z}}(t) =& A_\Delta \boldsymbol{z}(t) + B_\Delta \boldsymbol{u}(t), \quad t > 0,\ \boldsymbol{z}(0) = \boldsymbol{z}_0, \\ \boldsymbol{y}_\mathrm{pi}(t) =& H_{\Delta,\mathrm{pi}} \boldsymbol{z}(t), \quad \boldsymbol{y}_\mathrm{pm}(t) = H_{\Delta,\mathrm{pm}} \boldsymbol{z}(t), \quad t \geq 0, \end{aligned} \tag{5.2}$$

with $A_\Delta = V^{-1}AV = \mathrm{diag}\{\lambda_{\mathrm{r},1}, \ldots, \lambda_{\mathrm{r},2N_\mathrm{r}}\}$, $B_\Delta = V^{-1}B_\mathrm{r}$ and $H_{\Delta,\mathrm{pi|pm}} = H_{\mathrm{r,pi|pm}}V$. Note that the transformation relies on the quadratic eigenvector matrix $V \in \mathbb{R}^{2N_\mathrm{r} \times 2N_\mathrm{r}}$ of the reduced order system matrix A_r meaning that the inverse can determined with little effort due to the fact that the number of second order states of the reduced order system is small compared to the number of the original system $N_\mathrm{r} < N$. Hence, the l^th element of $\boldsymbol{z}$ is governed by

$$\dot{z}_l(t) = \lambda_{\mathrm{r},l} z_l(t) + \boldsymbol{b}_{\Delta,l}^T \boldsymbol{u}(t), \quad l \in \mathbb{L} \tag{5.3}$$

for $\mathbb{L} = \{1, \ldots, 2N_\mathrm{r}\}$ and $\boldsymbol{b}_{\Delta,l}^T$ denoting the l^th row of the transformed input matrix $B_\Delta = V^{-1}B_\mathrm{r}$.

If the underlying system is build considering modal truncation, see Section 4.1, then it is already described in its spectral form and the previous step can be omitted.

5.1.2. Construction of a Flat Output

The flat output is the core of the motion planning and feedforward control approach. Below, the derivation for the finite dimensional case is introduced and Appendix B.3 describes an infinite dimensional approach for the special case of spatial constant parameters considering a vertical beam configuration.

To construct the flat output the Laplace transformation is applied to the spectral state representation (5.3)

$$\hat{z}_l(s) = \frac{1}{s - \lambda_l} \boldsymbol{b}_{\Delta,l}^T \hat{\boldsymbol{u}}(s) = -\frac{1}{\lambda_l} \frac{1}{1 - \frac{s}{\lambda_l}} \boldsymbol{b}_{\Delta,l}^T \hat{\boldsymbol{u}}(s), \tag{5.4}$$

with $\hat{\boldsymbol{z}}(s) \bullet\!\!-\!\!\circ\, \boldsymbol{z}(t)$ and $\hat{\boldsymbol{u}}(s) \bullet\!\!-\!\!\circ\, \boldsymbol{u}(t)$. Extending the term $1/(1 - \frac{s}{\lambda_l})$ by unity yields

$$\hat{z}_l(s) = -\frac{1}{\lambda_l} \frac{\prod\limits_{i=1, i\neq l}^{|\mathbb{L}|} (1 - \frac{s}{\lambda_i})}{\prod\limits_{i=1}^{|\mathbb{L}|} (1 - \frac{s}{\lambda_i})} \boldsymbol{b}_{\Delta,l}^T \hat{\boldsymbol{u}}(s), \tag{5.5}$$

where $|\mathbb{L}| = 2N_\mathrm{r}$ denotes the number of considered states. The substitution

$$\hat{\boldsymbol{u}}(s) = \prod_{i=1}^{|\mathbb{L}|} \Big(1 - \frac{s}{\lambda_i}\Big) \hat{\boldsymbol{\xi}}(s) = \hat{D}_u(s) \hat{\boldsymbol{\xi}}(s) \tag{5.6a}$$

leads to

$$\hat{z}_l(s) = -\frac{1}{\lambda_l}\prod_{\substack{i=1,\\ i\neq l}}^{|\mathbb{L}|}\Big(1-\frac{s}{\lambda_i}\Big)\boldsymbol{b}_{\Delta,l}^T\hat{\boldsymbol{\xi}}(s) = -\frac{1}{\lambda_l}\hat{D}_z^{\,l}(s)\boldsymbol{b}_{\Delta,l}^T\hat{\boldsymbol{\xi}}(s). \tag{5.6b}$$

Hence, (5.6) states an input and state parameterization in terms of $\hat{\boldsymbol{\xi}}(s)$ in the operator domain. Reformulating the state and input operators into a polynomial formulation results in

$$\hat{D}_u(s) = \sum_{i=1}^{|\mathbb{L}|} c_i^u s^i, \quad \hat{D}_z^{\,l}(s) = \sum_{i=1}^{|\mathbb{L}-1|} c_i^{z,l} s^i. \tag{5.7}$$

Recalling that the operator s represents the time differentiation in the time domain leads to

$$\hat{\boldsymbol{u}}(s) = \sum_{i=1}^{|\mathbb{L}|} c_i^u s^i\hat{\boldsymbol{\xi}}(s) \quad \bullet\!\!-\!\!\circ \quad \boldsymbol{u}(t) = \sum_{i=1}^{|\mathbb{L}|} c_i^u \boldsymbol{\xi}^{(i)}(t) \tag{5.8a}$$

$$\hat{z}_l(s) = \sum_{i=1}^{|\mathbb{L}-1|} c_i^{z,l} s^i\hat{\boldsymbol{\xi}}(s) \quad \bullet\!\!-\!\!\circ \quad z_l(t) = \sum_{i=1}^{|\mathbb{L}-1|} c_i^{z,l}\boldsymbol{b}_{\Delta,l}^T\boldsymbol{\xi}^{(i)}(t). \tag{5.8b}$$

Similarly $\boldsymbol{x}_{\mathrm{r}}(t)$ can be computed by making use of $\boldsymbol{\xi}(t)$ and its derivatives, so that $\boldsymbol{\xi}(t)$ denotes a flat output for (5.1).

5.1.3. Motion Planning and Feedforward Control

The objective of motion planning is to design a desired rest-to-rest motion of the structure within a finite time span $t \in [0, T]$ starting at an arbitrary initial steady state deflection. Therefore, the flat input parametrization is used to set up an appropriate feedforward control, where the state parametrization can be used to determine the reference trajectory of the transient displacement profile. For these purposes, the series expansions of $\hat{D}_z^{\,l}(s)$ and $\hat{D}_u(s)$ require that the flat output fulfills $\boldsymbol{\xi}(t) \in C^{|\mathbb{L}|}(\mathbb{R})$. This requirement can be satisfied by the usage of Fourier series, polynomials or splines. Subsequently, a locally non-analytic smooth function $\Theta_{g,T}(t)$ of a particular Gevrey class is used (see also Definition B.1), that is defined by

$$\Theta_{g,T}(t) = \begin{cases} 0\,, & t \leq 0 \\ 1\,, & t \geq T \\ \dfrac{\int_0^t \theta_{g,T}(\tau)d\tau}{\int_0^T \theta_{g,T}(\tau)d\tau}, & t \in (0,T) \end{cases}, \tag{5.9}$$

where $\theta_{g,T}(t) = 0$ for $t \notin (0,T)$ and $\theta_{g,T}(t) = \exp(-([1-\frac{t}{T}]\frac{t}{T})^{-g})$ for $t \in (0,T)$ holds true. The desired flat output is build by

$$\boldsymbol{\xi}^*(t) = \boldsymbol{\xi}_0^* + \big(\boldsymbol{\xi}_T^* - \boldsymbol{\xi}_0^*\big)\Theta_{g,T}(t) \tag{5.10}$$

with $\boldsymbol{\xi}_0^*$ and $\boldsymbol{\xi}_T^*$ defining the start and end value of the flat output, respectively. In the next step, these values have to be determined w.r.t. $\boldsymbol{y}_{\mathrm{pi}}^*(0)$, $\boldsymbol{y}_{\mathrm{pi}}^*(T)$ the desired initial and final deflections of the points of interest, respectively. Thereby, the start and end profile can be determined by defining the desired defection at the points of interest of the structure taking the steady state equation of the system into account which considers the geometric constraints.

In steady state the input parametrization (5.8a) reduces to $\boldsymbol{u}_{\mathrm{st}} = \boldsymbol{\xi}_{\mathrm{st}}$, hence the solution of the steady state equation of (4.13) leads to

$$\begin{aligned} \boldsymbol{x}_{\mathrm{r,st}} &= -A_{\mathrm{r}}^{-1}B_{\mathrm{r}}\boldsymbol{u}_{\mathrm{st}} = -A_{\mathrm{r}}^{-1}B_{\mathrm{r}}\boldsymbol{\xi}_{\mathrm{st}}, \quad \text{with} \\ \boldsymbol{y}_{\mathrm{pi,st}} = H_{\mathrm{r,pi}}\boldsymbol{x}_{\mathrm{r,st}} \quad &\Rightarrow \quad \boldsymbol{\xi}_{\mathrm{st}} = \begin{cases} \big(-H_{\mathrm{r,pi}}A_{\mathrm{r}}^{-1}B_{\mathrm{r}}\big)^{-1}\boldsymbol{y}_{\mathrm{pi,st}} & n_{\mathrm{pi}} = n_u \\ \big(-H_{\mathrm{r,pi}}A_{\mathrm{r}}^{-1}B_{\mathrm{r}}\big)^{\dagger}\boldsymbol{y}_{\mathrm{pi,st}} & n_{\mathrm{pi}} \neq n_u \end{cases}, \end{aligned} \tag{5.11}$$

where $H_{\mathrm{r,pi}} A_{\mathrm{r}}^{-1} B_{\mathrm{r}} \in \mathbb{R}^{n_{\mathrm{pi}} \times n_u}$. Inserting the desired values $\boldsymbol{y}_{\mathrm{pi}}^*(t)$ at $t = 0$ and $t = T$ provides directly the start and end value of the flat output $\boldsymbol{\xi}_0^*$, $\boldsymbol{\xi}_T^*$, respectively. The substitution of (5.10) into (5.8) enables the determination of the reference trajectory considering $\boldsymbol{x}_{\mathrm{r}}(t) = V\boldsymbol{z}(t)$. As a result, the input parametrization (5.8a) defines the feedforward control law and the state parameterization (5.8b) provides the associated transient state trajectory.

This systematic approach enables the precalculation of the state and input trajectories. Hence, additional requirements of the experimental setup such as input saturations, restricted areas / deflections, etc. can be considered and included by an iterative process. Moreover, the approach is computationally efficient enabling the implementation in a real time process even for short sample times. In addition, it can be directly used in a time discrete setup.

Chapter 6 presents experimental and numeric results as well as the specific values of the design parameters of the flatness-based motion planning and feedforward control subject to the different elastic structures.

5.2. State Estimation

As mentioned before, the feedforward control provides the desired reference trajectories and the associated input trajectories of the system based on its mathematical description. This is an open loop process which does not use any measured signals. As a result, it can not react on unexpected events like disturbances or deviations between the experimental setup and the system description. Therefore, a feedback control is required ensuring that the given reference trajectory is reached. To close the control loop by a feedback controller some kind of measured signals have to be feedback to determine the tracking or control error. Depending on the control plant and the type of controller it can be hard or even impossible to measure the necessary signals required for the control error. E.g., the vertical beam configuration setup uses strain gauges to measure the strain on the beams at the points of measurement $\boldsymbol{y}_{\mathrm{pm}}(t)$, but the objective of the control is the deflection at the points of interest $\boldsymbol{y}_{\mathrm{pi}}(t)$. Another example is the usage of a state controller which requires the actual system states that are not completely measurable. To overcome this issue a so-called state observer can be used, which uses measurements to estimate the system states and reconstructs the control output on the basis of system description.

In the experimental setups considered in this work laser sensors or strain gauges are used to detect the displacement or the strain at specific points of measurement of the structure. Both measurement types provide electrical signals affected by measurement noise. To reduce the effect of noise and addressing the time discrete implementation on the real time control device the discrete Kalman filter is used.

Therefore, the discrete system description based on the reduced order system (5.1) is introduced

$$\begin{aligned} \boldsymbol{x}_k &= A_{\mathrm{d}}\boldsymbol{x}_{k-1} + B_{\mathrm{d}}\boldsymbol{u}_{k-1} + \mathfrak{w}_{k-1}, \quad k > 1, \quad \boldsymbol{x}_{\mathrm{r}}(0) = \boldsymbol{x}_0, \\ \boldsymbol{y}_{\mathrm{pi},k} &= H_{\Delta,\mathrm{pi}}\boldsymbol{x}_k, \quad \boldsymbol{y}_{\mathrm{pm},k} = H_{\Delta,\mathrm{pm}}\boldsymbol{x}_k + \mathfrak{v}_k, \end{aligned} \tag{5.12}$$

with $\boldsymbol{x}_k = \boldsymbol{x}_{\mathrm{r}}(kt_{\mathrm{d}})$, $\boldsymbol{u}_k = \boldsymbol{u}(kt_{\mathrm{d}})$ and $\boldsymbol{y}_{\mathrm{pi|pm},k} = \boldsymbol{y}_{\mathrm{pi|pm}}(kt_{\mathrm{d}})$, where t_{d} denotes the sample time. In addition, the system is extended by $\mathfrak{w}_{k-1} \sim \mathcal{N}(\mathbf{0}, Q_{\mathrm{o}})$ and $\mathfrak{v}_k \sim \mathcal{N}(\mathbf{0}, R_{\mathrm{o}})$ describing the process and measurement noise, respectively. Both are assumed to be white noise processes with expected value of $\mathbf{0}$ and covariance matrices Q_{o} and R_{o}. These matrices will be used later on as tuning factors. The discrete system and input matrix can be determined as [6]

$$A_{\mathrm{d}} = \exp(A_{\mathrm{r}} t_{\mathrm{d}}), \quad B_{\mathrm{d}} = \int_{(k-1)t_{\mathrm{d}}}^{kt_{\mathrm{d}}} \exp\big(A_{\mathrm{r}}(kt_{\mathrm{d}} - \tau)\big) B_{\mathrm{r}} \,\mathrm{d}\tau, \quad H_{\mathrm{d,pi|pm}} = H_{\mathrm{r,pi|pm}}. \tag{5.13}$$

The equations of the Kalman filter can be split into the extrapolation phase

$$\widehat{\boldsymbol{x}}_k^- = A_{\mathrm{d}}\widehat{\boldsymbol{x}}_{k-1} + B_{\mathrm{d}}\boldsymbol{u}_{k-1}, \quad P_k^- = A_{\mathrm{d}} P_{k-1} A_{\mathrm{d}}^T + Q_{\mathrm{o}} \tag{5.14a}$$

and the update or innovation phase [40, 70]

$$\begin{aligned} \widehat{\boldsymbol{x}}_k &= \widehat{\boldsymbol{x}}_k^- + L_k(\boldsymbol{y}_{\mathrm{pm},k} - H_{\mathrm{d,pm}}\widehat{\boldsymbol{x}}_k^-), \\ L_k &= P_k^- H_{\mathrm{r,pm}}^T (H_{\mathrm{r,pm}} P_k^- H_{\mathrm{r,pm}}^T + R_{\mathrm{o}})^{-1}, \\ P_k &= (I - L_k H_{\mathrm{r,pm}}) P_k^-, \end{aligned} \tag{5.14b}$$

where P_k denotes the error covariance matrix with the expected initial value of $P_0 = E(\widetilde{\boldsymbol{x}}_{\mathrm{o},0}\widetilde{\boldsymbol{x}}_{\mathrm{o},0}^T)$ considering the observer error $\widetilde{\boldsymbol{x}}_{\mathrm{o},k} = \boldsymbol{x}_k - \widehat{\boldsymbol{x}}_k$. In case of a stable observer error dynamics the error covariance approaches

a steady state $\lim_{k\to\infty} P_k^- = P$, which is provided by the solution of the algebraic Riccati equation. Hence, the Kalman gain becomes constant and reads

$$L = PH_{\mathrm{r,pm}}^T(H_{\mathrm{r,pm}}PH_{\mathrm{r,pi}}^T + R_{\mathrm{o}})^{-1}. \tag{5.14c}$$

With this the update phase simplifies to

$$\widehat{\boldsymbol{x}}_k = \widehat{\boldsymbol{x}}_k^- + L(\boldsymbol{y}_{\mathrm{pm},k-1} - H_{\mathrm{r,pm}}\widehat{\boldsymbol{x}}_{k-1}). \tag{5.14d}$$

As mentioned before, for the practical implementation the covariance matrices are used as tuning factors. For the measurement noise the structure of the covariance matrix is chosen as a weighted identity matrix

$$R_{\mathrm{o}} = r_{\mathrm{o}} I \in \mathbb{R}^{n_{\mathrm{pm}}\times n_{\mathrm{pm}}}. \tag{5.15}$$

It is assumed that the measurement noise is uncorrelated leading to the diagonal structure. The homogeneous weighting r_{o} of the different measurement signals is justified by the fact, that the same measurement devices are used, i.e., either laser sensors or strain gauges.

The choice of the elements and the structure of the process noise covariance matrix varies depending on the system and the applied MOR method. All presented designs assume uncorrelated process noise signals which leads to a diagonal structure of the covariance matrix. However, the weighting of the states differs. Each variation applies a partitioning of the matrix regarding the physical association of the elements to the position (or to be specific the displacement) or the velocity indicated by the indices p and v. This distinction is used later on for the choice of the weighting.

- Taking the full order system of the beam structures or the reduced order system considering modal truncation into account the partitioning of the covariance matrix is done per beam marked by the index $j = \{1, \dots, r\}$

$$\begin{aligned} Q_{\mathrm{o}} &= q_{\mathrm{o},t}\mathrm{diag}\{\boldsymbol{q}_{\mathrm{o,p},1},\ \boldsymbol{q}_{\mathrm{o,v},1},\ \dots,\ \boldsymbol{q}_{\mathrm{o,p},r},\ \boldsymbol{q}_{\mathrm{o,v},r}\},\\ \boldsymbol{q}_{\mathrm{o,p|v},j}^T &= q_{\mathrm{o,p|v}}\begin{bmatrix} q_{\mathrm{o,p|v},j}^{\mathrm{s}} & q_{\mathrm{o,p|v},j}^{\mathrm{s}} + 2\frac{q_{\mathrm{o,p|v},j}^{\mathrm{e}} - q_{\mathrm{o,p|v},j}^{\mathrm{s}}}{N_j - 1} & q_{\mathrm{o,p|v},j}^{\mathrm{s}} + 3\frac{q_{\mathrm{o,p|v},j}^{\mathrm{e}} - q_{\mathrm{o,p|v},j}^{\mathrm{s}}}{N_j - 1} & \dots & q_{\mathrm{o,p|v},j}^{\mathrm{e}} \end{bmatrix} \in \mathbb{R}^{N_j} \end{aligned} \tag{5.16a}$$

  with $q_{\mathrm{o},t}$ as unified weight, $q_{\mathrm{o,p|v},j}$ as an additional weighting of the position and velocity. The elements of $\boldsymbol{q}_{\mathrm{o,p|v},j}$ are determined by the linear interpolation between the start and end values $q_{\mathrm{o,p|v},j}^{\mathrm{s}}$, $q_{\mathrm{o,p|v},j}^{\mathrm{e}}$, respectively. Considering the characteristics of the modal truncation for mechanical systems it can be stated that the main amount of system energy is stored in the first few modes. As a result, these modes have a stronger impact and are more trustworthy compared to the higher modes which leads to $q_{\mathrm{o,p|v},j}^{\mathrm{s}} > q_{\mathrm{o,p|v},j}^{\mathrm{e}}$.

- If the governing reduced order model is build by second order balanced truncation the Hankel singular values $\zeta_{\mathrm{p|v},k}$ provide information about the observability of each state $k \in \mathbb{K} = [1, \dots, N_{\mathrm{r}}]$. They depict a kind of natural weighting reducing the complexity of possible combinations of the elements of Q_{o} as follows

$$Q_{\mathrm{o}} = q_{\mathrm{o},t}\mathrm{diag}\{\boldsymbol{q}_{\mathrm{o,p}},\ \boldsymbol{q}_{\mathrm{o,v}}\}, \quad \boldsymbol{q}_{\mathrm{o,p|v}}^T = q_{\mathrm{o,p|v}}\begin{bmatrix}\zeta_{\mathrm{p|v},1} & \dots & \zeta_{\mathrm{p|v},N_{\mathrm{r}}}\end{bmatrix}. \tag{5.16b}$$

  In this case, the weighting of the position and velocity is given by the fractions

$$q_{\mathrm{o,p}} = \frac{q_{\mathrm{o,p,a}}}{\sum_{k=1}^{N_{\mathrm{r}}}\zeta_{\mathrm{p},k}} \quad \text{and} \quad q_{\mathrm{o,v}} = \frac{q_{\mathrm{o,v,a}}}{\sum_{k=1}^{N_{\mathrm{r}}}\zeta_{\mathrm{v},k}}$$

  considering an additional weighting of the position and velocity $q_{\mathrm{o,p|v,a}}$.

- The simplest separation of position and velocity is given by a reduced system based on POD. Due to the second order structure, the first set of system states from 1 to N_{r} is related to the position or displacement and the second part from $N_{\mathrm{r}} + 1$ to $2N_{\mathrm{r}}$ is associated with the velocity. The weighting can be introduced as

$$\begin{aligned} Q_{\mathrm{o}} &= q_{\mathrm{o},t}\mathrm{diag}\{\boldsymbol{q}_{\mathrm{o,p}},\ \boldsymbol{q}_{\mathrm{o,v}}\},\\ \boldsymbol{q}_{\mathrm{o,p|v},j}^T &= q_{\mathrm{o,p|v}}\begin{bmatrix} q_{\mathrm{o,p|v},j}^{\mathrm{s}} & q_{\mathrm{o,p|v},j}^{\mathrm{s}} + 2\frac{q_{\mathrm{o,p|v},j}^{\mathrm{e}} - q_{\mathrm{o,p|v},j}^{\mathrm{s}}}{N_j - 1} & q_{\mathrm{o,p|v},j}^{\mathrm{s}} + 3\frac{q_{\mathrm{o,p|v},j}^{\mathrm{e}} - q_{\mathrm{o,p|v},j}^{\mathrm{s}}}{N_j - 1} & \dots & q_{\mathrm{o,p|v},j}^{\mathrm{e}} \end{bmatrix} \in \mathbb{R}^{N_j} \end{aligned} \tag{5.16c}$$

  As before the elements of $\boldsymbol{q}_{\mathrm{o,p|v}}$ are formed by the linear interpolation between the start and end values $q_{\mathrm{o,p|v}}^{\mathrm{s}}$, $q_{\mathrm{o,p|v}}^{\mathrm{e}}$, respectively. Analog to modal truncation the POD method sorts its bases according to their impact from high to low leading to the design choice $q_{\mathrm{o,p|v}}^{\mathrm{s}} > q_{\mathrm{o,p|v}}^{\mathrm{e}}$.

The numeric values are determined during hardware-in-the-loops tests and are presented in Chapter 6 considering the different experimental setups and used MOR methods.

5.3. Feedback Control Design

The experimental setup is affected by unknown disturbances and model uncertainties which influence the performance of the feedforward control approach. To decrease the resulting deviations the feedforward control approach is amended by a feedback controller ensuring that the desired reference trajectory $\boldsymbol{y}_{\mathrm{pi}}^{*}(t)$ is reached which completes the two-degrees-of-freedom control strategy introduced by Fig. 5.1. Below different classic feedback control approaches are introduced, where the considered design parameters as well as the associated simulation and experimental results are presented in Chapter 6.

5.3.1. Output Feedback Control Approach

Motivated by the results of [80] for the input-output stabilization of a single cantilever beam, an ID-T_1 control approach is proposed in terms of the transfer function

$$\hat{g}_{\mathrm{tr}}(s) = \frac{k_{\mathrm{I}}}{s} + \frac{k_{\mathrm{D}} s}{s T_{\mathrm{idt}} + 1}. \tag{5.17}$$

Here, k_{I} denotes the gain of the integrator part, k_{D} specifies the gain of the differentiator with realization term and $1/T_{\mathrm{idt}}$ defines the cutoff frequency of the associated low pass filter. The design parameter can be chosen in the continuous time implementation of the controller which can easily be transformed into the required time discrete realization [73] considering

$$\hat{g}_{\mathrm{tr}}(z) = \frac{k_{\mathrm{I}} t_{\mathrm{d}}}{2} \frac{z+1}{z-1} + \frac{k_{\mathrm{D}}}{T_{\mathrm{idt}}} \frac{z-1}{z - \exp\left(\frac{t_{\mathrm{d}}}{T_{\mathrm{idt}}}\right)}. \tag{5.18}$$

The feedback controller reduces the output error $\tilde{\boldsymbol{y}}_k = \boldsymbol{y}_{\mathrm{pi},k}^{*} - \widehat{\boldsymbol{y}}_{\mathrm{pi},k}$ taking the estimated output of the Kalman filter into account. The transition performance is achieved by the feedforward control with the feedback part addressing model errors, parameter uncertainties or external disturbances.

5.3.2. State Feedback Control Approach

Subsequently, two kind of state feedback controllers are designed namely a controller based on the Ackermann formula and the linear quadratic regulator (LQR). In general, both controllers work in the same manner and therefore generate the same dynamical behavior. The major difference is the tuning of the controllers. Due to this difference, the Ackermann controller or the LQR provide may provide an advantage for implementation depending on the different systems and used MOR concepts. At the end of this section both controllers are extended to accomplish stationary accuracy.

5.3.2.1. Ackermann State Feedback Controller

The control law of the Ackermann controller is given by

$$\boldsymbol{u}_{\mathrm{c},k} = K_{\mathrm{a}} \widetilde{\boldsymbol{x}}_{\mathrm{c},k}, \quad K_{\mathrm{a}} \in \mathbb{R}^{n_u \times 2N_{\mathrm{r}}} \tag{5.19}$$

where $\widetilde{\boldsymbol{x}}_{\mathrm{c},k} = \boldsymbol{x}_k^{*} - \widehat{\boldsymbol{x}}_k$ is the control error and K_{a} denotes the feedback gain. The desired reference trajectory of the states $\boldsymbol{x}_k^{*}$ is given by the flatness-based feedforward control relying on the system description (5.1) which is discretized for the implementation on a real time system, see (5.12). The associated control input of the feedforward control is $\boldsymbol{u}_k^{*}$, see Section 5.1. Hence, the input as well as the state trajectories fulfill as a result of their construction the time discrete system description (5.12). Therefore, the error dynamic is given by

$$\widetilde{\boldsymbol{x}}_{\mathrm{c},k} = A_{\mathrm{d}} \widetilde{\boldsymbol{x}}_{\mathrm{c},k-1} + B_{\mathrm{d}} \boldsymbol{u}_{\mathrm{c},k-1}. \tag{5.20}$$

The main idea of the feedback gain K_{a} is to place the eigenvalues of the control error dynamic matrix $A_{\mathrm{d,cl}}$ at desired location $\lambda_{\mathrm{d,cl},l} = \lambda_{\mathrm{d,cl},l}^{*}$, $l \in \mathbb{L}$, where the closed loop dynamics is given by

$$\widetilde{\boldsymbol{x}}_{\mathrm{c},k} = A_{\mathrm{d}} \widetilde{\boldsymbol{x}}_{\mathrm{c},k-1} + B_{\mathrm{d}} \boldsymbol{u}_{\mathrm{c},k-1} = \left(A_{\mathrm{d}} + B_{\mathrm{d}} K_{\mathrm{a}}\right) \widetilde{\boldsymbol{x}}_{\mathrm{c},k-1} = A_{\mathrm{d,cl}} \widetilde{\boldsymbol{x}}_{\mathrm{c},k-1}. \tag{5.21}$$

Taking the characteristic of the considered weakly damped structures into account the main objective for the feedback controller is to reduce emerging oscillations. This can be done by shifting the continuous eigenvalues λ_l of the original system A by a constant

$$\lambda_{\mathrm{cl},l}^{*} = \begin{cases} \lambda_l - \lambda_{\mathrm{sh}}^{+} & \forall\ l = 2i \\ \lambda_l - \lambda_{\mathrm{sh}}^{-} & \forall\ l = 2i+1 \end{cases}, \quad \text{with} \quad i = [1, \ldots, N_{\mathrm{r}}], \quad \lambda_{\mathrm{sh}}^{\pm} = \lambda_{\mathrm{sh,re}} \pm \mathrm{j}\lambda_{\mathrm{sh,im}}. \tag{5.22}$$

and transform the resulting eigenvalues into their time discrete representation

$$\lambda^*_{\mathrm{d,cl},l} = \exp(\lambda^*_{\mathrm{cl},l} t_\mathrm{d}) \quad \text{with} \quad l \in \mathbb{L} = [1, \ldots, 2N]. \tag{5.23}$$

The constant shifting, especially of the real part $\lambda_{\mathrm{sh,re}} > 0$, introduces an additional damping which affects mainly the significant eigenvalues characterized by a low magnitude, leading to the desired behavior. The feedback gain matrix can be determined using Ackermann's formula

$$K_\mathrm{a} = -\boldsymbol{w}^T \left(p_o I + p_1 A_\mathrm{d} + \ldots + p_{2N-1} A_\mathrm{d}^{2N-1} + A_\mathrm{d}^{2N}\right), \quad \boldsymbol{w}^T = \begin{bmatrix} 0 & 0 & \ldots & 1 \end{bmatrix} S^{-1}(A_\mathrm{d}, B_\mathrm{d}) \tag{5.24}$$

where p_i denote the coefficients of the characteristic polynomial of the desired eigenvalues and $S(A_\mathrm{d}, B_\mathrm{d}) = [B_\mathrm{d} \quad A_\mathrm{d} B_\mathrm{d} \quad A_\mathrm{d}^2 B_\mathrm{d} \quad \ldots \quad A_\mathrm{d}^{2N-1} B_\mathrm{d}]$ is the Kalman's controlability matrix. The actual determination of the feedback gain matrix uses the `place()` function of *MATLAB* which is based on the algorithms described by [60, 67] to improve the numerical robustness.

The control law of a state controller (5.19) applies the system states to calculate the necessary input signal. Most of the time the state information is not measured and has to be estimated by an observer like the presented Kalman filter. Considering the statement of the separation theorem, see, e.g., [73, chap. 8] the controller can be designed independent of the observer, as long the observer error $\widetilde{\boldsymbol{x}}_{\mathrm{o},k}$ declines fast enough.

5.3.2.2. Linear Quadratic Regulator

As an alternative approach the LQR is introduced to ensure that the desired trajectory $\boldsymbol{x}^*_k$ is reached. The associated control law is given by

$$\boldsymbol{u}_{\mathrm{c},k} = K_\mathrm{lq} \widetilde{\boldsymbol{x}}_{\mathrm{c},k}, \quad K_\mathrm{lq} \in \mathbb{R}^{n_u \times 2N_\mathrm{r}}. \tag{5.25}$$

Different to the eigenvalue placement in (5.19) the LQR approach minimizes a quadratic cost function [18] in terms of the the tracking error $\widetilde{\boldsymbol{x}}_{\mathrm{c},k} = \boldsymbol{x}^*_k - \widehat{\boldsymbol{x}}_k$ for an infinite horizon, i.e.,

$$J(\widetilde{\boldsymbol{x}}_{\mathrm{c},k}, \boldsymbol{u}_{\mathrm{c},k}) = \sum_{k=1}^{\infty} \left(\widetilde{\boldsymbol{x}}^T_{\mathrm{c},k} Q_\mathrm{c} \widetilde{\boldsymbol{x}}_{\mathrm{c},k} + \boldsymbol{u}^T_{\mathrm{c},k} R_\mathrm{c} \boldsymbol{u}_{\mathrm{c},k} \right). \tag{5.26}$$

The positive definite matrix R_c and positive semi-definite matrix Q_c can be interpreted as weighting matrices for the input as well as for the error state. The cost function has to be minimized subject to the system (5.1).

The solution of this optimization problem leads to a time dependent feedback gain matrix. Analog to the optimal observer, the feedback gain of the LQR for $k \to \infty$ simplifies to

$$K_\mathrm{lq} = (B_\mathrm{d}^T S B_\mathrm{d} + R_\mathrm{c})^{-1} B_\mathrm{d} S A_\mathrm{d} \tag{5.27}$$

where $S = \lim_{k \to \infty} S_k$ is given by the solution of the algebraic Riccati equation.

Similar to the observer design the second order representation allows the differentiation between position and velocity associated states. Furthermore, the characteristics of the different systems and used MOR methods can be exploited for the choice of the weighting matrices R_c and Q_c. The weighting structure of the control inputs can be used uniformly in terms of

$$R_\mathrm{c} = r_\mathrm{c} I \in \mathbb{R}^{n_u \times n_u}. \tag{5.28}$$

Similar to the observer design the weighting of the state errors depends on the used MOR method and is chosen as follows:

- In case of the full order system of the beam structures or a reduced order system considering modal truncation the partitioning of covariance matrix is done per beam as before and marked by the index $j = \{1, \ldots, r\}$

$$\begin{aligned} Q_\mathrm{c} &= q_{\mathrm{c},t} \mathrm{diag}\{\boldsymbol{q}_{\mathrm{c,p},1},\ \boldsymbol{q}_{\mathrm{c,v},1},\ \ldots,\ \boldsymbol{q}_{\mathrm{c,p},r},\ \boldsymbol{q}_{\mathrm{c,v},r}\}, \\ \boldsymbol{q}^T_{\mathrm{c,p|v},j} &= q_{\mathrm{c,p|v}} \left[q^\mathrm{s}_{\mathrm{c,p|v},j} \quad q^\mathrm{s}_{\mathrm{c,p|v},j} + 2\frac{q^\mathrm{e}_{\mathrm{c,p|v},j} - q^\mathrm{s}_{\mathrm{c,p|v},j}}{N_j - 1} \quad q^\mathrm{s}_{\mathrm{c,p|v},j} + 3\frac{q^\mathrm{e}_{\mathrm{c,p|v},j} - q^\mathrm{s}_{\mathrm{c,p|v},j}}{N_j - 1} \quad \ldots \quad q^\mathrm{e}_{\mathrm{c,p|v},j} \right] \in \mathbb{R}^{N_j} \end{aligned} \tag{5.29a}$$

  with $q_{\mathrm{c},t}$ as unified weight, $\boldsymbol{q}_{\mathrm{c,p|v},j}$ as an additional weighting of the position and velocity states. The elements of $\boldsymbol{q}_{\mathrm{c,p|v},j}$ are determined by the linear interpolation between the start and end values $q^\mathrm{s}_{\mathrm{c,p|v},j}$, $q^\mathrm{e}_{\mathrm{c,p|v},j}$, respectively. Similar to the observer design the lower modes are more important considering the stored energy which means a higher impact so $q^\mathrm{s}_{\mathrm{c,p|v},j} > q^\mathrm{e}_{\mathrm{c,p|v},j}$ is chosen.

- If second order balanced truncation is used to determine the reduced order model the Hankel singular values $\zeta_{\mathrm{p|v},k}$, $k \in \mathbb{K} = [1, \ldots, N_\mathrm{r}]$ can be used. They depict, similar to the observer design, a kind of natural weighting reducing the complexity of possible combinations of the elements of Q_c as follows

$$Q_\mathrm{c} = q_{\mathrm{c},t}\mathrm{diag}\{\boldsymbol{q}_{\mathrm{c,p}},\ \boldsymbol{q}_{\mathrm{c,v}}\}, \quad \boldsymbol{q}_{\mathrm{c,p|v}}^T = q_{\mathrm{c,p|v}} \begin{bmatrix} \zeta_{\mathrm{p|v},1} & \cdots & \zeta_{\mathrm{p|v},N_\mathrm{r}} \end{bmatrix}. \tag{5.29b}$$

  For the LQR approach the weighting of the position and velocity states are given by the fractions

$$q_{\mathrm{c,p}} = \frac{q_{\mathrm{c,p,a}}}{\sum_{k=1}^{N_\mathrm{r}} \zeta_{\mathrm{p},k}} \quad \text{and} \quad q_{\mathrm{c,v}} = \frac{q_{\mathrm{c,v,a}}}{\sum_{k=1}^{N_\mathrm{r}} \zeta_{\mathrm{v},k}}$$

  considering an additional weighting of the position and velocity $q_{\mathrm{c,p|v,a}}$.

- The POD method offers the simplest separation of position and velocity of the reduced order system. The first set of the reduced system states from 1 to N_r is related to the position or displacement and the second part from $N_\mathrm{r}+1$ to $2N_\mathrm{r}$ are associated with the the velocity. Similar to the observer design, the structure of weighting is chosen as

$$\begin{aligned} Q_\mathrm{c} &= q_{\mathrm{c},t}\mathrm{diag}\{\boldsymbol{q}_{\mathrm{c,p}},\ \boldsymbol{q}_{\mathrm{c,v}}\}, \\ \boldsymbol{q}_{\mathrm{c,p|v},j}^T &= q_{\mathrm{c,p|v}} \begin{bmatrix} q_{\mathrm{c,p|v},j}^\mathrm{s} & q_{\mathrm{c,p|v},j}^\mathrm{s} + 2\frac{q_{\mathrm{c,p|v},j}^\mathrm{e} - q_{\mathrm{c,p|v},j}^\mathrm{s}}{N_j - 1} & q_{\mathrm{c,p|v},j}^\mathrm{s} + 3\frac{q_{\mathrm{c,p|v},j}^\mathrm{e} - q_{\mathrm{c,p|v},j}^\mathrm{s}}{N_j - 1} & \cdots & q_{\mathrm{c,p|v},j}^\mathrm{e} \end{bmatrix} \in \mathbb{R}^{N_j} \end{aligned} \tag{5.29c}$$

  As before the elements of $\boldsymbol{q}_{\mathrm{c,p|v}}$ are formed by the linear interpolation between the start and end values $q_{\mathrm{c,p|v}}^\mathrm{s}$, $q_{\mathrm{c,p|v}}^\mathrm{e}$, respectively.

The numeric values of the design parameters are determined by hardware-in-the-loops tests and are presented in Chapter 6.

5.3.2.3. Extended State Feedback Control Approaches

The dynamic behavior of the state feedback approaches satisfies the requirements, i.e., the oscillation caused by the model uncertainties are quickly attenuated, but a small static error remains, mainly induced by the remaining hysteresis and creeping behavior of the actuators, which is not completely compensated as discussed in Section 2.1.1.3. Hence, the state feedback approaches are extended by PI-controllers

$$\boldsymbol{u}_{\mathrm{c,a},k} = K_\mathrm{a}\widetilde{\boldsymbol{x}}_{\mathrm{c},k} + k_\mathrm{a} \int H_{\mathrm{d,pi}}\widetilde{\boldsymbol{z}}_{\mathrm{c},k}\,\mathrm{d}t \tag{5.30}$$

$$\boldsymbol{u}_{\mathrm{c,lq},k} = K_\mathrm{lq}\widetilde{\boldsymbol{x}}_{\mathrm{c},k} + k_\mathrm{lq} \int H_{\mathrm{d,pi}}\widetilde{\boldsymbol{z}}_{\mathrm{c},k}\,\mathrm{d}t \tag{5.31}$$

with k_lq, k_a the gain of the integrated displacement error at the points of interest. Here, the previously discussed state feedback controllers provide the favored fast decaying error dynamics, where the second part of the control law leads to the required stationary accuracy. The tuning of both parts can be done independently from each other and is determined during hardware-in-the-loops tests. The chosen numeric values of the gains as well as the design parameters are presented in Chapter 6, where the control laws (5.30) and (5.31) will be referred to as extended Ackermann and extended LQ controller, respectively.

5.3.3. Lyapunov-Based Control Approach

This controller design is motivated by the results of [98]. The main idea of this approach is to passivate the tracking error dynamics by introducing artificial damping. This can be achieved by a Lyapunov-based control approach which belongs to the late lumping approaches relying on the infinite dimensional equations of motion. Below, this control approach is developed for the vertical beam configuration.

The main objective is to reduce the continuous displacement profile error $\tilde{s}_j(t,z) = s_j^*(t,z) - s_j(z,t)$ using the control signals of all actuators $U_{j,\mathrm{a}_k}^\mathrm{c} = U_{j,\mathrm{a}_k} - U_{j,\mathrm{a}_k}^*$ taking $j \in \{1, \ldots, r\}$ beams equipped with p_j MFC-actuators into account. The continuous control signal can be discretized afterwards considering the zero-order-hold method and therefore be implemented in the real time framework. Here, $s_j^*(t,z)$ denotes the desired trajectory of the displacement profile and U_{j,a_k}^* is the associated control input generated by the flatness-based feedforward controls relying on the infinite dimensional equations of motion (2.55), see Appendix B.3 or the finite dimensional description considering Galerkin's approximation, see Section 5.1. Hence, $s_j^*(t,z)$ fulfills (2.55) as a result of its construction, where in the finite dimensional approach a small approximation error appears.

The distributed parameter system description of the error dynamics is given by

$$0 = \mu_j(z)\partial_t^2\tilde{s}_j + \gamma_j^{\mathrm{v}}(z)\partial_t\tilde{s}_j - \partial_z\left[\gamma_j^{\mathrm{sv}}(z)\partial_t\partial_z\tilde{s}_j\right] + \partial_z^2\left[\Lambda_j(z)\partial_z^2\tilde{s}_j + \gamma_j^{\mathrm{kv}}(z)\partial_t\partial_z^2\tilde{s}_j\right] + \sum_{k=1}^{p_j}\partial_z^2\Gamma_{j,\mathrm{a}_k}(z)U^{\mathrm{c}}_{j,\mathrm{a}_k}, \quad (5.32a)$$

for $z \in (0,\ell)$ and $t > 0$ considering the equations of motion (2.55). At the boundaries the displacement error fulfills

$$\tilde{s}_j = 0, \quad \partial_z\tilde{s}_j = 0, \quad (5.32b)$$

for $z = 0,\ t > 0$ and

$$\begin{aligned} m_j\partial_t^2\tilde{s}_j + \kappa_j(\tilde{\boldsymbol{s}}) &= \partial_z\left[\Lambda_j(z)\partial_z^2\tilde{s}_j + \gamma_j^{\mathrm{kv}}(z)\partial_t\partial_z^2\tilde{s}_j\right] - \gamma_j^{\mathrm{sv}}(z)\partial_t\partial_z\tilde{s}_j \\ J_j\partial_t^2\partial_z\tilde{s}_j &= -\Lambda_j(z)\partial_z^2\tilde{s}_j - \gamma_j^{\mathrm{kv}}(z)\partial_t\partial_z^2\tilde{s}_j \end{aligned} \quad (5.32c)$$

at the free but coupled end $z = \ell$. The initial error at $t = 0$ is assumed as

$$\tilde{s}_j = \tilde{s}_{j,0}, \quad \partial_t\tilde{s}_j = \tilde{s}_{j,1}. \quad (5.32d)$$

As a first attempt for the Lyapunov functional the total energy of the error system is chosen. Therefore, the state space $\tilde{X}^e = \left((H_0^2(0,\ell))^r \times (L^2(0,\ell))^r \times \mathbb{R}^r \times \mathbb{R}^r \times \mathbb{R}^{r-1}\right)$ with the Hilbert space $H_0^2(0,\ell) = \{f \in H^2(0,\ell) : f(0) = \partial_z f(0) = 0\}$ and the inner product

$$\begin{aligned} \langle\boldsymbol{\phi},\boldsymbol{\psi}\rangle_{\tilde{X}^e} = \sum_{j=1}^{r}\Bigg(\int_0^{\ell}\Lambda_j(z)\partial_z^2\phi_{1,j}\overline{\partial_z^2\psi_{1,j}} + \mu_j(z)\phi_{2,j}\overline{\psi_{2,j}}\,\mathrm{d}z \\ + \frac{m_j}{2}\phi_{3,j}\overline{\psi_{3,j}} + \frac{J_j}{2}\phi_{4,j}\overline{\psi_{4,j}}\Bigg) + \sum_{j=1}^{r-1}\frac{k_{j,j+1}}{2}\phi_{5,j}\overline{\psi_{5,j}} \end{aligned} \quad (5.33)$$

is introduced. The associated norm is defined by $||\boldsymbol{\phi}||^2 = \langle\boldsymbol{\phi},\boldsymbol{\phi}\rangle_X \ \forall\ \boldsymbol{\phi} = [\boldsymbol{\phi}_1^T \quad \boldsymbol{\phi}_2^T \quad \boldsymbol{\phi}_3^T \quad \boldsymbol{\phi}_4^T \quad \boldsymbol{\phi}_5^T]^T$, $\boldsymbol{\psi} = [\boldsymbol{\psi}_1^T \quad \boldsymbol{\psi}_2^T \quad \boldsymbol{\psi}_3^T \quad \boldsymbol{\psi}_4^T \quad \boldsymbol{\psi}_5^T]^T \in X$. The state vector is given by $\tilde{\boldsymbol{x}}^e = [\tilde{\boldsymbol{x}}_1^e \quad \tilde{\boldsymbol{x}}_2^e \quad \tilde{\boldsymbol{x}}_3^e \quad \tilde{\boldsymbol{x}}_4^e \quad \tilde{\boldsymbol{x}}_5^e]^T$ with

$$\begin{aligned} \tilde{\boldsymbol{x}}_1^e(t) &= \left[\tilde{s}_1(\cdot\,,t) \quad \dots \quad \tilde{s}_r(\cdot\,,t)\right]^T, \quad \tilde{\boldsymbol{x}}_2^e(t) = \left[\partial_t\tilde{s}_1(\cdot\,,t) \quad \dots \quad \partial_t\tilde{s}_r(\cdot\,,t)\right]^T, \\ \tilde{\boldsymbol{x}}_3^e(t) &= \left[\partial_t\tilde{s}_1(\ell,t) \quad \dots \quad \partial_t\tilde{s}_r(\ell,t)\right]^T, \quad \tilde{\boldsymbol{x}}_4^e(t) = \left[\partial_t\partial_z\tilde{s}_1(\ell,t) \quad \dots \quad \partial_t\partial_z\tilde{s}_r(\ell,t)\right]^T, \\ \tilde{\boldsymbol{x}}_5^e(t) &= \left[\tilde{s}_1(\ell,t) - \tilde{s}_2(\ell,t) \quad \dots \quad \tilde{s}_{r-1}(\ell,t) - \tilde{s}_r(\ell,t)\right]^T. \end{aligned} \quad (5.34)$$

The total energy is given by

$$\begin{aligned} V = \langle\tilde{\boldsymbol{x}}^e(t),\tilde{\boldsymbol{x}}^e(t)\rangle_{\tilde{X}^e} = \frac{1}{2}\sum_{j=1}^{r}\Bigg(\int_0^{\ell}\Lambda_j(z)\left(\partial_z^2\tilde{s}_j\right)^2 + \mu_j(z)\left(\partial_t\tilde{s}_j\right)^2\mathrm{d}z + \frac{m_j}{2}\left(\partial_t\tilde{s}_j(\ell,t)\right)^2 \\ + \frac{J_j}{2}\left(\partial_t\partial_z\tilde{s}_j(\ell,t)\right)^2\Bigg) + \sum_{j=1}^{r-1}\frac{k_{j,j+1}}{2}\left(\tilde{s}_j(\ell,t) - \tilde{s}_{j+1}(\ell,t)\right)^2. \end{aligned} \quad (5.35)$$

For any $\tilde{\boldsymbol{x}}^e(t) \in \tilde{X}^e$ the functional is positive definite, i.e., $V > 0$ and is hence a valid Lyapunov functional candidate.

The rate of change of V along a solution trajectory of (5.32) yields

$$\begin{aligned} \dot{V} = \sum_{j=1}^{r}\Bigg(\int_0^{\ell}\Lambda_j(z)\partial_z^2\tilde{s}_j\partial_t\partial_z^2\tilde{s}_j + \mu_j(z)\partial_t\tilde{s}_j\partial_t^2\tilde{s}_j\,\mathrm{d}z + \frac{m_j}{2}\partial_t\tilde{s}_j(\ell,t)\partial_t^2\tilde{s}_j(\ell,t) \\ + \frac{J_j}{2}\partial_t\partial_z\tilde{s}_j(\ell,t)\partial_t^2\partial_z\tilde{s}_j(\ell,t)\Bigg) + \sum_{j=1}^{r-1}\frac{k_{j,j+1}}{2}\left(\partial_t\tilde{s}_j(\ell,t) - \partial_t\tilde{s}_{j+1}(\ell,t)\right)\left(\tilde{s}_j(\ell,t) - \tilde{s}_{j+1}(\ell,t)\right). \end{aligned} \quad (5.36)$$

Solving (5.32a) for $\mu_j(z)\partial_t^2\tilde{s}_j$, i.e.,

$$\mu_j(z)\partial_t^2\tilde{s}_j = -\gamma_j^{\mathrm{v}}(z)\partial_t\tilde{s}_j + \partial_z\left[\gamma_j^{\mathrm{sv}}(z)\partial_t\partial_z\tilde{s}_j\right] - \partial_z^2\left[\Lambda_j(z)\partial_z^2\tilde{s}_j + \gamma_j^{\mathrm{kv}}(z)\partial_t\partial_z^2\tilde{s}_j\right] - \sum_{k=1}^{p_j}\partial_z^2\Gamma_{j,\mathrm{a}_k}(z)U_{j,\mathrm{a}_k}^{\mathrm{c}}. \tag{5.37}$$

and substitution into (5.36) provides

$$\begin{aligned}\dot{V} = \sum_{j=1}^{r}\Bigg(\int_0^{\ell}&\Lambda_j(z)\partial_z^2\tilde{s}_j\partial_t\partial_z^2\tilde{s}_j - \gamma_j^{\mathrm{v}}(z)\partial_t\tilde{s}_j\partial_t\tilde{s}_j + \partial_z\left[\gamma_j^{\mathrm{sv}}(z)\partial_t\partial_z\tilde{s}_j\right]\partial_t\tilde{s}_j\\ &- \partial_z^2\left[\Lambda_j(z)\partial_z^2\tilde{s}_j + \gamma_j^{\mathrm{kv}}(z)\partial_t\partial_z^2\tilde{s}_j\right]\partial_t\tilde{s}_j - \sum_{k=1}^{p_j}\partial_z^2\Gamma_{j,\mathrm{a}_k}(z)U_{j,\mathrm{a}_k}^{\mathrm{c}}\partial_t\tilde{s}_j\,\mathrm{d}z\\ &+ \frac{m_j}{2}\partial_t\tilde{s}_j(\ell,t)\partial_t^2\tilde{s}_j(\ell,t) + \frac{J_j}{2}\partial_t\partial_z\tilde{s}_j(\ell,t)\partial_t^2\partial_z\tilde{s}_j(\ell,t)\Bigg)\\ &+\sum_{j=1}^{r-1}\frac{k_{j,j+1}}{2}\big(\partial_t\tilde{s}_j(\ell,t) - \partial_t\tilde{s}_{j+1}(\ell,t)\big)\big(\tilde{s}_j(\ell,t) - \tilde{s}_{j+1}(\ell,t)\big).\end{aligned} \tag{5.38}$$

Applying partial integration leads to

$$\begin{aligned}\dot{V} = \sum_{j=1}^{r}\Bigg(\int_0^{\ell}&-\gamma_j^{\mathrm{v}}(z)\big(\partial_t\tilde{s}_j\big)^2 - \gamma_j^{\mathrm{sv}}(z)\big(\partial_t\partial_z\tilde{s}_j\big)^2\\ &- \gamma_j^{\mathrm{kv}}(z)\big(\partial_t\partial_z^2\tilde{s}_j\big)^2 + \sum_{k=1}^{p_j}\partial_z\Gamma_{j,\mathrm{a}_k}(z)U_{j,\mathrm{a}_k}^{\mathrm{c}}\partial_t\partial_z\tilde{s}_j\,\mathrm{d}z\\ &+\Big[\partial_z^2\left[\Lambda_j(z)\partial_z^2\tilde{s}_j + \gamma_j^{\mathrm{kv}}(z)\partial_t\partial_z^2\tilde{s}_j\right]\partial_t\partial_z\tilde{s}_j - \partial_z\left[\Lambda_j(z)\partial_z^2\tilde{s}_j + \gamma_j^{\mathrm{kv}}(z)\partial_t\partial_z^2\tilde{s}_j\right]\partial_t\tilde{s}_j\\ &+\gamma_j^{\mathrm{sv}}(z)\partial_t\partial_z\tilde{s}_j\partial_t\tilde{s}_j - \sum_{k=1}^{p_j}\partial_z\Gamma_{j,\mathrm{a}_k}(z)U_{j,\mathrm{a}_k}^{\mathrm{c}}\partial_t\tilde{s}_j\Big]_0^{\ell}\\ &+\frac{m_j}{2}\partial_t\tilde{s}_j(\ell,t)\partial_t^2\tilde{s}_j(\ell,t) + \frac{J_j}{2}\partial_t\partial_z\tilde{s}_j(\ell,t)\partial_t^2\partial_z\tilde{s}_j(\ell,t)\Bigg)\\ &+\sum_{j=1}^{r-1}\frac{k_{j,j+1}}{2}\big(\partial_t\tilde{s}_j(\ell,t) - \partial_t\tilde{s}_{j+1}(\ell,t)\big)\big(\tilde{s}_j(\ell,t) - \tilde{s}_{j+1}(\ell,t)\big).\end{aligned} \tag{5.39}$$

Considering (2.54) the coupling terms can be reformulated as follows

$$\begin{aligned}\sum_{j=1}^{r}\mathcal{K}_j(\tilde{\boldsymbol{s}})\partial_t\tilde{s}_j(\ell,t) &= k_{1,2}\big(\tilde{s}_1 - \tilde{s}_2\big)\partial_t\tilde{s}_1(\ell,t) + k_{2,3}\big(\tilde{s}_2 - \tilde{s}_3\big)\partial_t\tilde{s}_2(\ell,t) - k_{1,2}\big(\tilde{s}_1 - \tilde{s}_2\big)\partial_t\tilde{s}_2(\ell,t)\\ &\quad + \ldots + k_{r-1,r}\big(\tilde{s}_{r-1} - \tilde{s}_r\big)\partial_t\tilde{s}_{r-1}(\ell,t) - k_{r-2,r-1}\big(\tilde{s}_{r-2} - \tilde{s}_{r-1}\big)\partial_t\tilde{s}_{r-1}(\ell,t)\\ &\quad - k_{r-1,r}\big(\tilde{s}_{r-1} - \tilde{s}_r\big)\tilde{s}_r(\ell,t)\\ &= \sum_{j=1}^{r-1}\frac{k_{j,j+1}}{2}\big(\partial_t\tilde{s}_j(\ell,t) - \partial_t\tilde{s}_{j+1}(\ell,t)\big)\big(\tilde{s}_j(\ell,t) - \tilde{s}_{j+1}(\ell,t)\big).\end{aligned} \tag{5.40}$$

As a result (5.39) can be simplified taking the boundary condition (5.32b) and (5.32c) into account

$$\begin{aligned}\dot{V} = \sum_{j=1}^{r}\int_0^{\ell}&-\gamma_j^{\mathrm{v}}(z)\big(\partial_t\tilde{s}_j\big)^2 - \gamma_j^{\mathrm{sv}}(z)\big(\partial_t\partial_z\tilde{s}_j\big)^2 - \gamma_j^{\mathrm{kv}}(z)\big(\partial_t\partial_z^2\tilde{s}_j\big)^2\\ &+\sum_{k=1}^{p_j}\partial_z\Gamma_{j,\mathrm{a}_k}(z)U_{j,\mathrm{a}_k}^{\mathrm{c}}\partial_t\partial_z\tilde{s}_j\,\mathrm{d}z - \sum_{k=1}^{p_j}\partial_z\Gamma_{j,\mathrm{a}_k}(\ell)U_{j,\mathrm{a}_k}^{\mathrm{c}}\partial_t\tilde{s}_j,\end{aligned} \tag{5.41}$$

where the last sum always vanishes unless one MFC-actuator pair is placed at the beam's tip. Due to the fact, that $\gamma_j^{\mathrm{v}}(z), \gamma_j^{\mathrm{kv}}(z), \gamma_j^{\mathrm{sv}}(z) \geq 0$ the following upper bound is introduced

$$\dot{V} \leq \sum_{j=1}^{r} \int_0^{\ell} \sum_{k=1}^{p_j} \partial_z \Gamma_{j,\mathrm{a}_k}(z) U_{j,\mathrm{a}_k}^{\mathrm{c}} \partial_t \partial_z \tilde{s}_j \, \mathrm{d}z. \tag{5.42}$$

To obtain $\dot{V} \leq 0$ it has to be ensured that

$$\sum_{j=1}^{r} \int_0^{\ell} \sum_{k=1}^{p_j} \partial_z \Gamma_{j,\mathrm{a}_k}(z) U_{j,\mathrm{a}_k}^{\mathrm{c}} \partial_t \partial_z \tilde{s}_j \, \mathrm{d}z \leq 0 \tag{5.43}$$

holds true. This can be achieved by the choice

$$\begin{aligned} U_{j,\mathrm{a}_k}^{\mathrm{c}} &= -k_{j,\mathrm{a}_k}^{\mathrm{ly}} \int_0^{\ell} \partial_z \Gamma_{j,\mathrm{a}_k}(z) \partial_t \partial_z \tilde{s}_j \, \mathrm{d}z \\ &= -k_{j,\mathrm{a}_k}^{\mathrm{ly}} \frac{A_{j,\mathrm{a}_k} a_{j,\mathrm{a}_k,1}^{11} (\hbar_j + \hbar_{j,\mathrm{a}_k})}{2\beta_{j,\mathrm{a}_k,11} e_s} \big(\partial_t \partial_z \tilde{s}_j(z_{j,\mathrm{a}_k} + \ell_{j,\mathrm{a}_k}) - \partial_t \partial_z \tilde{s}_j(z_{j,\mathrm{a}_k}) \big) \end{aligned} \tag{5.44}$$

with the second line following form the determination of the the notch function $\Omega_{j,\mathrm{a}_k}(z)$ (2.14) in terms of the Heaviside function. As a result the control law ensures that V is a Lyapunov functional as long as $k_{j,\mathrm{a}_k}^{\mathrm{ly}} > 0$ which means that the error dynamic is asymptotically stable. Alternative the stabilization of the tracking error can be shown by use of semigroup and contraction theory, see [98].

Analog to the extended state feedback control approaches, see Section 5.3.2.3, the Lyapunov-based control approach is also extended by a PI-controller. This variation of the control law will be referred to as extended Lyapunov-based controller.

The numeric value of of the gain $k_{j,\mathrm{a}_k}^{\mathrm{ly}}$ is determined during hardware-in-the-loops test and is presented in Section 6.1.

5.4. Model Predictive Control

As an alternative control approach to the previously discussed two-degrees-of-freedom control approach the so-called model predictive control (MPC) approach is introduced. This approach unites the feedforward and the tracking control. The main idea of the concept is based on a prediction of the system's trajectories within a specific temporal horizon. The control input is determined taking a minimization of a cost functional into account, which consists of the predicted control error and the control input within the prediction horizon. The first time step of the resulting predicted input which minimizes the cost functional yields the actual control input. This procedure is applied in each time step.

The MPC concept allows to consider constraints imposed on the system, so the motion planning process as well as the design of a feedforward control can be omitted. Therefore, this approach provides a high level of usability. A rest-to-rest motion can be achieved by a simple reference trajectory in form of a step function.

In the following subsections, this control approach is developed for the vertical beam configuration based on [94, 95]. At first the basic concept is discussed considering an unconstrained problem formulation. Afterwards, the constraint case is introduced also addressing the real time capability of the concept by the applied Hildreth's quadratic programming procedure. In the end, the computational cost is discussed and further reduced considering the concept of move blocking by downsampling.

5.4.1. Basic Concept

The previously discussed two-degrees-of-freedom control approach the MPC concept also relies on the time-discrete state space formulation

$$\begin{aligned} \boldsymbol{x}_k &= A_{\mathrm{d}} \boldsymbol{x}_{k-1} + B_{\mathrm{d}} \boldsymbol{u}_{k-1}, \quad k > 1, \quad \boldsymbol{x}_0 = \boldsymbol{x}_{\mathrm{r}}(0), \\ \boldsymbol{y}_{\mathrm{pi},k} &= H_{\Delta,\mathrm{pi}} \boldsymbol{x}_k, \quad \boldsymbol{y}_{\mathrm{pm},k} = H_{\Delta,\mathrm{pm}} \boldsymbol{x}_k, \end{aligned} \tag{5.45}$$

with $\boldsymbol{x}_k = \boldsymbol{x}_{\mathrm{r}}(kt_{\mathrm{d}})$, $\boldsymbol{u}_k = \boldsymbol{u}(kt_{\mathrm{d}})$ and $\boldsymbol{y}_{\mathrm{pi|pm},k} = \boldsymbol{y}_{\mathrm{pi|pm}}(kt_{\mathrm{d}})$, where t_{d} denotes the sample time.

Below the system description is extended to introduce a new input vector in terms of the slew rate of the voltage signal $\Delta \boldsymbol{u}_k = \boldsymbol{u}_k - \boldsymbol{u}_{k-1}$. This reformulation based on the difference $\Delta \boldsymbol{x}_k = \boldsymbol{x}_k - \boldsymbol{x}_{k-1}$ provides the opportunity to consider constraints of the MFC-actuators' voltage slew rates in the control design. Furthermore, the extension of the state vector by the output vector $\boldsymbol{x}_{\mathrm{e},k} = [\Delta \boldsymbol{x}_k^T \quad \boldsymbol{y}_{\mathrm{pi},k}^T]^T$ implies an integral action in the feedback loop which leads to stationary accuracy taking constant disturbances into account, see [114]. Hence, the augmented system is given by

$$\begin{aligned} \boldsymbol{x}_{\mathrm{e},k} &= A_{\mathrm{e}} \boldsymbol{x}_{\mathrm{e},k-1} + B_{\mathrm{r}} \Delta \boldsymbol{u}_{k-1}, \quad k > 1,\ \boldsymbol{x}_{\mathrm{e},0} = \boldsymbol{x}_{\mathrm{e}}(0) \\ \boldsymbol{y}_k &= H_{\mathrm{e}} \boldsymbol{x}_{\mathrm{e},k}, \end{aligned} \tag{5.46}$$

where it is assumed that the system is stationary at $k = 0$ leading to $\boldsymbol{x}_{\mathrm{e},0} = [\boldsymbol{0}^T \quad \boldsymbol{y}_0^T]^T$. The associated augmented system matrices are given by

$$A_{\mathrm{e}} = \begin{bmatrix} A_{\mathrm{d}} & 0 \\ H_{\Delta,\mathrm{pi}} A_{\mathrm{d}} & I \end{bmatrix}, \quad B_{\mathrm{e}} = \begin{bmatrix} B_{\mathrm{d}} \\ H_{\Delta,\mathrm{pi}} B_{\mathrm{d}} \end{bmatrix}, \quad H_{\mathrm{e}} = \begin{bmatrix} 0 & I \end{bmatrix}, \tag{5.47}$$

where I is the identity matrix.

As mentioned above the MPC approach in predicts each time step the outputs and associated the inputs over the so-called prediction horizon h. The predicted outputs are given by

$$Y_k = \begin{bmatrix} \boldsymbol{y}_{k+1|k}^T & \boldsymbol{y}_{k+2|k}^T & \cdots & \boldsymbol{y}_{k+h|k}^T \end{bmatrix}^T \tag{5.48}$$

with

$$\boldsymbol{y}_{k+i|k} = H_{\mathrm{e}} A_{\mathrm{e}}^i \boldsymbol{x}_{\mathrm{e},k-1} + \sum_{m=0}^{i-1} H_{\mathrm{e}} A_{\mathrm{e}}^{i-m-1} B_{\mathrm{e}} \Delta \boldsymbol{u}_{k+m} \tag{5.49}$$

and $i \in \{1, \ldots, h\}$. Reformulating the predicted output considering the notation of [20] yields

$$Y_k = \mathcal{F} \boldsymbol{x}_{\mathrm{e},k} + \Phi \Delta \boldsymbol{U}, \tag{5.50}$$

where

$$\Delta \boldsymbol{U} = \begin{bmatrix} \Delta \boldsymbol{u}_k^T & \Delta \boldsymbol{u}_{k+1}^T & \cdots & \Delta \boldsymbol{u}_{k+h-1}^T \end{bmatrix}^T \tag{5.51}$$

denotes the associated input trajectory determined at time step k considering the prediction horizon h. In addition, the matrices $\mathcal{F}$ and Φ are given by

$$\mathcal{F} = \begin{bmatrix} H_{\mathrm{e}} A_{\mathrm{e}}^1 \\ H_{\mathrm{e}} A_{\mathrm{e}}^2 \\ \vdots \\ H_{\mathrm{e}} A_{\mathrm{e}}^h \end{bmatrix}, \quad \Phi = \begin{bmatrix} H_{\mathrm{e}} B_{\mathrm{e}} & 0 & \cdots & 0 \\ H_{\mathrm{e}} A_{\mathrm{e}}^1 B_{\mathrm{e}} & H_{\mathrm{e}} B_{\mathrm{e}} & \cdots & 0 \\ \vdots & \vdots & \ddots & \vdots \\ H_{\mathrm{e}} A_{\mathrm{e}}^{h-1} B_{\mathrm{e}} & H_{\mathrm{e}} A_{\mathrm{e}}^{h-2} B_{\mathrm{e}} & \cdots & H_{\mathrm{e}} B_{\mathrm{e}} \end{bmatrix}. \tag{5.52}$$

The calculation of the predicted trajectory in (5.50) requires information of the complete state vector $\boldsymbol{x}_{\mathrm{e},k}$ at each time step k. Since the state vector $\boldsymbol{x}_{\mathrm{e},k}$ is not measurable a Kalman filter, as introduced in Section 5.2, is used which provides the observed state vector $\widehat{\boldsymbol{x}}_{\mathrm{e},k}$.

The objective of the control approach is the adjustment of the predicted trajectory Y_k to remain as close as possible to the desired reference trajectory Y_k^* within the prediction horizon. Considering the reference signal

$$Y_k^* = \begin{bmatrix} {\boldsymbol{y}_{k+1}^*}^T & {\boldsymbol{y}_{k+2}^*}^T & \cdots & {\boldsymbol{y}_{k+h}^*}^T \end{bmatrix}^T, \tag{5.53}$$

where in case of the vertical beam configuration $\boldsymbol{y}_{k+1}^*$ denotes the displacement at the points of interest.

The optimal input trajectory $\Delta \boldsymbol{U}$ follows by minimizing the error defined by the difference of the reference signal Y_k^* and the predicted output signal Y_k. Furthermore, the control effort is included in the optimization process by considering the cost functional

$$J = (Y_k^* - Y_k)^T Q_{\mathrm{c}} (Y_k^* - Y_k) + \Delta \boldsymbol{U}^T R_{\mathrm{c}} \Delta \boldsymbol{U}, \tag{5.54}$$

where $Q_{\mathrm{c}} \in \mathbb{R}^{n_{\mathrm{pi}} \times n_{\mathrm{pi}}}$ and $R_{\mathrm{c}} \in \mathbb{R}^{n_u \times n_u}$ are the symmetric and positive definite output and input weighting matrices, respectively. Here, n_{pi} and n_u denote the number of points of interest as well as the number of system inputs. Compared to the LQR approach (5.26) this formulation shows some similarities.

The evaluation of the cost function considering the predicted output trajectory (5.50) results in

$$J = \left(Y_k^* - \mathcal{F}\widehat{\boldsymbol{x}}_{\mathrm{e},k}\right)^T Q_\mathrm{c} \left(Y_k^* - \mathcal{F}\widehat{\boldsymbol{x}}_{\mathrm{e},k}\right) - 2\Delta\boldsymbol{U}^T\Phi^T Q_\mathrm{c}\left(Y_k^* - \mathcal{F}\widehat{\boldsymbol{x}}_{\mathrm{e},k}\right) + \Delta\boldsymbol{U}^T\left(\Phi^T Q_\mathrm{c}\Phi + R_\mathrm{c}\right)\Delta\boldsymbol{U}. \tag{5.55}$$

Taking this formulation into account the decision variable $\Delta\boldsymbol{U}$ occurs only in a quadratic and a linear term. These are the terms which affect the solution of the optimization process. Therefore all other terms can be neglected leading to a condensed formulation of the cost functional

$$J^* = \frac{1}{2}\Delta\boldsymbol{U}^T\mathcal{H}_J\Delta\boldsymbol{U} + \Delta\boldsymbol{U}^T\boldsymbol{f}_J, \quad \text{with} \quad \mathcal{H}_J = (\Phi^T Q_\mathrm{c}\Phi + R_\mathrm{c}), \quad \boldsymbol{f}_J = -\Phi^T Q_\mathrm{c}(Y_k^* - \mathcal{F}\widehat{\boldsymbol{x}}_{\mathrm{e},k}). \tag{5.56}$$

The minimization of the cost functional leads to the control input trajectory considering the prediction horizon h, where only the first predicted step is implemented.

5.4.2. Constrained Model Predictive Control

Each physical actuator is characterized by outputs constraints, i.e., saturations of the generated forces or the associated slew rates. Some of these constraints are based on physical limitations others are introduced by safety concepts which protect the system, the user or the environment against damage. Taking the vertical beam configuration into account constraints imposed by the MFC-actuators are defined by the limited symmetric voltage range ($\pm 1000\,\mathrm{V}$) and by a safety algorithm which limits the associated slew rates $\Delta\boldsymbol{u}$. Such limitation can be described by

$$\underline{\boldsymbol{u}} \leq \boldsymbol{u}_k \leq \overline{\boldsymbol{u}}, \quad \Delta\underline{\boldsymbol{u}} \leq \Delta\boldsymbol{u}_k \leq \Delta\overline{\boldsymbol{u}}, \tag{5.57}$$

where the bounds of the input variables $\underline{\boldsymbol{u}}, \overline{\boldsymbol{u}} \in \mathbb{R}^{n_u}$ and the bounds of the associated slew rates $\Delta\underline{\boldsymbol{u}}, \Delta\overline{\boldsymbol{u}} \in \mathbb{R}^{n_u}$ satisfy $\underline{\boldsymbol{u}} < \overline{\boldsymbol{u}}$ and $\Delta\underline{\boldsymbol{u}} < \Delta\overline{\boldsymbol{u}}$, respectively.

Such constraints can easily be integrated in the optimization problem of the MPC approach which determines the future input trajectory considering the prediction horizon h. Hence, each element of the predicted input trajectory $\Delta\boldsymbol{U}$ has to fulfill the inequalities (5.57) at any discrete time step.

The formulation of the augmented system (5.46) enables directly the implementation of slew rates constraint. In order to impose the input constraints, the input variable $\boldsymbol{u}_k$ has to be expressed by the decision variable $\Delta\boldsymbol{u}_k$ leading to

$$\boldsymbol{u}_{k+i} = \boldsymbol{u}_{k-1} + \sum_{m=0}^{i} \Delta\boldsymbol{u}_{k+m} \tag{5.58}$$

with $i \in \{0, 1, \ldots, h-1\}$. With this, the input constraints within the prediction horizon read

$$\underline{\boldsymbol{U}} \leq \mathcal{C}_1\boldsymbol{u}_{k-1} + \mathcal{C}_2\Delta\boldsymbol{U} \leq \overline{\boldsymbol{U}} \tag{5.59}$$

where $\mathcal{C}_1$ is a $(hn_u) \times n_u$ matrix, consisting of h identity matrices $I \in \mathbb{R}^{n_u \times n_u}$ and $\mathcal{C}_2$ is a lower triangular matrix with identity matrices $I \in \mathbb{R}^{n_u \times n_u}$ as its non-null block entries. The vectors of the time-invariant boundaries over the prediction horizon are given by

$$\underline{\boldsymbol{U}} = [\underline{\boldsymbol{u}}^T, \ldots, \underline{\boldsymbol{u}}^T]^T, \quad \overline{\boldsymbol{U}} = [\overline{\boldsymbol{u}}^T, \ldots, \overline{\boldsymbol{u}}^T]^T \tag{5.60}$$

with $\underline{\boldsymbol{U}}, \overline{\boldsymbol{U}} \in \mathbb{R}^{hn_u}$.

The constraints on the slew rates of the elements of the predicted input trajectory $\Delta\boldsymbol{U}$ are given by the inequality

$$\Delta\underline{\boldsymbol{U}} \leq \Delta\boldsymbol{U} \leq \Delta\overline{\boldsymbol{U}} \tag{5.61}$$

with the vectors of the time-invariant boundaries over the prediction horizon

$$\Delta\underline{\boldsymbol{U}} = [\Delta\underline{\boldsymbol{u}}^T, \ldots, \Delta\underline{\boldsymbol{u}}^T]^T, \quad \Delta\overline{\boldsymbol{U}} = [\Delta\overline{\boldsymbol{u}}^T, \ldots, \Delta\overline{\boldsymbol{u}}^T]^T, \tag{5.62}$$

where $\Delta\underline{\boldsymbol{U}}, \Delta\overline{\boldsymbol{U}} \in \mathbb{R}^{hn_u}$. Both types of constraints can be combined as follows

$$\mathcal{A}_\mathrm{c}\Delta\boldsymbol{U} \leq \boldsymbol{b}_\mathrm{c}, \quad \text{with} \quad \mathcal{A}_\mathrm{c} = \begin{bmatrix} \mathcal{C}_2 \\ -\mathcal{C}_2 \\ I \\ -I \end{bmatrix}, \quad \boldsymbol{b}_\mathrm{c} = \begin{bmatrix} \overline{\boldsymbol{U}} - \mathcal{C}_1\boldsymbol{u}_{k-1} \\ -\underline{\boldsymbol{U}} + \mathcal{C}_1\boldsymbol{u}_{k-1} \\ \Delta\overline{\boldsymbol{U}} \\ -\Delta\underline{\boldsymbol{U}} \end{bmatrix} \tag{5.63}$$

with $\mathcal{A}_\mathrm{c} \in \mathbb{R}^{4hn_u \times hn_u}$ and $\boldsymbol{b}_\mathrm{c} \in \mathbb{R}^{4hn_u}$.

The constrained optimization problem follows as

$$\min_{\Delta \boldsymbol{U}} J(\Delta \boldsymbol{U}) = \min_{\Delta \boldsymbol{U}} \frac{1}{2} \Delta \boldsymbol{U}^T \mathcal{H}_J \Delta \boldsymbol{U} + \Delta \boldsymbol{U}^T \boldsymbol{f}_J \tag{5.64a}$$

subject to

$$\mathcal{A}_\mathrm{c} \Delta \boldsymbol{U} \leq \boldsymbol{b}_\mathrm{c} \tag{5.64b}$$

The constraints can either be active, i.e., $\boldsymbol{a}_{\mathrm{c},i}^T \Delta \boldsymbol{U} = \boldsymbol{b}_{\mathrm{c},i}^T$, or inactive, i.e., $\boldsymbol{a}_{\mathrm{c},i}^T \Delta \boldsymbol{U} < \boldsymbol{b}_{\mathrm{c},i}^T$. There, the index i denotes the considered constraint, i.e., the i^{th} row of $\mathcal{A}_\mathrm{c}$ and the i^{th} element of $\boldsymbol{b}_\mathrm{c}$, respectively. The active inequality constraints are assembled in the set

$$S_\mathrm{ieq}(\Delta \boldsymbol{U}) = \left\{ i \in \{1, \ldots, 4hn_u\} : \boldsymbol{a}_{\mathrm{c},i}^T \Delta \boldsymbol{U} = \boldsymbol{b}_{\mathrm{c},i}^T \right\}. \tag{5.65}$$

The active inequality constraints are included into the optimization problem by using the Lagrange multiplier $\boldsymbol{p}$. The modified cost function reads

$$J^\dagger(\Delta \boldsymbol{U}) = \frac{1}{2} \Delta \boldsymbol{U}^T \mathcal{H}_J \Delta \boldsymbol{U} + \Delta \boldsymbol{U}^T \boldsymbol{f}_J + \boldsymbol{p}^T \left(\mathcal{A}_\mathrm{c} \Delta \boldsymbol{U} - \boldsymbol{b}_\mathrm{c} \right). \tag{5.66}$$

The Karush-Kuhn-Tucker (KKT) [12] first order necessary optimality conditions for the optimization problem are given by

$$\mathcal{H}_J \Delta \boldsymbol{U} + \boldsymbol{f}_J + \mathcal{A}_\mathrm{c}^T \boldsymbol{p} = \boldsymbol{0}, \tag{5.67a}$$

$$\boldsymbol{p}^T \left(\mathcal{A}_\mathrm{c} \Delta \boldsymbol{U} - \boldsymbol{b}_\mathrm{c} \right) = \boldsymbol{0}, \tag{5.67b}$$

$$\boldsymbol{p} \geq \boldsymbol{0}, \tag{5.67c}$$

where (5.67a) describes the first derivative of $J^\dagger(\Delta \boldsymbol{U})$ w.r.t. $\Delta \boldsymbol{U}$. The conditions (5.67b) and (5.67c) correspond to the complementary slackness conditions.

The solution of the optimization problem is not affected by the inactive constraints. Hence, they can be neglected in the optimization problem. Furthermore, active inequality constraints are replaced by equality constraints as long as they are active

$$\mathcal{H}_J \Delta \boldsymbol{U} + \boldsymbol{f}_J + \sum_{i \in S_\mathrm{ieq}} \boldsymbol{a}_{\mathrm{c},i} p_i = \boldsymbol{0}, \tag{5.68a}$$

$$\boldsymbol{a}_{\mathrm{c},i}^T \Delta \boldsymbol{U} - \boldsymbol{b}_{\mathrm{c},i}^T = \boldsymbol{0}, \tag{5.68b}$$

$$p_i \geq 0, \quad i \in S_\mathrm{ieq}. \tag{5.68c}$$

For the purpose of solving the constrained optimization problem a primal-dual-method is used, in which the Lagrange multipliers are determined in a dual optimization problem. By the knowledge of the Lagrange multiplier the set of active inequality constraints is known and the solution of (5.68) follows straightforward.

According to [114], the primal problem is described by

$$\max_{\boldsymbol{p} \geq 0} \left(\min_{\Delta \boldsymbol{U}} J^\dagger \right) = \max_{\boldsymbol{p} \geq 0} \left(\min_{\Delta \boldsymbol{U}} \left(\frac{1}{2} \Delta \boldsymbol{U}^T \mathcal{H}_J \Delta \boldsymbol{U} + \Delta \boldsymbol{U}^T \boldsymbol{f}_J + \boldsymbol{p}^T \left(\mathcal{A}_\mathrm{c} \Delta \boldsymbol{U} - \boldsymbol{b}_\mathrm{c} \right) \right) \right). \tag{5.69}$$

The minimization w.r.t. $\Delta \boldsymbol{U}$ is unconstrained which means the optimal solution results in

$$\min_{\Delta \boldsymbol{U}} J^\dagger \quad \Rightarrow \quad \Delta \boldsymbol{U} = -\mathcal{H}_J^{-1} \left(\boldsymbol{f}_J + \mathcal{A}_\mathrm{c}^T \boldsymbol{p} \right) \tag{5.70}$$

taking (5.67a) into account. Substituting this result into (5.69) defines the dual problem which can be reformulated as a minimization problem taking $\mathcal{H}_J = \mathcal{H}_J^T$ into account

$$\min_{\boldsymbol{p} \geq 0} \left(\frac{1}{2} \boldsymbol{p}^T \mathcal{P} \boldsymbol{p} + \boldsymbol{p}^T \boldsymbol{r} + \frac{1}{2} \boldsymbol{f}_J{}^T \mathcal{H}_J^{-1} \boldsymbol{f}_J \right) \quad \text{with} \quad \mathcal{P} = \mathcal{A}_\mathrm{c} \mathcal{H}_J^{-1} \mathcal{A}_\mathrm{c}^T, \quad \boldsymbol{r} = \boldsymbol{b}_\mathrm{c} + \mathcal{A}_\mathrm{c} \mathcal{H}_J^{-1} \boldsymbol{f}_J. \tag{5.71}$$

The quadratic problem (5.71) is solved by using Hildreth's quadratic programming procedure [114]. This algorithm determines the Lagrange multiplier iteratively. In the i^{th} iteration the m^{th} element of the Lagrange multiplier $\overline{p}_m^i$ is obtained by

$$\overline{p}_m^i = \max\left(0, \overline{\mu}_m^i\right) \quad \text{with} \quad \overline{\mu}_m^i = -\frac{1}{\mathcal{P}_{mm}} \left(r_m + \sum_{l=1}^{m-1} \mathcal{P}_{ml} \overline{p}_l^i + \sum_{l=m+1}^{h} \mathcal{P}_{ml} \overline{p}_l^{i-1} \right). \tag{5.72}$$

Here, $\mathcal{P}_{ml}$ denotes the element of the m^{th} row and l^{th} column of the matrix $\mathcal{P}$ and r_m describes the m^{th} element of the vector $\boldsymbol{r}$. The optimal solution of the dual problem in terms of the maximum ensures non negative Lagrange multiplier elements, as it is required by (5.67c). The algorithm is initialized with $\overline{\boldsymbol{p}}^0 = \boldsymbol{0}$ and calculates all Lagrange multipliers $\overline{\boldsymbol{p}}_m^i$ with $m \in \{1, 2, \ldots, h\}$ for the i-th iteration. The algorithm's termination conditions are defined by the absolute error of two successive iterations results of the Lagrange multipliers

$$\left(\overline{\boldsymbol{p}}^i - \overline{\boldsymbol{p}}^{i-1}\right)^T \left(\overline{\boldsymbol{p}}^i - \overline{\boldsymbol{p}}^{i-1}\right) < \varepsilon = 10^{-8} \tag{5.73a}$$

and by the number of iteration i limited to maximum value

$$i \geq i_{max} = 10. \tag{5.73b}$$

If one of these conditions is fulfilled the algorithm stops.

Hildreth's quadratic programming procedure is based on an element-by-element search and does not require any matrix inversion. Due to this, the computational complexity is low and the limitation of the maximum number of iteration (5.73b) enables the execution within a real time framework. In case of a termination of the optimization process before convergence is reached (5.73b) the obtained non-optimal solution can be used for further calculations so that the algorithms continues without interruption. Taking [114] into account the algorithm will provide near-optimal solutions and recovers automatically from ill-conditioned problems in the online execution.

In general, Hildreth's quadratic programming procedure has been shown to converge to a set of Lagrange multipliers $\overline{\boldsymbol{p}}^*$, where $\overline{\boldsymbol{p}}^*$ contains either zero or positive values and therefore determines the set of active inequality constraints [114]. The optimal solution for the Lagrange multiplier $\boldsymbol{p}^*$ fulfills the complementary slackness condition, see (5.67b) and (5.67c). Therefore, the optimal solution $\Delta\boldsymbol{U}$ is obtained by the substitution $\boldsymbol{p} = \boldsymbol{p}^*$ in (5.70), which yields

$$\Delta\boldsymbol{U} = -\mathcal{H}_J^{-1}\left(\boldsymbol{f}_J + \mathcal{A}_c^T\boldsymbol{p}^*\right). \tag{5.74}$$

The first element of the predicted input trajectory is implemented, i.e.,

$$\Delta\boldsymbol{u}_k = \begin{bmatrix} I & 0 \end{bmatrix} \Delta\boldsymbol{U}, \tag{5.75}$$

where the dimension of the identity matrix is defined by the number of inputs $I \in \mathbb{R}^{n_u \times n_u}$. The optimization is repeated in each sampling step with the updated measurements and estimated states provided by the Kalman filter.

5.4.3. Move Blocking by Downsampling

Although Hildreth's quadratic programming procedure reduces the computation effort the MPC approach has to deal with a weakly damped structures. This type of system is characterized by high eigenfrequencies which requires small sample times to cover the dynamics. Simultaneously the objective of a large rest-to-rest motion leads to large prediction horizons. Hence, the computational effort is still high. This is why, a move blocking method by downsampling is introduced to improve the real time capability.

The main idea is a simple downsampling of the prediction horizon, i.e., only every ν^{th} element of the originally predicted time span is calculated, where the prediction horizon h is an integer multiple of ν. Hence, the input variables are only determined every ν^{th} time step and stay fixed in between which is typical for move blocking. With this procedure the start and end of the predicted time span remain untouched, where the time used for the determination of the control input is enlarged by the factor ν. The downsampled predicted input trajectory is given by

$$\Delta\boldsymbol{U} = \begin{bmatrix} \Delta\boldsymbol{u}_k^T & \Delta\boldsymbol{u}_{k+\nu}^T & \ldots & \Delta\boldsymbol{u}_{k+h-\nu+1}^T \end{bmatrix}^T \tag{5.76}$$

and the downsampled predicted output trajectory is obtained as

$$Y_k = \mathcal{F}\widehat{\boldsymbol{x}}_{e,k} + \Phi\Delta\boldsymbol{U} \tag{5.77}$$

with

$$\mathcal{F}^T = \begin{bmatrix} H_e A_e & H_e A_e^\nu & \ldots & H_e A_e^{h-\nu+1} \end{bmatrix}, \quad \Phi = \begin{bmatrix} H_e B_e & 0 & \ldots & 0 \\ H_e A_e^\nu B_e & H_e B_e & \ldots & 0 \\ \vdots & \vdots & \ddots & \vdots \\ H_e A_e^{h-\nu} B_e & H_e A_e^{h-\nu-1} B_e & \ldots & H_e B_e \end{bmatrix}. \tag{5.78}$$

The reference signal Y_k^* and the maximal and minimal values of the amplitude and the change of the input variable, $\underline{\boldsymbol{U}}$, $\overline{\boldsymbol{U}}$, $\Delta\underline{\boldsymbol{U}}$ and $\Delta\overline{\boldsymbol{U}}$, respectively are modified in the same way.

6. Results

The previously discussed control approaches are evaluated below in terms of transient simulations as well as by the full integration within experimental setups. At the beginning, the results of the interconnected beam structures are summarized. These structures are proof of concept studies as well as benchmark tests for the wingsail's mechanical and control design, whose results are subsequently discussed in detail.

6.1. Pointwise Interconnected Beam Structure

Below the simulation as well as experimental results of the two vertical beam configuration are presented. At first the results of the triple beam setup are analyzed. The considered control concept is the two-degrees-of-freedom control approach. This model based control approach considers a reduced order system description which relies on the second order balanced truncation approach. Secondly, the results of the MPC approach are presented for the double beam setup.

Both subsections provide a brief repetition concerning the associated experimental setup. The used MOR method as well as the control approach including the observer design are presented providing all necessary design parameters. Finally, the simulations and experimental results are illustrated and discussed.

6.1.1. Triple Beam Configuration

As presented in Section 2.1.2 the experimental setup is based on $r = 3$ vertically aligned carbon beams. All beams are equipped with aluminum made tip masses which are used as mounting point for the elastic strings connecting the neighboring beams. In addition, the beams are equipped with voltage controlled embedded MFC-patches displaying the system's actuators. Furthermore, two kinds of sensors are used, the embedded strain gauges and external laser sensors, see Fig. 2.5 for the schematic of the vertical beam configuration and Table 2.2 for the precise locations of the points of interest and measurement. The laser sensors are placed at the points of interest to evaluate the performance of the reconstructed displacement of the observer. The observer uses the measurements of the strain gauges as input which are gathered at the points of measurement. All control approaches rely on the states or outputs provided by the observer in terms of the Kalman filter.

6.1.1.1. Evaluation of the Model Order Reduction

The finite dimensional system description of the triple beam configuration is driven by a set of $N_j = 10$ test and trail functions per beam, see (2.60). The resulting first order system is characterized by $2N = 2rN_j = 60$ states.

To reduce the computational effort, especially in view of the real time capability, a MOR method in terms of the second order balanced truncation is applied, see Section 4.2. Table 6.1 lists the associated Hankel singular values of the full system. In addition, Table 6.2 compares the relative amount of considered energy of the reduced system with the energy of the full system ε, see also (4.15), for different choices of the number of reduced second order states $N_{j,\mathrm{r}}$.

To evaluate the accuracy of different reduced order systems w.r.t. the full order system the simulation results are compared considering a stepwise actuation

$$\boldsymbol{u}(t) = \begin{bmatrix} 670 & 670 & 670 & 670 \end{bmatrix}^T \mathrm{V}\, h(t - 0.1s). \tag{6.1}$$

Fig. 6.1 displays the resulting transversal deflections at the points of interest $\boldsymbol{y}_{\mathrm{pi}}(t)$ of the full order system $N_j = 10$ and of three different reduced order systems. The reduced system based on $N_{j,\mathrm{r}} = 3$ second order states (green line) clearly shows a huge systematic error compared to the full order system (blue line). In contrast, the reduced systems based on $N_{j,\mathrm{r}} = 4$ and $N_{j,\mathrm{r}} = 5$ second order states (red and orange line) seems to completely cover the behavior of the full order system.

For a further analysis Fig. 6.2 depicts the temporal difference between the full order and the reduced order system defined by the error

$$\tilde{y}^{\mathrm{r}}_{\mathrm{pi},f}(t) = y_{\mathrm{pi},f,N}(t) - y_{\mathrm{pi},f,N_{j,\mathrm{r}}}(t). \tag{6.2}$$

Table 6.1.: Hankel singular values scaled by 100 used for the construction of weighting matrices of the state observer (5.29b) and state controller (5.29b).

i	$\zeta_{\mathrm{p},i}$	$\zeta_{\mathrm{v},i}$	i	$\zeta_{\mathrm{p},i}$	$\zeta_{\mathrm{v},i}$	i	$\zeta_{\mathrm{p},i}$	$\zeta_{\mathrm{v},i}$
1	1.378349	1.378050	11	0.678621	0.678329	21	0.088991	0.088978
2	1.313073	1.312782	12	0.633459	0.633265	22	0.085209	0.085194
3	1.243174	1.242712	13	0.608382	0.608198	23	0.073384	0.073367
4	1.162754	1.162673	14	0.562492	0.562289	24	0.068237	0.068226
5	1.073687	1.073562	15	0.437648	0.437561	25	0.066446	0.066442
6	0.909155	0.909010	16	0.360763	0.360802	26	0.064682	0.064663
7	0.862658	0.862642	17	0.353424	0.353462	27	0.024695	0.024694
8	0.824224	0.824044	18	0.336417	0.336344	28	0.020243	0.020222
9	0.784702	0.784433	19	0.247365	0.247317	29	0.018217	0.018190
10	0.730939	0.730647	20	0.147528	0.147498	30	0.011651	0.011617

Table 6.2.: Comparison of the relative amount of considered energy of the reduced system for different number of reduced second order states $N_{j,\mathrm{r}}$.

$N_{j,\mathrm{r}}$	2	3	4	5	6	7	8	9
ε	0.39727	0.56584	0.71494	0.82021	0.89900	0.94292	0.9734	0.99457

Here, three reduced systems defined by $N_{j,\mathrm{r}} = 4$, $N_{j,\mathrm{r}} = 5$, and $N_{j,\mathrm{r}} = 6$ second order states are analyzed. These systems cover 71.5 %, 82.0 %, and 89.9 % of the energy w.r.t. the full order system, respectively see Table 6.2.

Considering Fig. 6.2, it strikes that the first system $N_{j,\mathrm{r}} = 4$ (blue line) displays significant high errors at both points of interest of the second beam ($\tilde{y}^{\mathrm{r}}_{\mathrm{pi},2}$, $\tilde{y}^{\mathrm{r}}_{\mathrm{pi},3}$). In contrast, the error magnitudes of the reduced systems defined by $N_{j,\mathrm{r}} = 5$ and $N_{j,\mathrm{r}} = 6$ are in the same range for the first three points of interest. Due to the small difference between these systems the reduced system with $N_{j,\mathrm{r}} = 5$ second order states is chosen as basis for the control design process. Hence, the first order system is characterized by $2N_{\mathrm{r}} = 2rN_{j,\mathrm{r}} = 30$ states.

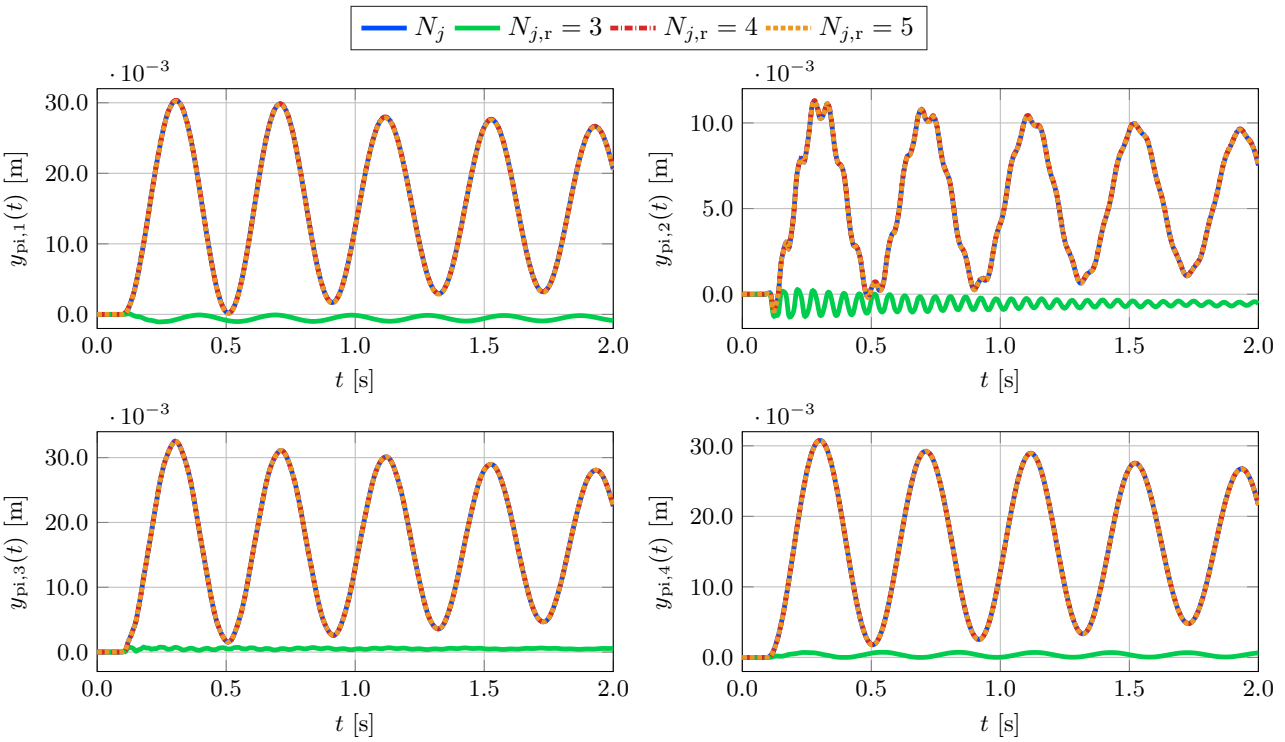

Figure 6.1.: Comparison of the displacements at the points of interest $y_{\mathrm{pi},f}(t)$ with $f = \{1, \ldots, 4\}$ of the full order system ($N_j = 10$) with the reduced order systems ($N_{j,\mathrm{r}} = \{3, 4, 5\}$) for the stepwise input signal (6.9).

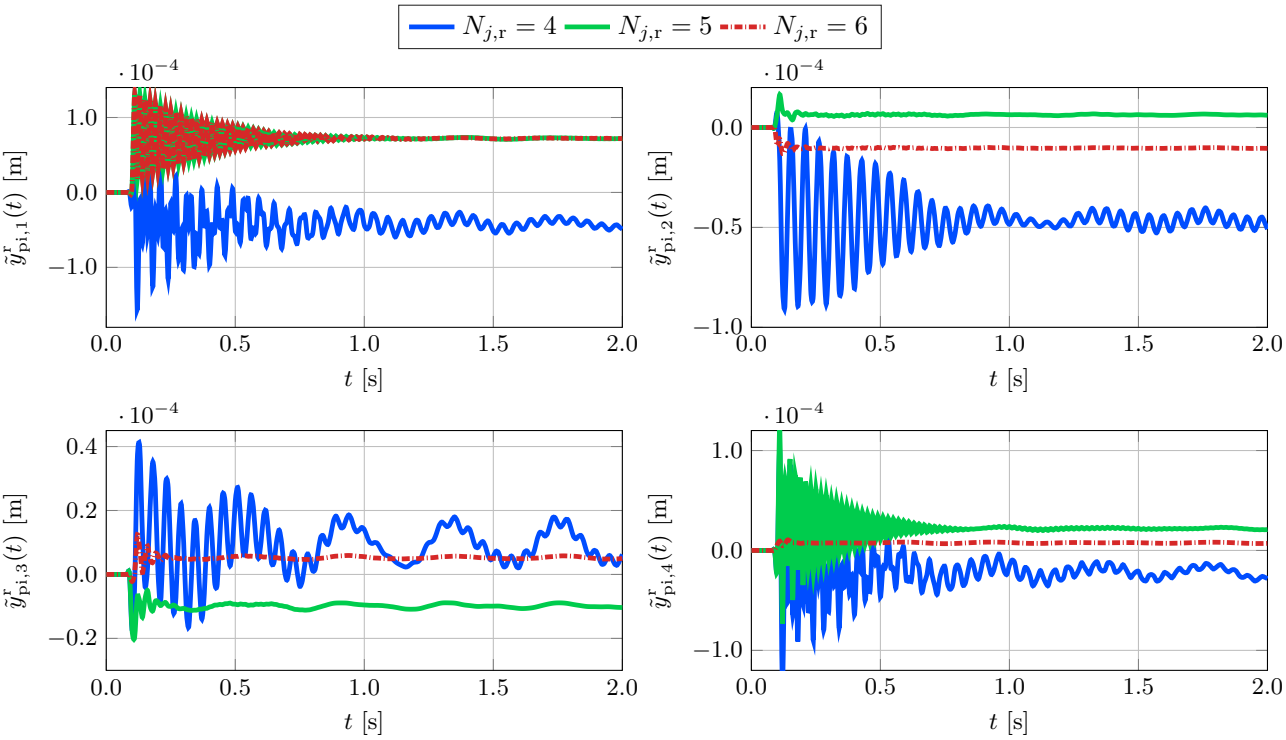

Figure 6.2.: Comparison of the errors (6.2) introduced by the second order balanced truncation method considering the reduced order systems based on $N_{j,\mathrm{r}} = \{4, 5, 6\}$ second order system states per beam.

6.1.1.2. Evaluation of the Open and Closed Loop System

The simulations and experimental results of the triple beam configuration are analyzed below. These results are organized as follows, At first the results of the open loop behavior are discussed considering the experimental step response. In addition, a comparison between simulation results of a rest-to-rest motion achieved by the flatness-based feedforward controls and a simple voltage ramp are analyzed. Secondly, the experimental results of the two-degrees-of-freedom control approach stay in the focus of the analysis.

Step Response To illustrate the open loop dynamics of the interconnected structure Fig. 6.3 displays the response of the transversal deflection of the points of interest $y_{\mathrm{pi},i} = s(z_{\mathrm{pi},i}, t)$ with $i \in \{1, 3, 4\}$ for a voltage step

$$\boldsymbol{u}(t) = \begin{bmatrix} 817 & -770 & -807 & 781 \end{bmatrix}^T \mathrm{V}\, h(t - 1\,\mathrm{s}). \tag{6.3}$$

These voltage values correspond to a steady state deflection of $\boldsymbol{y}_{\mathrm{pi}} = \begin{bmatrix} -8 & 1 & 4 & -6 \end{bmatrix}^T \times 10^{-3}\mathrm{m}$, where the second beam deflects in the opposite direction as the first and third beam. The applied voltage step leads to rather large oscillations of all three beams with amplitudes between $[4, 6] \times 10^{-3}\mathrm{m}$. Due to the beam configuration, the second beam endures the highest relative overshoot of 150 % w.r.t. the steady state values. The settling time of the oscillations is about 18 s. It has to be pointed out that this steady state denotes a challenging configuration, due to the opposite displacements of the coupled beams. Therefore, it is later on used to evaluate the closed loop behavior.

In addition, Fig. 6.3 provides a comparison between the laser measurements $y_{\mathrm{ol,L}}$ (blue line) and the observed output $\widehat{y}_{\mathrm{ol}}$ (green line). The laser measurement directly captures the transversal displacement near the beams' tip $z_{\mathrm{pi},i}$ with $i \in \{1, 3, 4\}$, see Fig. 2.5 and Table 2.2. To reduce the measurement noise these signals are filtered by a first order low pass filter characterized by the cutoff frequency $f_{\mathrm{c}} = 100\,\mathrm{Hz}$.

The observer in terms of a Kalman filter, see Section 5.2, is driven by the measurements of the embedded strain gauges located at $z_{\mathrm{pm},m} \neq z_{\mathrm{pi},i}\ \forall i, m$ and determines the transversal displacement at all points of interest $z_{\mathrm{pi},i}$ with $i \in \{1, \ldots, 4\}$. The necessary design parameters of the Kalman filter introduced in (5.15) and (5.29b) are summarized in Table 6.3. In addition, the weighting vectors $\boldsymbol{q}_{\mathrm{c,p}}^T$ and $\boldsymbol{q}_{\mathrm{c,p}}^T$ (5.15) and (5.29b) are given by the Hankel singular values of Table 6.1.

For the implementation of the voltage step and the recording of measurements a *dSPACE* MicroLabBox [31] is used with the sample time $t_{\mathrm{d}} = 2 \times 10^{-4}\,\mathrm{s}$.

As it can be seen, the observed output coincides with the laser measurements, which indicates a good performance of the observer and the underlying MOR with $N_{j,\mathrm{r}} = 5$. This is crucial for the implementation of the presented state feedback controller.

Remark 6.1 *To improve the comparability between the results recorded at the experimental setup the output of the Kalman filter is presented instead of the laser measurements due to the enhanced signal to noise ratio. Subsequently, these signals are denoted as observed displacements.*

Table 6.3.: Design parameters of the applied Kalman Filter introduced in (5.15) and (5.29b) considering $r = 3$ beams $j = \{1, \ldots, r\}$, $N_j = 5$ reduced second order system states per beam and $n_{\mathrm{pm}} = 7$ points of measurement using the installed strain gauges (type HBM 1-Ly48-6/350).

r_{o}	$q_{\mathrm{o},t}$	$q_{\mathrm{o,p,c}}$	$q_{\mathrm{o,v,c}}$
2.0×10^1	5.0×10^1	5.0×10^3	1.0×10^1

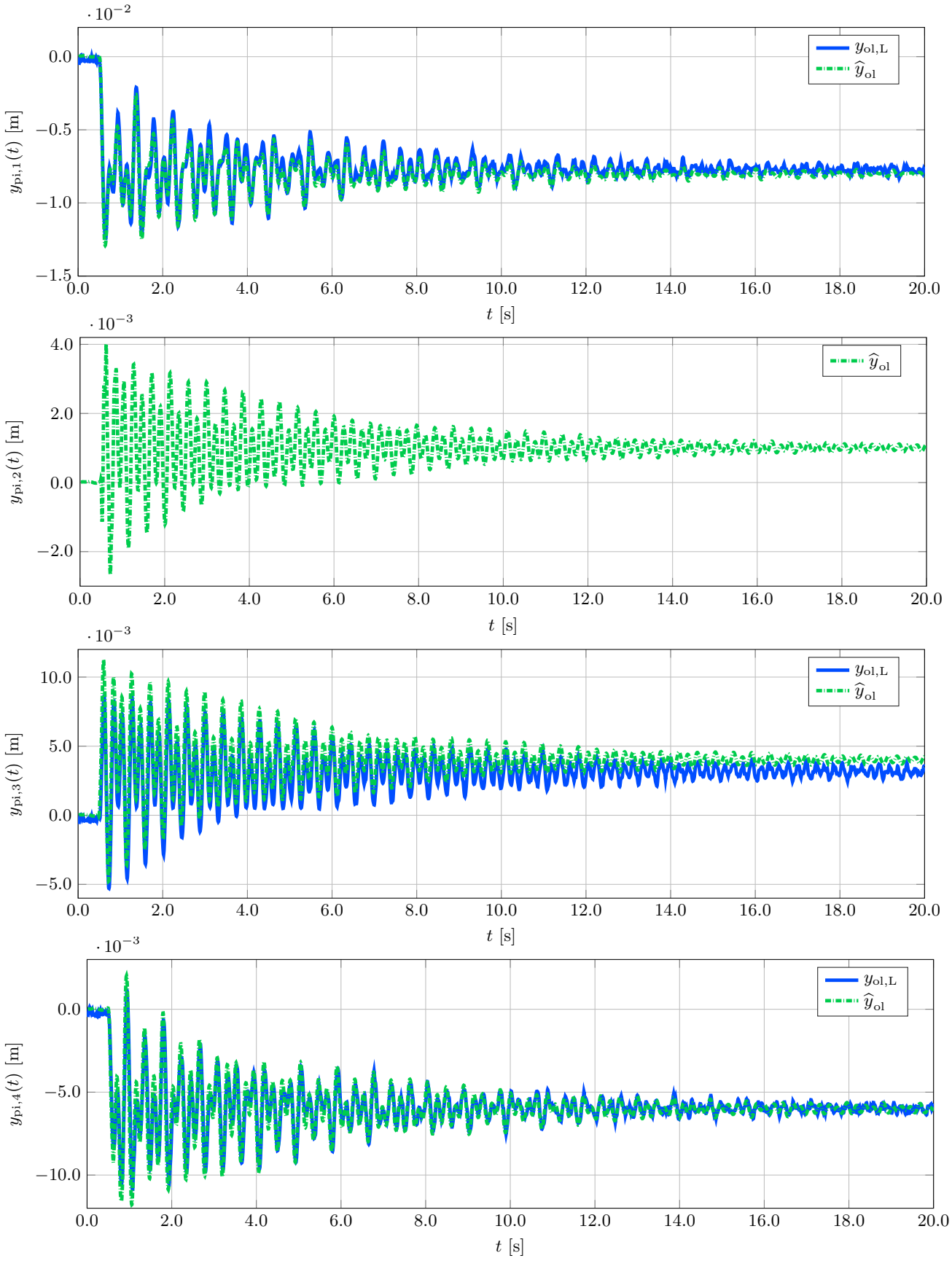

Figure 6.3.: Step response for the voltage step (6.3). The laser measurements $y_{\mathrm{ol,L}}$ are filtered using a first order low pass filter characterized by the cutoff frequency $f_{\mathrm{c}} = 100\,\mathrm{Hz}$. Note that no laser sensor is mounted at the second point of interest, therefore the associated displacement can only be observed. The observed displacements at the points of interest are determined by a Kalman filter which relies only on the seven embedded strain gauges.

Comparison Between the Numeric Results of the Feedforward Control and a Simple Voltage Ramp As a first numeric evaluation of the motion planning and the flatness-based feedforward control introduced by Section 5.1 a rest-to-rest motion is considered. This scenario starts at $t = 0\,\mathrm{s}$ in the undeformed state $\boldsymbol{y}_{\mathrm{pi}}^{*}(0\,\mathrm{s}) = [0 \quad 0 \quad 0 \quad 0]^{T} \times 10^{-3}\,\mathrm{m}$ and ends at $t = 1.1\,\mathrm{s}$ with the desired transversal deflection at the points of interest $\boldsymbol{y}_{\mathrm{pi}}^{*}(1.1\,\mathrm{s}) = [20 \quad 7 \quad 22 \quad 21] \times 10^{-3}\,\mathrm{m}$ which corresponds to 90 % of the maximal displacement. The associated steady state input signals are given by $\boldsymbol{u}_{\mathrm{ff}}(0\,\mathrm{s}) = [0 \quad 0 \quad 0 \quad 0]\,\mathrm{V}$ and $\boldsymbol{u}_{\mathrm{ff}}(1.1\,\mathrm{s}) = [874.9 \quad 874.0 \quad 950.3 \quad 890.6]\,\mathrm{V}$. Table 6.4 lists the necessary parameter of the used flatness-based feedforward controls (5.8a) taking (5.10) into account.

Fig. 6.1 displays the simulation results of the transversal deflection $\boldsymbol{y}_{\mathrm{ff}}(t)$ and its associated voltages $\boldsymbol{u}_{\mathrm{ff}}(t)$ (blue lines). Due to the fact that in the simulation all material parameters are known and no disturbances are considered, the result completely coincides with the reference trajectory $\boldsymbol{y}_{\mathrm{pi}}^{*}(t)$. The considered scenario provides the highest displacements because all actuators deflect in the same direction. Furthermore, it minimizes the coupling effect which is proportional to the difference of the tips' displacement of neighboring beams.

As a comparison approach the result of a simple voltage ramp which connects the same steady state inputs within the same time span

$$\boldsymbol{u}_{\mathrm{ra}}(t) = \begin{cases} \begin{bmatrix} 0 & 0 & 0 & 0 \end{bmatrix} \mathrm{V} & 0\,\mathrm{s} \leq t < 0.1\,\mathrm{s} \\ \frac{t - 0.1\,\mathrm{s}}{0.7\,\mathrm{s}} \begin{bmatrix} 874.9 & 874.0 & 950.3 & 890.6 \end{bmatrix} \mathrm{V} & 0.1\,\mathrm{s} \leq t < 0.8\,\mathrm{s} \\ \begin{bmatrix} 874.9 & 874.0 & 950.3 & 890.6 \end{bmatrix} \mathrm{V} & 0.8\,\mathrm{s} \leq t \end{cases} \tag{6.4}$$

is presented (green line). The resulting displacement shows an oscillation characterized by amplitudes of $4 \times 10^{-3}\,\mathrm{m}$ which corresponds to a relative overshoot of 20 %. Furthermore it depicts a large settling time of about 16 s.

Concluding the comparison the flatness-based feedforward control displays the expected behavior of a fast and oscillation free rest-to-rest motion. This result can only be achieved because all material parameters are known within the simulation environment. Taking an experimental setup into account parameter uncertainties and disturbance lead to deviations and small oscillation in the open loop. In contrast, a comparable voltage ramp is not able to achieve a similar performance on the weakly damped system.

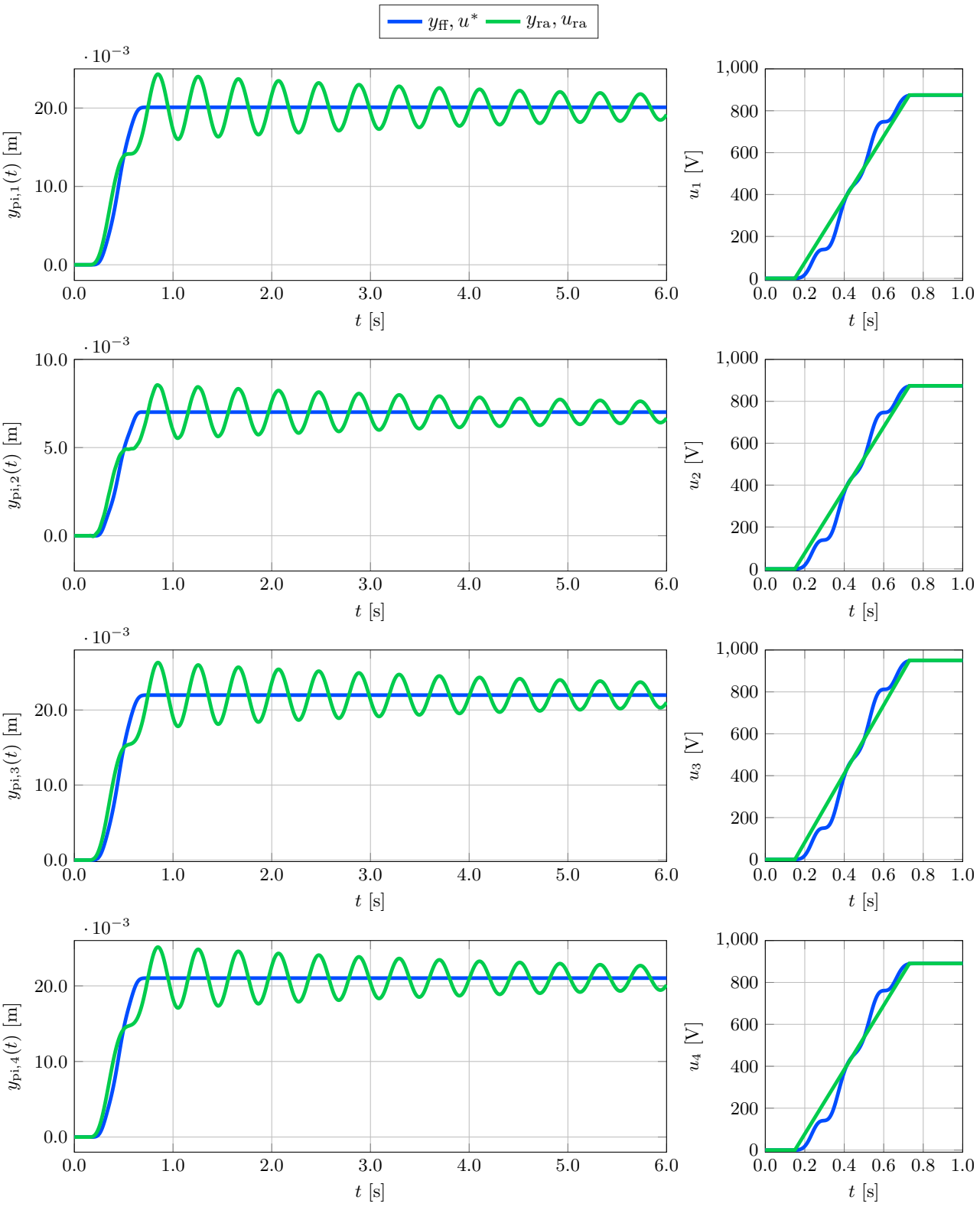

Figure 6.4.: Comparison of the simulation results of the transversal displacement at the points of interest $y_{\mathrm{pi},f}(t)$ with $f \in \{1, \ldots, 4\}$ considering the presented flatness-based feedforward controls approach ($y_{\mathrm{ff}},\ u^*$) see (5.8a) taking (5.10) into account with a ramp shaped voltage input ($y_{\mathrm{ra}},\ u_{\mathrm{ra}}$), see (6.4).

Experimental Results of the Two-Degrees-of-Freedom Control Approach Below, the performance of the flatness-based feedforward controls and of the two-degrees-of-freedom control approach are analyzed taking the implementation on the experimental setup into account using a *dSPACE* MicroLabBox [31] with a given sample time $t_\mathrm{d} = 2 \times 10^{-4}\,\mathrm{s}$.

The performance is analyzed by two different scenarios.

1. At first, the control performance is evaluated for a rest-to-rest motion scenario. For this, three transitions between different steady states displacements are considered, see Fig. 6.5. At the beginning of the scenario, the system stays in the undeformed state $\boldsymbol{y}^*_\mathrm{pi}(0\,\mathrm{s}) = [0 \quad 0 \quad 0 \quad 0]^T \times 10^{-3}\,\mathrm{m}$. After $t = 1.9\,\mathrm{s}$ the steady state $\boldsymbol{y}^*_\mathrm{pi}(1.9\,\mathrm{s}) = [-8 \quad 1 \quad 4 \quad -6]^T \times 10^{-3}\mathrm{m}$ should be reached which depicts the identical transversal displacement as is imposed in the step response, see Fig. 6.3. The second transition starts at $t = 6\,\mathrm{s}$, where the desired steady state $\boldsymbol{y}^*_\mathrm{pi}(6.9\,\mathrm{s}) = -\boldsymbol{y}^*_\mathrm{pi}(1.9\,\mathrm{s}) = [8 \quad -1 \quad -4 \quad 6]^T \times 10^{-3}\mathrm{m}$ should be reached at $t = 6.9\,\mathrm{s}$. This transition describes a rest-to-rest motion connecting the positive and negative transversal displacement of the beams which correspond to 80 % of the maximal reachable steady state displacement. Finally, the last transition leads the system back into the undeformed state $\boldsymbol{y}^*_\mathrm{pi}(11.9\,\mathrm{s}) = [0 \quad 0 \quad 0 \quad 0]^T \times 10^{-3}\,\mathrm{m}$.

2. Thereafter, the system behavior and the control performance are evaluated taking a disturbance introduced by a pulse hammer into account while the system stays in the undeformed state $\boldsymbol{y}^*_\mathrm{pi}(t) = [0 \quad 0 \quad 0 \quad 0]^T \times 10^{-3}\,\mathrm{m}$. This scenario is referred to as disturbance rejection.

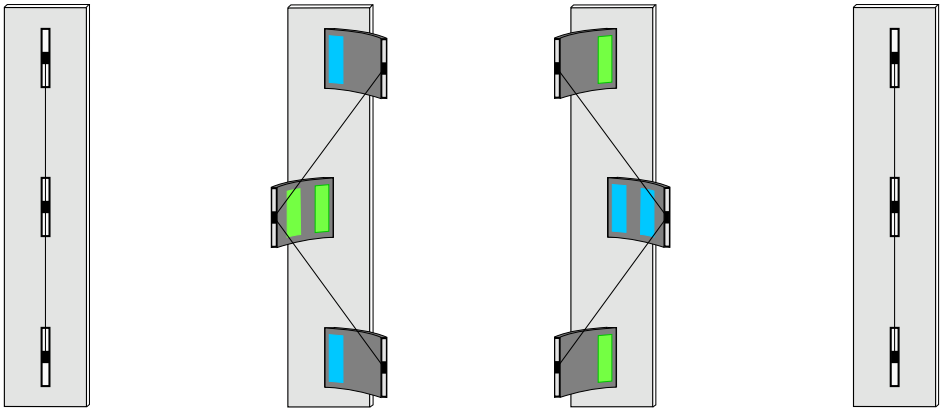

Figure 6.5.: Schematic visualization (front view) of the desired steady state displacement profiles of the designed scenario, see Figs. 6.6 and 6.8, chronologically sorted from left to right.

In both scenarios the two-degrees-of-freedom control approach is considered which is based on the flatness-based feedforward control (5.8a) with different feedback control approaches. For the rest-to-rest motion the results of the feedforward control are compared with the results of the tracking controller based on the ID-T_1, the linear quadratic (LQR), the extended LQR, the Lyapunov-based feedback control approach and its extension. Due to the fact, that the Ackermann state feedback controller and its extension achieve similar performances compared to the LQ feedback controller the analysis concentrates only on the LQR approach.

The analysis of the disturbance rejection, in which a pulse hammer is used to disturb the beam structure, is focused on the result of the open loop system, the ID-T_1 control, the extended LQR and the extended Lyapunov-based control approach. The associated design parameters are identical for both scenarios and are listed in Table 6.4.

Rest-to-Rest-Motion Scenario The evaluation of the rest-to-rest motion is split in two parts. At first, the results of the feedforward control and the two-degrees-of-freedom controls which do not ensure steady state accuracy are considered. Hereinafter, the ID-T_1, extended LQ and the extended Lyapunov-based two-degrees-of-freedom control approach are considered.

Remark 6.2 *To improve the readability of the achieved transversal deflections considering all points of interest and the associated input signals, they are placed on double pages.*

Fig. 6.6 shows the transversal deflection at points of interest of the feedforward control $\widehat{y}_\mathrm{ff}$ (green line), where the reference trajectory y^* is depicted by the blue line. Compared to the step response, see Fig. 6.3, the feedforward

Table 6.4.: Design parameters of the considered two-degrees-of-freedom control approaches considering the flatness-based feedforward control (5.8a) taking (5.10) into account as well as the ID-T_1 (5.18), the LQR (5.29b), the extended LQR (5.31), and the Lyapunov-based feedback control approach (5.44).

feedforward control		ID-T_1 control		
T	g	k_I	k_D	$1/T_\mathrm{idt}$
0.9×10^0	1.1×10^0	1.7×10^1	5.5×10^6	150 Hz

LQR			
r_c	$q_{\mathrm{c},t}$	$q_\mathrm{c,p}$	$q_\mathrm{c,v}$
1.0×10^{-2}	2.0×10^2	1.0×10^1	1.0×10^{-3}

extended LQR		Lyapunov
k_a	k_lq	$k^\mathrm{ly}_{j,\mathrm{a}_k}$
2.0×10^1	2.0×10^1	5.5×10^6

control results in a far smaller oscillation at all four points of interest, although the steady voltage after the first transition is identical to the stepwise voltage signal (6.3). Considering the second point of interest $f = 2$ the oscillation does not decay completely during the steady state phase of the scenario. However, the largest relative overshooting considering the points of interest is given by an amplitude of 10 %, which is caused by the remaining uncertainties of the material parameters. The remaining steady state deviation can be neglected as long as no external disturbance is applied. In addition Fig. 6.7 displays the feedforward control signal u^*.

Remark 6.3 *The proposed flatness-based motion planning and feedforward control approach is capable to almost completely achieve the desired rest-to-rest motion without the need to perform intensive computations or optimization. The approach is real time capable and implemented in the real time processing unit for each experimental setup. This implementation allows to adjust the motion planning online.*

The two-degrees-of-freedom control approach based on the LQ feedback control displays a significant improvement especially during and right after the transition phases, see the red lines of Fig. 6.6. The remaining oscillations of the displacement $\widehat{y}_\mathrm{lq}$ decays within $t = 1.5\,\mathrm{s}$. Considering Fig. 6.7 the applied voltages u_lq differ only slightly from the voltages of the feedforward controller.

In contrast, the application of the Lyapunov-based feedback controller $\widehat{y}_\mathrm{ly}$ (orange line) displays only small performance improvements within the transition phases compared to the result of the feedforward control approach. The settling time is given by about 4.2 s. However, the steady state deviation is larger compared to the open loop especially for the second point of interest located behind the second beam's first MFC-actuator.

Concluding the evaluation of this first set of control approaches, the two-degrees-of-freedom control approach based on the LQ feedback controller displays the best performance regarding dynamic and control error defined by

$$\tilde{\boldsymbol{y}}(t) = \boldsymbol{y}^*(t) - \widehat{\boldsymbol{y}}(t). \tag{6.5}$$

The results of the second set of feedback controllers which ensure steady state accuracy are shown by Fig. 6.8, while Fig. 6.9 depicts the associated voltages, and Fig. 6.10 displays the corresponding control error (6.5).

Taking the application of the ID-T_1 $\widehat{y}_\mathrm{idt}$ and extended LQ feedback controller $\widehat{y}_\text{ex-lq}$ (green and red line, respectively) into account it can be seen that both controllers achieve a nearly identical dynamic. During the transition phases the associated control errors $\tilde{y}_\mathrm{idt}$ and $\tilde{y}_\text{ex-lq}$ results in a maximum of about $0.5 \times 10^{-3}\,\mathrm{m}$, although this transition connects the maximal positive and negative deflection. These absolute errors correspond to a relative error of about 16 % w.r.t. the desired steady state. It seems that the ID-T_1 control achieves slightly better results in the second transition, where the extended LQR displays an improved performance within the first transition. However, in the end the performance deviation is marginal, which is why the associated input signals u_idt and $u_\text{ex-lq}$ display only small deviations, see Fig. 6.9.

In contrast, the performance of the extended Lyapunov-based feedback controller's displayed by its displacement $y_\text{ex-ly}$ is weak compared to the previously discussed controllers. The extension provides the desired steady state accuracy but no significant improvement of the transients.

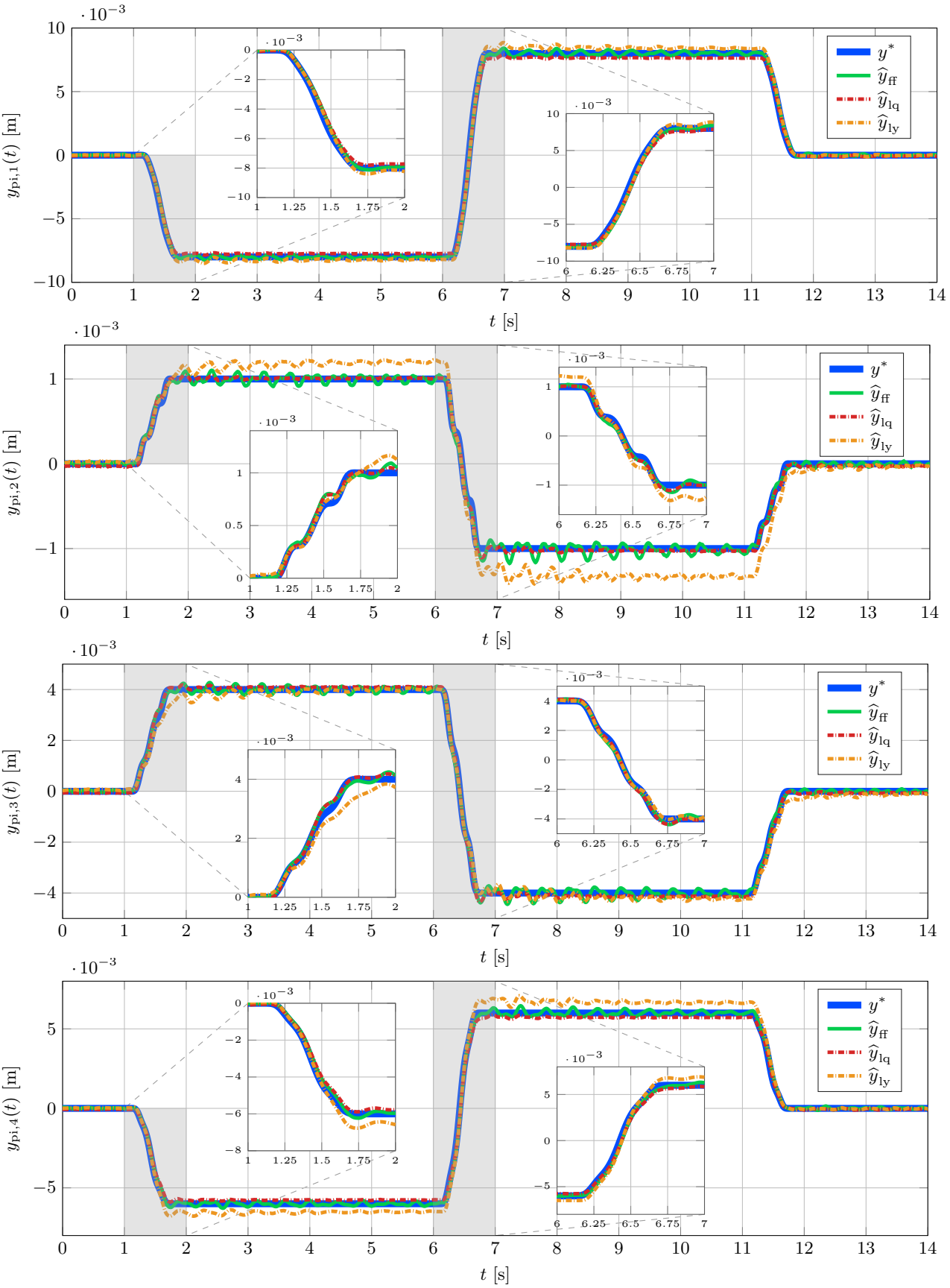

Figure 6.6.: Experimental results of the observed transversal displacement at the points of interest $\widehat{y}_{\mathrm{pi},f}(t)$ with $f \in \{1, \ldots, 4\}$ of the reference trajectory y^*, the flatness-based feedforward control $\widehat{y}_{\mathrm{ff}}$, and the two-degrees-of-freedom control approach based on the LQ and the Lyapunov-based controller denoted as $\widehat{y}_{\mathrm{lq}}$ and $\widehat{y}_{\mathrm{ly}}$, respectively, for the rest-to-rest motion scenario.

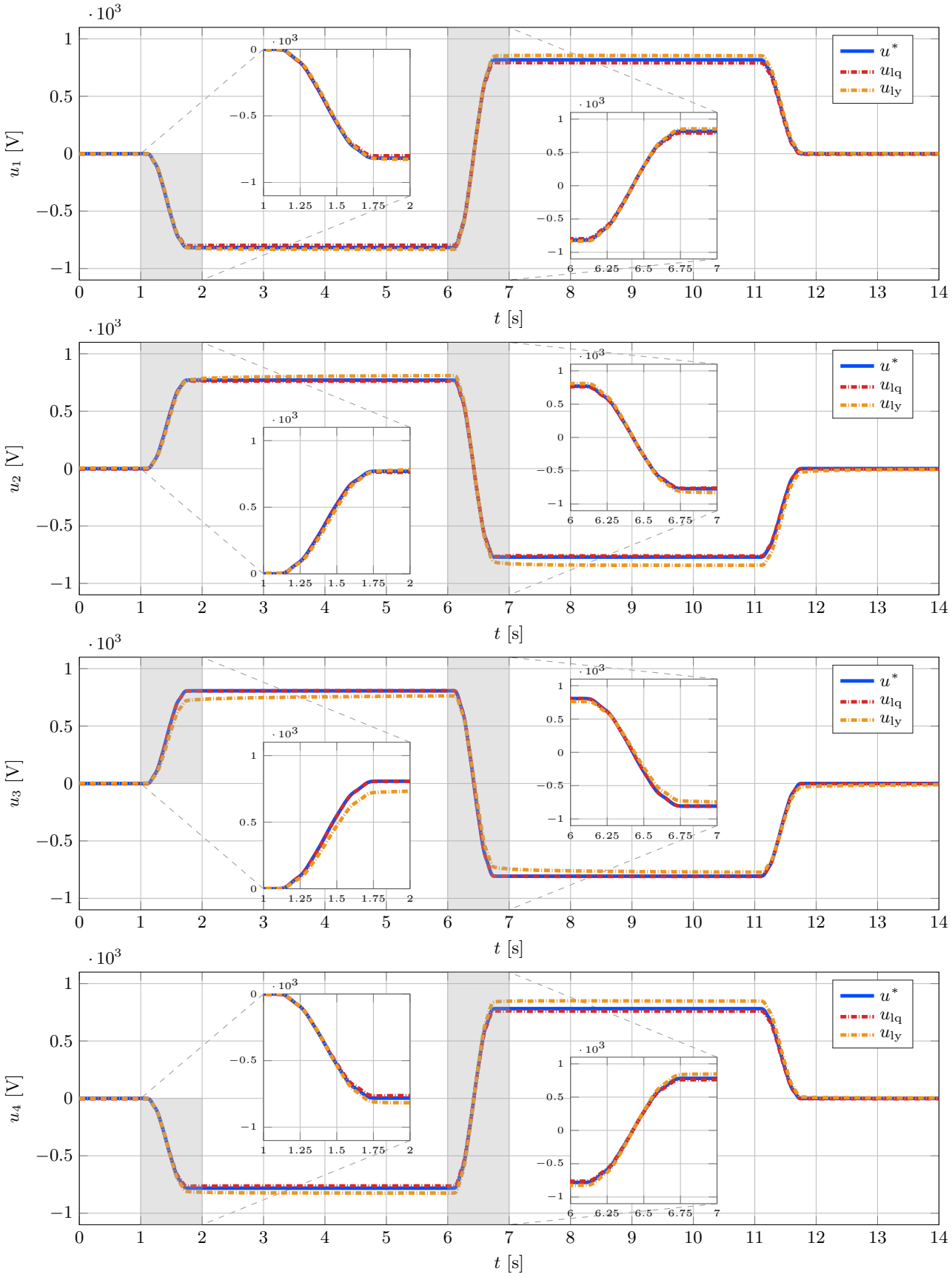

Figure 6.7.: Input signals of the MFC-actuators $k \in \{1, \ldots, 4\}$ of the feedforward controls u^* and the two-degrees-of-freedom control approach based on the LQ and the Lyapunov-based control approaches denoted as u_{lq} and u_{ly}, respectively, for the rest-to-rest motion scenario.

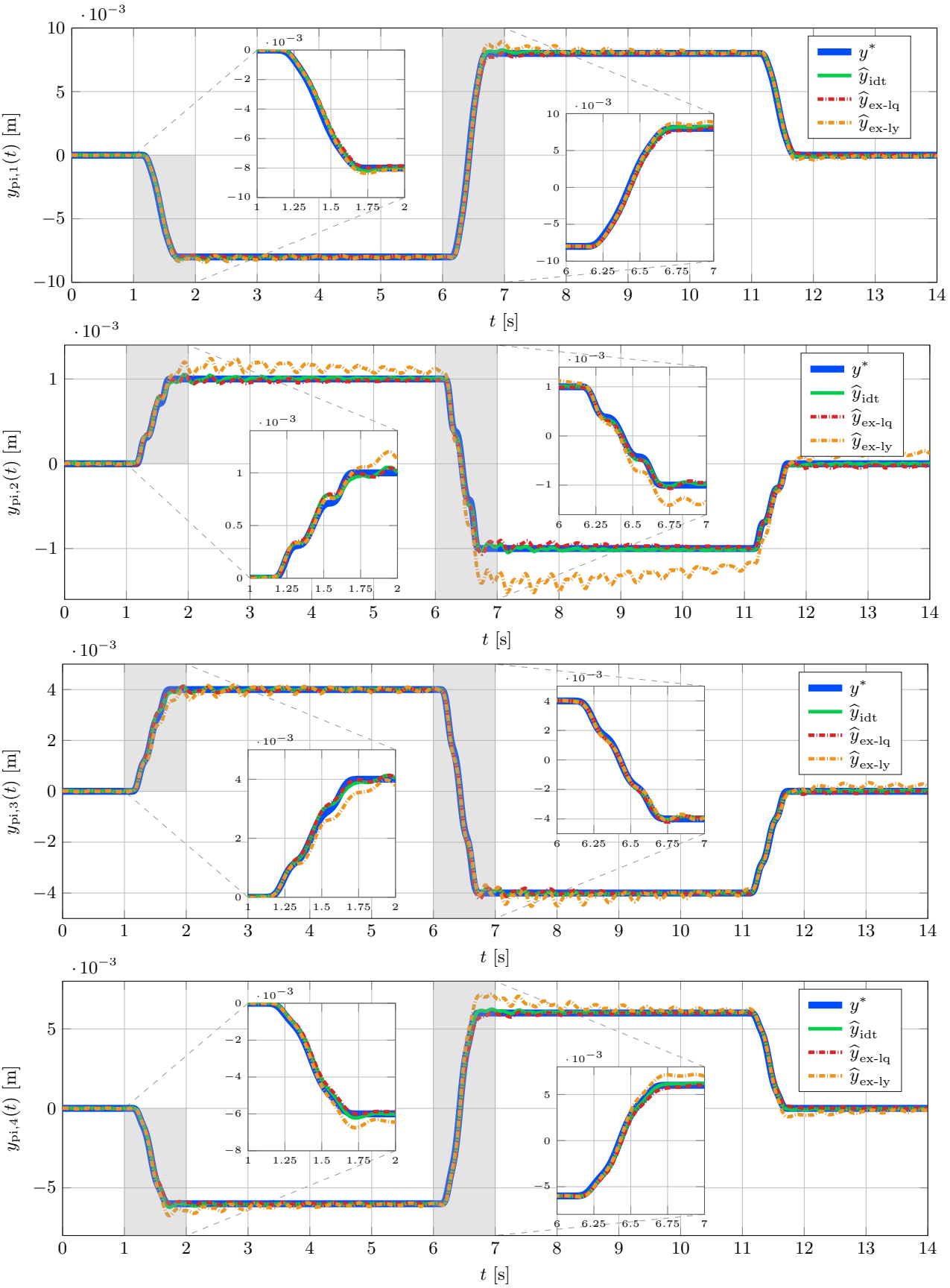

Figure 6.8.: Experimental results of the observed transversal displacement at the points of interest $\widehat{y}_{\mathrm{pi},f}(t)$ with $f \in \{1, \ldots, 4\}$ of the reference trajectory y^* and the two-degrees-of-freedom control approach based on the ID-T_1, the extended LQ, and the extended Lyapunov-based controller denoted as $\widehat{y}_{\mathrm{idt}}$, $\widehat{y}_{\mathrm{ex\text{-}lq}}$, and $\widehat{y}_{\mathrm{ex\text{-}ly}}$, respectively, for the rest-to-rest motion scenario.

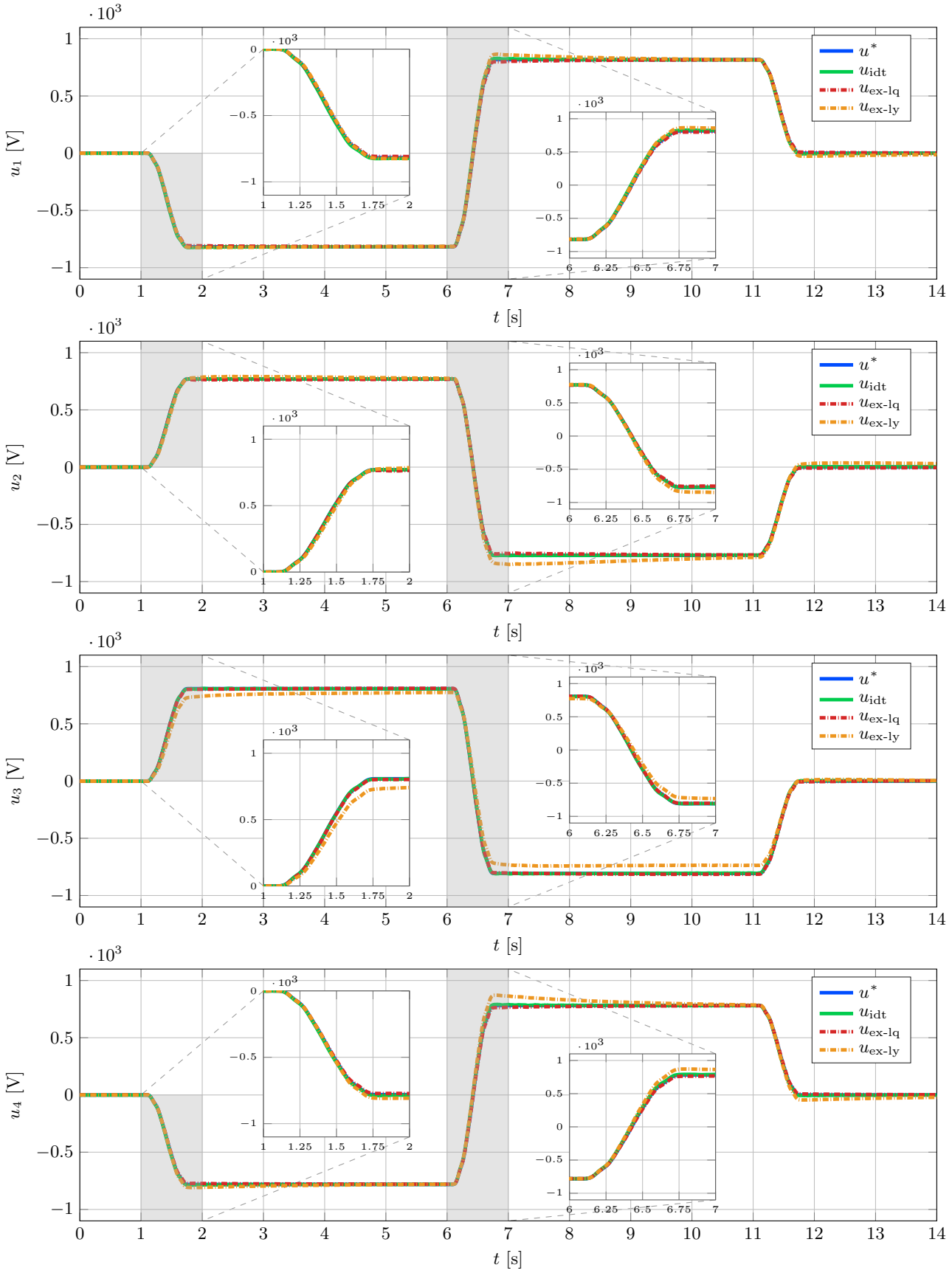

Figure 6.9.: Input signals of the MFC-actuators $k \in \{1, \ldots, 4\}$ of the two-degrees-of-freedom control approach based on the ID-T_1, the extended LQ, and the Lyapunov-based controller denoted as u_{idt}, $u_{\text{ex-lq}}$, and $u_{\text{ex-ly}}$, respectively, for the rest-to-rest motion scenario.

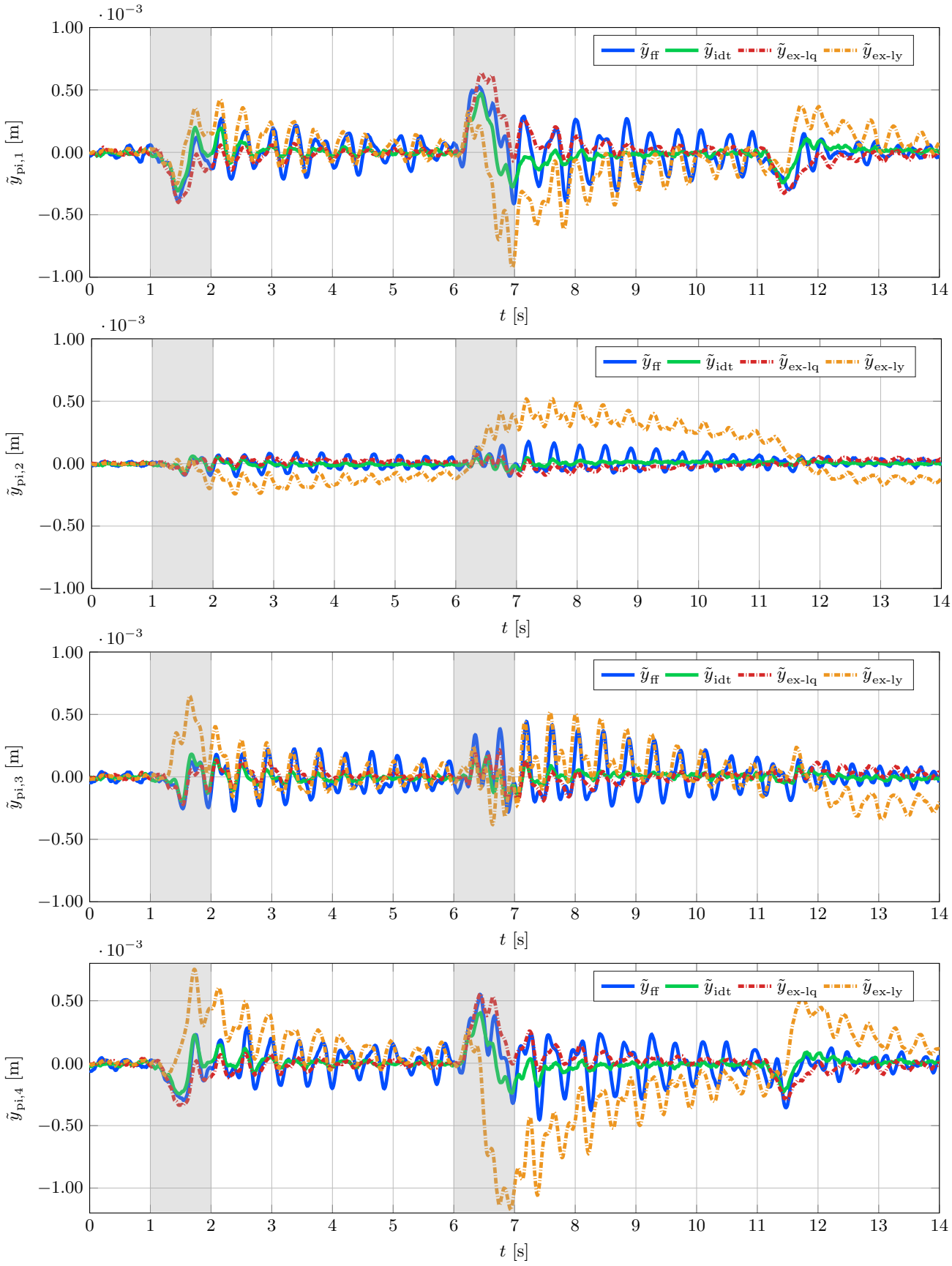

Figure 6.10.: Control errors (6.5) of the feedforward controls $\tilde{y}_{\mathrm{ff}}$ and the two-degrees-of-freedom control approach based on the ID-T$_1$, the extended LQ, and the Lyapunov-based controller denoted as $\tilde{y}_{\mathrm{idt}}$, $\tilde{y}_{\mathrm{ex\text{-}lq}}$, and $\tilde{y}_{\mathrm{ex\text{-}ly}}$, respectively, for the rest-to-rest motion scenario.

Disturbance Rejection Scenario The evaluation of this scenario concentrates only on the system's response to an external disturbance introduced by a pulse hammer of the open loop ($y_{\text{ol}},\ u_{\text{ol}}$), the ID-$T_1$ ($y_{\text{idt}},\ u_{\text{idt}}$), the extended LQ ($y_{\text{ex-lq}},\ u_{\text{ex-lq}}$), and the extended Lyapunov-based based feedback controllers ($y_{\text{ex-ly}},\ u_{\text{ex-ly}}$).

Fig. 6.11 displays the observed transversal deflections under disturbances. At $t = 0.5\,\text{s}$ a pulse hammer applied to the second beam excites the complete structure. The weakly damped system reacts in the open loop (blue line) with an oscillation characterized by amplitudes of 0.03 m and a decay time of about 25 s.

The application of the Lyapunov-based based controller reduces the decay time to 20 s by introducing a damping effect which can be seen by the frequency of the oscillation compared to the open loop. Comparing the four points of interest it appears that the controller also synchronizes the displacement of all beams. In addition, the amplitudes of the oscillation are slightly damped (orange line). The associated voltages are depicted in Fig. 6.12.

In contrast, the extended LQR approach results in a decay time of about 4 s (red line). Furthermore, the amplitudes of the oscillation are reduced significantly after the first period.

The best performance is achieved by the ID-T_1 controller (green) slightly improving the results of the LQR. After the first oscillation's period the error amplitude is reduced by approximately the factor 2. Comparing the applied voltages of the ID-T_1 and LQ controller it appears that this slight performance improvement comes with a much higher energy consumption. In general, the ID-T_1 controller reacts faster and with higher voltages. Furthermore, it appears that the LQR uses the first MFC-patch pair to control the deflections at the points of interest, especially of the second beam. In contrast, the ID-T_1 approach seems to focus on the second patch pair, which provides a shorter lever. This is why the ID-T_1 control requires higher amplitudes to control the second beam.

Concluding the evaluation of both scenarios, the two-degrees-of-freedom control approaches based on the ID-T_1 and the extended LQ are characterized by a fast dynamic, a strong damping of the remaining oscillations as well as steady state accuracy considering short sampling times. Due to the comparable performance the slightly lower energy consumption of the LQR should be preferred. Nevertheless, the motion planning and control concept displays remarkable results and ensures that the desired shape is reached.

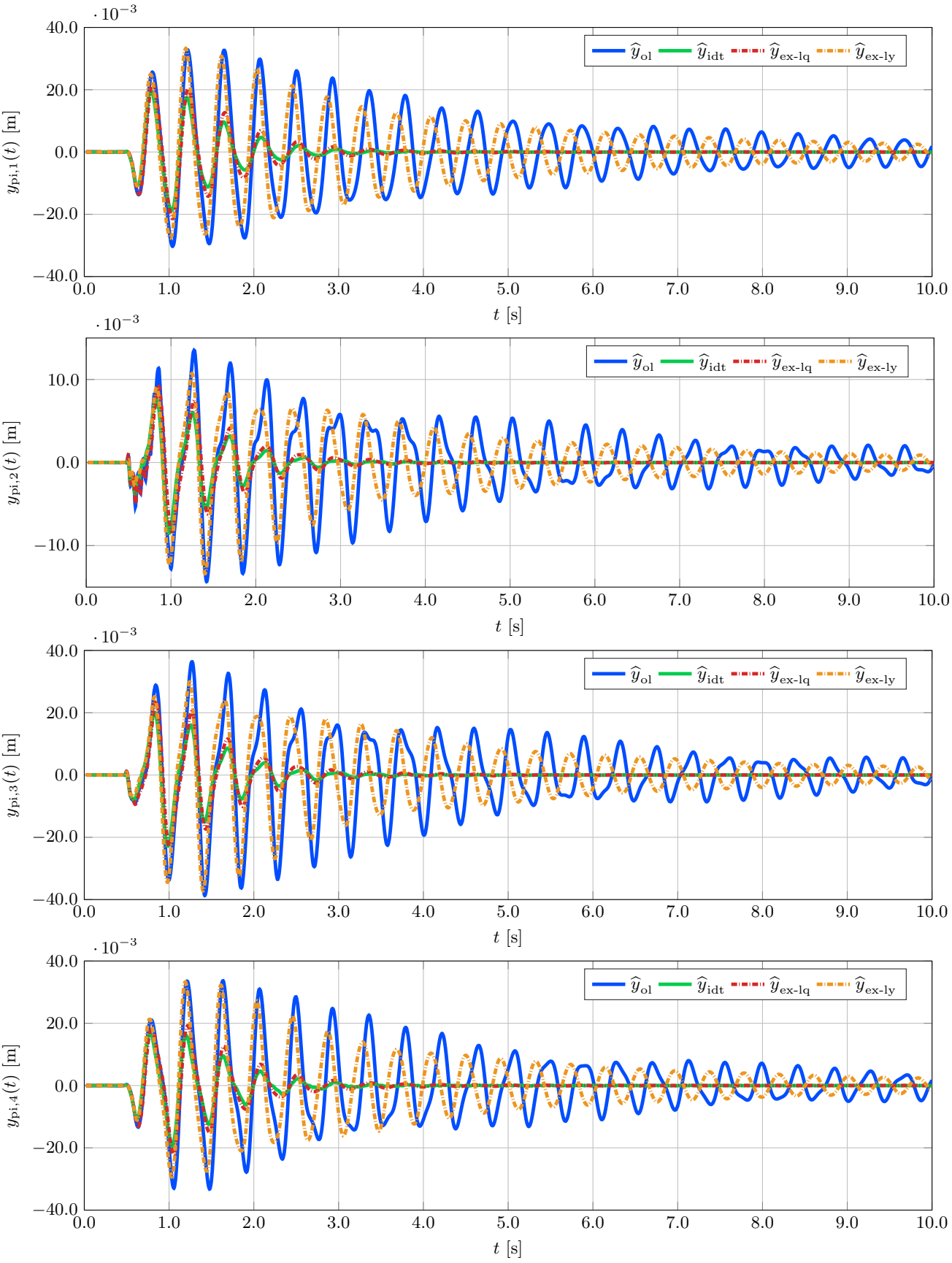

Figure 6.11.: Experimental results of the observed transversal displacement at the points of interest $\widehat{y}_{\mathrm{pi},f}(t)$ with $f \in \{1, \ldots, 4\}$ of the open loop system $\widehat{y}_{\mathrm{ol}}$ and the two-degrees-of-freedom control approach based on the ID-T_1, the extended LQ, and the extended Lyapunov-based controller denoted as $\widehat{y}_{\mathrm{idt}}$, $\widehat{y}_{\text{ex-lq}}$, and $\widehat{y}_{\text{ex-ly}}$, respectively, considering the disturbance rejection scenario. The disturbance is introduced by a pulse hammer applied at $t = 0.5\,\mathrm{s}$ to the second beam.

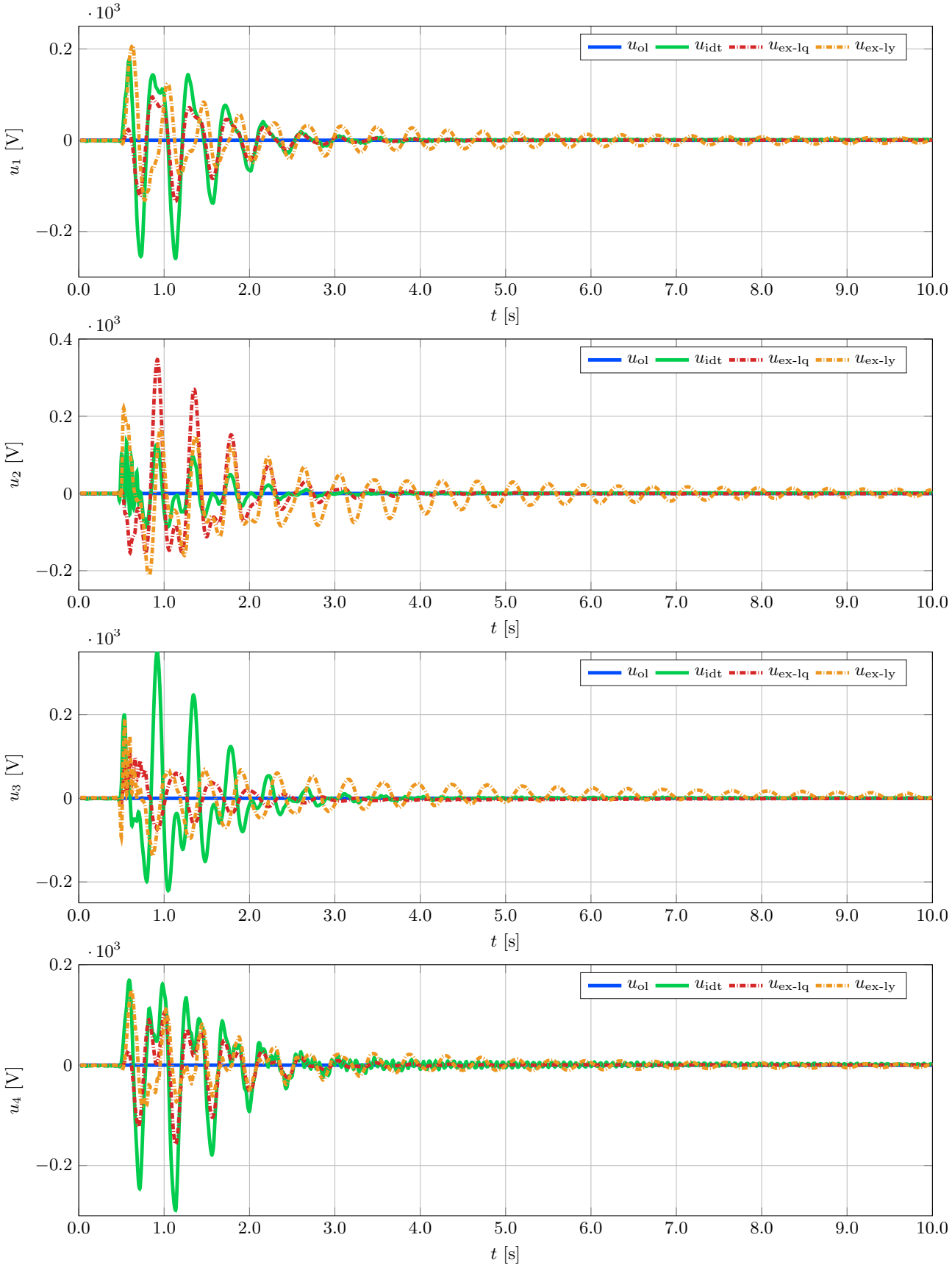

Figure 6.12.: Input signals of the MFC-actuators $k \in \{1, \ldots, 4\}$ of the two-degrees-of-freedom control approach based on the ID-T_1, the extended LQ, and the Lyapunov-based controller denoted as u_{idt}, $u_{\text{ex-lq}}$, and $u_{\text{ex-ly}}$, respectively, considering the disturbance rejection scenario. The disturbance is introduced by a pulse hammer applied at $t = 0.5\,\mathrm{s}$ to the second beam.

6.1.2. Double Beam Configuration

As mentioned before the double beam setup denotes a subset of the previously discussed triple beam configuration which is reduced by the second beam. Hence, the double beam setup is based on $r = 2$ vertical aligned carbon beams coupled with each other by a rubber band mounted at their tip masses. Both beams are equipped with voltage controlled embedded MFC-patches serving as actuators. In contrast to the triple beam setup only the external laser sensors are used as measurement devices and also as input for the Kalman filter. The laser sensors are placed at the points of interest near the beams' tips so that the points of measurement coincide with the points of interest, see Fig. 2.5 for the schematics of the vertical beam configuration and Table 2.2 for the precise locations. Below, the results of the MPC approach of Section 5.4 are discussed, see also [94, 95]. It has to be mentioned that due to its computational effort the MPC approach is restricted to the double beam setup. Therefore no direct comparison with the two-degrees-of-freedom control approach is provided to avoid redundant information. However, [56] presents results of the two-degrees-of-freedom control approach based on ID-T_1 feedback controls considering a comparable scenario.

6.1.2.1. Evaluation of the Model Order Reduction

Analog to the triple beam setup, the finite dimensional system description of the double beam is based on a set of $N_j = 10$ test and trail functions per beam, see (2.60). The resulting first order system is characterized by $2N = 2rN_j = 40$ states.

Again, the second order balanced truncation is applied as MOR method, see Section 4.2, to reduce the computational effort. In contrast to the triple beam the output matrix is given by $H_{\mathrm{pm}} = H_{\mathrm{pi}}$ due to the use of the laser sensors. This directly affects the observability Gramian $\mathcal{W}_{\mathrm{o}}$ and leads to the fast decaying Hankel singular values listed in Table 6.5. The relative amount of energy $\varepsilon(N_{j,\mathrm{r}})$ (4.15) w.r.t. different choices of the number of reduced second order states $N_{j,\mathrm{r}}$ is listed in Table 6.6. Compared with the triple beam results in Table 6.2 the relative amount of energy is significantly higher, where the major difference between both setups is given by the method of measurement. The used laser measurement directly provides the desired deflection, where the embedded strain gauges which are used in the triple beam setup only measure the strain at the points of measurement.

Table 6.5.: Hankel singular values.

i	$\zeta_{\mathrm{p},i}$	$\zeta_{\mathrm{v},i}$	i	$\zeta_{\mathrm{p},i}$	$\zeta_{\mathrm{v},i}$	i	$\zeta_{\mathrm{p},i}$	$\zeta_{\mathrm{v},i}$
1	3.25×10^{-4}	3.25×10^{-4}	8	7.66×10^{-7}	5.30×10^{-7}	15	3.69×10^{-8}	2.69×10^{-8}
2	3.25×10^{-4}	3.25×10^{-4}	9	5.45×10^{-7}	3.89×10^{-7}	16	3.69×10^{-8}	2.69×10^{-8}
3	1.06×10^{-5}	4.86×10^{-6}	10	5.45×10^{-7}	3.89×10^{-7}	17	1.61×10^{-8}	8.26×10^{-9}
4	1.06×10^{-5}	4.86×10^{-6}	11	3.03×10^{-7}	1.88×10^{-7}	18	1.61×10^{-8}	8.26×10^{-9}
5	3.25×10^{-6}	9.63×10^{-7}	12	3.03×10^{-7}	1.88×10^{-7}	19	8.63×10^{-9}	1.35×10^{-9}
6	3.25×10^{-6}	9.63×10^{-7}	13	1.38×10^{-7}	7.42×10^{-8}	20	8.63×10^{-9}	1.35×10^{-9}
7	7.66×10^{-7}	5.30×10^{-7}	14	1.38×10^{-7}	7.42×10^{-8}			

Table 6.6.: Comparison of the relative amount of considered energy of the reduced system for different numbers of reduced second order states $N_{j,\mathrm{r}}$.

$N_{j,\mathrm{r}}$	1	2	3	4	5	6	7
ε	0.9663	0.9892	0.9955	0.9974	0.9988	0.9995	0.9999

To evaluate the accuracy of different reduced order systems and the full order system the simulation results are compared considering a stepwise actuation

$$\boldsymbol{u}(t) = \begin{bmatrix} 600 & -600 \end{bmatrix}^T \mathrm{V}\, h(t - 0.1s). \tag{6.6}$$

Fig. 6.13 displays the resulting transversal deflections at the points of interest $\boldsymbol{y}_{\mathrm{pi}}(t)$ of the full order system $N_j = 10$ (blue line) and the reduced order systems considering $N_{j,\mathrm{r}} = 1$ second order states (green line). The considered reduced order system covers 96.9 % of the full order system's total energy. Hence, nearly no deviation between the simulation results is detected.

In addition, the observed displacements using a Kalman filter based on the reduced order system with the covariance matrices $R_\mathrm{o} = \mathrm{diag}\{1\times10^{-2}, 1\times10^{-2}\}$ and $Q_\mathrm{o} = \mathrm{diag}\{1\times10^{7}, 1\times10^{7}\}$ using the laser measurements of the experimental setup are depicted by y_ol (red line). The simulation results match the experimental results quite well. There is only a small deviation in the amplitude of both displacements and in the frequency of the second beam.

Analog to the triple beam, the system response displays the characteristic behavior of a weakly damped structure. The amplitudes are about two times those of the steady state displacement and the decay time is about 25 s.

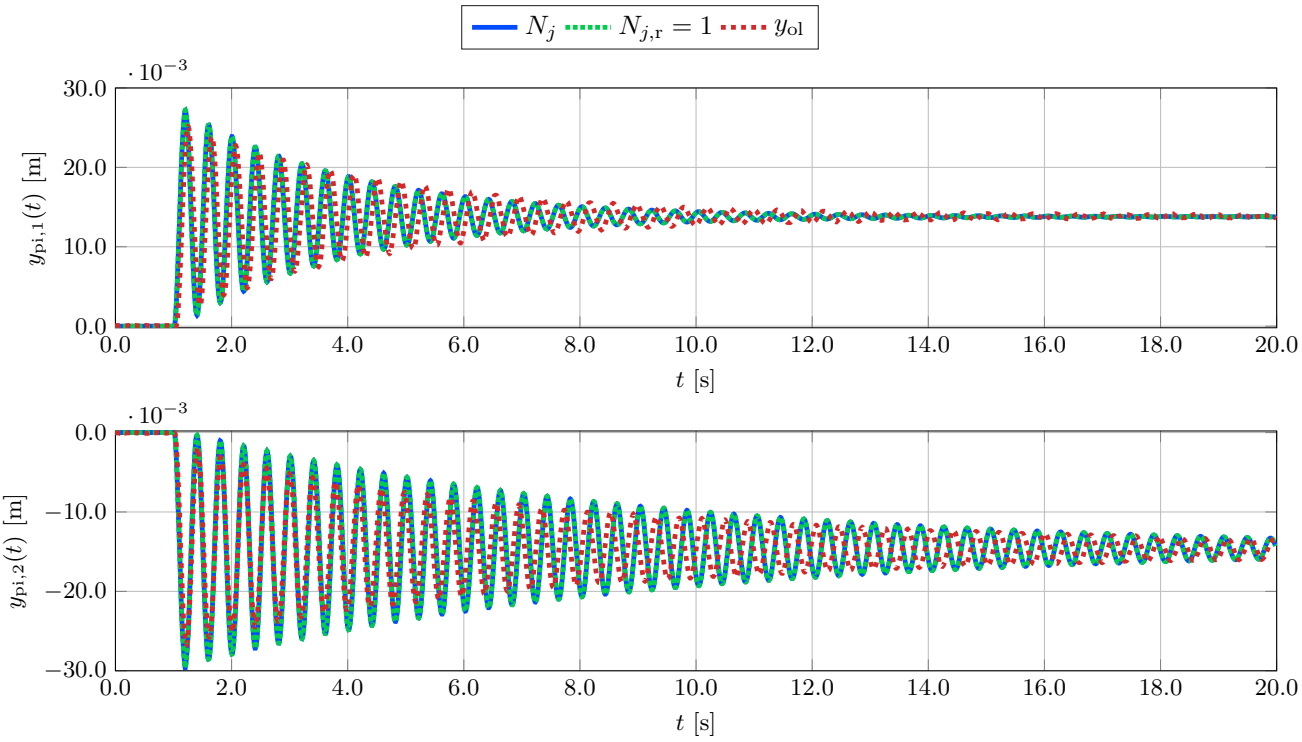

Figure 6.13.: Comparison of the simulated displacements at the points of interest $y_{\mathrm{pi},f}(t)$ with $f = \{1,\ldots,4\}$ of the full order system ($N_j = 10$), the reduced order systems ($N_{j,\mathrm{r}} = 1$), and the observed displacements recorded at the experimental setup y_ol taking the stepwise input signal (6.6) into account.

6.1.2.2. Evaluation of Model Predictive Control Approach

Below the results of the MPC approach are discussed. These results are based on the common weighting matrices $R_\mathrm{c} = 1\times10^{-9} I$ and $Q_\mathrm{c} = I$, see Section 5.4. Furthermore, the simulation as well as the real time implementation consider a fixed sample time of $t_\mathrm{d} = 3\times10^{-3}$s.

Fig. 6.14 displays on the left side the simulation and experimental results of the MPC approach in terms of the transversal displacement taking into account a stepwise reference signal

$$\boldsymbol{y}^*(t) = \begin{bmatrix} 0.01 & -0.01 \end{bmatrix}^T \text{ m } h(t - 0.5\,\text{s}) \tag{6.7}$$

depicted as blue line. In addition the right side displays the associated control input signals.

At first the results of the constrained MPC approach $\widehat{y}_\mathrm{MPC}$ are displayed (green line). This approach uses a prediction horizon of $h = 200$ time steps leading to a prediction time of 0.6 s. The considered constraints are given by the limitation of the actuators in terms of the absolute voltages $\overline{\boldsymbol{u}} = -\underline{\boldsymbol{u}} = [1000 \quad 1000]^T$ V and the associated slew rates $\Delta\overline{\boldsymbol{u}} = -\Delta\underline{\boldsymbol{u}} = [120 \quad 120]^T$ V as introduced by (5.57).

The resulting simulated displacement reaches the reference within 0.3 s with a small overshoot of about 8 %. The low magnitudes of the elements of the input weighting matrix R_c leads to a small impact or penalty within the cost function. Therefore, the resulting input signals are characterized by high absolute voltages and also high slew rates, see u_MPC on the right side of Fig. 6.14, where the constraints are fulfilled at all times.

The high and fast changing voltages as reaction to the step of the reference signal point out why the prediction horizon is crucial. The controller has to compensate the system response to the fast changes to prevent oscillation of the weakly damped system. Therefore, the prediction horizon has to be chosen long enough to consider the compensation of the fast reaction.

However, the full simulation of the presented approach with a prediction horizon of $h = 200$ time steps takes about 74.586 s on a PC equipped with an Intel i5 and 16 GB ram. A real time implementation is not feasible. To reduce the computational cost the prediction horizon can be shortened, but this would lead to a significant decrease in control performance, as previously discussed and verified by experiments. This is why the move blocking by downsampling is introduced.

The simulation results of the move blocking approach considering a downsampling factor $\nu = 10$ are displayed by the red lines. In contrast to the original MPC approach, the closed loop behavior in terms of the displacement $y_{\mathrm{MPC,ds}}$ takes about 0.5 s to reach the desired steady state, where the overshooting is further reduced. This temporal deflection profile is caused by smoother input signals $y_{\mathrm{MPC,ds}}$. However, the downsampling approach significantly reduces the computational effort leading to a total simulation time of 0.5181 s on the same hardware as before.

Therefore, the MPC approach considering move blocking by downsampling is tested on the experimental setup driven by a *dSPACE* DS1103. The resulting displacement $\widehat{y}_{\mathrm{MPC,exp}}$ and associated input signal $u_{\mathrm{MPC,exp}}$ are depicted by the orange lines in Fig. 6.13. Comparing the results, the observed displacements nearly match with the simulation. Only in the end an oscillation with low amplitudes can be seen. Due to this, the steady state is reached after about 1.0 s. This deviation is caused by the existing uncertainties, e.g., remaining creeping and hysteresis effects of the actuators, or the nonlinear behavior of the connecting rubber band which is modeled as a spring. Especially the higher voltages during the steady state indicates that the controller has to compensate a constant disturbance.

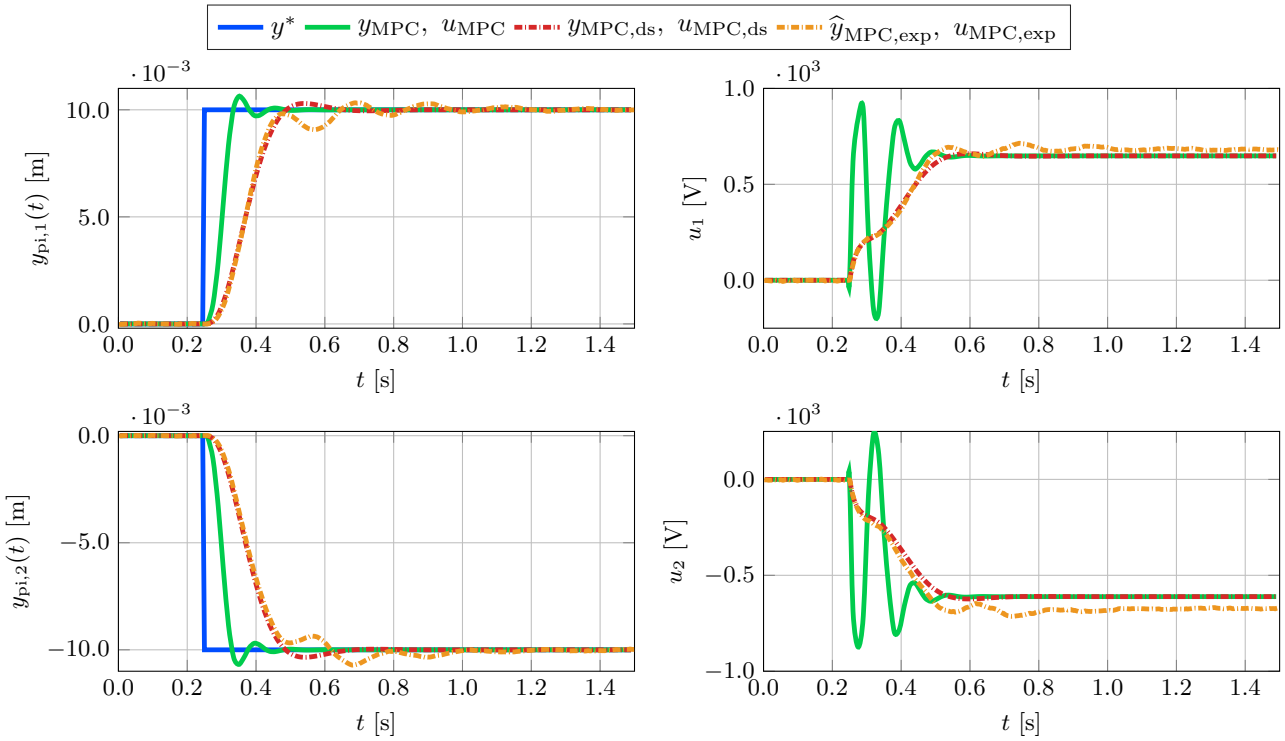

Figure 6.14.: Comparison of the transversal displacement at the points of interest $\widehat{y}_{\mathrm{pi},f}(t)$ with $f \in \{1, \ldots, 2\}$ of the simulation results of the original MPC (y_{MPC}, u_{MPC}), the move blocking by downsampling ($y_{\mathrm{MPC,ds}}$, $u_{\mathrm{MPC,ds}}$), and experimental results ($\widehat{y}_{\mathrm{MPC,exp}}$, $u_{\mathrm{MPC,exp}}$) of the move blocking approach, respectively.

Analog to the triple beam setup, the closed loop behavior is evaluated taking an external disturbance into account. Fig. 6.15 displays the resulting displacement after the disturbance is manually applied at $t = 0.4$ s. The resulting oscillation is attenuated by the MPC in less than 2 s, which displays a good performance.

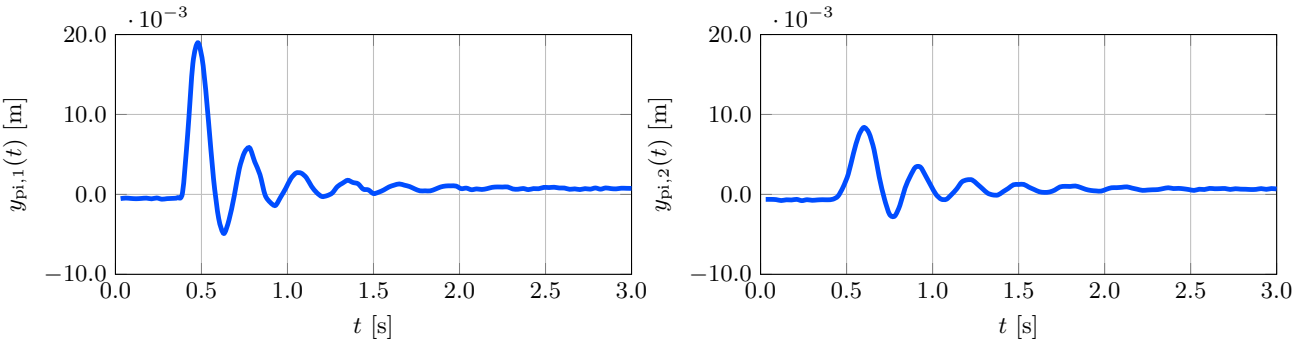

Figure 6.15.: Experimental results of the observed transversal displacement at the points of interest $\widehat{y}_{\mathrm{pi},f}(t)$ with $f \in \{1, \ldots, 2\}$ of the MPC approach using move blocking by downsampling considering an external disturbance.

In general, the MPC approach displays an overall good control performance considering the double beam setup. Nevertheless, this control concept is not further investigated in view of the wingsail project, due to its computational cost. This decision is based on two reasons.

At first, the question appears if the MPC approach is capable to deal with larger structures, e.g., the triple beam setup whose reduced system is described by 30 states and the embedded measurement concept. In contrast, the smaller double beam setup can be described by four states and already requires an enlarged sample time $t_{\mathrm{d}} = 3 \times 10^{-3}\,\mathrm{s}$ instead of $t_{\mathrm{d}} = 0.2 \times 10^{-3}\,\mathrm{s}$ and downsampling. A further decreasing of the prediction time is not feasible on a weakly damped structure as previously discussed. Compared to the double and triple beam the wingsail setup's geometry provides a higher amount of stiffness, so that the horizon should be shortened which is in contrast to the higher system dimension requiring larger evaluation times. However, the higher systems dimension requires larger evaluation times compared to the double beam.

Furthermore, the vision of the wingsail project is the design of an autonomous sailing yacht, which means the presented motion planning and tracking control approach is only one part of the full system and is not allowed to consume the complete computational power for itself. Considering the double beam setup the implementation of the MPC is done on a *dSPACE* DS1103. This system denotes a powerful rapid prototyping environment which can not be implemented on the model yacht due to a lack of space and capacity of payload in terms of weight. Therefore, all control algorithms have to run on an embedded real time controller like the `stm32` family. Such a system is lightweight and small, but it does not provide a comparable amount of computational power. However, the development in this area is high, so maybe the computational power will rise in the next years but on the other hand a rising amount of computational power most of the time goes hand in hand with a higher consumption of electric energy. For an autonomous vehicle, this means that the requirement of the battery capacity rises which leads to an increase of weight and / or space.

Due to this reasons and the fact that the MPC approach provides a comparable performance compared to the two-degrees-of-freedom control approach, the MPC approach is not further investigated.

6.2. Surface Interconnected Structure of Beams

As presented in Section 2.1.3 the experimental setup is based on $r = 2$ horizontal aligned carbon beams which touch each other at their free tip. This is why this delta beam configuration can be imagined as a segment of the wingsail. In addition, both beams are equipped with voltage controlled embedded MFC-patches displaying the system's actuators mounted on the inward facing surface of the beams. Analog to the double beam configuration, the delta beam configuration uses external laser sensors, see Fig. 2.6 and Table 2.3 for the precise location of the points of interest and the placement of the actuators. These measurements provide the input information of the Kalman filter, on which all control approaches rely in terms of the observed states or the observed outputs. Table 6.7 lists the considered design parameters of the Kalman filter.

Table 6.7.: Design parameters of the applied Kalman filter according to (5.15) and (5.16a) considering $r = 2$ beams $j = \{1,\ 2\}$ touching each other at the tip. The second order system is based on $N_j = 10$ second order system states per beam and $n_{\mathrm{pm}} = 1$ point of measurement using a laser sensor (Welotec GmbH type OWLF 4030 FA S1).

r_{o}	$q_{\mathrm{o},t}$	$q_{\mathrm{o,p},j}$	$q_{\mathrm{o,v},j}$	$q^{\mathrm{s}}_{\mathrm{o,p},j}$	$q^{\mathrm{e}}_{\mathrm{o,p},j}$	$q^{\mathrm{s}}_{\mathrm{o,v},j}$	$q^{\mathrm{e}}_{\mathrm{o,v},j}$
2.0×10^2	1.0×10^3	5.0×10^0	1.5×10^2	8.0×10^0	1.0×10^0	2.0×10^0	1.0×10^0

6.2.1. Evaluation of System Behavior Considering the Touching Constraint

To analyze the introduced model description, see Section 2.1.3 a series of voltage steps

$$\boldsymbol{u}(t) = \begin{bmatrix} u_1(t) \\ u_2(t) \end{bmatrix}, \quad \text{with} \quad \begin{aligned} u_1(t) &= 920\,\mathrm{V}\big(h(t-1\,\mathrm{s}) - h(t-13\,\mathrm{s})\big), \\ u_2(t) &= -920\,\mathrm{V}\big(h(t-7\,\mathrm{s}) + h(t-13\,\mathrm{s})\big), \end{aligned} \tag{6.8}$$

is applied in the simulation environment. Fig. 6.16 presents the results of the simulation considering the input signal (6.8).

This scenario considers a single actuation of the first beam at $t = 1\,\mathrm{s}$. If the touching constraint is fulfilled both beams have to move, where their tips have to display the same transversal deflection at all times $y_{\mathrm{tip},1} = y_{\mathrm{tip},2}\ \forall\, t$ due to the Lagrange multiplier $p(t)$ which can be interpreted as constraining force. At $t = 7\,\mathrm{s}$ the second beam is actuated which should result in a larger amplitude of the displacement due to the agonist-antagonist behavior of the setup's actuator configuration. Finally, at $t = 13\,\mathrm{s}$ both voltages are reduced to zero simultaneously, as depicted by the third subplot of Fig. 6.16.

The first subplot of Fig. 6.16 displays the transversal displacements $y_{\mathrm{tip},j}$ of the first ($j = 1$ depicted by the blue line) and second beam tip ($j = 2$ depicted by the green line). The results show that both deflections completely coincide. Hence, the touching constraint is fulfilled at all times. In addition, the resulting displacement is characterized by strong oscillations. However, in contrast to the vertical beam configuration their decay time is reduced to about 5 s due to the increased stiffness of the delta beam configuration.

The second subplot displays the Lagrange multiplier. It is noticeable that the Lagrange multiplier reacts with highly frequent oscillations at each voltage step considering amplitudes of at least a factor four of the following steady state. These oscillations decay within 1 s. After the first voltage step the multiplier remains at a steady state of about 0.0356 which can be interpreted as constraining force acting at the beam tips. This force ensures that both tips stay together. The first voltage step is applied only at the first beam which hence deflects. However, the actuators of second beam are not excited, this beam deflects only due to the constraining force acting at the beam's tip.

After a second voltage step the steady state of the constraining force's shrinks to 0.0047. This force results from the fact that without the touching constraint both beams would show a slightly other displacement. Concluding the simulation result the introduced system description displays the expected behavior. Therefore, the two-degrees-of-freedom control approach is designed based on this description and evaluated below of the experimental setup.

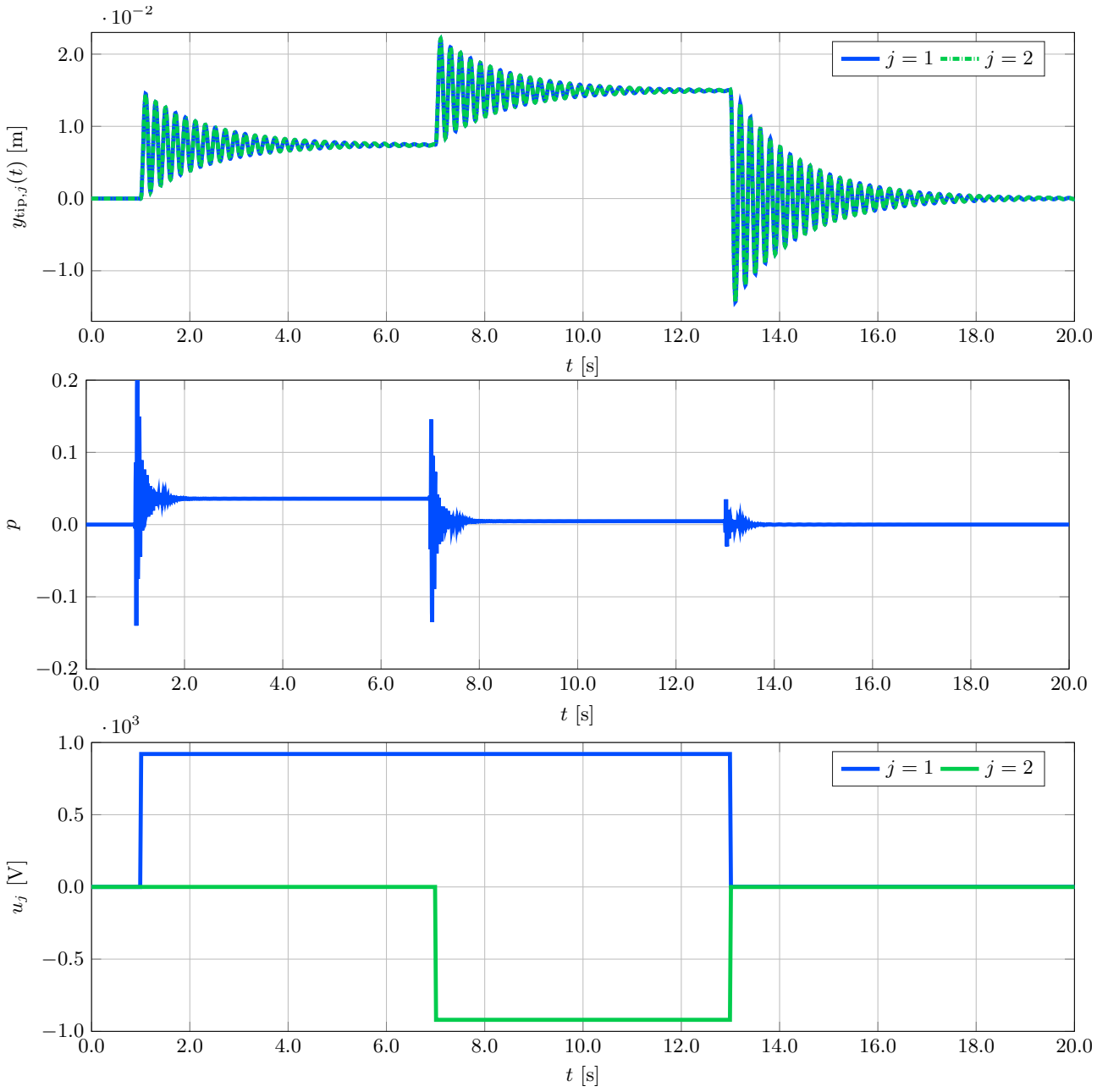

Figure 6.16.: Simulation result for the beams' tip displacement ($y_{\mathrm{tip},j}(t) = s_j(t, \ell) \ \forall \ j \in \{1, 2\}$) considering the input signal $\boldsymbol{u}(t) = \begin{bmatrix} u_1(t) & u_2(t) \end{bmatrix}^T$ given by (6.8).

6.2.2. Experimental Evaluation of the Open and Closed Loop System

To illustrate the open loop dynamics and to evaluate the designed Kalman filter, the same voltage signal (6.8) as used in the simulation is applied at the experimental setup. Fig. 6.17 displays the resulting transversal displacement measured by the laser sensor $y_{\mathrm{ol,L}}$ (blue line) and observed by the Kalman filter $\widehat{y}_{\mathrm{ol}}$ (green line) at the point of measurement located near the tip of the first beam. Note that in the following analysis only the deflection at the point of measurement is displayed. This location is identical to the first point of interest. In addition, the second point of interest yields the same deflection, due to the symmetric geometry of the delta beam configuration. To improve the comparability of the signals the measurement noise of the laser sensor are reduced by a first order low pass filter characterized by the cutoff frequency $f_{\mathrm{c}} = 100\,\mathrm{Hz}$. However, the observer uses the original data of the laser measurement. For the implementation and recording of the measurements a *dSPACE* DS1103 considering a sample time $t_{\mathrm{d}} = 2 \times 10^{-4}\,\mathrm{s}$ is used.

The resulting displacement shows a similar behavior compared to the simulation results. The small deviation is caused by model uncertainties and the neglected friction which applies on the beams' tips, where both beams slide on each others surfaces. Due to the friction, the decay time of the oscillation varies. This is why the friction depends on the beams' displacement or to be more precise the contact area on which both beams slide on depends on the displacement.

Comparing the actual measurement with the result of the observer reveals a good performance which fits the requirements of the feedback controller. Only small deviations between the laser measurements and the observer of less than 0.5 % are noticed. These errors result from remaining hysteresis and creeping effects, see Section 2.1.1.3.

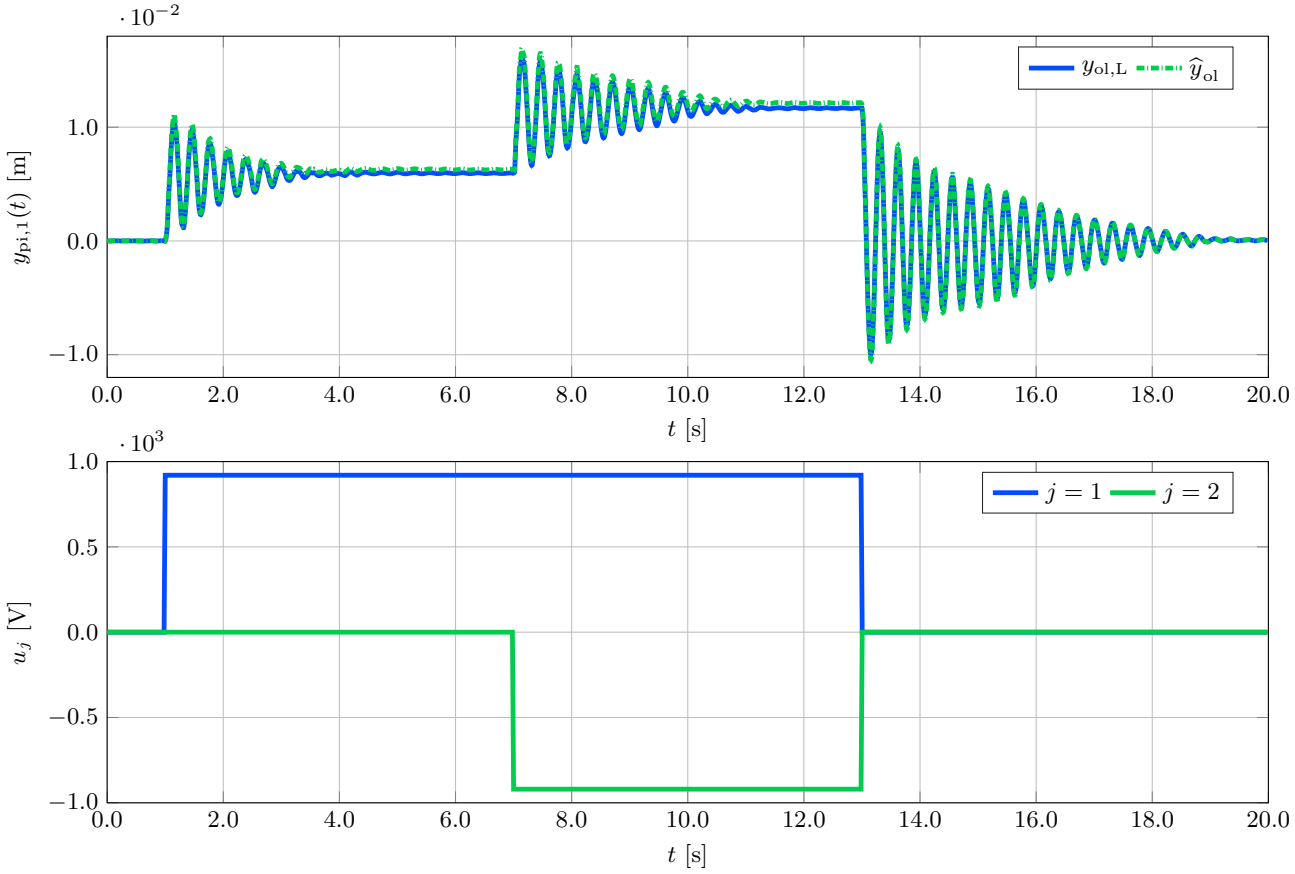

Figure 6.17.: System response to the applied input signals u_j (6.8). Comparison of the laser measurements $y_{\mathrm{ol,L}}$ and the observed displacement using a Kalman filter $\widehat{y}_{\mathrm{ol}}$ at the point of measurement. The laser measurements are processed by a first order low pass filter characterized by a cutoff frequency $f_{\mathrm{c}} = 100\,\mathrm{Hz}$ to reduce the measurement noise.

Analog to the triple beam configuration a rest-to-rest motion scenario is considered to evaluate the performance of the feedforward control and the two-degrees-of-freedom control approach. For this, three transitions between different steady state displacements are considered, see Fig. 6.18. At the beginning of the scenario, the system stays in the undeformed state $\boldsymbol{y}_{\mathrm{pi}}^{*}(0\,\mathrm{s}) = [0 \quad 0]^T \times 10^{-3}\,\mathrm{m}$. After $t = 1.5\,\mathrm{s}$ the steady state $\boldsymbol{y}_{\mathrm{pi}}^{*}(1.5\,\mathrm{s}) = [-17 \quad -17]^T \times 10^{-3}\mathrm{m}$ should be reached. The second transition starts at $t = 6\,\mathrm{s}$, where the desired steady state $\boldsymbol{y}_{\mathrm{pi}}^{*}(6.5\,\mathrm{s}) = -\boldsymbol{y}_{\mathrm{pi}}^{*}(1.9\,\mathrm{s}) = [17 \quad 17]^T \times 10^{-3}\mathrm{m}$ should be reached at $t = 6.5\,\mathrm{s}$. This transition describes a rest-to-rest motion connecting the positive and negative transversal displacement of the beams which correspond to 93.7 % of the maximal reachable steady state displacement. Finally, the last transition leads the system back into the undeformed state $\boldsymbol{y}_{\mathrm{pi}}^{*}(11.5\,\mathrm{s}) = [0 \quad 0]^T \times 10^{-3}\,\mathrm{m}$.

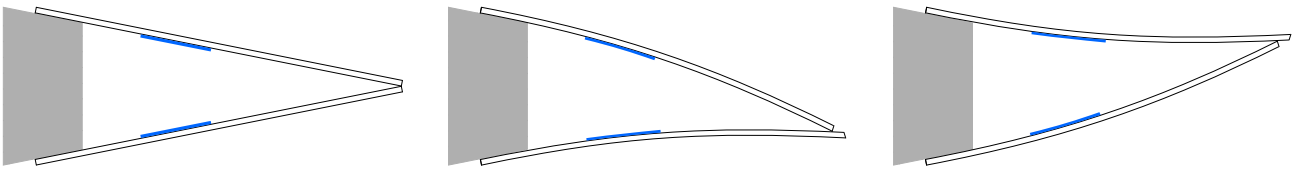

Figure 6.18.: Schematic visualization (top view) of the desired steady state displacement profiles of the designed rest-to-rest motion scenario chronologically sorted from left to right.

The focus of the evaluation is the control performance of the flatness-based motion planning and feedforward control as well as the two-degrees-of-freedom control approach based on an ID-T_1 and an extended Ackermann state feedback controller. The design parameters of these control approaches are listed in Table 6.8.

Table 6.8.: Design parameters of the considered two-degrees-of-freedom control approaches considering the flatness-based feedforward control (5.8a) taking (5.10) into account as well as the ID-T_1 (5.18), and an extended Ackermann state feedback controller (5.22) and (5.30).

feedforward control		ID-T_1 control		
T	g	k_{I}	k_{D}	$1/T_{\mathrm{idt}}$
5.0×10^{-1}	9.0×10^{-1}	1.4×10^{1}	2.0×10^{6}	150 Hz

extended Ackermann		
$\lambda_{\mathrm{sh,re}}$	$\lambda_{\mathrm{sh,im}}$	k_{a}
1.6×10^{0}	1.5×10^{0}	1.7×10^{1}

The first subplot of Fig. 6.19 displays the transversal displacement achieved for the rest-to-rest motion scenario, where the second subplot shows the control error defined by (6.5). The last two subplots display the associated input signals of the corresponding control approaches.

Comparing the reference trajectory y^* (blue line) with the result of the feedforward controls (green line) displays a feasible performance. The first transition is achieved without any oscillation. However, it takes about $t = 3.6\,\mathrm{s}$ until the desired steady state is reached, see also the associated error $\tilde{y}_{\mathrm{ff}}$. The second and last transitions are characterized by small oscillations which decay fast compared to the step response, see Fig. 6.17. Here, the control error $\tilde{y}_{\mathrm{ff}}$ reveals that the feedforward control is not capable to achieve steady state accuracy, especially the second steady state shows a deviation of about $0.5 \times 10^{-3}\,\mathrm{m}$.

To overcome this issue, the two-degrees-of-freedom control approaches are introduced considering an ID-T_1 (red line) and an extended Ackermann state feedback controller (orange). Both concepts result in a similar behavior and achieve steady state accuracy, where the ID-T_1 controller displays a slightly better performance. This slightly improved performance is characterized by a shorter decay time within the second transition and smaller voltage amplitudes.

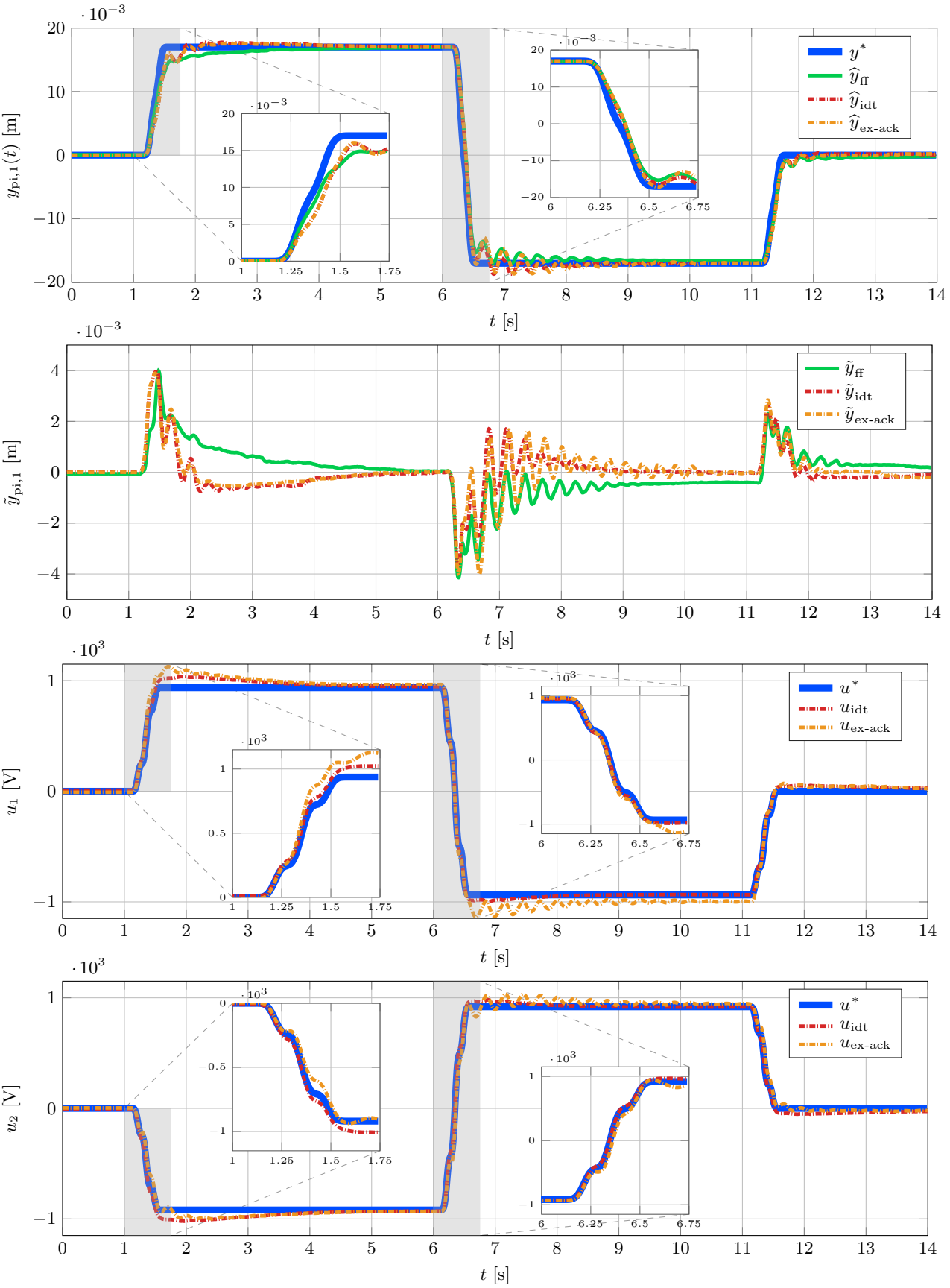

Figure 6.19.: Experimental results of the observed transversal displacement at the first point of interest $\widehat{y}_{\mathrm{pm},1}(t) = \widehat{y}_{\mathrm{pi},1}(t)$ of the reference trajectory y^*, the flatness-based feedforward control $\widehat{y}_{\mathrm{ff}}$, and the two-degrees-of-freedom control approach based on the ID-T_1 and the extended Ackermann controller $\widehat{y}_{\mathrm{idt}}$ and $\widehat{y}_{\text{ex-ack}}$, respectively, for the rest-to-rest motion scenario. The corresponding control errors and control inputs are depicted as well.

6.3. Wingsail Structure

The evaluation of the wingsail structure is split into two parts. At first, the results of the MOR method and of the flatness-based feedforward control are analyzed in numerical studies for different sets of design parameters. Afterwards, the feedforward control and the two-degrees-of-freedom control approach are tested on the experimental setup.

6.3.1. Simulation Results

The main objective of these numeric studies is to analyze and configure the MOR method leading to a proper reduced order system which fits the requirements of a real time implementation. Furthermore, a set of design parameters of the flatness-based feedforward control has to be determined in terms of the parameter of the Gevrey function T and g.

6.3.1.1. Validation of the Reduced Order Model

The finite dimensional system description of the wingsail structure introduced in Section 2.2 is characterized by $N = 93255$ DoFs, see Section 2.2.3.5. Hence, the first order system description results in $2N = 186510$ states.

To reduce the computational effort, especially in view of the real time capability, the POD is applied as MOR method, see Section 4.3. It is also possible to reduce the system order through the use of the modal truncation method as discussed by [59], see Section 4.1. Also the second order balanced truncation could be used, see Section 4.2. However, the POD method offers the best performance w.r.t. the system description. The modal truncation requires more reduced order states to cover the system behavior with the same accuracy as the POD approach, see [59]. In addition, the second order balanced truncation is based on the Gramians of the system. Considering the system of the wingsail structure the Gramians are difficult to determine due to the dimension of the system and the fact that the system matrices are ill-conditioned due to the characteristic eigenvalue distribution of a weakly damped and thin structure.

Below, three different choices of the number of POD bases $N_\mathrm{r} = \{1, 5, 10\}$ are analyzed, where the number of basis coincides with the number of second order system states of the reduced system. As mentioned before, the implementation of the POD method in the *Firedrake* framework is done by the MOR-projector [4].

To evaluate the accuracy of the resulting reduced order systems compared to the full order system the stepwise actuation

$$\boldsymbol{u}(t) = -\begin{bmatrix}700 & 700 & 700 & 700\end{bmatrix}^T \mathrm{V}\, h(t - 0.1s) \tag{6.9}$$

is applied. Fig. 6.20 displays the resulting transversal displacement at the points of interest $y_{\mathrm{pi},f}(t) = s^1(t, \boldsymbol{z}_{\mathrm{pi},f})$ with $f \in \{1, \ldots, 4\}$ of the full order system $N = 93255$ and three different reduced order systems. The reduced system based on $N_\mathrm{r} = 1$ second order states (green line) clearly shows a significant systematic error compared to the full order system (blue line). In contrast, the reduced systems based on $N_\mathrm{r} = 5$ and $N_\mathrm{r} = 10$ second order states (red and orange line, respectively) seem to completely cover the behavior of the full order system, except for the small deviation at the 4^{th} point of interest.

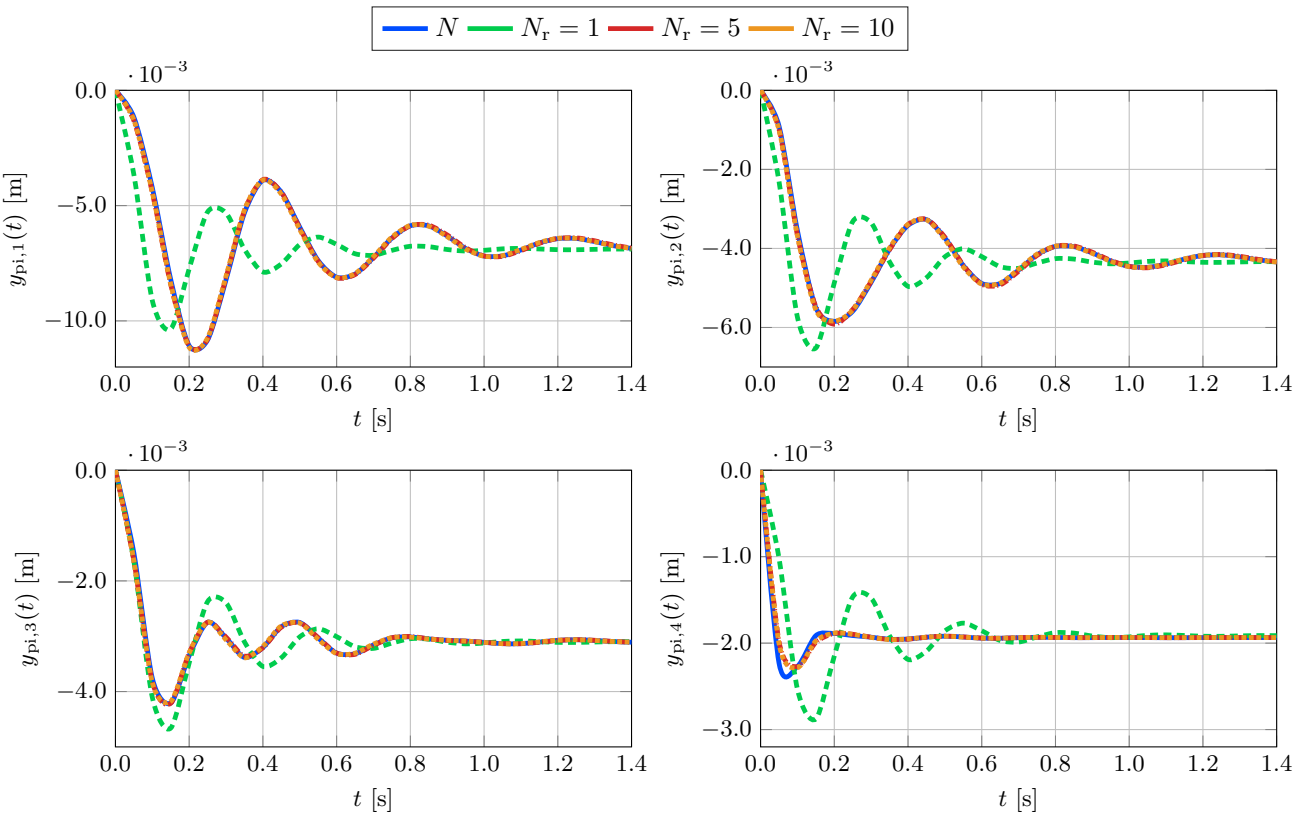

Figure 6.20.: Comparison of the step response of the full order system ($N = 93255$ DoFs) with the reduced order systems considering $N_\mathrm{r} = \{1, 5, 10\}$ POD bases.

Considering the time dependent displacement at the points of interest $N_\mathrm{r} = 5$ seems to provide a good trade-off between accuracy and computational effort. However, this conclusion is only based on a pointwise analysis, so it is possible that the reduced model only displays a good behavior on these specific locations. Therefore, a performance measure is required, which considers the full displacement profile according to the used function space of the FEM implementation. Such a measure is given by the H^1 error norm [17] between the displacement profile of the full order system $\boldsymbol{s}_N(t, \boldsymbol{z})$ and the recovered (or projected) profile $\boldsymbol{s}_{N_\mathrm{r}}(t, \boldsymbol{z})$ based on the reduced order simulation

$$\left\| \boldsymbol{s}_N(t, \boldsymbol{z}) - \boldsymbol{s}_{N_\mathrm{r}}(t, \boldsymbol{z}) \right\|_{H^1} = \left(\left\| \boldsymbol{s}_N(t, \boldsymbol{z}) - \boldsymbol{s}_{N_\mathrm{r}}(t, \boldsymbol{z}) \right\|_{L^2}^2 + \left\| \nabla \cdot \left(\boldsymbol{s}_N(t, \boldsymbol{z}) \right) - \nabla \cdot \left(\boldsymbol{s}_{N_\mathrm{r}}(t, \boldsymbol{z}) \right) \right\|_{L^2}^2 \right)^{\frac{1}{2}}. \tag{6.10}$$

Fig. 6.21 depicts the temporal behavior of the norm. As seen before the increasing number of considered POD bases from $N_\mathrm{r} = 1$ to $N_\mathrm{r} = 5$ improves the performance substantially. However, the comparison of higher values leads to a similar performance, because the error caused by the MOR approaches is provoked by the numerical approximation of the spatial and temporal integrations. In summary, the norm supports the conclusion of a good trade-off between accuracy and computational effort. Therefore, the number of considered POD bases is set to $N_\mathrm{r} = 5$, where the resulting reduced order system defines the origin of the flatness-based feedforward control design which is analyzed below.

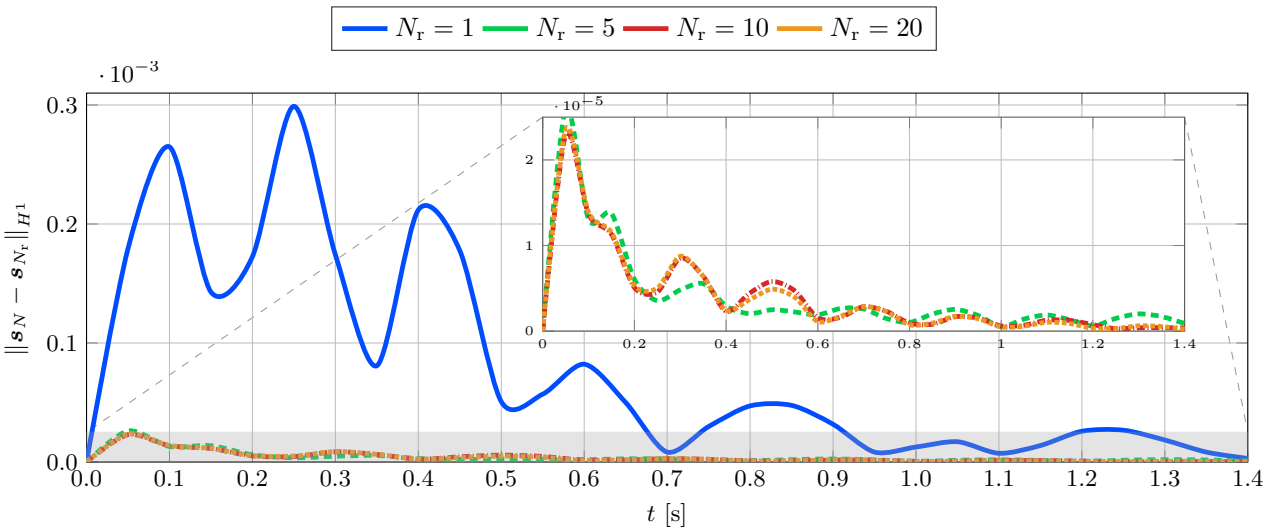

Figure 6.21.: Validation of MOR's performance by the comparison of the H^1 error norm (6.10) over time considering different numbers of POD bases $N_r = \{1, 5, 10, 20\}$.

6.3.1.2. Evaluation of the Flatness-Based Feedforward Control

Below, different configurations of the feedforward controls are analyzed, see Table 6.9. For this purpose, a rest-to-rest motion scenario is considered connecting the undeformed state $\boldsymbol{y}_{\mathrm{pi}}^* = [0 \quad 0 \quad 0 \quad 0]^T \times 10^{-3}\,\mathrm{m}$ with a deflected state $\boldsymbol{y}_{\mathrm{pi}}^* = -[7.6 \quad 4.9 \quad 3.5 \quad 2.2]^T \times 10^{-3}$ which denotes about 80 % of the maximally reachable displacement.

Table 6.9.: Analyzed configuration sets of feedforward control design parameters.

param. \ config.	$\mathcal{S}_1$	$\mathcal{S}_2$	$\mathcal{S}_3$	$\mathcal{S}_4$
T	0.5 s	0.6 s	0.6 s	0.7 s
g	0.5	0.7	0.5	0.5

Fig. 6.22 shows the simulation results of the feedforward control approach for the different parameter sets. The flatness-based feedforward controller design is based on the reduced order system. The resulting reference trajectories are displayed on the right side of Fig. 6.22 by the solid lines. In addition, the left side displays the associated input signals. The resulting displacements (dashed lines) are determined by the application of the input signals designed on the reduced system to the full order system.

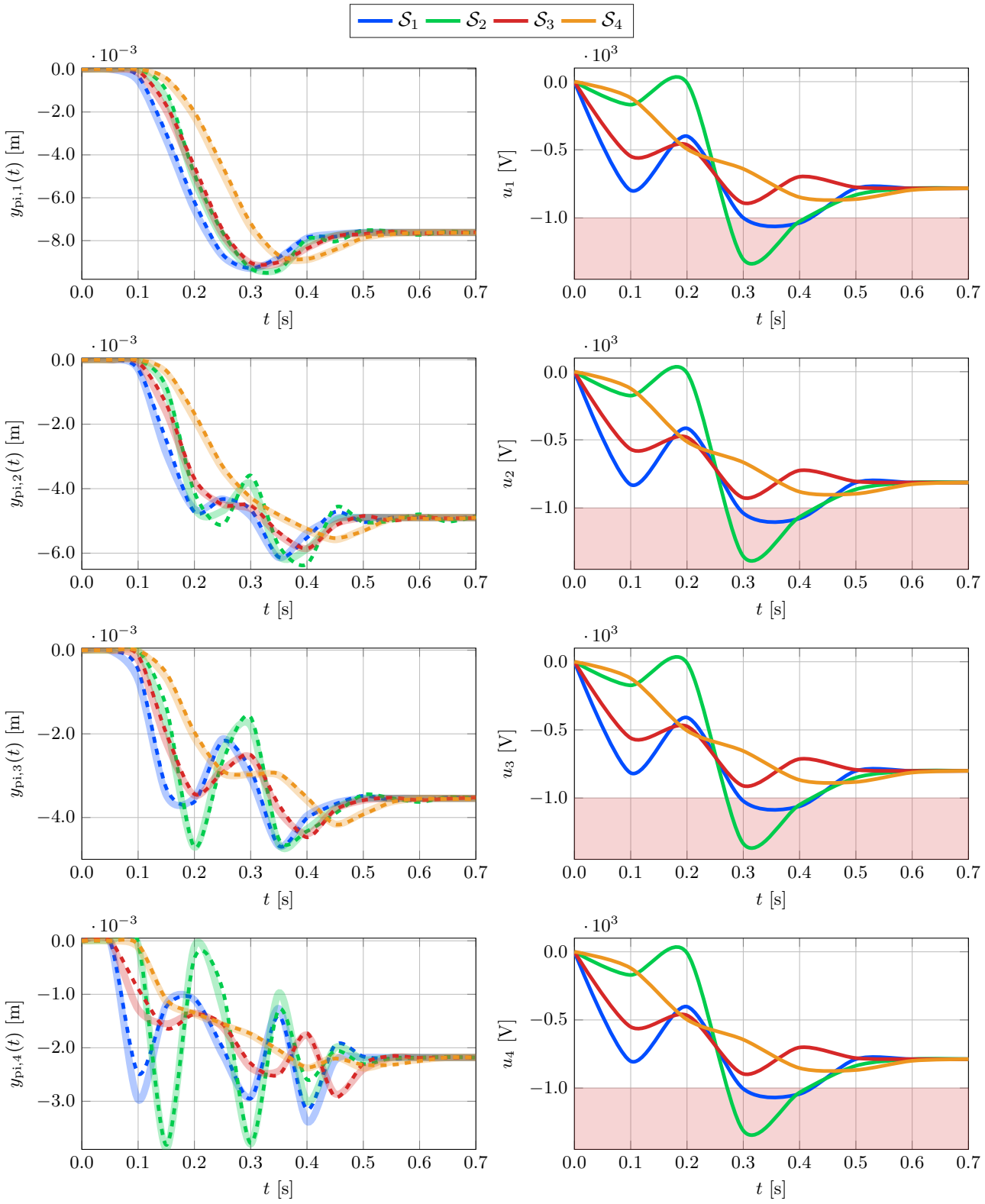

Figure 6.22.: *Left:* Transversal displacements over time at the points of interest. The dashed lines display the simulation results considering the full order system and the solid lines depict the pre-calculated reference trajectories taking the flatness-based feedforward control approach into account with the parameter sets listed by Table 6.9 based on the reduced order system.
Right: The associated input signals are shown, where the red areas mark the input's saturations at the experimental setup.

The difference between the actual displacement and the reference trajectory is marginal. The only exception is the second point of interest considering the $\mathcal{S}_2$ configuration which means that the accuracy of the reduced order system matches the requirements of the feedforward control design. This result supports the previous choice regarding the number of considered POD bases. In addition, each configuration reaches the desired steady state within its expected finite transition time T.

However, the different choices of T and g affect the transition phase. Taking the voltage signals into account the $\mathcal{S}_1$ and $\mathcal{S}_2$ configurations enter the area of saturation, this is why both configurations are excluded for the real time implementation. The remaining results based on the $\mathcal{S}_3$ and $\mathcal{S}_4$ parameter sets stay in the feasible area and are further investigated for their energy consumption.

For this purpose, the electric work of the feedforward control is analyzed. The electric work is defined as the integral of electric power P_{elec} over time

$$W_{\mathrm{elec}} = \int_{t_1}^{t_2} P_{\mathrm{elec}} \,\mathrm{d}t = \int_{t_1}^{t_2} U(t) I(t) \,\mathrm{d}t, \tag{6.11}$$

where $U(t)$ and $I(t)$ denote the applied voltage and electric current, respectively, see [102]. The current can be reformulated as $I(t) = \frac{U(t)}{Z}$ considering the constant impedance $Z = R + \mathrm{j}X$ composed of the resistance R and the reactance X of the circuit leading to

$$W_{\mathrm{elec}} = \int_{t_1}^{t_2} \frac{U^2(t)}{Z} \,\mathrm{d}t. \tag{6.12}$$

For the experimental setup of the wingsail the impedance is based on the resistance of the wires connecting the voltage amplifiers and the MFC-patches, the soldering joints as well as the capacities of the patches itself. The exact values of the single impedances are unknown and have to be measured by using special measuring circuits. Nevertheless, to answer the question which setting of the feedforward controls consumes the most energy a proportional measure to the electric work can be used neglecting the specific value of the impedance. Taking the experimental setup into account this measure yields

$$W_{\mathrm{elec}}^{\sim} = \sum_{k=1}^{4} \int_{0}^{t} U_{\mathrm{a}_k}^2(\tau) \,\mathrm{d}\tau. \tag{6.13}$$

Below, this proportional measure is referred to as the consumed energy. Fig. 6.23 displays the temporal behavior taking the different feedforward control parameterizations listed in Table 6.9 into account. In general, the comparison reveals that the fastest configuration requires the highest amount of energy as expected. However, in particular there are some deviations from this expectation. The input trajectory of the $\mathcal{S}_2$ configuration consumes more energy than the $\mathcal{S}_1$ configuration, although the $\mathcal{S}_1$ configuration is about 0.1 s faster. Here, the higher value of g of the $\mathcal{S}_2$ configuration results in higher amplitudes of the voltage signal, see right side of Fig. 6.22, which in total leads to a higher energy consumption.

Focusing on the results of the $\mathcal{S}_3$ and $\mathcal{S}_4$ parameter sets, which lead to feasible voltage trajectories, reveals a higher energy consumption of the $\mathcal{S}_3$ configuration. In contrast, the temporal improvements within the transient phase are marginal. This is why the $\mathcal{S}_4$ configuration is used for the experimental evaluation.

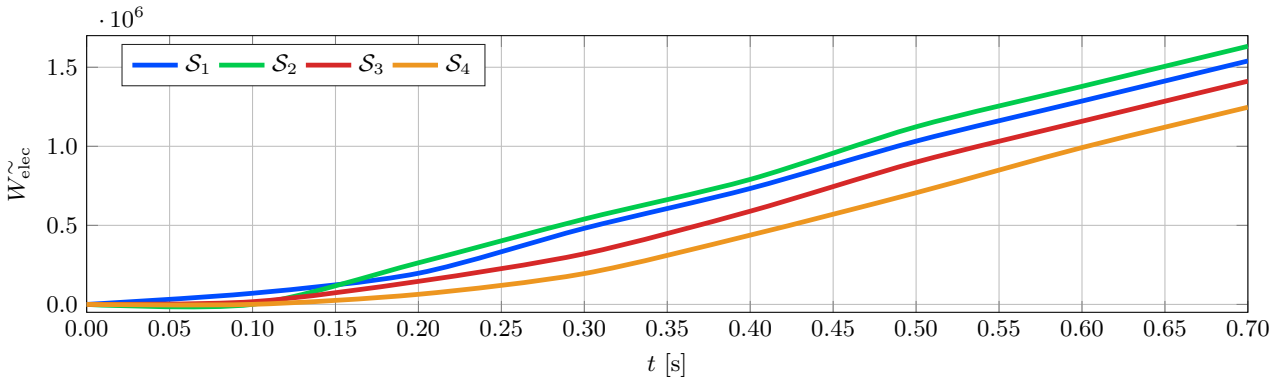

Figure 6.23.: Comparison of the energy consumption of the different parameter settings, see Table 6.9, of the feedforward controls input trajectories depicted by Fig. 6.22.

6.3.2. Experimental Results

Below the experimental results are discussed. At first the step response of the open loop system is analyzed. Secondly, the performance of the flatness-based feedforward control and the two-degrees-of-freedom control approach are evaluated taking three different scenarios into account. Analog to the triple beam configuration, the results of the LQ and the Ackermann state feedback controllers display a similar behavior. This is why the Ackermann state feedback controller is neglected in the following discussion. Hence, the considered feedback controllers are the ID-T_1, the LQ and the extended LQ based approaches, where the necessary design parameters are listed in Table 6.10.

6.3.2.1. Step Response

To illustrate the open loop dynamic of the wingsail Fig. 6.24 displays the transversal deflection at the points of interest $y_{\text{pi},i}$ with $i \in \{1, \ldots, 4\}$ for a voltage step

$$\boldsymbol{u}(t) = -\begin{bmatrix}700 & 700 & 700 & 700\end{bmatrix}^T \text{V}\, h(t - 0.5\,\text{s}). \tag{6.14}$$

These voltage values correspond to a steady state deflection of $\boldsymbol{y}_{\text{pi}}^* = -[7.0 \quad 4.5 \quad 3.4 \quad 2.2]^T \times 10^{-3}$ which is similar to the simulation results for the evaluation of the feedforward controller, see Section 6.3.1.2. The frequency of the resulting oscillation depends on the distance between the point of measurement and the mast, leading to the statement that the shorter the distance gets the higher the frequency becomes. In fact, it is not the distance between the mast and the point of measurement it is the length of the segment which affects the eigenfrequency similar to a cantilever beam.

The oscillation's decay time at the different points of measurement varies depending on to the frequencies. Due to the stiffness of the flexible structure, the steady state is reached after three oscillation periods. At the first point of measurement ($g = 1$) located near the bottom of the sail the steady state is reached after about 1.2 s. Considering the last point of measurement ($g = 4$) located near the top the decay time is given by about 0.1 s. The oscillations are further characterized by an overshooting which is within a range of 200 % to 10 % from bottom to top.

In addition, Fig. 6.24 provides a comparison between the laser measurements $y_{\text{ol,L}}$ (blue line) and the observed output $\widehat{y}_{\text{ol}}$ (green line). The laser measurement directly captures the transversal displacement at the points of interest $z_{\text{pi},f} = z_{\text{pm},g}$ with $f, g \in \{1, \ldots, 4\}$, see Fig. 2.7 and Table 2.5. To reduce noise these signals passed through a first order low pass filter characterized by a cutoff frequency of $f_{\text{c}} = 100\,\text{Hz}$. The observer in terms of a Kalman filter, see Section 5.2, uses the previously discussed reduced order system based on $N_{\text{r}} = 5$ POD bases. Its design parameters are listed in Table 6.11. The implementation and recording of measurements is done considering a *dSPACE* MicroLabBox [31] with an fixed sample time $t_{\text{d}} = 2 \times 10^{-4}\,\text{s}$.

In general, the observer displays a good performance w.r.t. to the dynamics of the system and only the last point of interest displays larger deviations. This can be explained by the deviation between the experimental setup and the CAD design which states the origin of the mathematical description as discussed in the beginning of Section 3.2.2.3. Nevertheless, the resulting accuracy of the observed outputs and states matches the requirements of a closed loop control design. Furthermore, the observed states enable an offline post process which reconstructs the complete displacement field of the wingsail.

Table 6.10.: Design parameters of the considered two-degrees-of-freedom control approaches considering the flatness-based feedforward control (5.8a) taking (5.10) into account as well as the ID-T_1(5.18), the LQR (5.29c), and and the extended LQR feedback controller (5.31). For each feedback controller two parameter sets are provided, the default configuration is used within rest-to-rest motion scenarios and the second one deals with the disturbance rejection scenario (dist. rejc. scenario).

feedforward control					
T			g		
7.0×10^{-1}			5.0×10^{-1}		
ID-T_1 control – default configuration			ID-T_1 control – dist. rejc. scenario		
k_I	k_D	$1/T_\mathrm{idt}$	k_I	k_D	$1/T_\mathrm{idt}$
1.8×10^1	2.0×10^6	150 Hz	1.8×10^1	8.0×10^6	150 Hz
LQR – default configuration					
r_c	$q_{\mathrm{c},t}$		$q_\mathrm{c,p}$	$q_\mathrm{c,v}$	
1.0×10^{-3}	1.0×10^6		1.0×10^1	2.0×10^{-1}	
$q^\mathrm{s}_{\mathrm{c,p\|vp}}$	$q^\mathrm{e}_{\mathrm{c,p\|vp}}$		$q^\mathrm{s}_{\mathrm{c,p\|vv}}$	$q^\mathrm{e}_{\mathrm{c,p\|vv}}$	
1.0×10^0	4.0×10^0		1.0×10^0	4.0×10^0	
LQR – dist. rejc. scenario					
r_c	$q_{\mathrm{c},t}$		$q_\mathrm{c,p}$	$q_\mathrm{c,v}$	
1.0×10^{-3}	1.0×10^7		1.0×10^1	6.0×10^{-1}	
$q^\mathrm{s}_{\mathrm{c,p\|vp}}$	$q^\mathrm{e}_{\mathrm{c,p\|vp}}$		$q^\mathrm{s}_{\mathrm{c,p\|vv}}$	$q^\mathrm{e}_{\mathrm{c,p\|vv}}$	
1.0×10^0	4.0×10^0		1.0×10^0	4.0×10^0	
extended LQR – default configuration			extended LQR – dist. rejc. scenario		
k_lq			k_lq		
2.0×10^1			2.0×10^1		

Table 6.11.: Design parameters of the applied Kalman Filter according to (5.15) and (5.29b) considering $N_\mathrm{r} = 5$ reduced second order system states provided by the POD method and $n_\mathrm{pm} = 4$ points of measurement using the installed laser sensor (Welotec GmbH type OWLF 4030 FA S1).

r_o	$q_{\mathrm{o},t}$	$q_{\mathrm{o,p},j}$	$q_{\mathrm{o,v},j}$	$q^\mathrm{s}_\mathrm{o,p}$	$q^\mathrm{e}_\mathrm{o,p}$	$q^\mathrm{s}_\mathrm{o,v}$	$q^\mathrm{e}_\mathrm{o,v}$
5.0×10^2	1.0×10^0	5.0×10^2	5.0×10^4	2.0×10^0	1.0×10^0	2.0×10^0	1.0×10^0

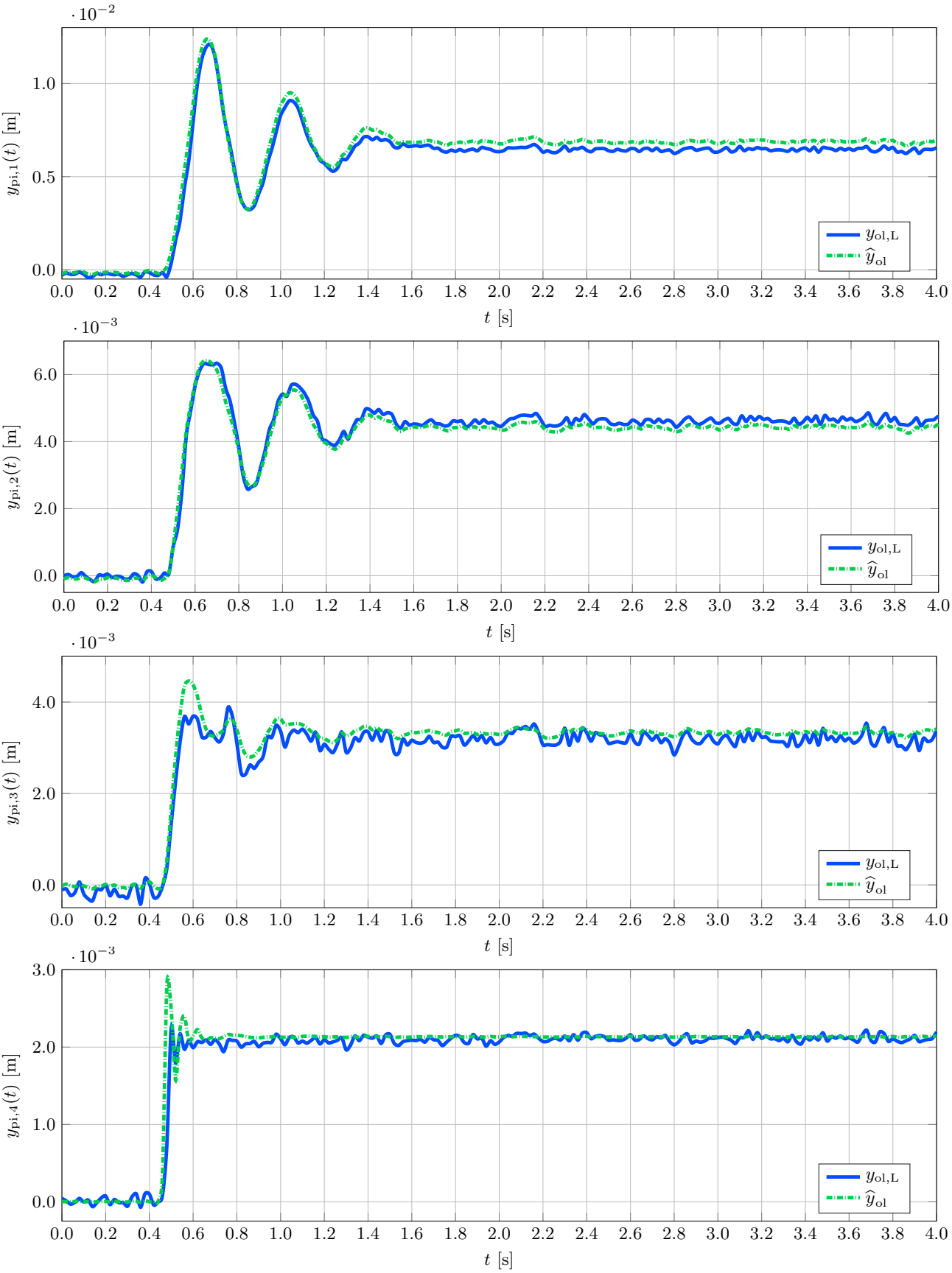

Figure 6.24.: Step response for the voltage step (6.14). The laser measurements $y_{\mathrm{ol,L}}$ consider a first order low pass filter characterized by a cutoff frequency of $f_{\mathrm{c}} = 100\,\mathrm{Hz}$. The observed deflections of the points of interest are determined by a Kalman filter with the used design parameters listed in Table 6.11.

6.3.2.2. Feedforward and Two-Degrees-of-Freedom Control Approach

Below, three different experimental scenarios are discussed and analyzed. To improve the readability each scenario arranges the figures of the displacements at the points of interest and the associated voltages on a double page.

Uniform Displacement Scenario The first scenario considers a rest-to-rest motion based on three transitions between different steady state displacements, see Fig. 6.31.

At the beginning of the scenario, the system is situated in the undeformed state $\boldsymbol{y}^*_{\mathrm{pi}}(0\,\mathrm{s}) = [0 \quad 0 \quad 0 \quad 0]^T \times 10^{-3}\,\mathrm{m}$. After $t = 1.7\,\mathrm{s}$ the steady state $\boldsymbol{y}^*_{\mathrm{pi}}(1.7\,\mathrm{s}) = -[8.4 \quad 5.4 \quad 3.9 \quad 2.4]^T \times 10^{-3}\mathrm{m}$ should be reached considering a steady input signal of $\boldsymbol{u}^*(t) = -[787 \quad 818 \quad 801 \quad 788]^T\,\mathrm{V}$.

The second transition starts at $t = 6\,\mathrm{s}$, where the desired steady state $\boldsymbol{y}^*_{\mathrm{pi}}(6.7\,\mathrm{s}) = -\boldsymbol{y}^*_{\mathrm{pi}}(1.7\,\mathrm{s})$ should be reached at $t = 6.7\,\mathrm{s}$. This transition describes a rest-to-rest motion connecting the positive and negative transversal displacement of the wingsail which correspond to 80 % of the maximally reachable steady state displacement. Finally, the last transition results in the undeformed state $\boldsymbol{y}^*_{\mathrm{pi}}(11.7\,\mathrm{s}) = \boldsymbol{y}^*_{\mathrm{pi}}(0\,\mathrm{s})$.

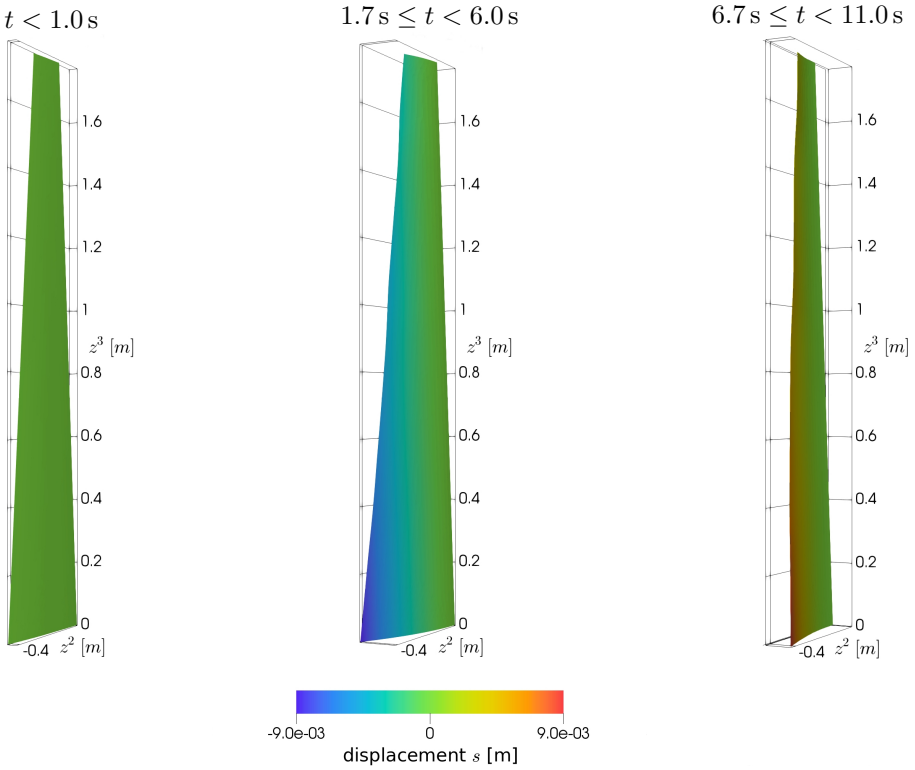

Figure 6.25.: Visualization of the desired steady state displacement profiles of the uniform displacement scenario scaled by a factor 10. All graphics are generated using *ParaView* [52, 7].

On the following two pages, the results of the flatness-based feedforward control are compared with a simple voltage ramp which connects the same steady state voltages as introduced in the scenario description. Below these figures the results are discussed. Thereafter, the two-degrees-of-freedom control approaches considering an ID-T_1, LQ, and extended LQ based feedback controller are analyzed.

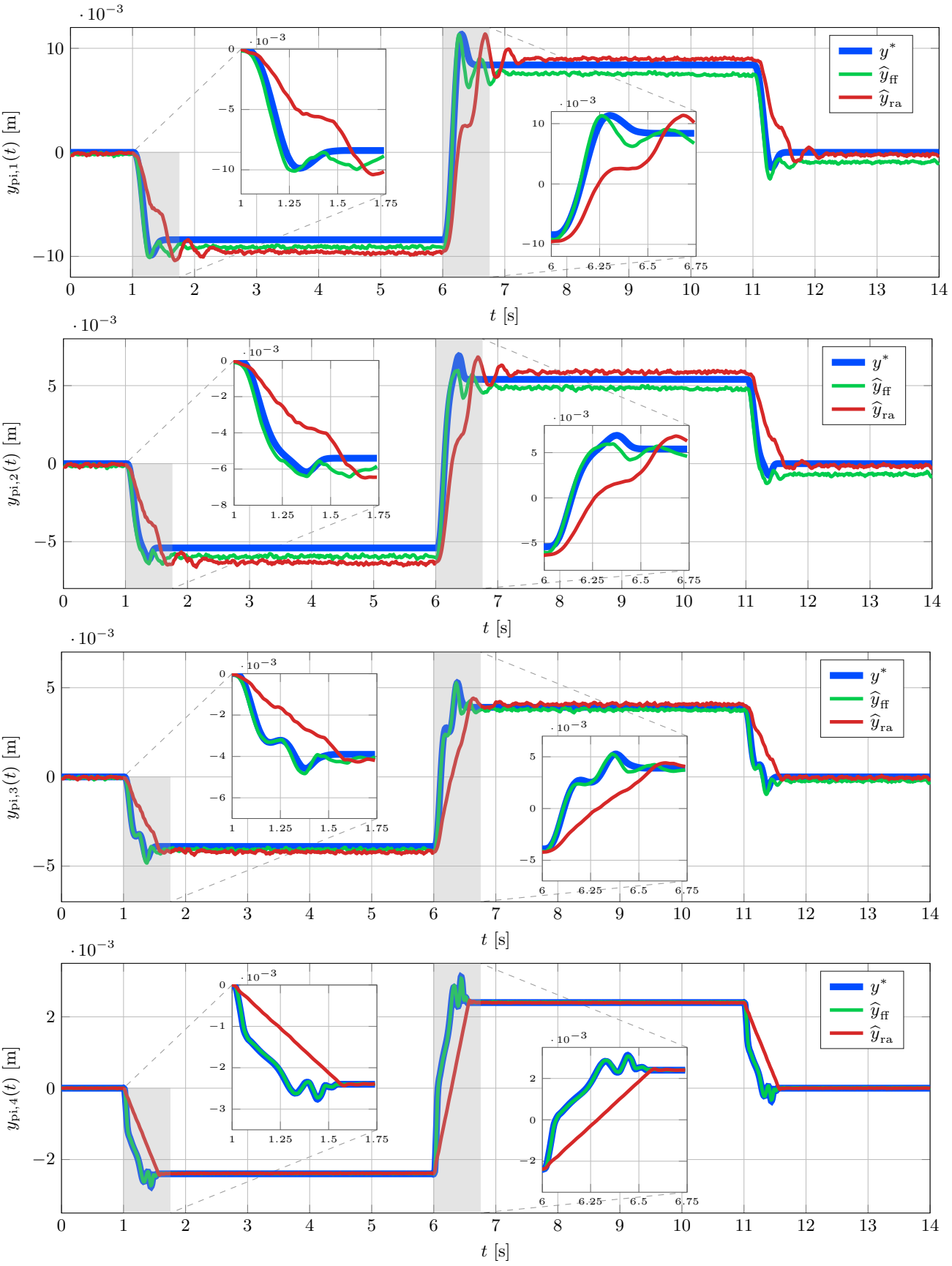

Figure 6.26.: Experimental results of the observed transversal displacement at the points of interest $\widehat{y}_{\mathrm{pi},f}(t)$ with $f \in \{1, \ldots, 4\}$ of the reference trajectory y^*, the flatness-based feedforward control $\widehat{y}_{\mathrm{ff}}$, and the results of a ramp shaped voltage input $\widehat{y}_{\mathrm{ra}}$ considering the uniform displacement scenario.

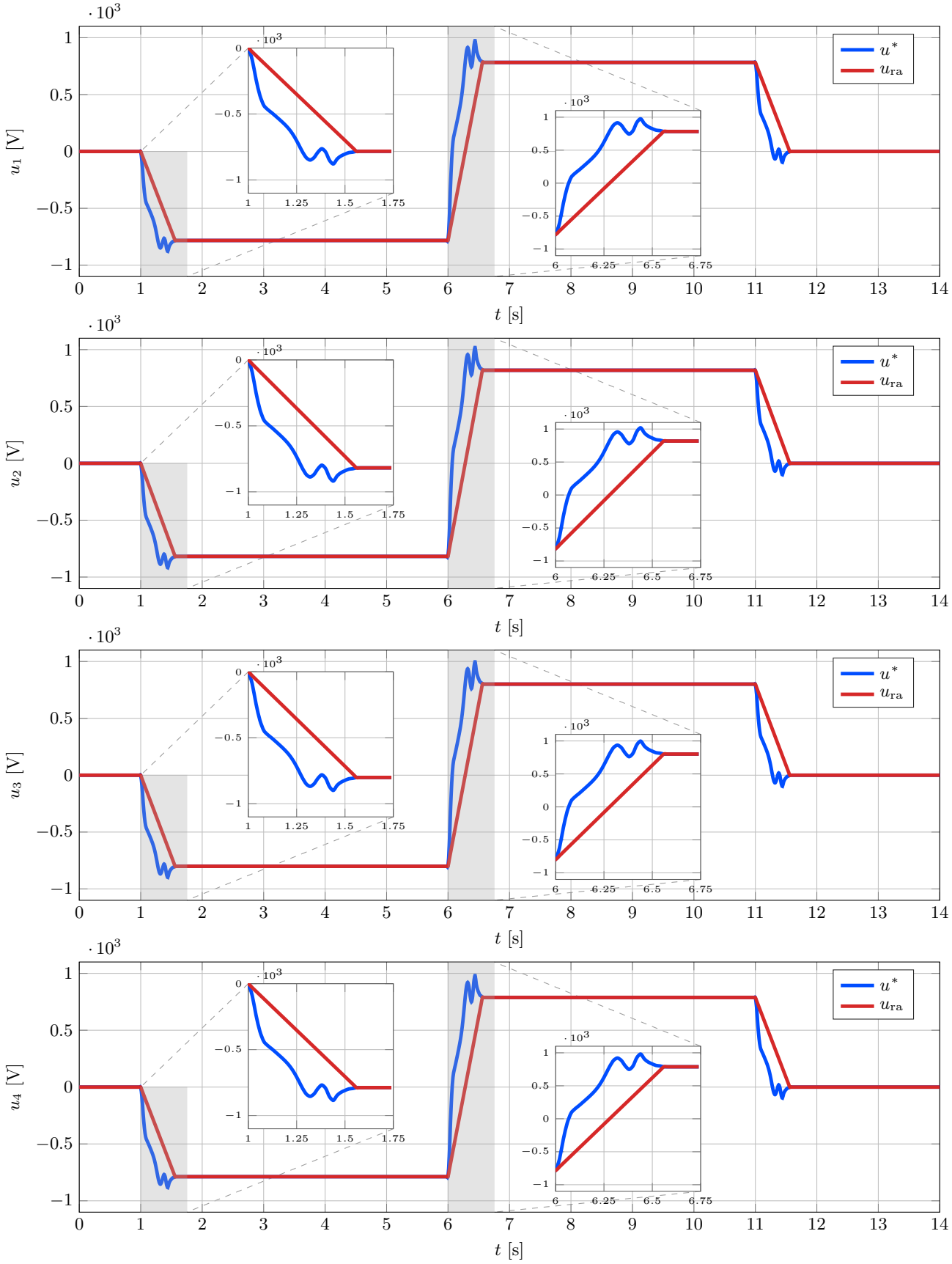

Figure 6.27.: Input signals of the MFC-actuators $k \in \{1, \ldots, 4\}$ of the flatness-based feedforward control u^* and the voltage ramp u_{ra} considering the uniform displacement scenario.

The reference trajectory y^* at the points of interest of the flatness-based motion planning approach (blue line of Fig. 6.26) displays the previously discussed transitions considering the finite transition time $T = 0.7\,\mathrm{s}$. To reach the desired steady state within the given time interval the motion planning approach induces an overshoot of about 15 % at the "small" first and of about 30 % at the "large" second transition.

Due to the numeric studies and the acquired design parameter set the associated input signal u^* stays within the feasible range of the actuators, see the blue lines of Fig. 6.27. The resulting displacement trajectories of the feedforward controller $\widehat{y}_{\mathrm{ff}}$ (Fig. 6.26 green lines) display a good fit with the reference trajectory during the transition phase. Only in the end of the transition a small deviation leads to a short oscillation for the first two points of interest. However, instead of the desired 0.7 s the steady state is reached after 1.0 s. The 3^{rd} and 4^{th} point of interest are not affected due to the stiffness and damping effect which rises from bottom to top of the structure, see the discussion in the beginning of Section 3.2.2. In addition, it appears that the small steady state error of about $1 \times 10^{-3}\,\mathrm{m}$ is caused by the remaining uncertainties. In contrast, the open loop response $\widehat{y}_{\mathrm{ra}}$ of the considered voltage ramp (red lines) leads to stronger oscillations. The amplitudes of these unintend oscillations are comparable with the result of the feedforward control. Nevertheless, the decay time rises to 1.5 s.

Compared to the results of the triple beam configuration for which the deviation between the flatness-based feedforward control and the applied ramp shaped voltage signal are rather large, see Fig. 6.4, the wingsail displays only moderate deviations. This is caused by the different characteristics of the structures, where the wingsail is characterized by an increased stiffness and damping which is introduced by its geometric configuration.

Below the results of the two-degrees-of-freedom control approaches are presented based on an ID-T_1, a LQR, and an extended LQR feedback controller, $\widehat{y}_{\text{idt}}$, $\widehat{y}_{\text{lq}}$, and $\widehat{y}_{\text{ex-lq}}$, respectively. The considered reference trajectory y^* at the points of interest is identical to the previous comparison, see the blue lines of Fig. 6.28. Hence, the associated input signals u^* (blue lines of Fig. 6.29) are also identical.

In fact, the resulting dynamic of the feedforward control displays a good performance, so the main focus of the two-degrees-of-freedom control approach is the reduction of the remaining steady state deviation. Here, the LQR reduces the steady state error about a factor two. In contrast, the ID-T_1 as well as the extended LQ feedback controller guarantee steady state accuracy taking constant disturbances or uncertainties into account. Comparing the resulting trajectories of the displacement, all three approaches display similar behavior. The actual deviations appear through the analysis of the input signals, see Fig. 6.29, and the resulting control errors $\tilde{y}_f(t)$ with $f \in \{1, \ldots, 4\}$ defined by (6.5), see Fig. 6.30.

The comparison of the voltage signals results in the observation, that the ID-T_1 controller in terms of the input signal u_{idt} consumes more energy than the other approaches, especially at the first two MFC-actuators which are used to reduce the error that appears at the first two points of interest. Nevertheless, this deviation is marginal. The comparison of the control errors reveals the control performance at a glance. The error accomplished by the feedforward control $\tilde{y}_{\text{ff}}$ (blue line) is reduced significantly by each of the considered two-degrees-of-freedom control approaches.

In general, the transition phases display the largest errors, as expected. Considering the magnified areas displaying the transversal displacement during the transition phases, see Fig. 6.28, leads to the impression that these errors occur because the results of the closed loop behavior are always ahead of the reference trajectory. Actually, the same behavior can be seen considering the open loop behavior, see the magnified areas of Fig. 6.29 and $\tilde{y}_{\text{ff}}$ (Fig. 6.30 blue lines). This indicates that the deviation of the results compared to the reference trajectory is caused by the feedforward control, most certainly due to remaining uncertainties. However, the error quickly decays and the magnitudes of the error are moderate. Furthermore, the two-degrees-of-freedom control approaches display a slight improvement.

During the steady state phases the main impact of the feedback controllers can be seen. Especially the ID-T_1 and the extended LQ feedback controller achieve a remarkable performance leading to steady state accuracy. This is why both approaches are further analyzed in second rest-to-rest motion scenario.

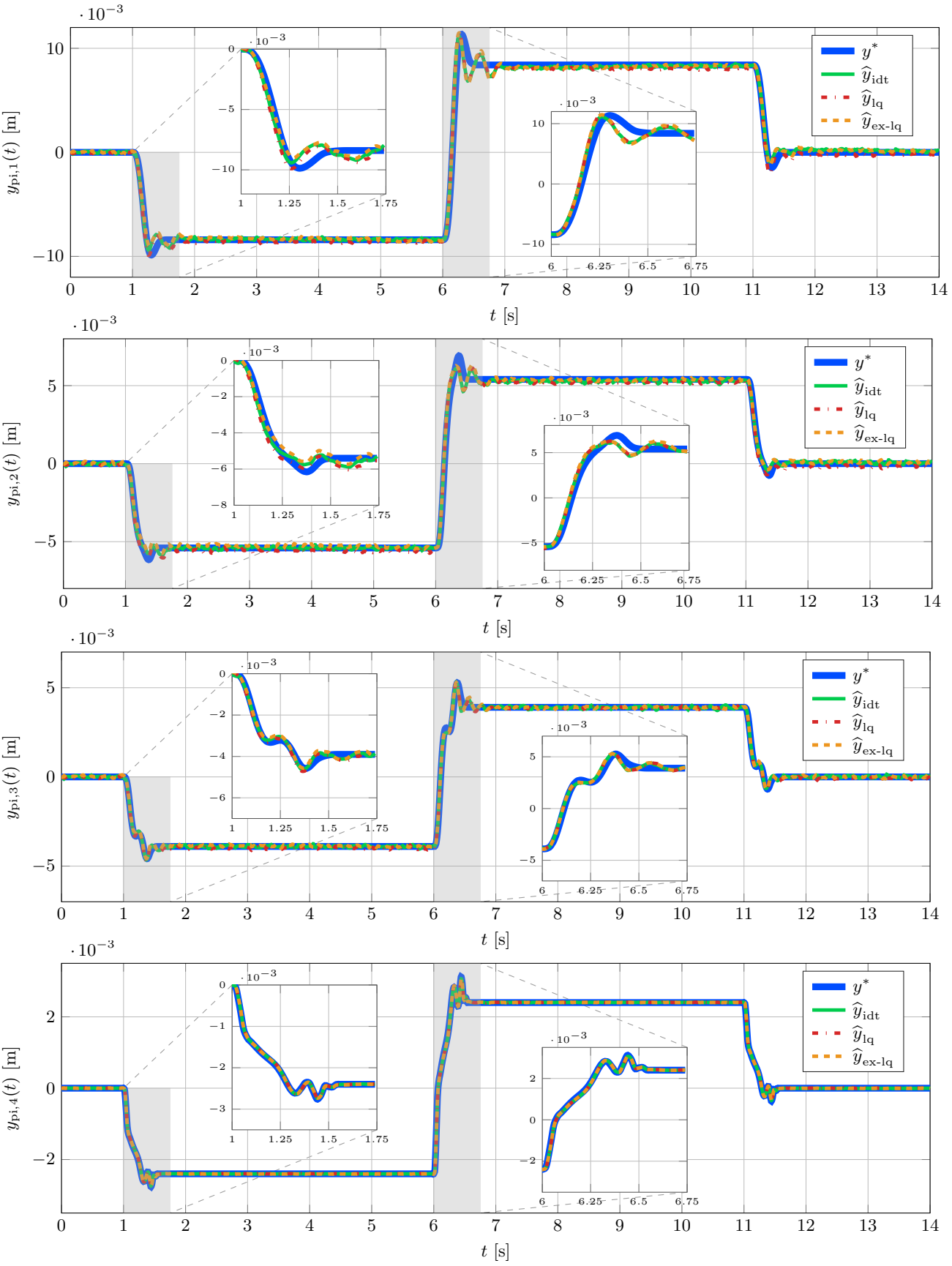

Figure 6.28.: Experimental results of the observed transversal displacement at the points of interest $\widehat{y}_{\mathrm{pi},f}(t)$ with $f \in \{1, \ldots, 4\}$ of the reference trajectory y^* and the two-degrees-of-freedom control approach based on the ID-T$_1$, LQ, and extended LQ controller denoted as $\widehat{y}_{\mathrm{idt}}$, $\widehat{y}_{\mathrm{lq}}$, and $\widehat{y}_{\text{ex-lq}}$, respectively, for the uniform displacement scenario.

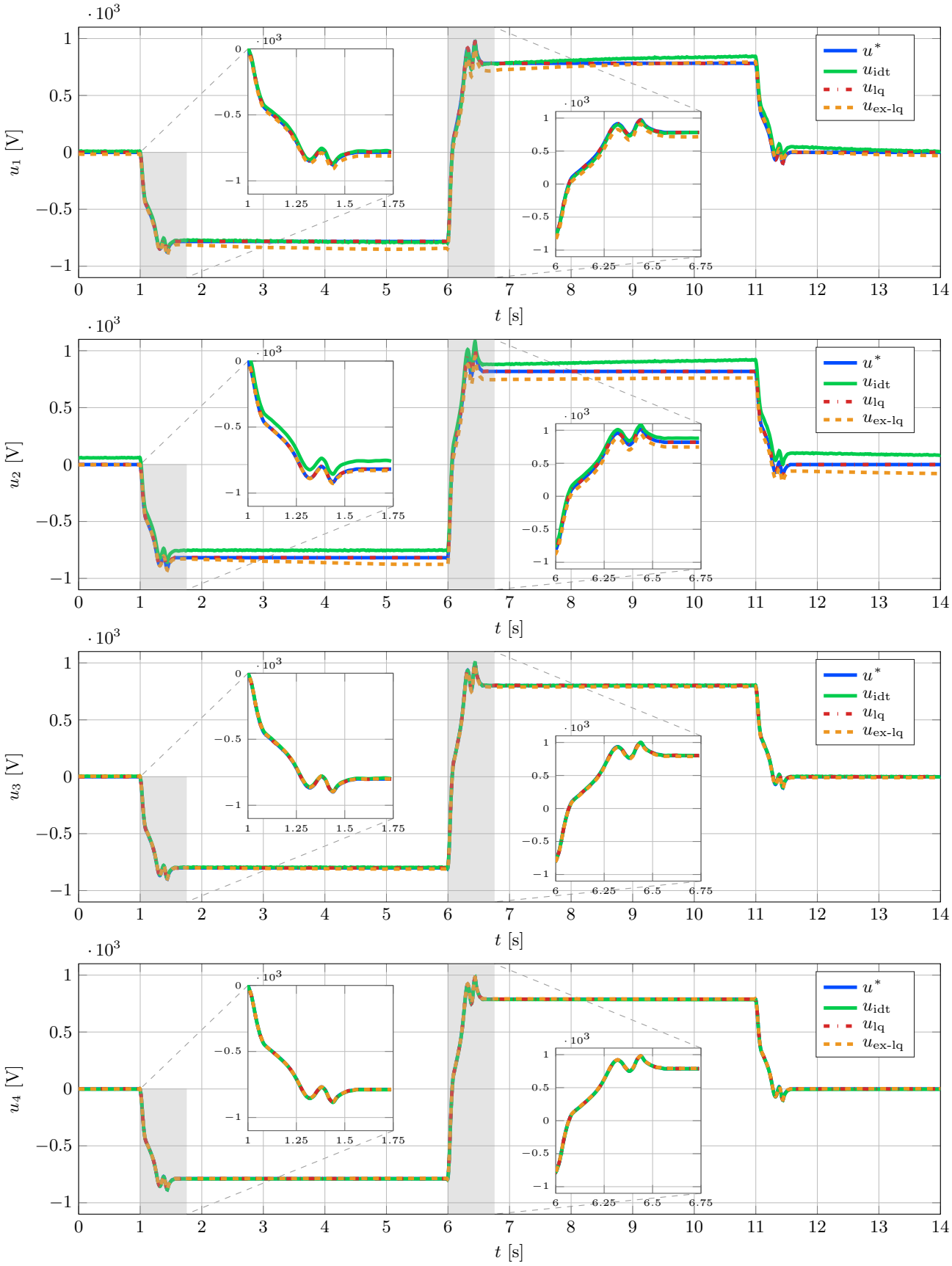

Figure 6.29.: Input signals of the MFC-actuators $k \in \{1, \ldots, 4\}$ of the flatness-based feedforward control u^* and the two-degrees-of-freedom control approach based on the ID-T$_1$, LQ, and extended LQ controller denoted as u_{idt}, $u_{\text{ex-lq}}$, and u_{lq}, respectively, for the uniform displacement scenario.

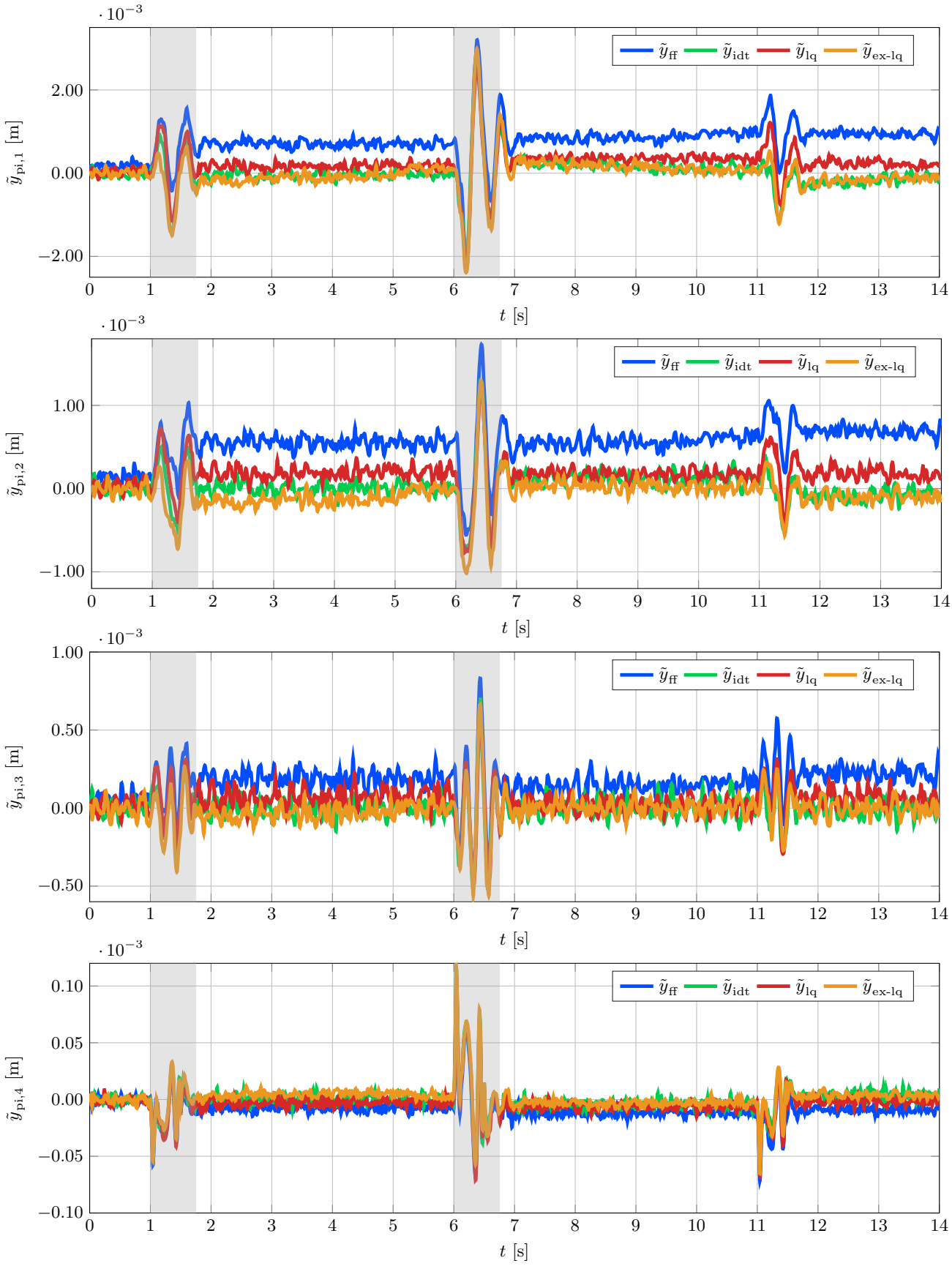

Figure 6.30.: Control errors $\tilde{y}_f(t)$ with $f \in \{1, \ldots, 4\}$, see (6.5), of the flatness-based feedforward control $\tilde{y}_{\mathrm{ff}}$ and the two-degrees-of-freedom control approach based on the ID-T$_1$, the LQ, and the extended LQ controller denoted as $\tilde{y}_{\mathrm{idt}}$, $\tilde{y}_{\mathrm{lq}}$, and $\tilde{y}_{\text{ex-lq}}$, respectively, for the uniform displacement scenario.

Diametrical Displacement Scenario This scenario also considers a rest-to-rest motion based on three transitions between different steady state displacements, see Fig. 6.31. The choice of the desired steady state is motivated by the sailing sport, where the top of the sail should be deflected opposite to the bottom. The resulting shape should reduce the pressure at the top of the sail preventing the serious damage of the wingsail and mast during strong winds.

At the beginning of the scenario, the system is situated in the undeformed state $\boldsymbol{y}^*_{\mathrm{pi}}(0\,\mathrm{s}) = [0 \quad 0 \quad 0 \quad 0]^T \times 10^{-3}\,\mathrm{m}$. After $t = 1.7\,\mathrm{s}$ the steady state $\boldsymbol{y}^*_{\mathrm{pi}}(1.7\,\mathrm{s}) = [-7.9 \quad -2.1 \quad 2.2 \quad 2.4]^T \times 10^{-3}\mathrm{m}$ should be reached considering a steady input signal of $\boldsymbol{u}^*(t) = -[787 \quad 818 \quad 801 \quad 788]^T\,\mathrm{V}$.

The second transition starts at $t = 6\,\mathrm{s}$, where the desired steady state $\boldsymbol{y}^*_{\mathrm{pi}}(6.7\,\mathrm{s}) = -\boldsymbol{y}^*_{\mathrm{pi}}(1.7\,\mathrm{s})$ should be reached at $t = 6.7\,\mathrm{s}$. Finally, the last transition results in the undeformed state $\boldsymbol{y}^*_{\mathrm{pi}}(11.7\,\mathrm{s}) = \boldsymbol{y}^*_{\mathrm{pi}}(0\,\mathrm{s})$.

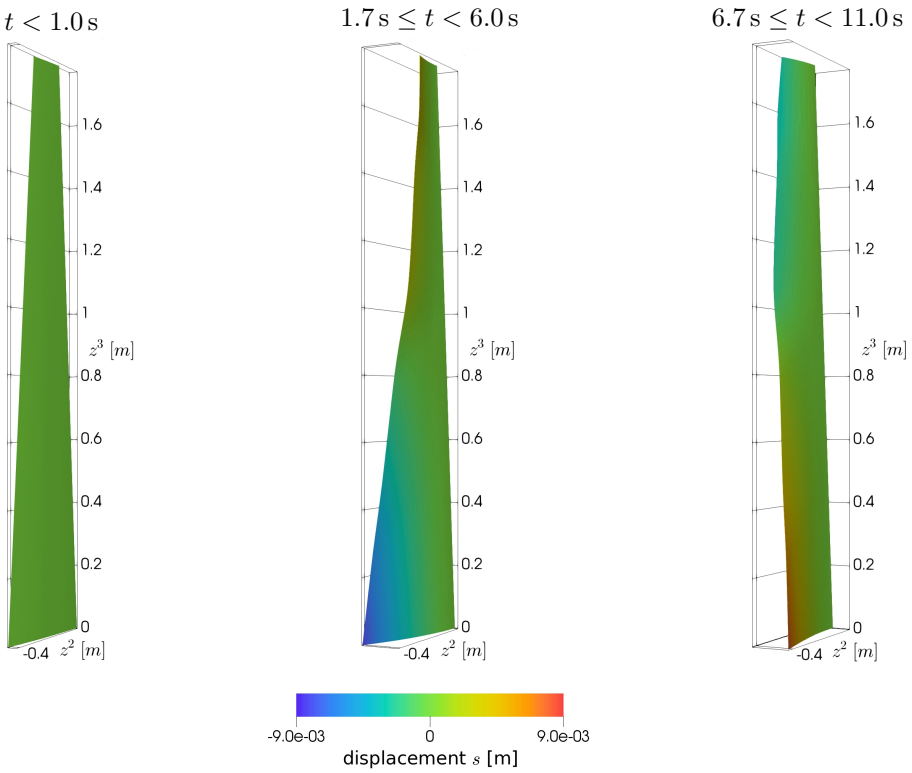

Figure 6.31.: Visualization of the desired steady state displacement profiles of the diametrical displacement scenario scaled by a factor 10. All graphics are generated using *ParaView* [52, 7].

Fig. 6.32 displays the resulting displacements at the points of interest. The reference trajectories y^* (blue lines) depict the previously discussed scenario. As in the uniform displacement scenario, the flatness-based feedforward control $\widehat{y}_{\mathrm{ff}}$ (green line) displays a good performance and follows the reference signal. Nevertheless, the displacements at the first two points of interest display significant steady states errors of about 8 %, see also the control error depicted by Fig. 6.34. In addition, the result of the feedforward controls is again ahead of the reference trajectory during the transition phases caused by parameter uncertainties, see the magnified areas of Fig. 6.32.

The two-degrees-of-freedom control approaches based on the ID-T_1 and the extended LQ feedback controller rapidly reduce the errors during the steady state $\tilde{y}_{\mathrm{idt}}$ and $\tilde{y}_{\text{ex-lq}}$, respectively, see Fig. 6.34 and Fig. 6.32 (red and orange lines). The resulting control performance of both feedback controllers is nearly identical, where the extended LQ feedback controller displays marginal improvements considering the noise of the control errors. In addition, both approaches lead to a reduction of the voltages compared to the feedforward control, see Fig. 6.33.

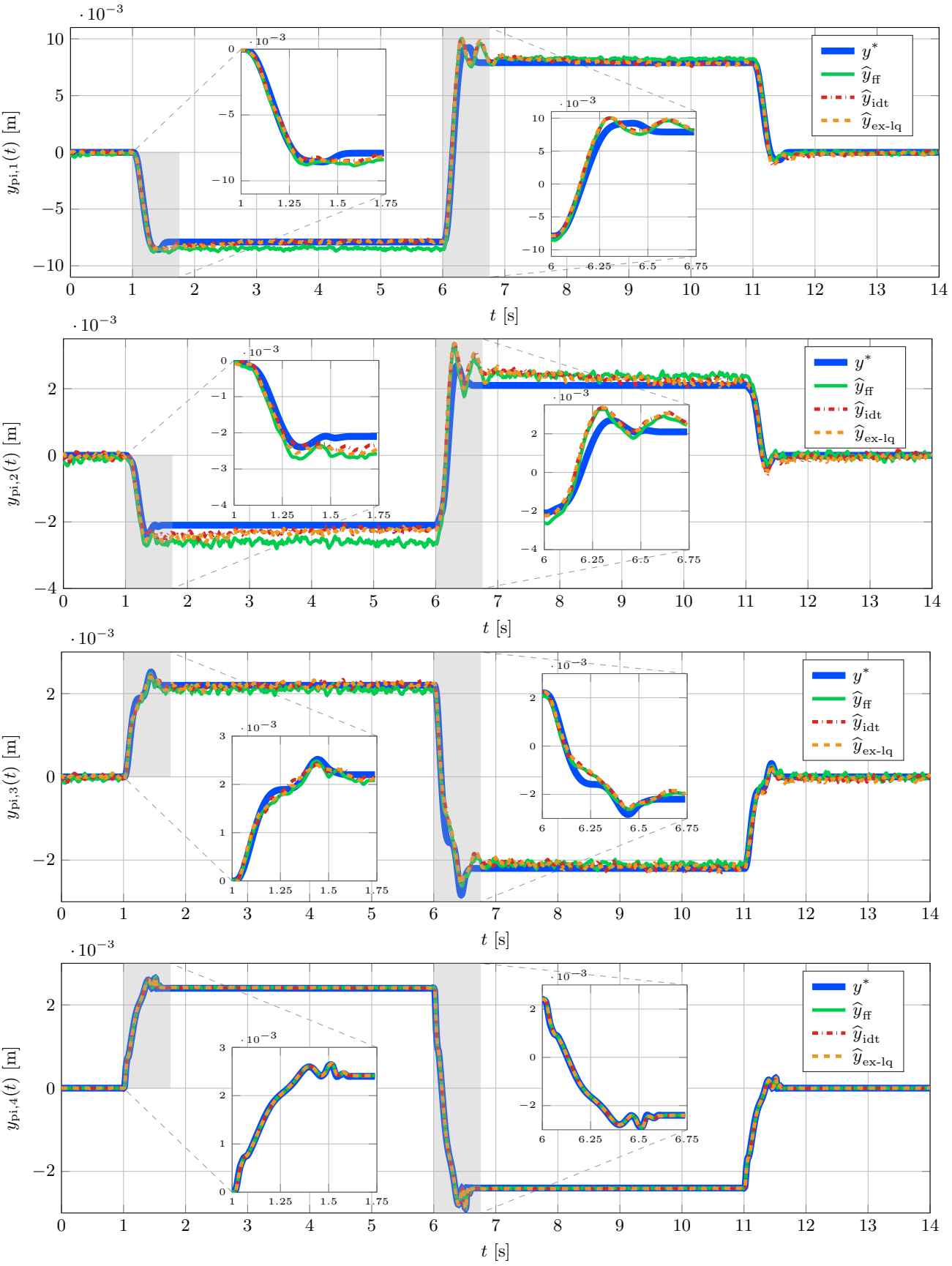

Figure 6.32.: Experimental results of the observed transversal displacement at the points of interest $\widehat{y}_{\mathrm{pi},f}(t)$ with $f \in \{1, \ldots, 4\}$ of the reference trajectory y^*, the flatness-based feedforward control $\widehat{y}_{\mathrm{ff}}$ and two-degrees-of-freedom control approach based on the ID-T_1 and extended LQ controller denoted as $\widehat{y}_{\mathrm{idt}}$ and $\widehat{y}_{\text{ex-lq}}$, respectively, for the diametrical displacement scenario.

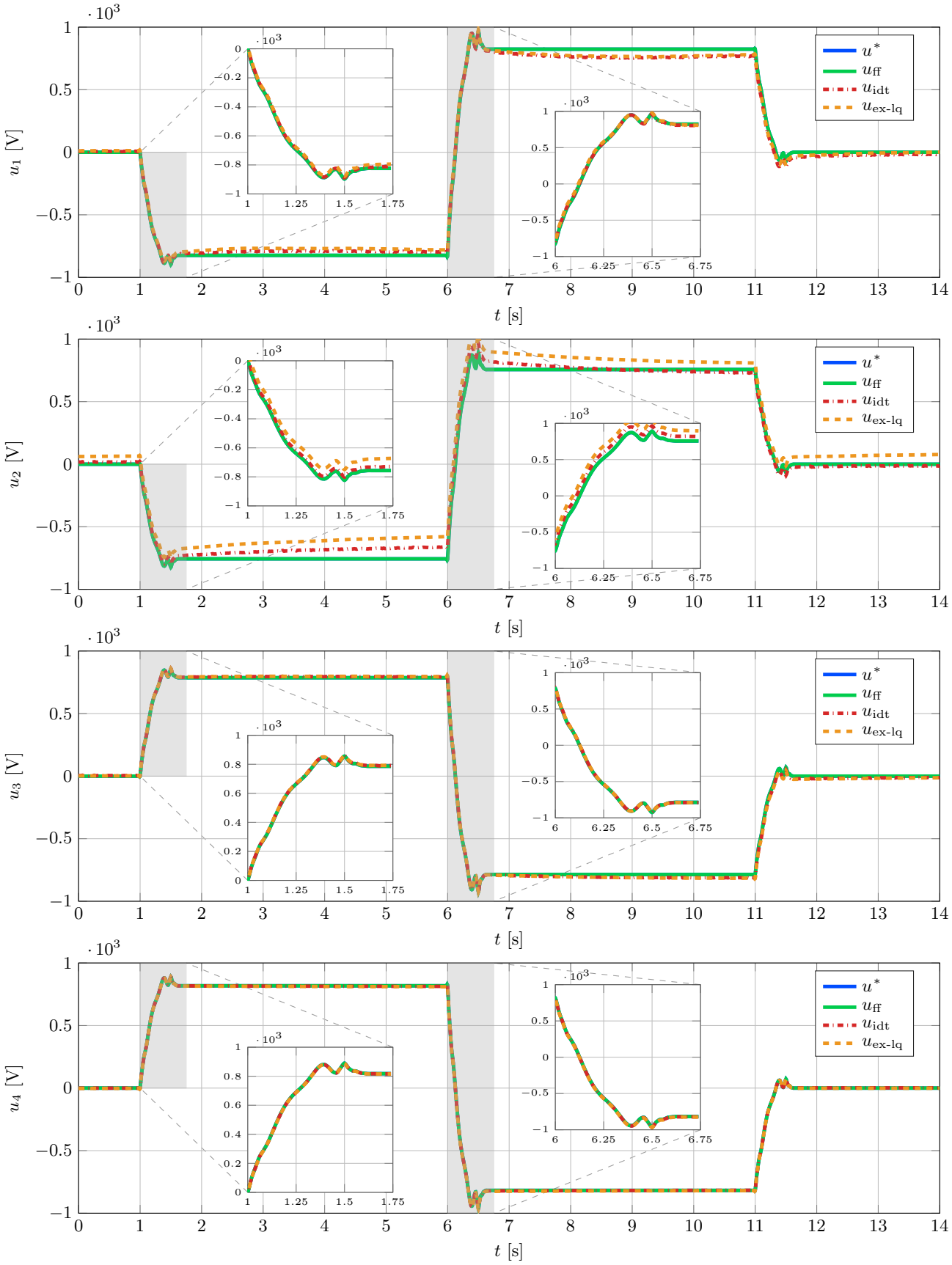

Figure 6.33.: Input signals of the MFC-actuators $k \in \{1, \ldots, 4\}$ of the flatness-based feedforward control $\widehat{y}_{\mathrm{ff}}$ and the two-degrees-of-freedom control approach based on the ID-T_1 and extended LQ controller denoted as u_{idt} and $u_{\text{ex-lq}}$, respectively, for the diametrical displacement scenario.

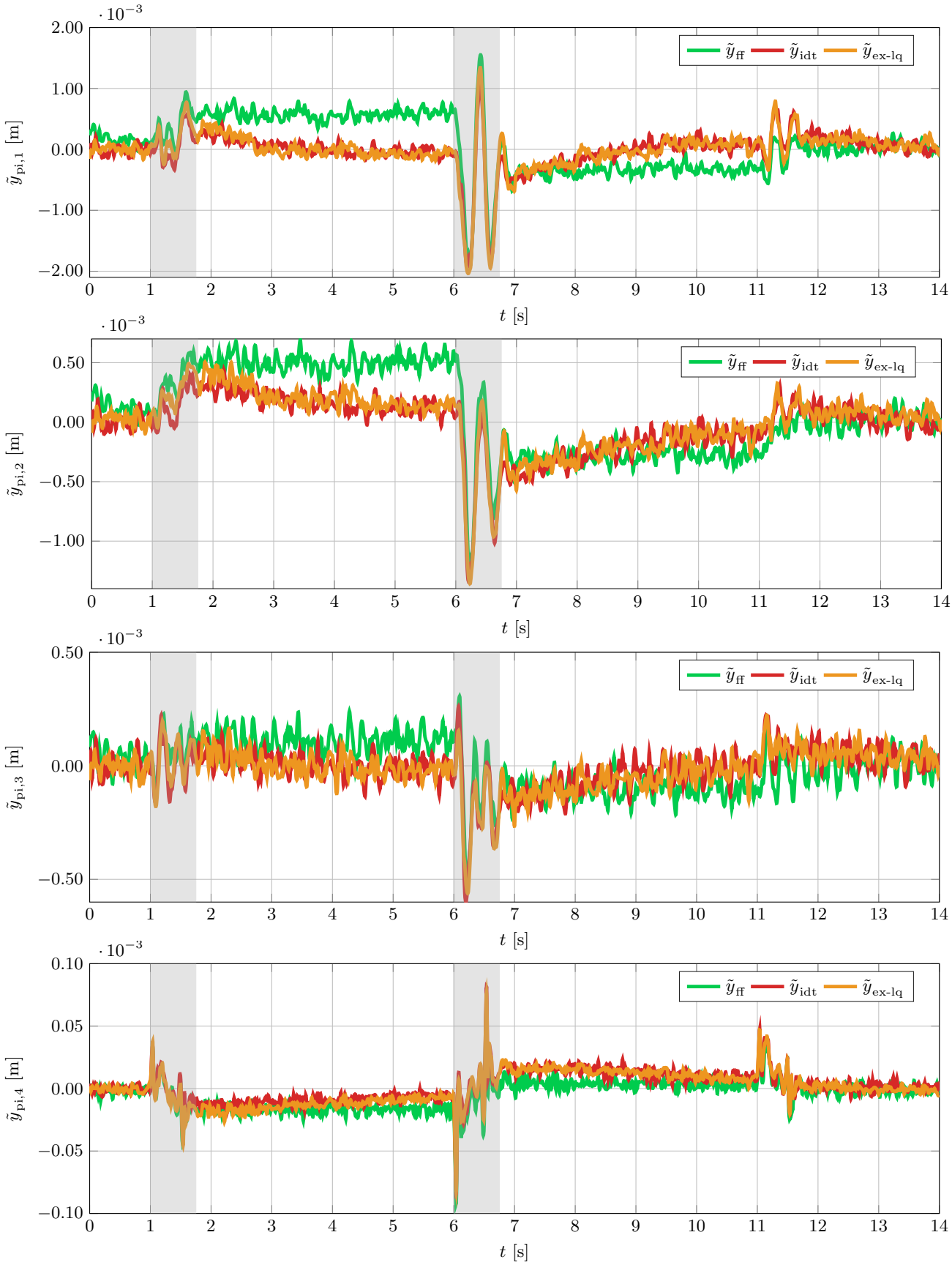

Figure 6.34.: Control errors $\tilde{y}_f(t)$ with $f \in \{1, \ldots, 4\}$, see (6.5), of the flatness-based feedforward control, and the two-degrees-of-freedom control approach based on the ID-T_1 and extended LQ controller denoted as $\tilde{y}_{\text{idt}}$ and $\tilde{y}_{\text{ex-lq}}$ respectively considering the diametrical displacement scenario.

Disturbance Rejection Scenario The last scenario considers an external disturbance applied by a pulse hammer, which hits the wingsail structure between the first and the second supply beam at $t = 0.5\,\mathrm{s}$. Fig. 6.35 displays the observed transversal displacement at the points of interest of the open loop system $\widehat{y}_{\mathrm{ol}}$ and the feedback controllers in terms of the ID-T_1, the LQ, and the extended LQ approach denoted as $\widehat{y}_{\mathrm{idt}}$, $\widehat{y}_{\mathrm{lq}}$, and $\widehat{y}_{\text{ex-lq}}$, respectively. In addition, Fig. 6.36 shows the associated input signals.

The response of the open loop system (blue lines) is characterized by an oscillation which decays after 2 s. Taking the feedback controllers into account this decay time is reduced to 1 s. Furthermore, all approaches damp the amplitude of the oscillation except for the 4^{th} point of interest. At this position the state controller approaches (red and orange lines) enhance the amplitudes during the first oscillation's period. However, the second period already displays smaller displacements as in the reactions of the open loop and the ID-T_1control. Overall, the control performance of all approaches is comparable.

Taking the resulting input signals of the control approaches into account a similar behavior appears, where the ID-T_1 feedback controller displays a lower energy consumption. Considering the input signals of ID-T_1 control u_{idt} the voltage signal of the second MFC-actuator stands out due to a bias of about 70 V in the second steady state. This bias is an artifact of the hysteresis and creep compensation, which becomes compensated by the controller mainly by its integral part. In addition, the extended LQR also shows such a bias at the second point of interest.

Concluding the results of the disturbance rejection and the rest-to-rest motion scenarios the flatness-based feedforward control display a good performance which is even improved by the two-degrees-of-freedom control concepts, especially by the ID-T_1 and the extended LQ feedback controllers. Due to the introduced MOR by the POD method, the full order system description could be reduced to a manageable system without a significant loss of accuracy enabling the design of the previously discussed model based control approaches. Furthermore, this procedure enables the implementation within a real time environment.

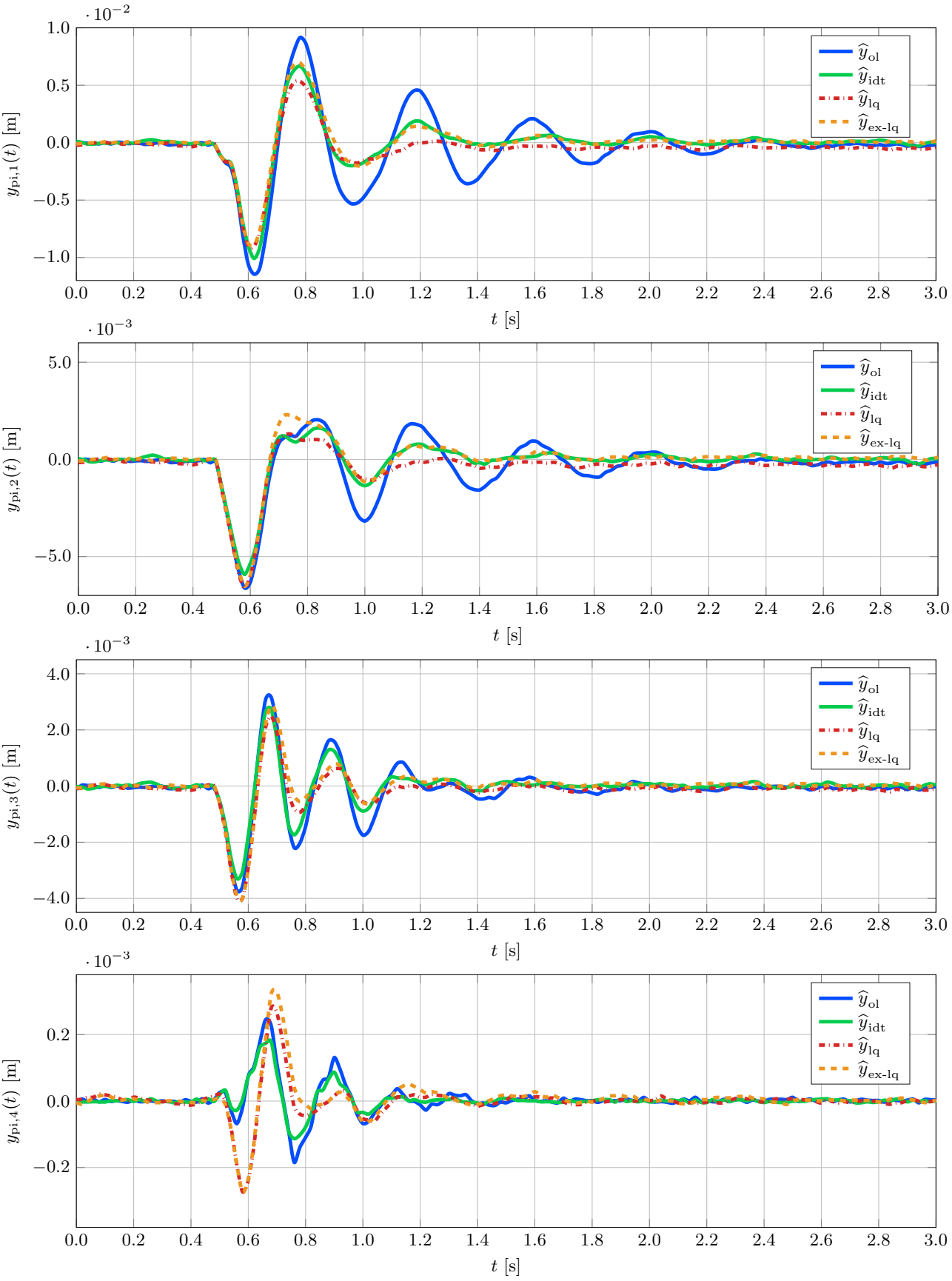

Figure 6.35.: Experimental results of the observed transversal displacement at the points of interest $\widehat{y}_{\mathrm{pi},f}(t)$ with $f \in \{1, \ldots, 4\}$ of the reference trajectory y^* and the two-degrees-of-freedom control approach based on the ID-T_1, LQ, and extended LQ controller denoted as $\widehat{y}_{\mathrm{idt}}$, $\widehat{y}_{\mathrm{lq}}$, and $\widehat{y}_{\text{ex-lq}}$, respectively, considering the disturbance rejection scenario. The disturbance is introduced by a pulse hammer at $t = 0.5\,\mathrm{s}$.

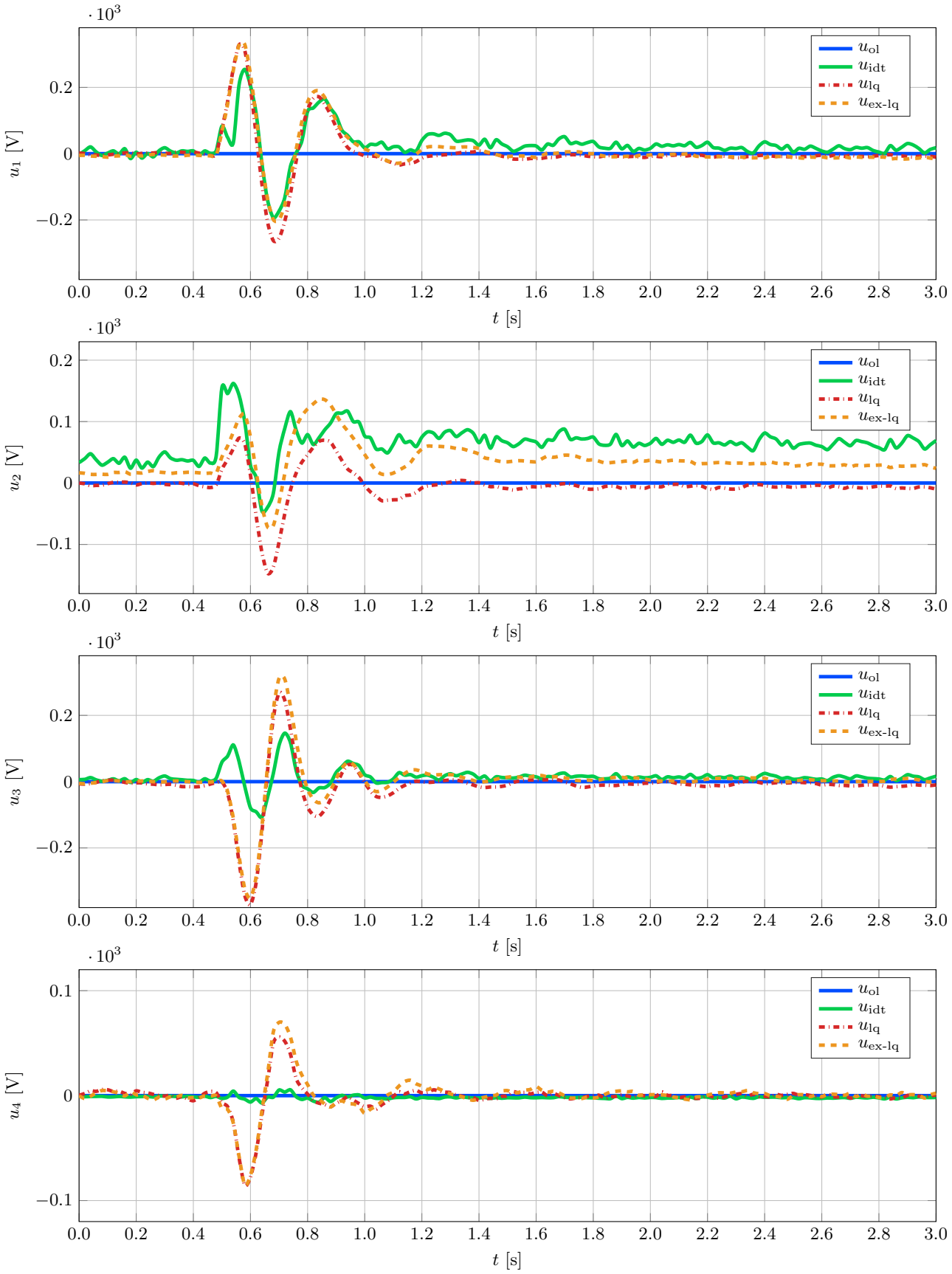

Figure 6.36.: Input signals of the MFC-actuators $k \in \{1, \ldots, 4\}$ of the flatness-based feedforward control u^* and the two-degrees-of-freedom control approach based on the ID-T_1, LQ, and extended LQ controller denoted as u_{idt}, $u_{\text{ex-lq}}$, and u_{lq}, respectively, considering the disturbance rejection scenario. The disturbance is introduced by a pulse hammer at $t = 0.5\,\mathrm{s}$.

7. Conclusion

The present work is dedicated to the motion planning and tracking control approach of elastic smart structures. Different control approaches are introduced and numerically as well as experimentally evaluated. For this purpose a so-called wingsail structure is designed considering embedded piezoelectric actuators. In addition, two weakly damped and coupled beam structures are considered which are used as proof of concept study of the wingsail design as well as benchmark tests for the control approaches. The results of the work are summarized below. Furthermore, an outlook on future activities of the wingsail project is provided.

7.1. Summary

This work considers two different model based control approaches to achieve a desired rest-to-rest motion of the transversal displacement of the wingsail and the interconnected beam strutures. The origin of both approaches is the mathematical description of the governing static and dynamic effects in terms of the equations of motion, which are introduced in Chapter 2. In fact two modeling methods are used to determine the system description of the coupled beams as well as the wingsail.

The beams structures are composed by carbon made beams equipped with embedded actuators and partially with embedded sensors. The modeling takes an analytical energy based method into account which applies the extended Hamilton's principle. For this purpose, the equations of motion of the transversal deflection of single beams are deduced at first by using the Euler-Bernoulli beam theory which denotes a special case of the linear elasticity. The resulting model considers different combinations of external, Kelvin-Voigt and structural damping. An analysis of the effect of these combinations regarding the eigenvalue distribution of the spatially varying parameter system is provided by Appendix B.2.

Subsequently, the mechanical setup of the interconnected beam structures is introduced and their spatial and time dependent equations of motion derived by the extended Hamilton's principle. In addition the different sensor concepts are discussed and modeled as well. The resulting description is important for the design of a state observer which is used later on. Finally a finite dimensional approximation is determined considering Galerkin's method. This defines the basis for the model based control approaches which are experimentally evaluated considering a real time implementation.

The modeling of the wingsail's displacement makes use of the FEM based on the linear elasticity. This method is used to handle the complexity of the curved structure. It directly yields a finite dimensional description due to the use of Galerkin's method. In contrast to the interconnected beam structures the modeling process considers the so-called Rayleigh damping which denotes a combination of external and Kelvin-Voigt damping. In addition, the sensor concept is discussed.

These system descriptions denote only the qualitative mathematical structures. To achieve a system description which truly describes the measured dynamics the knowledge of the material parameters is crucial. Due to the prototype characteristic of the experimental setups, only the parameters of the actuators and sensors are provided by datasheets. In addition, a small subset of parameters can be measured directly. However, most of the parameters have to be determined by an identification process. Chapter 3 presents two concepts which are applied for the beam structures as well as for the wingsail.

The first one relies on the physical understanding of the considered setup and can only be used efficiently for small systems. Therefore, the parameters of the coupled beam structure are identified by this concept. Due to their configuration both structures provide the possibility to detach elements whose parameters can be identified separately which reduces the cross effects.

The second concept is used to identify the material parameters of the wingsail. Here, an adjoint based optimization process is introduced to increase the numerical efficiency. Due to the fact that the full order system description is used in the identification process this improvement of the numerical efficiency is inevitable. The method relies on the sensitivity analysis, in which sensitivity functions (also called gradients of the objective function) are derived by the usage of the equations of motion and the variational calculus.

The resulting mathematical descriptions cover the measured behavior of the flexible structures. However, the finite dimensional systems are characterized by high dimensional systems of ODEs leading to a significant

computational effort. To satisfy the real time requirements of the control concept the computational effort has to be reduced. This is done by the application of MOR techniques introduced in Chapter 4 which focuses on the group of SVD based methods. In fact this work considers the following methods: The model truncation, the second order balanced truncation, and the POD.

Chapter 5 presents the two considered control strategies to accomplish a desired rest-to-rest motion of the elastic structures.

The first strategy is based on a systematic design of a two-degrees-of-freedom control approach composed by a flatness-based feedforward control, to systematically solve the motion planning problem, and a feedback control to acquire robustness against model uncertainties and external disturbances. The systematic flatness-based design of the motion planning uses the properties of a Riesz spectral system and addresses early as well as late lumping approaches. Amending the resulting feedforward control by a feedback controller which ensures that the reference trajectory is reached yields the two-degrees-of-freedom control approach. To analyze the impact of the feedback control different controllers are introduced and evaluated. The list of considered feedback controllers includes an output feedback approach in terms of ID-T_1 control, different state feedback controllers based on the Ackermann and the linear quadratic regulator as well as extensions to ensure steady state accuracy, and a Lyapunov-based control approach.

As an alternative approach the so-called MPC approach is introduced. MPC explicitly uses the mathematical model to predict the future dynamics of a system. It determines the optimal control input in each sample step by solving an optimization problem on the prediction horizon. The associated cost or objective function consists of the predicted control error and the control input within the prediction horizon. This procedure offers the possibility to introduce further constraints such as physical limitations of the actuators. In general, the MPC approach is applied to systems characterized by slow dynamics. Due to this, the optimization problem can be solved within each sampling step in real time. On the contrary the considered smart structures are characterized by fast oscillatory dynamics which reduces the sample time of the real time process. To reduce the computational effort the optimization problem is solved by using Hildreth's quadratic programming procedure. Furthermore, the degrees of freedom of the optimization problem can be reduced by fixing the input variables over several time-steps. Such a move blocking method by downsampling is introduced so that the MPC approach can be executed in real-time with a sufficiently high sampling frequency to cover the dynamic of the system.

Both control strategies rely on the state information of a state observer. To improve the signal to noise ratio a Kalman filter is used.

The evaluation of both control strategies is presented in Chapter 6. Both approaches display a good control performance considering the experimental setup of the vertical beam configuration. However, due to the computational effort the MPC approach is restricted to a double beam configuration which denotes a subset of the triple beam configuration on which the two-degrees-of-freedom control approach is tested. Due to this and the fact that the computational effort results in a higher energy consumption which is counterproductive on a autonomous vehicle with limited payload, the MPC approach is not further investigated.

The analysis of the different feedback controllers of the two-degrees-of-freedom control approach points out that the use of the ID-T_1 and an extended state space control approach lead to the best performance. Both concepts further improve the already remarkable performance of the flatness-based feedforward control, enabling fast transitions between different steady state displacement profiles for the coupled beams as well as for the wingsail structure. The characteristic strong oscillations of the weakly damped systems, which appear in the step response or a ramp shaped excitation, are reduced to a minimum, where the feedback controllers lead to a fast decay of the remaining small oscillations.

7.2. Outlook

Considering the motion planning and tracking control approach in general an optimization based motion planning and feedforward control may result in a similar performance as the flatness-based approach but provides the opportunity to consider additional constraints like the limitations of the actuators. In contrast to the presented MPC approach, which solves the motion planning problem for the whole prediction horizon in each sample step, the optimization based feedforward control can be calculated offline or within a second thread. To reduce the computational effort the adjoint based method could be considered as well.

Related to the wingsail project different actions could be considered in further research.

First of all, the displacement range of the wingsail can be enhanced by the usage of a combined actuation concept composed of the embedded MFC-actuators and winches. The fast MFC-actuators are able to deal the vibrations or remaining oscillations, whereas the winches increase the displacement range and are able to

deal with strong constant disturbances. The current experimental setup is already equipped with the necessary clamping anchors.

Furthermore, the strain gauges should be implemented to avoid the auxiliary laser measurement. The experimental setup is already equipped with the strain gauges, the necessary wiring, and measurement amplifiers. However, the system model has to be extended to consider the strain gauge measurements.

In general, this work states the origin for further work in the field of autonomous sailing. For this purpose, a superposed controller has to be designed which determines the necessary maneuvers and displacement profiles of the wingsail considering the current sailing and wind conditions. This denotes the basis of the main algorithm of an autonomous sailing yacht which deals with the guidance, path control and navigation relying on the propulsion system “smart wingsail”.

A. Numerical Solver

A numerical solution method is required to compute the time dependent displacement field $\boldsymbol{s}(t, \boldsymbol{z})$. For this propose, three implicit solvers are used. Two solvers directly rely on the backward differentiation formulas (BDF) and the third one is based on an approximation by means of the Taylor series.

Classically, such solvers are used for systems of first order ODEs or second order equations of motion in terms of mass, damping, stiffness and input matrices. However, these solvers can also be implemented in the FEM framework *Firedrake* to deal with the corresponding operators.

In the following, the used solvers are introduced and briefly discussed towards their use task within the *Firedrake* framework.

A.1. BDF-1 Solver

On the basis of the the weak form (2.118) of the linear elasticity

$$\begin{aligned} 0 = &\int_0^T \int_\Omega \rho \boldsymbol{\phi} \cdot \partial_t^2 \boldsymbol{s}(t, \boldsymbol{z}) + \nabla \boldsymbol{\phi} : \underline{\sigma}(\boldsymbol{s}) + \gamma^{\mathrm{v}} \rho \boldsymbol{\phi} \cdot \partial_t \boldsymbol{s} + \gamma^{\mathrm{kv}} \nabla \boldsymbol{\phi} : \underline{\sigma}(\partial_t \boldsymbol{s}) \, \mathrm{d}\Omega \, \mathrm{d}t \\ &- \int_0^T \int_{\Gamma_2} \boldsymbol{\phi} \cdot \boldsymbol{f}_\Gamma(t, \boldsymbol{z}) + \gamma^{\mathrm{kv}} \boldsymbol{\phi} \cdot \partial_t \boldsymbol{f}_\Gamma(t, \boldsymbol{z}) \, \mathrm{d}\Gamma_2 \, \mathrm{d}t, \end{aligned}$$

the operator formulation can be written as

$$\int_0^T \mathscr{M}\left(\partial_t^2 \boldsymbol{s}\right) + \mathscr{C}\left(\partial_t \boldsymbol{s}\right) + \mathscr{K}\left(\boldsymbol{s}\right) - \mathscr{L}(\boldsymbol{f}_\Omega, \boldsymbol{f}_\Gamma) \, \mathrm{d}t = \boldsymbol{0}, \tag{A.1}$$

with

$$\begin{aligned} \mathscr{M}\left(\partial_t^2 \boldsymbol{s}\right) &= \int_\Omega \rho \boldsymbol{\phi} \cdot \partial_t^2 \boldsymbol{s}(t, \boldsymbol{z}) \, \mathrm{d}\Omega, \quad \mathscr{C}\left(\partial_t \boldsymbol{s}\right) = \int_\Omega \gamma^{\mathrm{v}} \rho \boldsymbol{\phi} \cdot \partial_t \boldsymbol{s} + \gamma^{\mathrm{kv}} \nabla \boldsymbol{\phi} \cdot \underline{\sigma}(\partial_t \boldsymbol{s}) \, \mathrm{d}\Omega, \\ \mathscr{K}\left(\boldsymbol{s}\right) &= \int_\Omega \nabla \boldsymbol{\phi} \cdot \underline{\sigma}(\boldsymbol{s}) \, \mathrm{d}\Omega, \quad \mathscr{L}(\boldsymbol{f}_\Omega, \boldsymbol{f}_\Gamma) = \int_\Omega \boldsymbol{\phi} \cdot \boldsymbol{f}_\Omega(t, \boldsymbol{z}) \, \mathrm{d}\Omega + \int_{\Gamma_2} \boldsymbol{\phi} \cdot \boldsymbol{f}_\Gamma(t, \boldsymbol{z}) + \boldsymbol{\phi} \cdot \partial_t \boldsymbol{f}_\Gamma(t, \boldsymbol{z}) \, \mathrm{d}\Gamma_2 \end{aligned} \tag{A.2}$$

denoting the mass, damping, stiffness and forcing operator, respectively. Introducing the time discrete displacement, velocity and accelaration field as well as the discrete time force operator

$$\boldsymbol{s}_k = \boldsymbol{s}(t_k, \boldsymbol{z}), \quad \boldsymbol{v}_k = \partial_t \boldsymbol{s}(t, \boldsymbol{z})\big|_{t=t_k}, \quad \boldsymbol{a}_k = \partial_t^2 \boldsymbol{s}(t, \boldsymbol{z})\big|_{t=t_k}, \quad \boldsymbol{f}_{\Omega,k} = \boldsymbol{f}_\Omega(t_k, \boldsymbol{z}), \quad \boldsymbol{f}_{\Gamma,k} = \boldsymbol{f}_\Gamma(t_k, \boldsymbol{z}), \tag{A.3}$$

where t_k denotes the discrete time considering a fixed sample time period dt.

Applying the first order backward differentiation formula (BDF-1), e.g., see [48], the velocity and the displacement field of the subsequent time step are given by

$$\boldsymbol{v}_{k+1} = \boldsymbol{v}_k + dt \boldsymbol{a}_{k+1}, \quad \boldsymbol{s}_{k+1} = \boldsymbol{s}_k + dt \boldsymbol{v}_{k+1} = \boldsymbol{s}_k + dt \boldsymbol{v}_k + dt^2 \boldsymbol{a}_{k+1}. \tag{A.4}$$

Introducing this substitution into (A.1) yields

$$\begin{aligned} \boldsymbol{0} &= \mathscr{M}\left(\boldsymbol{a}_{k+1}\right) + \mathscr{C}\left(\boldsymbol{v}_{k+1}\right) + \mathscr{K}\left(\boldsymbol{s}_{k+1}\right) - \mathscr{L}(\boldsymbol{f}_{\Omega,k+1}, \boldsymbol{f}_{\Gamma,k+1}) \\ &= \mathscr{M}\left(\boldsymbol{a}_{k+1}\right) + \mathscr{C}\left(\boldsymbol{v}_k + dt \boldsymbol{a}_{k+1}\right) + \mathscr{K}\left(\boldsymbol{s}_k + dt \boldsymbol{v}_k + dt^2 \boldsymbol{a}_{k+1}\right) - \mathscr{L}(\boldsymbol{f}_{\Omega,k+1}, \boldsymbol{f}_{\Gamma,k+1}). \end{aligned} \tag{A.5}$$

Solving this equation for $\boldsymbol{a}_{k+1}$ provides the new displacement field taken into account (A.4). This requires that for the first step the initial values at $k = 0$ of $\boldsymbol{s}_k$, $\boldsymbol{v}_k$ as well as the current forces $\boldsymbol{f}_{\Omega,k+1}$ and $\boldsymbol{f}_{\Gamma,k+1}$ have to be known.

It is also possible and in some communities even common to substitute the highest derivations in (A.3). The resulting residuum provides the same numerical solutions.

The residuum formulation provided by (A.5) is easy to implement and to solve in *Firedrake*. This method is feasible for simple structure such as the beam structure of Section 3.2.2.2 or problems in heat conduction. However, on the wingsail structure numerical tests have revealed that the use of BDF-1 is not sufficient to achieve the required accuracy. To overcome this drawback the following solver methods are introduced.

A.2. BDF-2 Solver

One option to improve the performance is to consider more steps of previous data. Instead of (A.4) the following assumption which is based on the Lagrange interpolation polynominal [48] is used to determine the field evolution

$$\begin{aligned}\boldsymbol{v}_{k+2} &= \frac{4}{3}\boldsymbol{v}_{k+1} - \frac{1}{3}\boldsymbol{v}_k + \frac{2}{3}dt\boldsymbol{a}_{k+2},\\ \boldsymbol{s}_{k+2} &= \frac{4}{3}\boldsymbol{s}_{k+1} - \frac{1}{3}\boldsymbol{s}_k + \frac{2}{3}dt\boldsymbol{v}_{k+2} = \frac{4}{3}\boldsymbol{s}_{k+1} - \frac{1}{3}\boldsymbol{s}_k - \frac{2}{9}dt\boldsymbol{v}_k + \frac{8}{9}dt\boldsymbol{v}_{k+1} + \frac{4}{9}dt^2\boldsymbol{a}_{k+2}.\end{aligned} \tag{A.6}$$

Analog to the BDF-1 method, this substitution is introduced into (A.1) which leads to

$$\begin{aligned}\mathbf{0} &= \mathscr{M}\left(\boldsymbol{a}_{k+2}\right) + \mathscr{C}\left(\boldsymbol{v}_{k+2}\right) + \mathscr{K}\left(\boldsymbol{s}_{k+2}\right) - \mathscr{L}(\boldsymbol{f}_{\Omega,k+2}, \boldsymbol{f}_{\Gamma,k+2})\\ &= \mathscr{M}\left(\boldsymbol{a}_{k+2}\right) + \mathscr{C}\left(\frac{4}{3}\boldsymbol{v}_{k+1} - \frac{1}{3}\boldsymbol{v}_k + \frac{2}{3}dt\boldsymbol{a}_{k+2}\right)\\ &\quad + \mathscr{K}\left(\frac{4}{3}\boldsymbol{s}_{k+1} - \frac{1}{3}\boldsymbol{s}_k - \frac{2}{9}dt\boldsymbol{v}_k + \frac{8}{9}dt\boldsymbol{v}_{k+1} + \frac{4}{9}dt^2\boldsymbol{a}_{k+2}\right) - \mathscr{L}(\boldsymbol{f}_{\Omega,k+2}, \boldsymbol{f}_{\Gamma,k+2}).\end{aligned} \tag{A.7}$$

Solving for $\boldsymbol{a}_{k+2}$ yields the desired solution of the displacement field taking (A.6) into account. Due to the usage of the previous time steps, the initial conditions has to be extended. This can be done by one BDF-1 step for $k = 1$ to generate the required second initial condition based on the original one at $k = 0$. Also this procedure ensures that the considered first step is a valid profile.

Compared to the time solver based on BDF-1, this method displays an improvement in accuracy. Also the complexity and the computational effort stays low, but one issue remains. Both BDF based solvers can not guarantee energy conservation. In other words, both solver may introduce numerical damping to the system, which compromises the results. To overcome this issue the Newmark solver is introduced in the next subsection.

A.3. Newmark Solver

The main benefit of the Newmark solver [84] is the energy conservation characteristics. The method was developed by Newmark in the field of civil engineering and is designed for second order systems particularly. It relies directly on an approximation by means of the Taylor series, omitting derivatives higher than third order

$$\begin{aligned}\boldsymbol{s}_{k+1} &= \boldsymbol{s}_k + dt\boldsymbol{v}_k + \frac{1}{2}dt^2\boldsymbol{a}_k + \frac{1}{6}dt^3\boldsymbol{s}_k^{(3)} = \boldsymbol{s}_k + dt\boldsymbol{v}_k + \frac{1}{2}dt^2\boldsymbol{a}_k + \beta dt^3\boldsymbol{s}_k^{(3)},\\ \boldsymbol{v}_{k+1} &= \boldsymbol{v}_k + dt\boldsymbol{a}_k + \frac{1}{2}dt^2\boldsymbol{s}_k^{(3)} = \boldsymbol{v}_k + dt\boldsymbol{a}_k + \gamma dt^2\boldsymbol{s}_k^{(3)}.\end{aligned} \tag{A.8}$$

Assuming that the third time derivative can be determined by

$$\boldsymbol{s}_k^{(3)} = \frac{1}{dt}\big(\boldsymbol{a}_{k+1} - \boldsymbol{a}_k\big). \tag{A.9}$$

leads to

$$\begin{aligned}\boldsymbol{s}_{k+1} &= \boldsymbol{s}_k + dt\boldsymbol{v}_k + \Big(\frac{1}{2} - \beta\Big)dt^2\boldsymbol{a}_k + \beta dt^2\boldsymbol{a}_{k+1},\\ \boldsymbol{v}_{k+1} &= \boldsymbol{v}_k + \big(1 - \gamma\big)dt\boldsymbol{a}_k + \gamma dt\boldsymbol{a}_{k+1}.\end{aligned} \tag{A.10}$$

There are different parameter choices. The evaluation of the Taylor series leads to $\beta = \frac{1}{6}$, $\gamma = \frac{1}{2}$, which is also referred to as linear acceleration in the literature. Another common choice is $\beta = \frac{1}{4}$, $\gamma = \frac{1}{2}$ also known as average acceleration. This choice guarantees energy conservation according to [84]. Furthermore, Newmark states that conditional stability is assured for $\beta \geq \frac{\gamma}{2} \geq \frac{1}{4}$.

To determine the solution of the displacement field

$$\begin{aligned}&\mathscr{M}\left(\boldsymbol{a}_{k+1}\right)+\mathscr{C}\left(\boldsymbol{v}_k+(1-\gamma)dt\boldsymbol{a}_k+\gamma dt\boldsymbol{a}_{k+1}\right)\ +\\&\mathscr{K}\left(\boldsymbol{s}_k+dt\boldsymbol{v}_k+(0.5-\beta)dt^2\boldsymbol{a}_k+\beta dt^2\boldsymbol{a}_{k+1}\right)-\mathscr{L}(\boldsymbol{f}_{\Omega,k+1},\boldsymbol{f}_{\Gamma,k+1})=\mathbf{0}\end{aligned}\tag{A.11}$$

has to be solved for $\boldsymbol{a}_{k+1}$. After that, the displacement field is given by (A.10).

For the *Firedrake* implementation $\beta=\frac{1}{4}$ and $\gamma=\frac{1}{2}$ are chosen. The resulting temporal solution displays the required accuracy and is not affected by numerical damping, neither on the simple beam structure nor on the wingsail structure.

B. Motion Planning and Flatness-Based Feedforward Control in the Infinite Dimensional Case

Section 5.1 presents a flatness-based feedforward control approach for a spatially discretized system which denotes the general description for a practical implementation. Nevertheless, it is also possible to design the presented approach for the infinite dimensional case which is derived below, see also [78]. For this purpose, the vertical beam configuration is used to present the methodology taking the following assumptions into account.

Assumption B.1 *As a theoretical special case all beams of the structure are assumed to be identical and equipped with one MFC-patch pair. Furthermore, all parameters are constant, i.e.,* $m_j = m$, $\mu_j(z) = \mu$, $\Lambda_j(z) = \Lambda$, $\gamma^{v}_{(z)}(z^1) = \gamma^{v}$, $\gamma^{sv}_{(z)}(z^1) = \gamma^{sv}$, $\gamma^{kv}_{(z)}(z^1) = \gamma^{kv}$ *and* $\Gamma_{j,a_k}(z) = \Gamma_j(z)$.

Due to this, the equations of motion of the vertical beam configuration (2.55) reduce to the equations of motion of a system of classical Euler-Bernoulli-beams, which are elastically coupled at their free ends. The resulting equations are presented below.

B.1. Abstract Formulation of the Equations of Motion of a Beam Structure with Constant Parameters

Let $X = \big((H_0^2(0,\ell))^r \times (L^2(0,\ell))^r \times \mathbb{R}^r\big)$ denote the state space considering r Euler-Bernoulli beams of length ℓ, where $H_0^2(0,\ell) = \{f \in H^2(0,\ell) : f(0) = \partial_z f(0) = 0\}$ denotes a Hilbert space with inner product

$$\langle \boldsymbol{\phi}, \boldsymbol{\psi} \rangle_X = \sum_{j=1}^{r} \Big\{ \int_0^{\ell} \big(\Lambda \partial_z^2 \phi_{1,j} \overline{\partial_z^2 \psi_{1,j}} + \mu \phi_{2,j} \overline{\psi_{2,j}} \big) \,\mathrm{d}z + m \phi_{3,j} \overline{\psi_{3,j}} \Big\}. \tag{B.1}$$

The associated norm is defined by $||\boldsymbol{\phi}||^2 = \langle \boldsymbol{\phi}, \boldsymbol{\phi} \rangle_X \;\forall\; \boldsymbol{\phi} = \begin{bmatrix} \boldsymbol{\phi}_1^T & \boldsymbol{\phi}_2^T & \boldsymbol{\phi}_3^T \end{bmatrix}^T$, $\boldsymbol{\psi} = [\boldsymbol{\psi}_1^T \quad \boldsymbol{\psi}_2^T \quad \boldsymbol{\psi}_3^T]^T \in X$. The state vector is given by $\boldsymbol{x} = [\boldsymbol{x}_1 \quad \boldsymbol{x}_2 \quad \boldsymbol{x}_3]^T$ with

$$\begin{aligned} \boldsymbol{x}_1(t) &= \begin{bmatrix} s_1(\cdot\,,t) & \dots & s_r(\cdot\,,t) \end{bmatrix}^T, \\ \boldsymbol{x}_2(t) &= \begin{bmatrix} \partial_t s_1(\cdot\,,t) & \dots & \partial_t s_r(\cdot\,,t) \end{bmatrix}^T, \\ \boldsymbol{x}_3(t) &= \begin{bmatrix} \partial_t s_1(\ell,t) & \dots & \partial_t s_r(\ell,t) \end{bmatrix}^T. \end{aligned} \tag{B.2}$$

This choice leads to the abstract initial value problem

$$\dot{\boldsymbol{x}} = A(K)\boldsymbol{x} + B\boldsymbol{u}, \quad t > 0, \quad \boldsymbol{x}(0) = \boldsymbol{x}_0 \in \mathcal{D}(A) \tag{B.3a}$$

where $\boldsymbol{u}(t) = [U_1 \quad \dots \quad U_r]^T$ denotes the input vector. The abstract operators are given by

$$A(K)\boldsymbol{x} = \begin{bmatrix} \boldsymbol{x}_2 \\ -\frac{1}{\mu}\big(\Lambda \partial_z^4 \boldsymbol{x}_1 + \gamma^{\mathrm{v}} \boldsymbol{x}_2 - \gamma^{\mathrm{sv}} \partial_z^2 \boldsymbol{x}_2 + \gamma^{\mathrm{kv}} \partial_z^4 \boldsymbol{x}_2\big) \\ \frac{1}{m}\big(\Lambda \partial_z^3 \boldsymbol{x}_1 - \gamma^{\mathrm{sv}} \partial_z \boldsymbol{x}_2 + \gamma^{\mathrm{kv}} \partial_z^3 \boldsymbol{x}_2 - k_j \boldsymbol{x}_1\big)\big|_{z=\ell} \end{bmatrix}, \quad B = \begin{bmatrix} 0 & \dots & 0 \\ \partial_z^2 \Gamma(z) & \dots & \partial_z^2 \Gamma(z) \\ 0 & \dots & 0 \end{bmatrix} \tag{B.3b}$$

where for the domain holds

$$\begin{aligned} \mathcal{D}(A(K)) = \big\{ \boldsymbol{x} \in (H^4(0,\ell))^r \times (H_0^2(0,l))^r \times \mathbb{R}^r : (\Lambda \partial_z^4 \boldsymbol{x}_1 + \gamma^{\mathrm{kv}} \partial_z^4 \boldsymbol{x}_2 - \gamma^{\mathrm{sv}} \partial_z^2 \boldsymbol{x}_2) \in (L^2(0,\ell))^r, \\ \boldsymbol{x}_1(0) = \partial_z \boldsymbol{x}_1\big|_{z=0} = \boldsymbol{0},\; \Lambda \partial_z^2 \boldsymbol{x}_1 + \gamma^{\mathrm{kv}} \partial_z^2 \boldsymbol{x}_2\big|_{z=\ell} = \boldsymbol{0},\; \boldsymbol{x}_3 = \boldsymbol{x}_2(\ell) \big\}. \end{aligned} \tag{B.3c}$$

The coupling matrix K is derived from (2.54) and appears as a symmetric matrix $K = K^T$ of the form

$$K = \begin{bmatrix} k_{1,2} & -k_{1,2} & 0 & \cdots & 0 & 0 \\ -k_{1,2} & k_{1,2}+k_{2,3} & -k_{2,3} & \cdots & 0 & 0 \\ \vdots & & & & \vdots & \vdots \\ 0 & & \cdots & & -k_{r-1,r} & k_{r-1,r} \end{bmatrix} \tag{B.3d}$$

Taking the specific structure of K into account caused by the coupling of adjacent beams, the coupling matrix displays one zero eigenvalues. Therefore, there exists a regular transformation matrix V, which transforms K into a diagonal form $\bar{K} = V^{-1}KV$. Applying this transformation to the state vector

$$\boldsymbol{x} \mapsto \mathcal{V}\boldsymbol{x}, \quad \mathcal{V} = \begin{bmatrix} V & 0 & 0 \\ 0 & V & 0 \\ 0 & 0 & V \end{bmatrix} \tag{B.4}$$

results in the decoupled system description

$$\dot{\boldsymbol{x}} = \mathcal{A}\boldsymbol{x} + \mathcal{B}\boldsymbol{U}, \quad t > 0, \quad \boldsymbol{x}(0) = \boldsymbol{x}_0 \in \mathcal{D}(\mathcal{A}), \tag{B.5}$$

where $\mathcal{A} = A(\bar{K})$, $\mathcal{B} = \mathcal{V}^{-1}B$ and $\boldsymbol{x}_0 \mapsto \mathcal{V}\boldsymbol{x}_0$ for $\mathcal{D}(\mathcal{A}) = \mathcal{D}(A)$ holds true. The decoupling of the system operator $\mathcal{A}$ is obtained by shifting the coupling into the new input operator $\mathcal{B}$. In this representation every beam is actuated by multiple MFC-patch pairs. This leads to the fact, that the existence and the uniqueness can be proved by the analysis of a single beam, see, e.g., [10, 74].

B.2. Distribution of Eigenvalues

Before the actual flatness-based feedforward control is derived, the eigenvalue distribution of the vertical beam configuration is determined considering its asymptotic behavior. The distribution will be used later on to analyze the convergence of the flat parameterization.

Taking the decoupling of the beam structure by (B.4) into account the eigenvalue analysis for the decoupled abstract system (B.5) is sufficient.

Remark B.1 *As mentioned before, see Remark 3.1, a single damping model is not capable to describe the dynamics observed at the experimental setup. Hence, two combinations of damping models are taken into account, the combination of viscous and structural damping $\gamma^{kv} = 0$ as well as the combination of viscous and Kelvin-Voigt damping $\gamma^{sv} = 0$.*

For this purpose, the following analysis focuses on these two cases: At first the combination of viscous and secondly structural damping and after that the combination of viscous and Kelvin-Voigt damping are addressed. Considering [96, 24, 13, 29] the eigenvalues of the damped system are related to the undamped system. Therefore, the determination of the eigenvalue distribution begins with the examination of the distribution of the undamped system.

B.2.1. Undamped Case

The undamped ($\gamma^{\mathrm{v}} = \gamma^{\mathrm{sv}} = \gamma^{\mathrm{kv}} = 0$) system description is defined as

$$\dot{\boldsymbol{x}} = \mathcal{A}_{\mathrm{u}}\boldsymbol{x} + \mathcal{B}\boldsymbol{U}, \quad t > 0, \quad \boldsymbol{x}(0) = \boldsymbol{x}_0 \in \mathcal{D}(\mathcal{A}_{\mathrm{u}}) \tag{B.6a}$$

where the operator of the undamped system is given by

$$\mathcal{A}_{\mathrm{u}}\boldsymbol{x} = \begin{bmatrix} 0 & I & 0 \\ -T & 0 & 0 \\ \left(\frac{\Lambda}{m_j}\partial_z^3 + \frac{k_j}{m_j}\right)\Big|_{z=\ell} & 0 & 0 \end{bmatrix} \boldsymbol{x}, \tag{B.6b}$$

with $T = (\Lambda/\mu)\partial_z^4$ and I denoting the identity matrix. For the domain holds

$$\begin{aligned} \mathcal{D}(A(K)) = \big\{ \boldsymbol{x} \in (H^4(0,\ell))^r \times (H_0^2(0,l))^r \times \mathbb{R}^r : \ \Lambda\partial_z^4\boldsymbol{x}_1 \in (L^2(0,\ell))^r, \\ \boldsymbol{x}_1(0) = \partial_z\boldsymbol{x}_1\big|_{z=0} = \boldsymbol{0}, \ \Lambda\partial_z^2\boldsymbol{x}_1\big|_{z=\ell} = \boldsymbol{0}, \ \boldsymbol{x}_3 = \boldsymbol{x}_2(\ell) \big\}. \end{aligned} \tag{B.6c}$$

The evaluation of the eigenvalue problem $\mathcal{A}_{\mathrm{u}}\boldsymbol{\Phi}_{\mathrm{u}} = \lambda_{\mathrm{u}}\boldsymbol{\Phi}_{\mathrm{u}}$ is split into two parts. The first leads to $-T\Phi_{\mathrm{u},1} = \lambda_{\mathrm{u}}\Phi_{\mathrm{u},2} = \lambda_{\mathrm{u}}^2\Phi_{\mathrm{u},1}$, in which λ_{u} denotes the eigenvalues of the operator of the undamped system and $\omega = -\lambda_{\mathrm{u}}^2$

denotes the eigenvalues of the operator T. For the associated eigenvector $\mathbf{\Phi}_\mathrm{u}(z) \in \mathcal{D}(A(K))$ holds true. The second part yields $\frac{\Lambda}{m_j}\partial_z^3\Phi_\mathrm{u}\big|_{z=\ell} + \frac{k_j}{m_j}\Phi_\mathrm{u}(\ell) = \lambda_\mathrm{u}\Phi_{\mathrm{u},3} = \lambda_\mathrm{u}\Phi_{\mathrm{u},2}(\ell) = \lambda_\mathrm{u}^2\Phi_{\mathrm{u},1}(\ell)$.

Below the simplified notation $\Phi_\mathrm{u}(\,\cdot\,) = \Phi_{\mathrm{u},1}(\,\cdot\,)$ is used. The evaluation of the eigenvalue problem leads to

$$\partial_z^4\Phi_\mathrm{u} - \kappa^4\Phi_\mathrm{u} = 0, \quad \text{with} \quad -\kappa^4 = \frac{\mu\lambda_\mathrm{u}^2}{\Lambda}, \tag{B.7a}$$

taking the boundaries for $(0, \ell)$ into account

$$\Phi_\mathrm{u} = \partial_z\Phi_\mathrm{u}\big|_{z=0} = \mathbf{0}, \quad \Lambda\partial_z^2\Phi_\mathrm{u}\big|_{z=\ell} = \mathbf{0}, \quad \partial_z^3\Phi_\mathrm{u}\big|_{z=\ell} + \eta\Phi_\mathrm{u}(\ell) = \mathbf{0}, \quad \text{with} \quad \eta = \frac{k_j}{\Lambda} + \frac{m_j\kappa^4}{\mu}. \tag{B.7b}$$

The exponential approach in its trigonometric formulation

$$\Phi_\mathrm{u}(z) = a_1\sin(\kappa z) + a_2\cos(\kappa z) + a_3\sinh(\kappa z) + a_4\cosh(\kappa z) \tag{B.8}$$

is used as solution ansatz. Applying this approach to the boundary conditions (B.7b) results in the characteristic equation

$$0 = 2\kappa^3\big(\cos(\kappa\ell) + \operatorname{sech}(\kappa\ell)\big) - 2\eta\big(\sin(\kappa\ell) + \cos(\kappa\ell)\tanh(\kappa\ell)\big), \tag{B.9}$$

where $\kappa = 0$ only results in the trivial solution. Taking the properties of $\lim_{\kappa\to\pm\infty}\operatorname{sech}(\kappa\ell) = 0$ and $\lim_{\kappa\to\pm\infty}\tanh(\kappa\ell) = \pm 1$ into account the characteristic equation simplifies for $\kappa\ell \gg 1$ to

$$2(\eta + \kappa^3 - \eta\tan(\kappa\ell)) = 0. \tag{B.10}$$

The substitution for η considering (B.7b) and the reformulation of the approximation results in

$$\tan(\kappa\ell) = 1 + \frac{\Lambda\mu\kappa^3}{k_j\mu + \Lambda m_j\kappa^4}. \tag{B.11}$$

Hence, for $\kappa \to \infty$ the asymptotics of the eigenvalues is given by the zeros of $\tan(\kappa\ell) - 1 = 0$ leading to

$$\kappa = \frac{\pi}{\ell}\Big(\frac{1}{4} + k\Big) \quad \Rightarrow \quad -\lambda_\mathrm{u}^2 = \omega = \frac{\Lambda\pi^4}{\mu\ell^4}\Big(\frac{1}{4} + k\Big)^4, \tag{B.12}$$

with $k \in \mathbb{N}$. Therefore, the asymptotic eigenvalue distribution of the operator $\mathcal{A}_\mathrm{u}$ of the coupled and undamped system results in

$$\lambda_\mathrm{u}^{\pm} = \pm\mathrm{j}\sqrt{\frac{\Lambda\pi^4}{\mu\ell^4}\Big(\frac{1}{4} + k\Big)^4}. \tag{B.13}$$

As mentioned before the eigenvalues of the damped system are related to the undamped system. The referred literature [96, 24, 13] provides analyses for a single bending beam affected by distinct damping models like viscous, structural and Kelvin-Voigt damping. Below, the discussed combinations of these damping models are considered for the system of the coupled Euler-Bernoulli beams.

For a complete description of the eigenfunctions of the undamped beam $\Phi_\mathrm{u}(z)$ the coefficients a_1, a_2, a_3, and a_4 have to be determined. To do this the boundary conditions have to be taken into account providing a system of equations which leads to the relations

$$\begin{aligned} &a_1 = -a_3, \quad a_2 = -a_4, \quad a_2 = \chi a_1 \\ &\text{with} \quad \chi = \frac{-\sin(\kappa\ell) - \sinh(\kappa\ell)}{\cos(\kappa\ell) + \cosh(\kappa\ell)} = \frac{-\sin\Big(\pi\big(\frac{1}{4} + k\big)\Big) - \sinh\Big(\pi\big(\frac{1}{4} + k\big)\Big)}{\cos\Big(\pi\big(\frac{1}{4} + k\big)\Big) + \cosh\Big(\pi\big(\frac{1}{4} + k\big)\Big)}. \end{aligned} \tag{B.14}$$

Due to this, the eigenfunction results in

$$\Phi_\mathrm{u}(z, k) = a_1\big(\sin(\kappa z) + \cos(\kappa z) + \chi\sinh(\kappa z) - \chi\cosh(\kappa z)\big), \tag{B.15}$$

considering that χ depends on k, see (B.14). The determination of a_1 requires an additional condition. For this purpose it is chosen that the orthogonal eigenvectors

$$\begin{aligned}\boldsymbol{\Phi}_{\mathrm{u}}(z,k) &= \begin{bmatrix}\boldsymbol{\phi}_1^T & \boldsymbol{\phi}_2^T & \boldsymbol{\phi}_3^T\end{bmatrix}^T \in \mathbb{C}^{3r} \quad \text{with}\\ \boldsymbol{\phi}_1^T &= \begin{bmatrix}\Phi_{\mathrm{u},1}(z,k) & \dots & \Phi_{\mathrm{u},r}(z,k)\end{bmatrix}^T,\\ \boldsymbol{\phi}_2^T &= \begin{bmatrix}\lambda_{\mathrm{u},k}\Phi_{\mathrm{u},1}(z,k) & \dots & \lambda_{\mathrm{u},k}\Phi_{\mathrm{u},r}(z,k)\end{bmatrix}^T,\\ \boldsymbol{\phi}_3^T &= \begin{bmatrix}\lambda_{\mathrm{u},k}\Phi_{\mathrm{u},1}(\ell,k) & \dots & \lambda_{\mathrm{u},k}\Phi_{\mathrm{u},r}(\ell,k)\end{bmatrix}^T,\end{aligned} \tag{B.16}$$

should be normalized

$$\begin{aligned}\langle\boldsymbol{\Phi}_{\mathrm{u}}(z,i),\boldsymbol{\Phi}_{\mathrm{u}}(z,k)\rangle_X = \sum_{j=1}^{r}\Big\{\int_0^{\ell}\Big(&\Lambda\partial_z^2\Phi_{\mathrm{u},j}(z,i)\overline{\partial_z^2\Phi_{\mathrm{u},j}(z,k)} + \mu\lambda_{\mathrm{u},i}\Phi_{\mathrm{uj}}(z,i)\overline{\lambda_{\mathrm{u},k}\Phi_{\mathrm{u},j}(z,k)}\Big)\,\mathrm{d}z\\ &+ m\lambda_{\mathrm{u},i}\Phi_{\mathrm{u},j}(\ell,i)\overline{\lambda_{\mathrm{u},k}\Phi_{\mathrm{u},j}(\ell,k)}\Big\} \equiv \delta_{ik},\end{aligned} \tag{B.17}$$

where δ_{ik} describes the Kronecker delta. The solution of the integral can be solved for $a_1(\kappa)$ using a computer algebra system. However, the resulting solution is not presented here due to the length of the expression.

B.2.2. Combination of Viscous and Structural Damping

The case of combined viscous and structural damping ($\gamma^{\mathrm{kv}} = 0$) is addressed by

$$\dot{\boldsymbol{x}} = \mathcal{A}_{\mathrm{sv}}\boldsymbol{x} + \mathcal{B}\boldsymbol{U}, \quad t > 0, \quad \boldsymbol{x}(0) = \boldsymbol{x}_0 \in \mathcal{D}(\mathcal{A}_{\mathrm{sv}}) \tag{B.18a}$$

Taking the system operator into account

$$\mathcal{A}_{\mathrm{sv}}\boldsymbol{x} = \begin{bmatrix} 0 & I & 0\\ -T & -2\bar{\gamma}^{\mathrm{v}} + 2\bar{\gamma}^{\mathrm{sv}}T^{1/2} & 0\\ \left(\frac{\Lambda}{m_j}\partial_z^3 + \frac{k_j}{m_j}\right)\Big|_{z=\ell} & -\frac{2\mu\bar{\gamma}^{\mathrm{sv}}}{m_j}\sqrt{\frac{\Lambda}{\mu}}\partial_z\Big|_{z=\ell} & 0\end{bmatrix}\boldsymbol{x}, \tag{B.18b}$$

with $\bar{\gamma}^{\mathrm{v}} = \frac{\gamma^{\mathrm{v}}}{2\mu}$, $\bar{\gamma}^{\mathrm{sv}} = \frac{\gamma^{\mathrm{sv}}}{2\mu}\sqrt{\mu/\Lambda}$ and $T^{1/2} = \sqrt{\Lambda/\mu}\,\partial_z^2$. Furthermore, for the domain holds

$$\begin{aligned}\mathcal{D}(\mathcal{A}_{\mathrm{sv}}) = \big\{\boldsymbol{x} \in (H^4(0,\ell))^r \times (H_0^2(0,\ell))^r \times \mathbb{R}^r : (\Lambda\partial_z^4\boldsymbol{x}_1 - 2\bar{\gamma}^{\mathrm{sv}}\sqrt{\mu\Lambda}\partial_z^2\boldsymbol{x}_2) \in (L^2(0,\ell))^r,\\ \boldsymbol{x}_1(0) = \partial_z\boldsymbol{x}_1\big|_{z=0} = \boldsymbol{0},\ \Lambda\partial_z^2\boldsymbol{x}_1\big|_{z=\ell} = \boldsymbol{0},\ \boldsymbol{x}_3 = \boldsymbol{x}_2(\ell)\big\}.\end{aligned} \tag{B.18c}$$

The evaluation of the eigenvalue problem leads to

$$-T\Phi_{\mathrm{sv}} + \left(2\bar{\gamma}^{\mathrm{sv}}T^{1/2} - 2\bar{\gamma}^{\mathrm{v}}\right)\lambda_{\mathrm{sv}}\Phi_{\mathrm{sv}} = \lambda_{\mathrm{sv}}^2\Phi_{\mathrm{sv}}. \tag{B.19}$$

According to [29, 24] the eigenvalue problem of the operator can be split into $T\Phi_{\mathrm{sv}} = \omega\Phi_{\mathrm{sv}}$ and $T^{1/2}\Phi_{\mathrm{sv}} = \pm\sqrt{\omega}\Phi_{\mathrm{sv}}$, in which two branches of eigenvalues of the operator $T^{1/2}$ exist. Choosing the negative branch leads to the expected stable behavior. Applying this to (B.19) results in

$$\omega\Phi_{\mathrm{sv}} + \left(2\bar{\gamma}^{\mathrm{v}} + 2\bar{\gamma}^{\mathrm{sv}}\sqrt{\omega}\right)\lambda_{\mathrm{sv}}\Phi_{\mathrm{sv}} + \lambda_{\mathrm{sv}}^2\Phi_{\mathrm{sv}} = 0 \quad \Rightarrow \quad \lambda_{\mathrm{sv}}^{\pm} = -\left(\bar{\gamma}^{\mathrm{v}} + \bar{\gamma}^{\mathrm{sv}}\sqrt{\omega}\right) \pm \mathrm{j}\sqrt{\omega - \left(\bar{\gamma}^{\mathrm{v}} + \bar{\gamma}^{\mathrm{sv}}\sqrt{\omega}\right)^2}. \tag{B.20}$$

B.2.3. Combination of Viscous and Kelvin-Voigt Damping

The asymptotic eigenvalue distribution for the system of combined viscous and Kelvin-Voigt damping ($\gamma^{\mathrm{sv}} = 0$) is analogously determined. The system is given by

$$\dot{\boldsymbol{x}} = \mathcal{A}_{\mathrm{kv}}\boldsymbol{x} + \mathcal{B}\boldsymbol{U}, \quad t > 0, \quad \boldsymbol{x}(0) = \boldsymbol{x}_0 \in \mathcal{D}(\mathcal{A}_{\mathrm{kv}}), \tag{B.21a}$$

considering the system operator

$$\mathcal{A}_{\mathrm{kv}}\boldsymbol{x} = \begin{bmatrix} 0 & I & 0\\ -T & -2\bar{\gamma}^{\mathrm{v}} + 2\bar{\gamma}^{\mathrm{kv}}T & 0\\ \left(\frac{\Lambda}{m_j}\partial_z^3 + \frac{k_j}{m_j}\right)\Big|_{z=\ell} & -\frac{2\Lambda\bar{\gamma}^{\mathrm{kv}}}{m_j}\partial_z^3\Big|_{z=\ell} & 0\end{bmatrix}\boldsymbol{x}, \tag{B.21b}$$

with $\bar{\gamma}^{\mathrm{kv}} = \frac{\gamma^{\mathrm{kv}}}{2\Lambda}$. The domain is defined by

$$\begin{aligned}\mathcal{D}(\mathcal{A}_{\mathrm{kv}}) = \big\{ \boldsymbol{x} \in (H^4(0,\ell))^r \times (H_0^2(0,l))^r \times \mathbb{R}^r : (\Lambda \partial_z^4 \boldsymbol{x}_1 + 2\bar{\gamma}^{\mathrm{kv}} \Lambda \partial_z^4 \boldsymbol{x}_2) \in (L^2(0,\ell))^r, \\ \boldsymbol{x}_1(0) = \partial_z \boldsymbol{x}_1\big|_{z=0} = \mathbf{0},\ \Lambda \partial_z^2 \boldsymbol{x}_1 + \gamma^{\mathrm{kv}} \partial_z^2 \boldsymbol{x}_2\big|_{z=\ell} = \mathbf{0},\ \boldsymbol{x}_3 = \boldsymbol{x}_2(\ell) \big\}.\end{aligned} \tag{B.21c}$$

The characteristic equation of the eigenvalue problem results in

$$-T\Phi_{\mathrm{kv}} - \big(2\bar{\gamma}^{\mathrm{v}} \Phi_{\mathrm{kv}} + 2\bar{\gamma}^{\mathrm{kv}} T \Phi_{\mathrm{kv}}\big)\lambda_{\mathrm{kv}} = \lambda_{\mathrm{kv}}^2 \Phi_{\mathrm{kv}}. \tag{B.22}$$

By applying $T\Phi_{\mathrm{kv}} = \omega \Phi_{\mathrm{kv}}$ one obtains the asymptotic distribution of eigenvalues for the combined viscous and Kelvin-Voigt damping, see also [56], in the form

$$\omega\Phi_{\mathrm{kv}} + \big(2\bar{\gamma}^{\mathrm{v}} \Phi_{\mathrm{kv}} + 2\bar{\gamma}^{\mathrm{kv}} \omega \Phi_{\mathrm{kv}}\big)\lambda_{\mathrm{kv}} + \lambda_{\mathrm{kv}}^2 \Phi_{\mathrm{kv}} = 0 \quad \Rightarrow \quad \lambda_{\mathrm{kv}}^{\pm} = -\big(\bar{\gamma}^{\mathrm{v}} + \bar{\gamma}^{\mathrm{kv}} \omega\big) \pm \mathrm{j}\sqrt{\omega - \big(\bar{\gamma}^{\mathrm{v}} + \bar{\gamma}^{\mathrm{kv}} \omega\big)^2}. \tag{B.23}$$

B.2.4. Comparison of the Asymptotic and Numeric Eigenvalue Distribution

Fig. B.1 compares the asymptotic and numeric distribution of eigenvalues for both cases of combined damping. The viscous and structural damping is displayed on the left, where on the right the results of the viscous and Kelvin-Voigt damping is displayed. As can be seen both cases show a consensus between the asymptotic and the numeric distribution, which validates the asymptotic eigenvalue distributions. The numeric calculation of eigenvalues is based on a finite dimensional Galerkin approximation considering $N_j = 2000$ test functions per beam, see (2.60). The considered geometric dimensions and material parameters of the three carriers used in the numeric and the asymptotic eigenvalue analysis are listed in Tables 2.1 and 3.1. These also denote the parameters of the actual experimental setup.

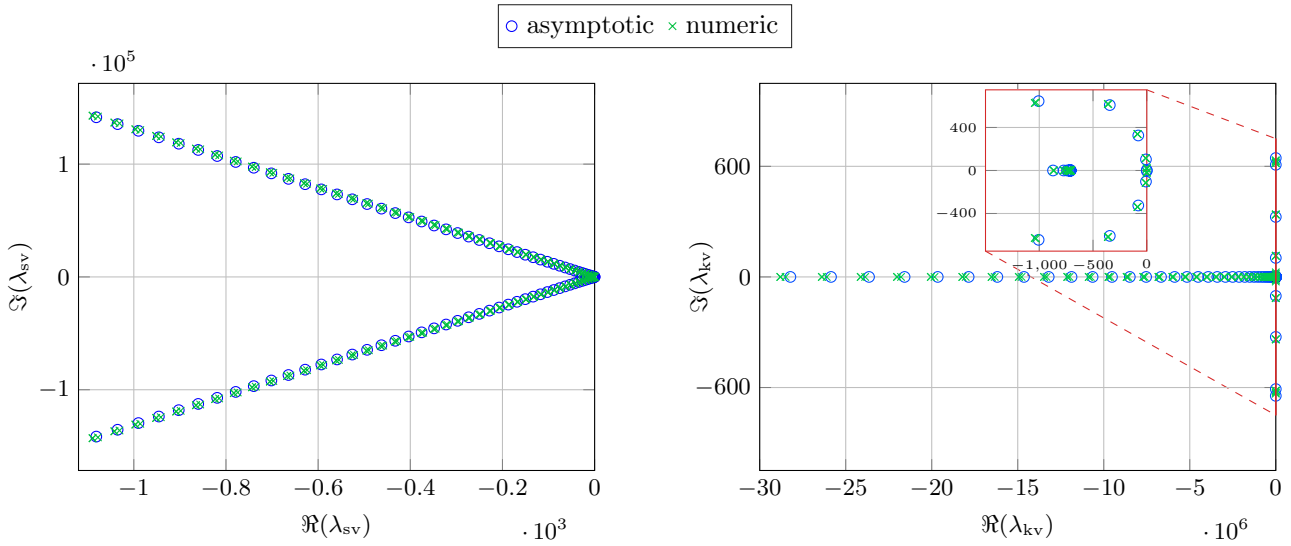

Figure B.1.: Comparison of asymptotic and numeric eigenvalue distribution of the vertical beam configuration considering the combined damping model of viscous and structural damping on the left and viscous and Kelvin-Voigt damping on the right.

B.3. Systematic Design of a Flat Output

For the differential parametrization of the system states and inputs an auxiliary operand, the so-called flat output, is necessary. This operand can be obtained by taking the spectral representation of the operator $\mathcal{A} = A(\bar{K})$ into account, assuming that $\mathcal{A}$ is a Riesz operator [41, 27, 45]. In this case the set of eigenvectors $\{\boldsymbol{\phi}_l\}_{l\in\mathcal{L}}$ of $\mathcal{A}$ and the set of eigenvectors $\{\boldsymbol{\psi}_l\}_{l\in\mathcal{L}}$ of the adjoint operator $\mathcal{A}^*$ form a bi-orthonomal Riesz-basis, where $\mathcal{L}$ is a countable infinite index set. As mentioned before the considered damping results in disjunct eigenvalues so that the operator can be formulated as

$$\mathcal{A}\boldsymbol{x} = \sum_{l\in\mathcal{L}} \lambda_l \langle \boldsymbol{x}, \boldsymbol{\psi}_l \rangle_X \boldsymbol{\phi}_l. \tag{B.24}$$

The resolvent of $\mathcal{A}$ is given by

$$R(s,\mathcal{A})\boldsymbol{x} = \sum_{l\in\mathcal{L}} \frac{1}{s-\lambda_l}\langle \boldsymbol{x}, \boldsymbol{\psi}_l\rangle_X \boldsymbol{\phi}_l. \tag{B.25}$$

Assumption B.2 *In the following it is supposed, that the system is approximately controllable, which means for a Riesz-system of the form* (B.5) *that*

$$rank\left[\langle \boldsymbol{b}_1^T, \boldsymbol{\psi}_l\rangle \quad \dots \quad \langle \boldsymbol{b}_r^T, \boldsymbol{\psi}_l\rangle\right] = 1 \quad \forall \quad l \in \mathcal{L}, \tag{B.26}$$

must apply, with $\boldsymbol{b}_k^T$ *denoting the* k^{th} *column of* $\mathcal{B}$ *[27].*

In the undamped case $\gamma^{\mathrm{v}} = \gamma^{\mathrm{sv}} = \gamma^{\mathrm{kv}} = 0$ and the case of viscous damping $\gamma^{\mathrm{v}} \neq 0$ the proof that $\mathcal{A}$ is a Riesz operator is given by the results of a single bending beam, see [44], due to the decoupled system and the distinct eigenvalues. Analogously the proof for the case of a viscous and / or structural damped system can be done, due to the distinct eigenvalue distribution, see Appendix B.2.2. The combination of damping models including the Kelvin-Voigt $\gamma^{\mathrm{kv}} \neq 0$ leads to an accumulation point of the distribution of the eigenvalues, which leads to a analysis of the spectrum of $\mathcal{A}$. Such kind of analyses can be found in [45, 53] or for the case of spatial varying parameters in [118].

Applying the Laplace-transformation to (B.5), considering (B.24) and (B.25), yields

$$\hat{\boldsymbol{x}}(s) = \sum_{l\in\mathcal{L}} \frac{1}{s-\lambda_l}\langle \mathcal{B}\hat{\boldsymbol{u}}(s), \boldsymbol{\psi}_l\rangle_X \boldsymbol{\phi}_l$$

with $s \in \rho(\mathcal{A})$, $\Re\{s\} > \sup_l \Re\{\lambda_l\}$ and $\rho(\mathcal{A})$ denoting the resolvent set of $\mathcal{A}$. A systematic design approach for the flat output is given by [78] considering the extension of the term $1/(s-\lambda_l)$, i.e.,

$$\hat{\boldsymbol{x}}(s) = -\sum_{l\in\mathcal{L}} \frac{1}{\lambda_l}\frac{1}{1-\frac{s}{\lambda_l}}\langle \mathcal{B}\hat{\boldsymbol{u}}(s), \boldsymbol{\psi}_l\rangle_X \boldsymbol{\phi}_l = -\sum_{l\in\mathcal{L}} \frac{1}{\lambda_l}\frac{\prod\limits_{i,i\neq l}\left(1-\frac{s}{\lambda_i}\right)}{\prod\limits_{i}\left(1-\frac{s}{\lambda_i}\right)}\langle \mathcal{B}\hat{\boldsymbol{u}}(s), \boldsymbol{\psi}_l\rangle_X \boldsymbol{\phi}_l. \tag{B.27}$$

Substitution of the auxiliary operand $\hat{\boldsymbol{\xi}}(s)$ by means of

$$\hat{\boldsymbol{u}}(s) = \hat{D}_u(s)\hat{\boldsymbol{\xi}}(s), \quad \hat{D}_u(s) = \prod_i \left(1-\frac{s}{\lambda_i}\right) \tag{B.28a}$$

yields

$$\hat{\boldsymbol{x}}(s) = -\sum_{l\in\mathcal{L}} \frac{1}{\lambda_l}\hat{D}_x(s)\langle \mathcal{B}\hat{\boldsymbol{\xi}}(s), \boldsymbol{\psi}_l\rangle_X \boldsymbol{\phi}_l \quad \text{with} \quad \hat{D}_x(s) = \prod_{i,i\neq l}\left(1-\frac{s}{\lambda_i}\right). \tag{B.28b}$$

Due to this, the desired parametrization of state $\hat{\boldsymbol{x}}(s)$ and input $\hat{\boldsymbol{u}}(s)$ can be formally obtained by the flat output $\hat{\boldsymbol{\xi}}(s)$.

The consideration of the distinct damping models, see Remark B.1, leads to distinct index sets $\mathcal{L}$. In the case of viscous and structural damping $\gamma^{\mathrm{kv}} = 0$ all eigenvalues are distinct so that the set $\mathcal{L}$ contains no accumulation point. Hence, all series and products are evaluated by the countable infinite number of eigenvalues of operator $\mathcal{A}$. For this purpose the Hadamard factorization theorem states that the infinite series $\hat{D}_x(s)$ and $\hat{D}_u(s)$ correspond to factorizations of entire functions [14], provided that the set of zeros $\{\lambda_i\}_i$ of $\hat{D}_x(s)$ and $\hat{D}_u(s)$ is described by genus $g_s = 0$, see also [56]. Here, the genus is defined as the least positive integer g_s for which the series

$$\sum_i |\lambda_i|^{g_s+1} \tag{B.29}$$

converges [14, 69]. However, if $g_s \neq 0$ holds true the series $\hat{D}_x(s)$ and $\hat{D}_u(s)$ has to be replaced by corresponding Weierstraß products, e.g., [79, 78, 101, 56]. Such an entire function defined by the finite order ρ and finite type τ can be expanded to a MacLaurin series in s, which converges $\forall s \in \mathbb{C}$. Hence, the operators $\hat{D}_x(s)$ and $\hat{D}_u(s)$ result in

$$\begin{aligned}
\hat{D}_x(s) &= \sum_{i\in\mathbb{N}_0} c_i^x s^i \;\bullet\!\!-\!\!\circ\; D_x(\partial_t) = \sum_{i\in\mathbb{N}_0} c_i^x \partial_t^i, \\
\hat{D}_u(s) &= \sum_{i\in\mathbb{N}_0} c_i^u s^i \;\bullet\!\!-\!\!\circ\; D_u(\partial_t) = \sum_{i\in\mathbb{N}_0} c_i^u \partial_t^i
\end{aligned} \tag{B.30}$$

with $\mathbb{N}_0 := \mathbb{N} \cup \{0\}$ and recalling that the operator s represents the time derivative. Taking (B.28a) and (B.28b) into account yields

$$\boldsymbol{x}(t) = -\sum_{l\in\mathbb{N}_0} \frac{1}{\lambda_l} \sum_{i\in\mathbb{N}_0} c_i^x \langle \mathcal{B}\partial_t^i \boldsymbol{\xi}(t), \boldsymbol{\psi}_l \rangle_X \boldsymbol{\phi}_l, \tag{B.31}$$

$$\boldsymbol{u}(t) = \sum_{i\in\mathbb{N}_0} c_i^u \partial_t^i \boldsymbol{\xi}(t). \tag{B.32}$$

Accordingly the associated trajectory for the flat output $\boldsymbol{\xi}(t)$ has to be a smooth function. Furthermore, the choice of this function must ensure convergence of the parametrization.

In the case of viscous and Kelvin-Voigt damping $\gamma^{\mathrm{sv}} = 0$ the distribution of eigenvalues displays an accumulation point. Due to this, the operators $\hat{D}_x(s)$ and $\hat{D}_u(s)$ can not be reformulated as a factorization of an entire function. Unless the following approximation is introduced, where the complete spectrum is split into two infinite subsets. The first subset Σ^- contains the set of eigenvalues tending to $-\infty$ and the second subset Σ^+ the set of eigenvalues, which tend to the accumulation point, see Fig. B.1. The considered index set is defined as $\mathcal{L} = \Sigma^- \cup \Sigma_0^+$ with the finite set $\Sigma_0^+ \subset \Sigma^+$. This definition enables us to apply the previously discussed approach taking the entire function theory into account considering only Σ^-. The resulting approximation error can be assumed negligible if a sufficiently large number of eigenvalues in Σ_0^+ is considered.

B.4. Convergence Analysis

Below, the convergence of the presented flatness-based parameterization is analyzed. A general convergence analysis of spatial varying parameter systems described by Riesz-operators is given by [78]. This analysis restricts the choice of trajectory functions of the flat output to the class of so-called Gevrey functions.

Definition B.1 *The function ξ is in the Gevrey class $G_{M,\alpha}(\Omega)$ of order α in $\Omega \subset \mathbb{R}$ if $\xi \in C^\infty(\Omega)$ and if two positive constants M and α exist so that*

$$\sup_{t\in\Omega'} \left|\partial_t^l \xi\right| \leq M^{l+1}(l!)^\alpha, \quad l \in \mathbb{N} \cup \{0\}$$

for all closed subsets Ω' of Ω.

Remark B.2 *Taking Assumption B.2 (approximate controllability) into account [78] reveals convergent behavior of the time dependent input parameterization* (B.32)*, if $D_u(\partial_t)$ is an entire function of order ρ and finite type τ provided that $\xi_p \in G_{M,\alpha}(\mathbb{R})$, where $p = 1, \cdots, \sum_j^r p_j$ and $\alpha \leq 1/\rho$.*

For this reason the analysis is focused on the type and order of $D_u(\partial_t)$, which are evaluated by the asymptotic distribution of eigenvalues of the two considered damping cases (B.20) and (B.23).

As a consequence of the Weierstrass Theorem every entire function can be expressed by an infinite product [14, Chap. 2], [69, Chap. 4]. Furthermore, the order ρ of such a canonical product correlates with the convergence exponent of the set of zeros $\{\lambda_i\}$ [14, Theorem 2.6.5], [69, Theorem 3]. Hence, the convergence exponent ρ_1 of the sequence $(\lambda_i)_{i\in\mathbb{N}}$, $\lambda_i \in \mathbb{C}$ with $\lambda_i \neq 0$ and $\lim_{i\to\infty} \lambda_i = \infty$ is defined as $\rho_1 = \inf(\theta)$ with $\theta > 0$ for which the series $\sum_i |\lambda_i|^{-\theta}$ converges. Alternatively (see [14, Theorem 2.5.8] or [69, Chap. 3.2]) the convergence exponent can be determined by

$$\rho_1 = \lim_{r\to\infty} \sup \frac{\log(n(r))}{\log(r)}, \tag{B.33}$$

where $n(r) = \{\lambda_i, i \in \mathbb{N} : |\lambda_i| \leq r\}$ denotes the counting function depending on the radius in the complex domain r. For $i \gg 1$ the counting function can be determined by the asymptotic distribution of eigenvalues of Appendix B.2. Taking the case study of Remark B.1 into account the convergence exponent is determined for the combination of viscous and structural damping and for the case of viscous and Kelvin-Voigt damping, respectively.

B.4.1. Counting Number for Combined Viscous and Structural Damping

Reformulating the asymptotic distribution of eigenvalues (B.20) results in

$$\omega = \pm 2\sqrt{-2\bar{\gamma}^{\mathrm{sv}^2}\bar{\gamma}^{\mathrm{v}}\lambda_{\mathrm{sv}}^3 + (\bar{\gamma}^{\mathrm{sv}^4} - \bar{\gamma}^{\mathrm{sv}^2})\lambda_{\mathrm{sv}}^4} - 2\bar{\gamma}^{\mathrm{v}}\lambda_{\mathrm{sv}} + (2\bar{\gamma}^{\mathrm{sv}^2} - 1)\lambda_{\mathrm{sv}}^2, \tag{B.34}$$

applying (B.12) for ω and solving for $k_{\mathrm{sv}} = k$ leads to

$$k_{\mathrm{sv}}(\lambda_{\mathrm{sv}}) = -\frac{1}{4} + \frac{\ell}{\pi}\Big(\frac{\mu}{\Lambda}\big(-2\bar{\gamma}^{\mathrm{v}}\lambda_{\mathrm{sv}} + (2\bar{\gamma}^{\mathrm{sv}^2} - 1)\lambda_{\mathrm{sv}}^2 \pm 2\sqrt{-2\bar{\gamma}^{\mathrm{sv}^2}\bar{\gamma}^{\mathrm{v}}\lambda_{\mathrm{sv}}^3 + (\bar{\gamma}^{\mathrm{sv}^4} - \bar{\gamma}^{\mathrm{sv}^2})\lambda_{\mathrm{sv}}^4}\big)\Big)^{1/4}, \tag{B.35}$$

which directly provides the counting function $n_{\mathrm{sv}}(r) = k_{\mathrm{sv}}(r)$ with $\bar{\gamma}^{\mathrm{v}} = \frac{\gamma^{\mathrm{v}}}{2\mu}$ and $\bar{\gamma}^{\mathrm{sv}} = \frac{\gamma^{\mathrm{sv}}}{2\mu}\sqrt{\mu/\Lambda}$. Considering (B.33) the convergence exponent results in $\rho_{1,\mathrm{sv}} = 1/2$.

B.4.2. Counting Number for Combined Viscous and Kelvin-Voigt Damping

Analogously for the second case the reformulation of (B.23) yields

$$\omega = \frac{-2\bar{\gamma}^{\mathrm{v}}\lambda_{\mathrm{kv}} - \lambda_{\mathrm{kv}}^2}{1 + 2\bar{\gamma}^{\mathrm{kv}}\lambda_{\mathrm{kv}}}, \tag{B.36}$$

substituting (B.12) for ω and solving the result for $k_{\mathrm{kv}} = k$ leads to

$$k_{\mathrm{kv}}(\lambda_{\mathrm{kv}}) = -\frac{1}{4} + \frac{\ell}{\pi}\Big(\frac{2\bar{\gamma}^{\mathrm{v}}\lambda_{\mathrm{kv}} - \lambda_{\mathrm{kv}}^2}{1 + 2\bar{\gamma}^{\mathrm{kv}}\lambda_{\mathrm{kv}}}\frac{\mu}{\Lambda}\Big)^{1/4}, \tag{B.37}$$

which can be treated directly as counting function $n_{\mathrm{kv}}(r) = k_{\mathrm{kv}}(r)$ with $\bar{\gamma}^{\mathrm{kv}} = \frac{\gamma^{\mathrm{kv}}}{2\Lambda}$. Hence, the convergence exponent follows from (B.33) to $\rho_{1,\mathrm{kv}} = 1/4$ considering the complete spectrum of eigenvalues. If only the reduced set of eigenvalues $\mathcal{L} = \Sigma^- \cup \Sigma_0^+$ is considered neglecting the accumulation point, the convergence exponent results in $\rho_{1,\mathrm{kv}} = 1/2$.

B.4.3. Final Results of the Convergence Analysis

The finite type τ of $\hat{D}_u(s)$ for both damping combinations can be determined regarding [14, 69] by the limit

$$\tau = \lim_{r\to\infty} \sup \frac{\log \max_{|s|=r} |\hat{D}_u(s)|}{r^\rho}. \tag{B.38}$$

Considering the asymptotic distribution of eigenvalues (B.20) and (B.23) of both cases $\max_{|s|=r}|\hat{D}_u(s)|$ can be determined by

$$\max_{|s|=r}|\hat{D}_u(s)| = \prod_l \Big(1 + \frac{r}{\lambda^+_{\mathrm{sv|kv}}}\Big)\Big(1 + \frac{r}{\lambda^-_{\mathrm{sv|kv}}}\Big) = \prod_l \Big(1 + \frac{r^2}{\lambda^+_{\mathrm{sv|kv}}\lambda^-_{\mathrm{sv|kv}}}\Big). \tag{B.39}$$

For the viscous and structural damping this leads to

$$\max_{|s|=r}|\hat{D}_u(s)| = \prod_l \Big(1 + \frac{256\ell^4\mu r(2\bar{\gamma}^{\mathrm{v}} + r)}{\Lambda\pi^4(1+4l)^4} - \frac{32\bar{\gamma}^{\mathrm{sv}}\ell^4\sqrt{\frac{(1+4l)^4\Lambda}{\ell^4\mu}}\mu r\pi^2}{\Lambda\pi^4(1+4l)^4}\Big). \tag{B.40}$$

Here, two cases $\sqrt{(1+4l)^4} = \pm(1+4l)^2$ has to be analyzed. Both solutions converge to $\tau \approx 0.55$ leading to a convergent behavior of the parameterization $\hat{D}_u(s)$ using a Gevrey function with order $\alpha < 2$. Similarly the convergence of $\hat{D}_x(s)$ can be analyzed.

For the case of combined viscous and Kelvin-Voigt damping (B.39) results in

$$\max_{|s|=r}|\hat{D}_u(s)| = \prod_l \Big(1 + 2\gamma^{\mathrm{kv}}r + \frac{256\ell^4\mu r(2\gamma^{\mathrm{v}} + r)}{\Lambda\pi^4(1+4l)^4}\Big). \tag{B.41}$$

Considering the reduced set $\mathcal{L} = \Sigma^- \cup \Sigma_0^+$ the limit converges to $\tau \approx 0.55$. Using the complete set including the accumulation point the type becomes $\tau = \infty$ suggesting a divergent behavior of the parameterization $\hat{D}_u(s)$.

C. Second Order System Matrices

Below, the system matrices obtained form the approximations of the equations of motion of the presented beam structures are summarized.

C.1. Pointwise Interconnected Beam Structure

Subsequently the structures and elements of the mass, damping, stiffness, and input matrix introduced in Section 2.1.2.4 by (2.63) are summarized. The structures of the matrices are given by

$$\begin{aligned}
M &= \operatorname{diag}\{M_{1,\mathrm{c}} + M_{1,\mathrm{a}} + M_{1,\mathrm{m}}, \ldots, M_{r,\mathrm{c}} + M_{r,\mathrm{a}} + M_{r,\mathrm{m}}\},\\
C &= \operatorname{diag}\{C_{j,\mathrm{c}} + C_{j,\mathrm{a}}, \ldots, C_{r,\mathrm{c}} + C_{r,\mathrm{a}}\},\\
K &= \operatorname{diag}\{K_{j,\mathrm{c}} + K_{j,\mathrm{a}}, \ldots, K_{r,\mathrm{c}} + K_{r,\mathrm{a}}\} + \begin{bmatrix} K_{\mathrm{sp,mid},1} & -K_{\mathrm{sp,post},1} & 0 & 0\\ -K_{\mathrm{sp,pre},2} & K_{\mathrm{sp,mid},2} & -K_{\mathrm{sp,post},2} & 0\\ 0 & \ddots & \ddots & \ddots\\ 0 & -K_{\mathrm{sp,pre},j-1} & K_{\mathrm{sp,mid},j-1} & -K_{\mathrm{sp,post},j-1}\\ 0 & 0 & -K_{\mathrm{sp,pre},r} & K_{\mathrm{sp,mid},r} \end{bmatrix},\\
L &= \begin{bmatrix} \boldsymbol{l}_{1,1} & 0 & 0\\ 0 & \ddots & 0\\ 0 & 0 & \boldsymbol{l}_{r,p_r} \end{bmatrix},
\end{aligned} \tag{C.1}$$

where the second index characterizes the component of the structure, c denotes the carrier structure, a designates the actuator, and m indicates the tip mass. The elements are determined by the evaluation of the integrals over the beam's length or the evaluation of products of test functions at specific locations of (2.61) taking Definition 2.1 into account. Therefore, for the structure composed of $j \in \{1, \ldots, r\}$ beams equipped with $k \in 1, \ldots, p_j$ MFC-actuators this leads to

$$\begin{aligned}
[M_{j,\mathrm{c}}]_{i,m} &= \rho_j A_j \int_0^{\ell} \phi_{j,i}\phi_{j,m}\,\mathrm{d}z, \quad [M_{j,\mathrm{a}}]_{i,m} = \sum_k^{p_j} \Big(\rho_{j,\mathrm{a}_k} A_{j,\mathrm{a}_k} \int_{z_{j,\mathrm{a}_k}}^{z_{j,\mathrm{a}_k}+\ell_{\mathrm{a}}} \phi_{j,i}\phi_{j,m}\,\mathrm{d}z\Big),\\
[M_{j,m_j}]_{i,m} &= m_j \phi_{j,i}(\ell)\phi_{j,m}(\ell),
\end{aligned} \tag{C.2}$$

$$\begin{aligned}
[C_{j,\mathrm{c}}]_{i,m} &= \int_0^{\ell} \gamma_{\mathrm{c}}^{\mathrm{sv}}(z^1)\partial_z\phi_{j,i}\partial_z\phi_{j,m} + \gamma_{\mathrm{c}}^{\mathrm{v}}(z^1)\phi_{j,i}\phi_{j,m}\,\mathrm{d}z,\\
[C_{j,\mathrm{a}}]_{i,m} &= \sum_k^{p_j} \Big(\int_{z_{j,\mathrm{a}_k}}^{z_{j,\mathrm{a}_k}+\ell_{\mathrm{a}}} \gamma_{\mathrm{a}_k}^{\mathrm{sv}}(z^1)\partial_z\phi_{j,i}\partial_z\phi_{j,m} + \gamma_{\mathrm{a}_k}^{\mathrm{v}}(z^1)\phi_{j,i}\phi_{j,m}\,\mathrm{d}z\Big),
\end{aligned} \tag{C.3}$$

$$\begin{aligned}
[K_{j,\mathrm{c}}]_{i,m} &= E_j^{1111} I_j \int_0^{\ell} \partial_z^2\phi_{j,i}\partial_z^2\phi_{j,m}\,\mathrm{d}z, \qquad [K_{j,\mathrm{a}}]_{i,m} = \sum_k^{p_j} \Big(E_{j,\mathrm{a}_k}^{1111} I_{j,\mathrm{a}_k} \int_{z_{j,\mathrm{a}_k}}^{z_{j,\mathrm{a}_k}+\ell_{\mathrm{a}}} \partial_z^2\phi_{j,i}\partial_z^2\phi_{j,m}dz\Big),\\
[K_{\mathrm{sp,pre},j}]_{i,m} &= k_{j-1,j}\phi_{j-1,i}(\ell_{j-1})\phi_{j,m}(\ell_j), \quad [K_{\mathrm{sp,mid},j}]_{i,m} = (k_{j-1,j} + k_{j,j+1})\phi_{j,i}(\ell_j)\phi_{j,m}(\ell_j),\\
[K_{\mathrm{sp,post},j}]_{i,m} &= k_{j,j+1}\phi_{j+1,i}(\ell_{j+1})\phi_{j,m}(\ell_j).
\end{aligned} \tag{C.4}$$

Here, $\{\{\phi_{j,i}\}_j^r\}_i^{N_j}$ denotes the finite set of test functions chosen as the first N_j eigenfunctions of the undamped beam (B.15). In addition, for the spring constant of the first and the last beam holds $k_{0,1} = k_{r,r+1} = 0$.

Analog, the elements of the input vectors follow as

$$[\boldsymbol{l}_{j,\mathrm{a}_k}]_i = -\Gamma_{j,\mathrm{a}_k} \int\limits_{z_{j,\mathrm{a}_k}}^{z_{j,\mathrm{a}_k}+\ell_\mathrm{a}} \partial_z^2 \phi_{j,i}\,\mathrm{d}z. \tag{C.5}$$

C.2. Surface Interconnected Beam Structure

Subsequently the elements of the mass, damping and the stiffness matrix introduced in Section 2.1.3.4 by (2.91) are summarized. The structure of the matrices is given by

$$M_j = M_{j,c} + M_{j,a}, \quad C_j = C_{j,c} + C_{j,a}, \quad K_j = K_{j,c} + K_{j,a}, \tag{C.6}$$

where the second index characterizes the component of the structure, c denotes the carrier structure and a denotes the MFC-actuator. The elements are determined by the evaluation of the integrals over the beam's length or the evaluation of products of test functions at specific locations, see (2.90) considering Definition 2.1. Hence, for the structure composed by $j \in \{1,2\}$ beams yields

$$[M_{j,c}]_{i,m} = \rho_j A_j \int\limits_0^{\ell} \phi_{j,i}\phi_{j,m}\,\mathrm{d}z, \quad [M_{j,a}]_{i,m} = \rho_{j,a} A_{j,a} \int\limits_{z_{j,\mathrm{a}_k}}^{z_{j,\mathrm{a}_k}+\ell_\mathrm{a}} \phi_{j,i}\phi_{j,m}\,\mathrm{d}z, \tag{C.7}$$

$$[C_{j,c}]_{i,m} = \int\limits_0^{\ell} \gamma_j^{sv}\partial_z\phi_{j,i}\partial_z\phi_{j,m} + \gamma_j^{v}\phi_{j,i}\phi_{j,m}\,\mathrm{d}z, \quad [C_{j,a}]_{i,m} = \int\limits_{z_{j,\mathrm{a}_k}}^{z_{j,\mathrm{a}_k}+\ell_\mathrm{a}} \gamma_{j,a}^{sv}\partial_z\phi_{j,i}\partial_z\phi_{j,m} + \gamma_{j,a}^{v}\phi_{j,i}\phi_{j,m}\,\mathrm{d}z, \tag{C.8}$$

$$[K_{j,c}]_{i,m} = E_j^{1111} I_j \int\limits_0^{\ell} \partial_z^2\phi_{j,i}\partial_z^2\phi_{j,m}\,\mathrm{d}z, \quad [K_{j,a}]_{i,m} = E_{j,\mathrm{a}_k}^{1111} I_{j,\mathrm{a}_k} \int\limits_{z_{j,\mathrm{a}_k}}^{z_{j,\mathrm{a}_k}+\ell_\mathrm{a}} \partial_z^2\phi_{j,i}\partial_z^2\phi_{j,m} dz. \tag{C.9}$$

The elements of the second order input vector of the system $\boldsymbol{l}_j$ and the constraining vector which induces the constraining forces $\boldsymbol{f}_j$ can be displayed as

$$[\boldsymbol{l}_j]_m = (-1)^j \Gamma_{j,\mathrm{a}_k}(z^1) \int\limits_{z_{j,\mathrm{a}_k}}^{z_{j,\mathrm{a}_k}+\ell_\mathrm{a}} \partial_z^2\phi_{j,m}\,\mathrm{d}z, \tag{C.10}$$

$$[\boldsymbol{f}_j]_m = (-1)^{j+1}\big(\mathrm{c}_\Theta\phi_{j,m}(\ell) + (\hbar_j/2)\mathrm{s}_\Theta\partial_{z1}\phi_{j,m}(\ell)\big). \tag{C.11}$$

The substitutions of (2.95) result in

$$\begin{aligned} \boldsymbol{c}_{p_j}^T &= \kappa_p^{-1}\boldsymbol{g}_j^T M_j^{-1}\big(K_j - C_j M_j^{-1} C_j M_j^{-1}\big), \quad & \boldsymbol{k}_{p_j}^T &= \kappa_p^{-1}\boldsymbol{g}_j^T M_j^{-1} C_j M_j^{-1} K_j, \\ b_{p_j} &= \kappa_p^{-1}\boldsymbol{g}_j^T M_j^{-1} C_j M_j^{-1}\boldsymbol{l}_j, & b_{dp_j} &= \kappa_p^{-1}\boldsymbol{g}_j^T M_j^{-1}\boldsymbol{l}_j, \\ \eta_p &= \kappa_p^{-1}\big(\boldsymbol{g}_1^T M_1^{-1} C_1 M_1^{-1}\boldsymbol{f}_1 + \boldsymbol{g}_2^T M_2^{-1} C_2 M_2^{-1}\boldsymbol{f}_2\big), \end{aligned} \tag{C.12}$$

with $\kappa_p = \boldsymbol{g}_1^T M_1^{-1}\boldsymbol{f}_1 + \boldsymbol{g}_2^T M_2^{-1}\boldsymbol{f}_2$.

The matrix elements of (2.99) are given by

$$\begin{aligned} A_x &= \begin{bmatrix} 0 & I \\ -A_{MK} & -A_{MC} \end{bmatrix}, \text{ with} \\ A_{MK} &= \mathrm{diag}\{M_1^{-1}K_1, M_2^{-1}K_2\} \quad A_{MC} = \mathrm{diag}\{M_1^{-1}C_1, M_2^{-1}C_2\}, \end{aligned} \tag{C.13}$$

$$\begin{aligned} B_x &= \begin{bmatrix} \boldsymbol{b}_{1,x} & \boldsymbol{b}_{2,x} \end{bmatrix}, \text{ with} \\ \boldsymbol{b}_{1,x}^T &= \begin{bmatrix} 0 & 0 & -M_1^{-1}\boldsymbol{l}_1 & 0 \end{bmatrix}, \quad \boldsymbol{b}_{2,x}^T = \begin{bmatrix} 0 & 0 & 0 & -M_2^{-1}\boldsymbol{l}_2 \end{bmatrix}, \end{aligned} \tag{C.14}$$

$$\boldsymbol{\alpha}_{xp}^T = \begin{bmatrix} 0 & 0 & M_1^{-1}\boldsymbol{f}_1 & M_2^{-1}\boldsymbol{f}_2 \end{bmatrix}, \tag{C.15}$$

$$\boldsymbol{\alpha}_{px}^T = \begin{bmatrix} -\boldsymbol{k}_{p_1}^T & -\boldsymbol{k}_{p_2}^T & \boldsymbol{c}_{p_1}^T & \boldsymbol{c}_{p_2}^T \end{bmatrix}, \tag{C.16}$$

$$\boldsymbol{b}_p^T = \begin{bmatrix} -b_{p_1} & -b_{p_2} \end{bmatrix}, \tag{C.17}$$

where I denotes the identity matrix.

C.3. Wingsail

Subsequently the mass, stiffness and input matrix of the finite dimensional description of the equations of motion (2.124) are introduced considering [120, chap. 16]

$$M = \sum_{i=1} M_i = \sum_{i=1} \int_{\Omega_i} \rho_i \Phi_i(z)^T \Phi_i(z) \, \mathrm{d}\Omega_i, \tag{C.18}$$

$$K = \sum_{i=1} K_i = \sum_{i=1} \int_{\Omega_i} \lambda_i \mathrm{Tr}\big(\partial_z \Phi_1(z)\big) I + \mu \Big(\partial_z \Phi_1(z) + \big(\partial_z \Phi_1(z)\big)^T \Big) \, \mathrm{d}\Omega_i, \tag{C.19}$$

$$L = \int_{\Gamma_{2,\mathrm{f}}} \beta \partial_z \Phi_1(z) \, \mathrm{d}\Gamma_{2,\mathrm{f}} - \int_{\Gamma_{2,\mathrm{r}}} \beta \partial_z \Phi_1(z) \, \mathrm{d}\Gamma_{2,\mathrm{r}}, \tag{C.20}$$

where the considered domains of the wingsail structure are the sailing area, the four supply beams as well as the four MFC-patches $i \in \{\mathrm{ws}, \mathrm{s}_1, \ldots, \mathrm{s}_4, \mathrm{a}\}$, respectively. Furthermore, $\Gamma_{2,\mathrm{f}}$, $\Gamma_{2,\mathrm{r}}$ denote the actuated boundaries, which means the front and the rear surface of the voltage actuated MFC-actuators. It has to be mentioned that the temporal differentiation of the force which acts in the weak form (2.118) is assumed to be zero $\partial_t \boldsymbol{f}_\Gamma(t, \boldsymbol{z}) = \boldsymbol{0}$. This assumption is based on the previously discussed reaction time of the mechanical and the electric part of the structure.

As discussed in Section 2.2.2 the damping matrix results in

$$C = \sum_{i=1} \Big(\gamma_i^{\mathrm{v}} M_i + \gamma_i^{\mathrm{kv}} K_i \Big), \tag{C.21}$$

due to the beneficial characteristic of the considered Rayleigh damping (2.112), see also [77, chap. 7] and [120, chap. 16].

Finally, it has to be mentioned that the Dirichlet boundary condition describing the clamping of the wingsail at the mast has to be included. For this purpose different methods exist to properly include the Dirichlet condition like Nitsche's method and the penalized Robin boundary condition. However, in case of the used FE framework *Firedrake* a gradient-based nonlinear solver is used to consider the Dirichlet conditions. Further information is provided in [46].

List of Abbreviations

BC	boundary conditions
BDF	backward differentiation formulas
BLMVM	bound-constrained limited-memory variable-metric method
CAD	computer aided design
DAE	differential algebraic equations
DoF	degrees of freedom
FD	finite-difference
FE	finite element
FEM	finite element method
IC	initial condition
KKT	Karush-Kuhn-Tucker
LQR	linear quadratic regulator
MFC	macro-fiber composite
MOR	model order reduction
MPC	model predictive control
ODE	ordinary differential equations
PCA	principal component analysis
PDE	partial differential equation
POD	proper orthogonal decomposition
UAV	unmanned aerial vehicle
SVD	singular value decomposition

Bibliography

[1] Airbus Operations GmbH. "Wing unit's aerodynamic characteristics adapting device for e.g. aircraft, has winglet rotatable in relation to wing unit, such that angle between rotary axis and main direction of extension of unit differs from specified degree". Englisch, German. Patent DE102005028688A1. 2006.

[2] F. Allgöwer et al. "Nonlinear Predictive Control and Moving Horizon Estimation - An Introductory Overview". In: *Advances in Control: Highlights of ECC'99*. Edited by P. M. Frank. London: Springer London, 1999, pages 391–449.

[3] F. Allgöwer and A. Zheng, editors. *Nonlinear Model Predictive Control*. Basel: Birkhäuser, 2012.

[4] J. Andrej, D. Siebelts, and A. Kater. *firedrake backend based model order reduction tools based on Proper Orthogonal Decomposition*. Nov. 2018. DOI: 10.5281/zenodo.1684236.

[5] A. C. Antoulas. *Approximation of Large-Scale Dynamical Systems*. Volume 53. SIAM, 2005, page 479. DOI: 10.1017/CBO9781107415324.004. arXiv: arXiv:1011.1669v3.

[6] K. J. Åström and B. Wittenmark. *Computer-Controlled Systems: Theory and Design, Third Edition*. Dover Books on Electrical Engineering. Dover Publications, 2011, page 555. DOI: 10.1002/1521-3773(20010316)40:6<9823::AID-ANIE9823>3.3.CO;2-C. arXiv: arXiv:1011.1669v3.

[7] U. Ayachit. *The ParaView Guide: A Parallel Visualization Application*. USA: Kitware, Inc., 2015.

[8] S. Balay et al. *PETSc Users Manual*. Technical report ANL-95/11 - Revision 3.7. Argonne National Laboratory, 2016.

[9] H. T. Banks, R. C. H. del Rosario, and H. T. Tran. "Proper orthogonal decomposition-based control of transverse beam vibrations: experimental implementation". In: *IEEE Transactions on Control Systems Technology* 10.5 (2002), pages 717–726. DOI: 10.1109/TCST.2002.801793.

[10] H. Banks, R. Smith, and Y. Wang. *Smart Material Structures: Modeling, Estimation and Control*. Chichester: John Wiley & Sons, 1996.

[11] S. Barbarino et al. "A Review of Morphing Aircraft". In: *Journal of Intelligent Material Systems and Structures - J INTEL MAT SYST STRUCT* 22 (Aug. 2011). DOI: 10.1177/1045389X11414084.

[12] M. Bazaraa, H. Sherali, and C. Shetty. *Nonlinear Programming: Theory and Algorithms*. Wiley, 2006.

[13] G. D. Blasio, K. Kunisch, and E. Sinestrari. "Mathematical Models for the Elastic Beam with Structural Damping". In: *Applicable Analysis* 48.1-4 (1993), pages 133–156. DOI: 10.1080/00036819308840155.

[14] R. Boas. *Entire Functions*. New York: Academic Press Inc., 1954.

[15] M. Böhm et al. "Delay Compensation for Real Time Disturbance Estimation at Extremely Large Telescopes". In: *IEEE Transactions on Control Systems Technology* 25.4 (2017), pages 1384–1393. DOI: 10.1109/TCST.2016.2601627.

[16] M. Böhm et al. "Real-time vibration compensation for large telescopes". In: *Monthly Notices of the Royal Astronomical Society* 442.3 (2014), pages 2446–2455. DOI: 10.1093/mnras/stu1012.

[17] S. Brenner and L. Scott. *The Mathematical Theory of Finite Element Methods*. Texts in Applied Mathematics. Springer New York, 1996.

[18] A. E. Bryson. *Applied Linear Optimal Control: Examples and Algorithms*. Cambridge: Cambridge University Press, 2002. DOI: 10.1115/1.1579457.

[19] R. Cagienard et al. "Move blocking strategies in receding horizon control". In: *Journal of Process Control* 17.6 (2007), pages 563–570.

[20] E. Camacho and C. Bordons. *Model Predictive Control*. London: Springer- Verlag, 2007, page 422.

[21] J. Carlos Gomez and E. Garcia. "Morphing unmanned aerial vehicles". In: *Smart Materials and Structures* 20 (Sept. 2011), page 103001. DOI: 10.1088/0964-1726/20/10/103001.

[22] Y. Chahlaoui et al. "Second-Order Balanced Truncation". In: *Linear Algebra and Its Applications* 415.2-3 (2006), pages 373–384. DOI: 10.1016/j.laa.2004.03.032.

[23] D. Chandrasekharaiah and L. Debnath. *Continuum Mechanics*. Academic Press, 1994.

[24] G. Chen and D. L. Russell. "A Mathematical Model for Linear Elastic Systems with Structural Damping". In: *The Quarterly of Applied Mathematics* 39.4 (1981), pages 433–454.

[25] O. Civalek and Çiğdem Demir. "Buckling and bending analyses of cantilever carbon nanotubes using the Euler-Bernoulli beam theory based on non-local continuum model". In: *Asian Journal of Civil Engineering* 12 (Sept. 2011).

[26] COMSOL Inc. *COMSOL Multiphysics*. `https://www.comsol.com/`. 2019.

[27] R. F. Curtain and H. Zwart. *An Introduction to Infinite-dimensional Linear Systems Theory*. New York, NY, USA: Springer-Verlag New York, Inc., 1995.

[28] G. L. C. De Abreu and J. F. Ribeiro. "A self-organizing fuzzy logic controller for the active control of flexible structures using piezoelectric actuators". In: *Applied Soft Computing* 1.4 (2002), pages 271–283.

[29] M. Delfour and M. Polis. "On Issues Related to Stabilization of Large Flexible Structures". In: *Control and Estimation in Distributed Parameter Systems*. Edited by H. Banks. Frontiers in Applied Mathematics. Philadelphia: Society for Industrial and Applied Mathematics, 1992. Chapter 2, pages 41–84.

[30] O. Dorn and D. Lesselier. "Level Set Methods for Inverse Scattering". In: *Inverse Problems* 22.4 (2006). DOI: `10.1088/0266-5611/22/4/R01`.

[31] dSPACE GmbH - Product Information. *MicroLabBox*. www.dspace.com. Paderborn, 2017.

[32] A. Fichtner, H. P. Bunge, and H. Igel. "The Adjoint Method in Seismology. I. Theory". In: *Physics of the Earth and Planetary Interiors* 157.1-2 (2006), pages 86–104. DOI: `10.1016/j.pepi.2006.03.016`.

[33] R. Findeisen and F. Allgöwer. "An Introduction to Nonlinear Model Predictive Control". In: *21st Benelux Meeting on Systems and Control* 20 (2002), pages 119–141.

[34] M. Fliess et al. "Flatness and Defect of Non–linear Systems: Introductory Theory and Examples". In: *Int. J. Control* 61 (1995), pages 1327–1361.

[35] FreeCAD. *FreeCAD project*. `http://www.freecadweb.org/`. 2019.

[36] W. Freitag and S. Terry. "Blended winglets improve performance". In: *Aeromagazine Boeing* QTR 3/09 (Jan. 2009), pages 9–12.

[37] C. Führer and B. Leimkuhler. "Numerical Solution of Differential-Algebraic Equations for Constrained Mechanical Motion". In: *Numerische Mathematik* 59.1 (1991), pages 55–69.

[38] O. Ş. Gabor, A. Koreanschi, and R. M. Botez. "Aerodynamic analysis of upper surface wing morphing efficiency for the S4 Éhecatl unmanned aerial system". In: (2016), pages 185–194. DOI: `10.1109/ICUAS.2016.7502530`.

[39] N. R. Gauger. "The Adjoint Approach in Aerodynamic Shape Optimization". In: *D L R - Forschungsberichte*. Edited by N. Kroll and J. K. Fassbender. Berlin, Heidelberg: Springer Berlin Heidelberg, 2003, pages 181–193.

[40] A. Gelb. *Applied Optimal Estimation*. Applied Optimal Estimation. MIT Press, 1974.

[41] I. Gohberg and M. Krein. *Introduction to the Theory of Linear Nonselfadjoint Operators*. Rhode Island: American Mathematical Society, 1969.

[42] L. Grüne and J. Pannek. *Nonlinear Model Predictive Control*. London: Springer-Verlag, 2011.

[43] M. Gunzburger. *Perspectives in Flow Control and Optimization*. Advances in Design and Control. Society for Industrial and Applied Mathematics, 2002. DOI: `10.1137/1.9780898718720`.

[44] B.-Z. Guo. "On the Boundary Control of a Hybrid System with Variable Coefficients". In: *Journal of Optimization Theory and Applications* 114.2 (2002), pages 373–395.

[45] B. Guo and H. Zwart. "Riesz spectral systems". In: *Faculty of Mathematical Sciences, University of Twente The Netherlands* Memorandum (2001).

[46] D. A. Ham et al. *Firedrake Manual*. https://www.firedrakeproject.org/documentation.html: Departments of Mathematics, Computing, et al., 2019.

[47] J. Hetrick et al. "Flight Testing of Mission Adaptive Compliant Wing". In: Apr. 2007. DOI: `10.2514/6.2007-1709`.

[48] A. C. Hindmarsh et al. “SUNDIALS: Suite of Nonlinear and Differential/Algebraic Equation Solvers”. In: *ACM Transactions on Mathematical Software* 31.3 (2005), pages 363–396. DOI: 10.1145/1089014.1089020.

[49] G. Holzapfel. *Nonlinear Solid Mechanics: A Continuum Approach for Engineering*. West Sussex, 2000. DOI: 10.1023/A:1020843529530. arXiv: arXiv:1511.03484v1.

[50] M. Homolya et al. *TSFC: A Structure-preserving Form Compiler*. 2017. arXiv: 1705.03667 [cs.MS].

[51] T. Ivanco et al. “Validation of the Lockheed Martin Morphing Concept with Wind Tunnel Testing”. In: *48th AIAA/ASME/ASCE/AHS/ASC Structures, Structural Dynamics, and Materials Conference* (2007).

[52] C. L. J. Ahrens B. Geveci. *ParaView and An End-User and Tool for Large and Data Visualization*. Technical report. Los Alamos National Laboratory, 2005.

[53] B. Jacob, C. Trunk, and M. Winklmeier. “Analyticity and Riesz Basis Property of Semigroups Associated to Damped Vibrations”. In: *Journal of Evolution Equations* 8.2 (2008), pages 263–281. DOI: 10.1007/s00028-007-0351-6. arXiv: 0703247v1 [arXiv:math].

[54] J. M. Jani et al. “A review of shape memory alloy research, applications and opportunities”. In: *Materials & Design (1980-2015)* 56 (2014), pages 1078 –1113. DOI: https://doi.org/10.1016/j.matdes.2013.11.084.

[55] M. Kamlet. *NASA Flight Tests Advance Research of Flexible, Twistable Wing Flaps for Improved Aerodynamic Efficiency*. online. 2017.

[56] A. Kater and T. Meurer. “Flachheitsbasierte Bewegungsplanung für gekoppelte elastische Balken (Flatness-Based Motion Planning for Coupled Elastic Beams)”. In: *at-Automatisierungstechnik* 63.3 (2015), pages 684–699.

[57] A. Kater and T. Meurer. “Modelling and Flatness-based Motion Planning for an Interconnected Flexible Beam Structure”. In: *IEEE Conference on Decision and Control (CDC Las Vegas)* 55 (2016), pages 520–525. DOI: 10.1109/CDC.2016.7798321.

[58] A. Kater and T. Meurer. “Motion planning and tracking control for coupled flexible beam structures”. In: *Control Engineering Practice* 84 (2019), pages 389 –398. DOI: https://doi.org/10.1016/j.conengprac.2018.12.012.

[59] A. Kater, J.-P. Wriedt, and T. Meurer. “Finite Element Modeling and Motion Planning of an Adaptive Elastic Wingsail”. In: *IFAC-PapersOnLine* 50.1 (2017). 20th IFAC World Congress, pages 6768 –6773. DOI: https://doi.org/10.1016/j.ifacol.2017.08.1194.

[60] J. Kautsky and K. N. Nichols. “Robust Pole Assignment in Linear State Feedback”. In: *Int. J. Control, 41* (May 1985), pages 1129–1155. DOI: 10.1080/0020718508961188.

[61] T. Knüppel and F. Woittennek. “Control Design for Quasi-linear Hyperbolic Systems with an Application to the Heavy Rope”. In: *IEEE Transactions on Automatic Control* 60.1 (2015), pages 5–18. DOI: 10.1109/TAC.2014.2336451.

[62] A. Kugi, D. Thull, and K. Kuhnen. “An Infinite–Dimensional Control Concept for Piezoelectric Structures with Complex Hysteresis”. In: *Struct. Control Health Monit.* 13.6 (2006), pages 1099–1119.

[63] A. Kugi. *Non-linear control based on physical models*. Springer-Verlag London, 2001.

[64] A. Kugi and K. Schlacher. “Passivitätsbasierte Regelung piezoelektrischer Strukturen”. In: *at - Automatisierungstechnik* 50.9_2002 (2002), page 422.

[65] P. Kunkel and V. Mehrmann. *Differential-Algebraic Equations: Analysis and Numerical Solution*. Zurich: European Mathematical Society Publish House, 2006.

[66] K. T. Ladas and A. J. Devaney. “Generalized ART algorithm for diffraction tomography”. In: *Inverse Problems* 7.1 (1991), pages 109–125. DOI: 10.1088/0266-5611/7/1/011.

[67] J. A. Laub and M. Wette. “Algorithms and software for pole assignment and observers. Revision 1”. In: *UCRL-15646 Rev. 1, EE Dept., Univ. of Calif., Santa Barbara, CA* (Jan. 1985).

[68] J. H. Lee et al. “Improving computational efficiency of model predictive control algorithm using wavelet transformation”. In: *International Journal of Control* 61.4 (1995), pages 859–883.

[69] B. Y. Levin. *Lectures on Entire Functions*. Rhode Island: American Mathematical Society, 1996, page 248.

[70] F. L. Lewis, L Xie, and D Popa. *Optimal and Robust Estimation: With an Introduction to Stochastic Control Theory*. Second Edi. Automation and Control Engineering. CRC Press, 2008.

[71] J. Lin and W. Z. Liu. "Experimental evaluation of a piezoelectric vibration absorber using a simplified fuzzy controller in a cantilever beam". In: *Journal of Sound and Vibration* 296.3 (2006), pages 567–582.

[72] Q. Liu and J. Tromp. "Finite-frequency kernels based on adjoint methods". In: *Bulletin of the Seismological Society of America* 96.6 (2006), pages 2383–2397. DOI: 10.1785/0120060041.

[73] J. Lunze. *Regelungstechnik 2: Mehrgrößensysteme, Digitale Regelung*. Springer-Lehrbuch. Springer Berlin Heidelberg, 2013.

[74] Z. H. Luo, B. Z. Guo, and O. Morgul. *Stability and Stabilization of Infinite Dimensional Systems with Applications*. London: Springer-Verlag, 1999.

[75] J. Maciejowski. *Predictive Control with Constraints*. Harlow: Prentice Hall, 2002.

[76] J. Marsden and T. Hughes. *Mathematical Foundations of Elasticity*. New-York: Dover Publications, Inc., 1983.

[77] L. Meirovitch. *Principles and Techniques of Vibrations*. New Jersey: Prentice Hall, 1997.

[78] T. Meurer. *Control of Higher–Dimensional PDEs: Flatness and Backstepping Designs*. Communications and Control Engineering Series. Springer–Verlag, 2013.

[79] T. Meurer. "Flatness-Based Trajectory Planning for Diffusionreaction Systems in a Parallelepipedon - A Spectral Approach". In: *Automatica* 47.5 (2011), pages 935–949. DOI: 10.1016/j.automatica.2011.02.004.

[80] T. Meurer, D. Thull, and A. Kugi. "Flatness–based tracking control of a piezoactuated Euler–Bernoulli beam with non–collocated output feedback: theory and experiments". In: *Int. J. Contr.* 81.3 (2008), pages 475–493.

[81] T. F. Miller, F. Gandhi, and R. J. Rufino. "Morphing hull implementation for unmanned underwater vehicles". In: *Smart Materials and Structures* 22.11 (2013), page 115014. DOI: 10.1088/0964-1726/22/11/115014.

[82] J. J. Moré and D. J. Thuente. "Line search algorithms with guaranteed sufficient decrease". In: *ACM Transactions on Mathematical Software* 20.3 (1992), pages 286–307. DOI: 10.1145/192115.192132.

[83] T. Munson et al. *Toolkit for Advanced Optimization (TAO) Users Manual*. Technical report ANL/MCS-TM-322 - Revision 3.5. Argonne National Laboratory, 2014.

[84] N. Newmark. "A Method of Computation for Structural Dynamics". In: *Journal of the Engineering Mechanics* 85.7 (1959), pages 67–94. DOI: 0.1016/j.compgeo.2015.08.008.

[85] P. Olver and C. Shakiban. *Applied Linear Algebra*. Prentice Hall, 2006.

[86] K. Ou and A. Jameson. "Unsteady adjoint method for the optimal control of advection and Burgers' equations using high order spectral difference method". In: *49th AIAA Aerospace Sciences Meeting*. January. 2011, pages 1–18.

[87] A. Preumont. *Vibration Control of Active Structures, An Introduction 3rd Edition*. Berlin: Springer, 2011.

[88] Z. Qiu, X. Zhang, and C. Ye. "Vibration suppression of a flexible piezoelectric beam using BP neural network controller". In: *Acta Mechanica Solida Sinica* 25.4 (2012), pages 417–428.

[89] F. Rathgeber et al. "Firedrake: automating the finite element method by composing abstractions". In: *ACM Trans. Math. Softw.* 43.3 (2016), 24:1–24:27. DOI: 10.1145/2998441. arXiv: 1501.01809.

[90] J. B. Rawlings and D. Q. Mayne. *Model Predictive Control: Theory and Design*. Madison, Wisconsin: Nob Hill Publishing, 2009.

[91] J. N. Reddy. *Energy Principles and Variational Methods in Applied Mechanics*. 2nd. Hoboken: John Wiley & Sons, 2002.

[92] T. Reis and T. Stykel. "Balanced Truncation Model Reduction of Second-Order Systems". In: *Mathematical and Computer Modelling of Dynamical Systems* 14.5 (2008), pages 391–406. DOI: 10.1080/13873950701844170.

[93] U. Release et al. *Dakota, A Multilevel Parallel Object-Oriented Framework for Design Optimization, Parameter Estimation, Uncertainty Quantification, and Sensitivity Analysis: Version 6.6 Theory Manual*. Technical report July 2014. Albuquerque: Sandia National Laboratories, 2017, page 104.

[94] P. Rosenzweig. “Model Predictive Control of Piezoelectric Structures”. Master’s thesis. Christian-Albrechts-Universität zu Kiel, 2016.

[95] P. Rosenzweig, A. Kater, and T. Meurer. “Model predictive control of piezo-actuated structures using reduced order models”. In: *Control Engineering Practice* 80 (2018), pages 83 –93. DOI: https://doi.org/10.1016/j.conengprac.2018.08.001.

[96] D. L. Russell. “On Mathematical Models for the Elastic Beam with Frequency-Proportional Damping”. In: *Control and Estimation in Distributed Parameter Systems*. Edited by H. T. Banks. Frontiers in Applied Mathematics. Philadelphia: Society for Industrial and Applied Mathematics, 1992. Chapter 4, pages 125–170. DOI: 10.1137/1.9781611970982.ch4.

[97] B. Schörkhuber, T. Meurer, and A. Jüngel. “Flatness of Semilinear Parabolic PDEs - A Generalized Cauchy-Kowalevski Approach”. In: *IEEE Transactions on Automatic Control* 58.9 (2013), pages 2277–2291. DOI: 10.1109/TAC.2013.2256013.

[98] J. Schröck. *Mathematical Modeling and Tracking Control of Piezo-actuated Flexible Structures*. Modellierung und Regelung komplexer dynamischer Systeme. Shaker, 2012.

[99] J. Schröck, T. Meurer, and A. Kugi. “Control of a Flexible Beam Actuated by Macro-Fiber Composite Patches – Part I: Modelling and Feedforward Trajectory Control”. In: *Smart Mater. Struct.* 20.1 (2011). Article 015015 (7 pages).

[100] J. Schröck, T. Meurer, and A. Kugi. “Control of a Flexible Beam Actuated by Macro-Fiber Composite Patches – Part II: Hysteresis and Creep Compensation, Experimental Results”. In: *Smart Mater. Struct.* 20.1 (2011). Article 015016 (11 pages).

[101] J. Schröck, T. Meurer, and A. Kugi. “Motion Planning for Piezo-Actuated Flexible Structures: Modeling, Design, and Experiment”. In: *IEEE Transactions on Control Systems Technology* 21.3 (2013), pages 807–819. DOI: 10.1109/TCST.2012.2196043.

[102] W. Schulz et al. *Physik für Ingenieure*. Springer-Lehrbuch. Springer Berlin Heidelberg, 2007.

[103] D. Siebelts. “Systems Design, Modeling and Control of an Artificial Fish”. Master’s thesis. Christian-Albrechts-Universität zu Kiel, 2017.

[104] D. Siebelts, A. Kater, and T. Meurer. “Modeling and Motion Planning for an Artificial Fishtail”. In: *IFAC-PapersOnLine* 51.2 (2018). 9th Vienna International Conference on Mathematical Modelling, pages 319 –324. DOI: https://doi.org/10.1016/j.ifacol.2018.03.055.

[105] Smart Materials GmbH. *Datasheet*. http://www.smart-material.com. 2014.

[106] E. Stanewsky. “Adaptive wing and flow control technology”. In: *Progress in Aerospace Sciences - PROG AEROSP SCI* 37 (Oct. 2001), pages 583–667. DOI: 10.1016/S0376-0421(01)00017-3.

[107] M. H. Straathof, G Carpentieri, and M. J. L. Van Tooren. “Aerodynamic shape optimization using the adjoint Euler equations”. In: *Engineering Computations (Swansea, Wales)* 30.4 (2013), pages 469–493. DOI: 10.1108/02644401311329334.

[108] Tamarack Aerospace Group Inc. “Adjustable lift modification wingtip”. English, German, French. Patent EP2881322A1. 2017.

[109] R. Temam and A. Miranville. *Mathematical Modeling in Continuum Mechanics*. Second Edi. Cambridge: Cambridge University Press, 2005. DOI: 10.1017/CBO9780511755422.

[110] E. D. Valentina. *Adaptive Bulb Concepts*. online. Feb. 2019.

[111] M. Y. Van Vorst and D. G. “Tutorial on the continuous and discrete adjoint state method and basic implementation”. In: *CREWES Research Report* 22 (2010), pages 1–11.

[112] S. Volkwein. *Model Reduction Using Proper Orthogonal Decompostion*. University of Konstanz - Lecture Notes. Feb. 2018.

[113] S. Volkwein. *Proper Orthogonal Decomposition: Theory and Reduced-Order Modelling*. University of Konstanz - Lecture Notes. Aug. 2013.

[114] L. Wang. *Model Predictive Control System Design and Implementation Using MATLAB*. London: Springer- Verlag, 2009, page 403.

[115] J. Wloka. *Partial Differential Equations*. Cambridge: Cambridge University Press, 1987.

[116] J.-P. Wriedt. “Modellierung und Regelung flexibler Strukturen unter Verwendung von FEM-Werkzeugen”. Master’s thesis. Christian-Albrechts-Universität zu Kiel, 2016.

[117] C. Yan, H. Xiao-qing, and M. You-fa. "Coupling vibration of vehicle-bridge system". In: *Applied Mathematics and Mechanics* 25.4 (2004), pages 390–395. DOI: 10.1007/BF02437522.

[118] G. D. Zhang and B. Z. Guo. "On the Spectrum of Euler-Bernoulli Beam Equation with Kelvin-Voigt Damping". In: *Journal of Mathematical Analysis and Applications* 374.1 (2011), pages 210–229. DOI: 10.1016/j.jmaa.2010.08.070.

[119] X. Zhu and H. Hao. "Damage detection of bridge beam structures under moving loads". In: *Conference Proceedings of the Society for Experimental Mechanics Series* (2007).

[120] O. Zienkiewicz, R. Taylor, and J. Zhu. *The Finite Element Method: Its Basis and Fundamentals*. 6. Elsevier Science, 2005.

Index